MINISTÉRIO DA EDUCAÇÃO
UNIVERSIDADE FEDERAL DO RIO GRANDE DO SUL
PROGRAMA DE PÓS-GRADUAÇÃO EM ENGENHARIA MECÂNICA

MODELAGEM DA FORMAÇÃO DE FULIGEM BASEADA NO MÉTODO DAS SEÇÕES: EFEITOS DO CO2 E ACOPLAMENTO COM A TÉCNICA FGM

por

Cristian Alex Hoerlle

Tese para obtenção do Título de
Doutor em Engenharia

Porto Alegre, Fevereiro de 2020

MODELAGEM DA FORMAÇÃO DE FULIGEM BASEADA NO MÉTODO DAS SEÇÕES: EFEITOS DO CO2 E ACOPLAMENTO COM A TÉCNICA FGM

por

Cristian Alex Hoerlle
Mestre

Tese submetida ao Corpo Docente do Programa de Pós-Graduação em Engenharia Mecânica, PROMEC, da Escola de Engenharia da Universidade Federal do Rio Grande do Sul, como parte dos requisitos necessários para a obtenção do Título de

Doutor em Engenharia

Área de Concentração: Energia

Orientador: Prof. Dr. Fernando Marcelo Pereira

Aprovada por:

Prof. Dr. Luis F. F. da Silva .... PEM / PUC-Rio

Prof. Dr. Francis H. R. França .... PROMEC / UFRGS

Profa. Dra. Thamy C. Hayashi .... DEMEC / UFRGS

Prof. Dr. Andreas Mendiburu .... PROMEC / UFRGS

Prof. Dr. fernando Marcelo Pereira
Coordenador do PROMEC

Porto Alegre, 04 de Fevereiro de 2020

AGRADECIMENTOS

Essa Tese de Doutorado não poderia ter sido produzida sem a ajuda de muitas pessoas: professores, colegas, amigos e família. Eu gostaria de agradecer o Prof. Dr. Fernando Marcelo Pereira, meu orientador, por suas contribuições, seu tempo e dedicação durante a realização deste trabalho, e ao Prof. Dr Jeroen van Oijen (Universidade de Tecnologia de Eindhoven) pelo auxílio com a técnica FGM. Também gostaria de expressar meus agradecimentos aos demais integrantes do Laboratório de Combustão pelas produtivas discussões, cobranças e também pelos momentos de descontração. Todos contribuíram muito para meu desenvolvimento profissional e pessoal. Também agradeço a CAPES pelo auxílio financeiro e a equipe do Departamento de Engenharia Mecânica - UFRGS - pelo auxílio institucional.

Por último e mais importante, deixo o mais caloroso obrigado ao meu pai Pércio, a minha mãe Cledi e a minha irmã Sara pela confiança, compreensão e incentivo; e em especial, a minha namorada Camila pelo amor, apoio, senso de humor e otimismo que me dão energias para seguir em frente e tornam minha vida muito mais agradável.

Ratificando, a todas estas pessoas que contribuíram, de maneira direta ou indireta, para o sucesso de mais essa etapa na minha vida: muito obrigado.

RESUMO

Regulamentações relacionadas as emissões de fuligem estão se tornando mais restritivas devido ao impacto negativo da fuligem no meio ambiente e na saúde humana. Desta forma, a massa total de fuligem e o tamanho das partículas emitidas devem ser controlados. Novas tecnologias de combustão, como *oxy-fuel* aliado a recirculação de gases de exaustão, tem demonstrado um grande potencial de redução da formação de poluentes. Neste contexto, este trabalho explora os efeitos da adição do CO_2 na formação de fuligem em chamas de etileno enriquecidas em oxigênio. Chamas unidimensionais laminares contra-corrente foram estudadas numericamente considerando cinética química detalhada, modelos avançados de radiação térmica e o método das seções para a formação de fuligem. O método das seções contabiliza processos físicos (nucleação, condensação e coagulação) e químicos (crescimento superficial e oxidação) da formação da fuligem e é capaz de descrever a distribuição de distintos tamanhos de partículas. A radiação é resolvida através da equação da transferência radiante considerando o modelo da soma ponderada dos gases cinzas (WSGG) ou o método linha-por-linha (LBL) para a integração espectral. Os efeitos químicos, termo-físicos e radiantes do CO_2 sobre formação de fuligem foram investigados através da adição de CO_2 nas misturas de combustível e oxidante. Foi observado que o CO_2 suprime a formação e o crescimento dos PAHs, levando a redução da produção de fuligem. Enquanto os efeitos químicos são mais importantes para a supressão dos PAHs quando o CO_2 é adicionado ao oxidante, efeitos químicos e termo-físicos são igualmente importantes quando o CO_2 é adicionado ao combustível. Em ambos os casos, efeitos químicos são mais significativos para a supressão da formação de fuligem. Uma vez que modelos globais de radiação térmica devem ser capazes de predizer adequadamente a estrutura de chamas, soluções obtidas com o modelo WSGG de superposição foram comparadas com soluções empregando a integração LBL. Pela primeira vez a abordagem LBL é empregada de forma acoplada com modelo detalhado de cinética química e o método das seções. Observou-se que o modelo WSGG de superposição obteve resultados similares aqueles encontrados com a integração LBL para a estrutura geral da chama e as predições de fuligem. Também foi mostrado que a reabsorção de radiação pelo meio participante é fundamental para as predições de fuligem, mesmo para baixos níveis de adição de CO_2. No entanto, essas simulações detalhadas são computacionalmente demandantes mesmo para simulações unidimensionais. Visto que as técnicas *flamelets* são capazes de modelar a cinética química detalhada de forma eficiente e acurada, simulações numéricas também foram conduzidas visando explorar a modelagem da formação de fuligem utilizando a técnica *Flamelet-Generated Manifold* (FGM). Os resultados indicaram que a técnica FGM, considerando efeitos de difusão preferencial e a abordagem simplifica de PAHs agrupados (atuando como conexão entre a fase gás e sólida), foi capaz de prever a formação de fuligem para uma ampla faixa de taxas de deformação de chamas planas (sem efeitos de curvatura) quando comparadas com simulações detalhadas. Por outro lado, a técnica FGM, considerando um manifold formado somente por chamas planas, capturou apenas qualitativamente os processos de formação de fuligem em chamas curvadas, demonstrando a necessidade de expandir o manifold atual para contabilizar os efeitos de curvatura. Ainda é importante ressaltar que a técnica FGM foi aproximadamente três vezes mais rápida que a abordagem de cinética química detalhada para as simulações da formação de fuligem, e aproximadamente setenta vezes mais rápida quando somente a fase gás foi resolvida.

Palavras-chave: Método das Seções para fuligem; WSGG/LBL; Flamelet-Generated Manifold; Diluição com CO2; Chamas laminares contra-corrente não pré-misturadas.

ABSTRACT

Soot emissions severely damage the environment and human health. Thus, total mass and particles size of soot released from hydrocarbon combustion has to be controlled and reduced. Combustion technologies such as oxygen-enriched and oxyfuel allied with flue gas recirculation have demonstrated their potential for reducing pollutants. In this context, this work explores the effect of CO_2 addition on the soot formation process under an oxygen enriched atmosphere. A set of one-dimensional laminar counterflow ethylene flames are numerically studied accounting for detailed chemistry together with an advanced model for thermal radiation and the discrete sectional model for soot formation. The radiation is solved by the radiative transfer equation with with the superposition weight-sum-of-gray-gases (WSGG) model or the line-by-line (LBL) approach for the spectral integration. The effects of CO_2 on soot formation was addressed for CO_2 addition on either the fuel and on the oxidizer mixtures and different contributions by chemical, thermophysical and radiation effects were identified. It was observed that CO_2 suppresses the formation of PAHs building block species, leading to a suppression of larger PAHS and, consequently, in the soot formation. Regarding the suppression of larger PAHs formation, it was found that whereas chemical effects played a major role for the CO_2 addition on the oxidizer side, both chemical and thermophysical effects are important for CO_2 addition on the fuel side. Soot is mainly suppressed by chemical effects of CO_2 addition. Since, global radiative models should be able to reproduce detailed radiation simulations at conditions found in flames, solutions with the global superposition WSGG radiation model were compared to the LBL integration. For the first time, the LBL radiation model was coupled to detailed chemical kinetics and the discrete sectional model. It was observed that the superposition WSGG model is able to accurately describe general flame structure and soot predictions respective to the LBL integration approach for the current flames and that radiation reabsorption is important for soot predictions even for low levels of CO_2 addition. However, those detailed simulations of soot formation are computationally intensive even for one-dimensional simulations. Because flamelet techniques are powerful tools for modelling complex chemical kinetics with efficiency and good accuracy, numerical investigations were also conducted to gain insight about the soot formation modelling with the Flamelet-Generated Manifold (FGM) technique. The results indicated that the

FGM technique, considering differential diffusion effect and the solution of lumped PAHs (acting as a link between the gas- and the solid-phases), was able to predict soot formation over a wide range of strain rates for flat (zero curvature) flames when compared to detailed simulations. On the other hand, curved flames obtained with a manifold formed solely by flat flamelets showed that soot formation was only qualitatively reproduced by the technique, making clear the necessity of expanding the current manifold to take into account curvature effects. It is worth pointing out that the FGM technique was up to three times faster than the detailed approach for soot modeling, and up to seventy times faster when only the gas-phase was solved.

Keywords: Soot Sectional Method; Flamelet-Generated Manifold; WSGG/LBL radiation models; CO2 dilution; Laminar counterflow non-premixed flame.

INDEX

LIST OF FIGURES

LIST OF TABLES

LIST OF ACRONYMS AND ABBREVIATIONS

CFD	Computational Fluid Dynamics
CHEM1D	One-dimensional laminar flame code
DOM	Discrete Ordinates Method
DSM	Discrete Sectional Method
PROMEC	Programa de Pós-Graduação em Engenharia Mecânica
FGM	Flamelet-Generated Manifold
FPI	Flame Prolongation of the ILDM
FPV	Flamelet/Progress Variable Model
HACA	H-abstraction-C_2H_2-addition
LBL	Line-by-Line
L.H.S.	Left Hand Side
MOM	Method of Moments
OTA	Optically Thin Approximation
PAH	Polycyclic Aromatic Hydrocarbon
PBE	Population Balance Equation
PSDF	Particle Size Distribution Function
R.H.S.	Right Hand Side
SLFM	Steady Laminar Flamelet model
SR	Surface Reactions
RTE	Radiative Transfer Equation
ULFM	Unsteady Laminar Flamelet model
UFRGS	Universidade Federal do Rio Grande do Sul
WSGG	Weighted-Sum-of-Gray-Gases

LIST OF SYMBOLS

Latin Symbols

a	Strain rate, 1/s
c_p	Specific heat capacity at constant pressure of the mixture, J/(g K)
$c_{p,i}$	Specific heat capacity at constant pressure of species i, J/(g K)
C_1	Sutherland's constant (1.4558E-5), g/(cm s K^0.5)
C_2	Sutherland's reference temperature (110.4), K
$C_{\kappa,s}$	Soot radiation dimensionless constant, -
C_{P2}	Second Plank's constant (1.4388), cm K
C_{S_i}	Cunningham slip factor, -
$\mathrm{d}_{Y_{cv}}$	Preferential diffusion of control variables, g/(cm s)
D_p	Soot particle diameter, cm
$\mathcal{D}_{i,j}$	Ordinary binary diffusion coefficients of species i into species j, cm^2/s
$\mathcal{D}_{i,M}$	Mixture-averaged diffusion coefficient, cm^2/s
$\mathcal{D}_{s,i}$	Soot diffusion coefficient of particle class ith, cm^2/s
E_a	Activation energy, J/mol
f_v	Soot volume fraction, -
$\vec{g}$	Gravitational acceleration, $\mathrm{cm/s}^2$
h	Total specific enthalpy of the mixture, J/g
h_i	Specific enthalpy of species i, J/g
h_i^0	Specific enthalpy of formation of species i, J/g
$\hat{I}$	Identity tensor, -
I_b	Total blackbody intensity, $\mathrm{W/cm}^2$
I_i	Partial intensity related to the ith gray gas, $\mathrm{W/cm}^2$
I_η	Spectral intensity, $\mathrm{W/(m^2\ cm^{-1}\ )}$
I_η, b	Spectral blackbody intensity, $\mathrm{W/(m^2\ cm^{-1}\ )}$
k	Flame curvature, 1/cm k_B
k_{ss}	Steady-state constant for soot surface reactions, -
K	Stretch rate, 1/s

K_c	Equilibrium constant, -
K_n	Knudsen number, -
Le_i	Lewis number of species i, -
$Le_{Y_{cv}}$	Lewis number of control variables, -
m	Mass burning rate, g/(cm)^2 s)
MW_i	Molecular weight of species i, g/mol
MW	Molecular weight of the mixture, g/mol
$\mathcal{M}_i$	Species i, -
$\vec{n}$	Normal vector, -
$\bar{n}_{C_{atoms}}$	Average number of carbon atoms
n_i	Soot number density distribution of section i
$\mathcal{N}_A$	Avogadro's number (6.022×10^{26}), particles/mol
$\mathcal{N}_{cv}$	Number of control variables, -
$\mathcal{N}_j$	Number of gray-gases of the participating species i, -
$\mathcal{N}_{j_m}$	Number of gray-gases of the mixture, -
$\mathcal{N}_l$	Number of directions, -
$\mathcal{N}_{pc}$	Number of polinomial constants, -
$\mathcal{N}_r$	Number of reactions, -
$\mathcal{N}_s$	Number of species, -
$\mathcal{N}_{sec}$	Number of sections, -
N_i	Number density of particle (molecule) i, units/cm^3
p	Pressure of the mixture, N/m
p_i	Partial pressure of species i, N/m
p_0	Ambient pressure, atm
P_i	Partial pressure of species i, atm
q_i	Soot volume fraction density of section i
$Q_{s,i}$	Soot volume fraction of particles size class i, -
$\dot{Q}_i$	Soot source term of particles size class i, cm$^3_{soot}$/(cm^3 s)
$\dot{q_R}$	Radiation heat source term, W/cm^3
$\vec{q}$	Heat flux vector, W/cm^2
R_u	Universal gas constant, J/(mol K)
S	Specific soot surface area, cm^2/cm^3

s	Coodinate perpendicular to the flame front, cm
t	Time, s
T	Temperature, K
T^{ref}	Reference temperature, K
T_∞	Ambient temperature, K
$\vec{v}$	Flow velocity vector, cm/s
v_C	Volume of carbon atom, cm^3
$\vec{V_c}$	Diffusion velocity correction
v_i	Volume of section i , cm^3
$\vec{V_i}$	Molecular diffusion velocity vector of species i, cm/s
v_T	Thermophoretic velocity of the soot particles, cm/s
x	Cartesian coordinate, cm
X_i	Molar fraction of species i, -
$\mathcal{Y}$	Progress variable, mol/g
Y_i	Mass fraction of species i, -
$Y_{s,i}$	Soot mass fraction of particles size class i, -
Z	Mixture fraction, -
Z_j	Element mass fraction of element j, -
Z_t	Transported mixture fraction, -

Greek Symbols

α	Steric factor, -
α_i	Weight factor of species i, mol/g
β	Collision frequency factor, 1/s
$\beta^{1...4}$	Coagulation coefficients, -
$\chi_{C_{soot}}$	Number of sites on soot surface (2.3E+15), sites/cm^2
$\chi_{C^*_{soot}}$	Number of radical sites on soot surface, sites/cm^2
$\Delta\dot{Q}_i$	Rate of change of soot volume in section i, cm$^3_{soot}$/(cm^3 s)
$\epsilon_{i,j}$	Van der Waals coagulation enhanced factor, -
η	Wavenumber, 1/cm
θ	Spliting factor of the coagulation model, -
γ_l	Cosine in the l direction, -
κ	Absorption coefficient of the mixture, 1/m
κ_i	Absorption coefficient of species i, Pa/m
λ	Thermal conductivity coefficient, W/(cm K)
λ_i	Thermal conductivity coefficient of species i, W/(cm K)
μ	Dynamic viscosity, g/(cm s)
μ_i	Dynamic viscosity of species i, g/(cm s)
ν	Stoichiometric oxidizer-to-fuel ratio, -
$\nu_{i,j}$	Stoichiometric number of moles of species i participating in the reaction j, -
$\dot{\omega}_i$	Reaction source term of the species i, g/(cm^3 s)
$\bar{\dot{\omega}}_i$	Molar reaction rate of the species i, mol/(cm^3 s)
Φ_{kj}	Dimensionless quantity, -
ρ	Mixture density, g/cm^3
ρ_i	The partial density of species i, g/cm^3
ρ_s	Soot density, g/cm^3
σ	Stefan-Boltzmann constant (5.669×10^{-8}), W/(cm^2 K^4)
$\vec{\tau}$	Stress tensor, N/cm^2
ς	Flame surface are function, cm^2
φ	Generic scalar, -

1 THESIS CONTEXT

The world energetic matrix depends mostly on combustion processes. The energy provided by combustion represents approximately 80% of the braziliam energetic matrix [IEA, 2016] and 90% of the world total energy supply [EPE, 2016]. Among the flame types, non-premixed flames present a prominent position given their extensive usage in industrial applications. Those flames present a yellowish luminosity owing to their high soot load and, consequently, intense heat thermal radiation emission. Soot is formed by solid particles composed of carbon (with additional elements in small quantities, such as hydrogen and oxygen) and exist as individual spherical particles (of the order of 10 nm) or in the form of agglomerated particles (with size up to 1 μm).

These particles can be dispersed through long-range in the air and are easily inhaled, becoming a great concern for human health and for the environment contamination [Lighty et al., 2000; Seaton and Donaldson, 2005; Kum, 2009; Shrestha et al., 2010; Kim et al., 2013]. They are toxic, carcinogenic, mutagenic and responsible for many respiratory and heart illnesses. Environmentally, soot particles can cause haze and produce deposits of solid matter that contaminates soils and river basins. In addition, soot also plays a role in the global warming and climate change in two ways: atmospheric soot particles absorbs solar radiation and directly heat the atmosphere, and soot deposits changes the Earth's surface albedo increasing its absorptivity. The strong adverse effect of soot particles has led to restricted legislation governing soot emissions. The EURO5 norm of 2009 (European emission standards), for example, constrains soot emission in five times up to one order lower than EURO4 (2004) and limits the number of particles emitted. The more recent EURO6 focus on the reduction of nitrogen oxides, maintaining the limits of particulate matter.

Soot solid particles emit radiation in a broad wavelength range. Thus, the presence of soot significantly increase the thermal radiation emission in combustion devices. This heat transfer, for example, is undesirable for gas-turbines and diesel engines because of the reduction of devices performance. On the other hand, it may be beneficial for industrial furnaces that require high heat transfer rates.

1.1 Effect of CO_2 on soot formation

New combustion technologies have demonstrated to be good strategies in reducing pollutants while improving combustion efficiency. Such technologies include oxygen-enriched flames [Baukal Jr, 2010; Escudero et al., 2016] and oxyfuel flames [Nemitallah et al., 2017; Zhang et al., 2018], which can be allied with flue gas recirculation. In oxy-combustion technologies, the high oxygen concentration accelerates the fuel consumption and increases the flame temperature. This condition is very favorable to the formation of soot, but at some level the oxygen enrichment can also promote soot oxidation in the post flame region [Zhang et al., 2018; Hwang and Chung, 2001; Kalvakala et al., 2018]. Therefore, higher local peaks of soot volume fraction can be achieved while the release of soot to the atmosphere may be suppressed. Complementary, the recirculation of combustion products, principally dry CO_2, helps to control flame temperature, enhances radiation heat transfer and drops the generation of NO_x by reducing both the temperature and the nitrogen content of the mixture. Moreover, oxy-combustion technologies, allied to flue gas recirculation, facilitate the carbon dioxide capture and storage [Boot-Handford et al., 2014; Underschultz et al., 2016]. Significant amounts of CO_2 are also frequently found in renewable fuels such as biogas or syngas. Despite the peculiarities of each combustion process and fuel composition, in all of them CO_2 plays an important role.

The amount of CO_2 influences the combustion process in several ways. CO_2 dilution limits the concentration of reactants, participates in elementary reactions and changes the thermodynamic properties (mainly to its higher heat capacity when compared to N_2) and by modifying the transport properties of the mixture [Du et al., 1991; Liu et al., 2001]. CO_2 also acts as a participating species in radiative heat transfer [Dorigon et al., 2013; Cassol et al., 2014]. As a consequence, the CO_2 is found to reduce the soot volume fraction by limiting the formation of soot precursors and species responsible for surface growth [Liu et al., 2001; Guo and Smallwood, 2008; Wang and Chung, 2016a; Naseri et al., 2017] due to chemical and thermodynamic effects. The multiple effects of CO_2 addition, in the fuel and oxidizer mixtures, on flame behavior has been explored by many investigators. However, a direct comparison of CO_2 addition on the fuel or on the oxidizer side has to be carefully interpreted because the same CO_2 molar fraction on the fuel or oxidizer streams represents two very distinct flame conditions. A better comparison between fuel/oxidant dilution can be obtained by considering flames with the same amount of CO_2 in a stoichiometric mixture of fuel and oxidant, according to Hoerlle et al., 2017. There is still room for further clarification on the detailed mechanisms through which the CO_2 influences the sooting flame structure.

1.2 Detailed modelling of soot formation

The development of efficient and low emission combustion processes and devices makes the ability to predict soot formation and thermal radiation to be crucial for industrial applications. Models for soot formation and radiation emission are complex due to the strong solid-gas phase iterations and the iteration among physical (particles collisions), chemical (particles surface reactions) and thermal sub-process. Since chemical kinetics is strongly dependent on the system temperature, the adequate prediction of the radiation relies on an adequate prediction of soot yield, that also depends on a good description of the chemical kinetics of the gas phase. All these phenomena are strongly coupled and occur simultaneously with the flow that, in general, is turbulent. Although much progress has been made to deepen the knowledge in soot formation [Kennedy, 1997; Richter and Howard, 2000; Frenklach, 2002b; Mansurov, 2005; Wang, 2011; Modest and Haworth, 2016a,b], many details of these phenomena remain not well understood, for example, the exact transition process from PAH to first particles, the effect of ageing in surface sites, the intermediate process between the limits of pure aggregation and pure coalescence for particles coagulation and the clusters radiation properties.

The complexity of the soot formation and thermal radiation emission has led to the development of several models that differ in the computational requirements and in the detailing the physical processes considered.

Models for soot formation are grouped in purely empiric, semi-empiric and detailed [Kennedy, 1997]. Empiric and semi-empiric models are based on empirical correlations and can incorporate only simple phenomenological soot formation process, therefore they are limited inherently to specific conditions for which their rates or constants were adjusted. On the other hand, detailed methods can account for poly-dispersed particles by including more sophisticated soot formation processes. This category of soot models deals with the dynamics and the distribution of different particle sizes and with different soot structures, such as the formation of aggregates. Detailed models deal with the dynamics of soot particles with distinct sizes by incorporating physical (nucleation, condensation and coagulation) and chemical (precursors formation, superficial growth and oxidation) processes. Emphasis is given in this work to the Discrete Sectional method [Gelbard et al., 1980; Park and Rogak, 2004; Zhang, 2009; Roy, 2014; Aubagnac-Karkar et al., 2015]. This kind of model proposes a methodology to solve the continuous particle size distribution by discretizing it into in a finite number of sections, each one representing a different particle size. Discrete sectional methods have being successfully used for soot predictions in a wide range of flames conditions [Zhang, 2009; Roy, 2014; Charest et al., 2014; Saffaripour et al., 2014; Liu et al., 2015; Aubagnac-Karkar et al., 2015; Kholghy et al., 2016; Naseri et al., 2017; Aubagnac-Karkar et al., 2018].

The radiation heat transfer is physically represented in detail by the Radiative Transfer Equation (RTE). It describes the variation of the radiation intensity in a participating medium. The models for thermal radiation are classified according to the spectral and the spatial dependency of the phenomenon [Modest, 2003]. For a participating medium that emits, absorbs and scatters thermal radiation, the spectral dependency of the absorption coefficient may be computed through the integration over all spectral lines (line-by-line integration method, LBL, [Taine, 1983]) or, in a more simplified way, by assuming that the radiative spectrum is formed by a finite number of gray gases with constant absorption coefficients (as in the weighted-sum-of-gray-gases model, WSGG, [Hottel and Sarofim, 1967]). The spatial dependency of the radiation transfer phenomenon is solved by integrating the radiative intesities over all directions, where the Discrete Ordinate method [Thynell, 1998] is frequently used to solve the radiation spatial dependency.

The LBL approach can provide solutions with high level of accuracy and can deal with local variation in the thermodynamic state (temperature and concentration of participating species). Since this approach is excessively costly and not feasible for practical applications, it is commonly restricted to be the reference for the development of global radiation models in standard benchmark problems that usually do not take into account the intense gradients of temperature and composition found in real flames. In this way, simpler radiation models are commonly assumed for combustion simulations [Liu et al., 2004; Zhang et al., 2009a; Demarco et al., 2013; Eaves et al., 2015; Zimmer, 2016; Zhang et al., 2018], principally when soot formation is considered. Only few studies have compared different radiation models with the LBL approach in combustion simulations [Centeno et al., 2015, 2016, 2018; Rodrigues et al., 2019] but assuming that the temperature and the composition fields are frozen. Therefore, it is important to evaluate the capabilities of global radiation models (such as the WSGG) relative to the LBL approach when they are coupled with detailed soot formation models to predict soot quantities.

1.3 Soot modelling by flamelet techniques

Detailed soot models require a good prediction of the thermodynamic state of the system and gaseous species related to soot inception, growth and oxidation. It is well known that polycyclic-aromatic-hydrocarbons (PAH) are the main soot precursors. Thus, the necessity to model the growth of hydrocarbon aromatic compounds up to several rings results in large kinetic mechanism that can easily reach hundreds of species and thousands of reactions.

Theoretical studies using large kinetic mechanisms are computationally challenging, specially when dealing with the complexity of detailed soot and thermal radiation models. The high computational time demanded turn the use of such mechanisms inconceivable for most practical and industrial applications. Therefore, techniques to reduce chemical kinetic mechanism have been proposed to overcome these limitations. Such reduction may be obtained by employing steady state and partial equilibrium assumptions, but automatic reduction techniques based on tabulated chemistry are usually preferred. Among the automatic reduction techniques, the flamelet approach is one of the most popular. In this approach, it is assumed that a flame can be represented by several one-dimensional flames (flamelets) whose solutions are stored in look-up tables as function of some controlling variables for further use in the solution of multidimensional flames. One of the most used methods is the Steady Laminar Flamelet Model (SLFM) [Peters, 1984] that is based on the mixture fraction and scalar dissipation rate as controlling variables. Since this approach was developed based on fast chemistry it may be limited and not accurate for the modelling of slow processes like pollutants formation. Thus, Unsteady/Interative Laminar Flamelet Models (ULFM) [Pitsch et al., 1998; Barths et al., 1998] were proposed as an evolution of the SLFM to handle slow processes. The latter concept presents good accuracy in relation to experiments or detailed transport solutions but requires more computational resources than pre-tabulated methods.

There are, however, many different flamelet techniques and forms of building the database. Such approaches include the Flamelet/Progress Variable Model (FPV) [Pierce and Moin, 2004], the Flame-Prolongation of ILDM (FPI) [Gicquel et al., 2000] and the Flamelet-Generated Manifold (FGM) [van Oijen and de Goey, 2000]. These models are very similar, presenting small differences in the flamelet equations and in the code implementation. Both of them are based on pre-tabulating flamelet solutions into a manifold (look-up table) as function of the reaction progress variable. It is a controlling variable that indicates where reactions takes place, mapping though the thermal composition space. For premixed flames the reaction progress variable may be sufficient to map the thermal-composition space, however for non-premixed and partially-premixed flames the mixture fraction becomes an addition controlling variable. According to van Oijen and de Goey, 2000 the FGM technique is able to reduce computational time of multidimensional simulations up to 100 times with good quality results.

Most of the studies about soot formation with flamelet techniques were conducted for Steady [Balthasar et al., 1996; Bai et al., 1998; Demarco et al., 2013; Xuan and Blanquart, 2013, 2014] and Unsteady/Interactive [Mauss et al., 2006; Netzell et al., 2007; Carbonell et al., 2009; Kim and Kim, 2015] Laminar Flamelet models. Soot modelling through the FPV/FPI approaches are limited to a reduced number of works [Ihme and Pitsch, 2008; Mueller and Pitsch, 2012; Lecocq et al., 2014; Yen and Abraham, 2016; Xuan and Blanquart, 2015]. What the author is aware, there are solely few studies on soot [Zimmer, 2016] and PAHs [Verhoeven et al., 2013] formation employing the FGM technique, both for non-premixed coflow flames. Furthermore, for soot formation, the majority of these works implemented semi-empirical models or the Method of Moments and only a reduced number of them implemented a soot Sectional Method [Mauss et al., 2006; Netzell et al., 2007].

Flamelet techniques have been used to simulate sooting flames with a good qualitative accuracy, but there is still no consensus about the best practices. The literature review indicated that a promising approach is to solve transport equations for soot properties with source terms retrieved from flamelet libraries. However, modelling soot formation with flamelet techniques is not so straightforward and some care must be taken into account. Those flamelet techniques are usually employed based on several assumptions that are not truly valid in the context of soot formation, viz.: the assumption of fast-chemistry, the assumption of equal mass and thermal diffusion (i.e., $Le = 1$) for all species and the consideration of only planar flamelets for the construction of the manifolds. Moreover, the coupling between the gas- and the solid-phases which is due to the mass transfer between these two phases usually requires special treatments, mainly regarding soot precursors modelling. Furthermore, there is still scarce information about modelling soot formation together with flamelet concepts, principally in terms of detailed particle dynamics.

1.4 Objectives

The objectives of this research are twofold:

1 To investigate the role of CO_2 addition on soot formation thought detailed simulations. In this context, the role of CO_2 addition on soot formation will be analyzed by exploring its influence on the soot formation processes and thermal radiation while clarifying the peculiarities of fuel and oxidant dilution. Differences between CO_2 addition in the fuel and in the oxidizer mixtures are still not well documented. Numerical studies will be conducted in one-dimensional non-premixed counterflow flames of ethylene under oxyfuel conditions with CO_2 addition. This one-dimensional framework allows the detailed soot formation model to be simultaneously solved with complex chemistry and advanced radiation models (such as the LBL spectral integration) for a wide range of conditions.

2 To build a model for soot prediction based on the Discrete Sectional Method with the gas-phase chemistry described by the Flamelet-Generated Manifold reduction technique. Flamelet techniques are characterized by low computational requirements while keeping results comparable to detailed kinetics. Furthermore, studies of FGM coupling with detailed soot models are very limited in the literature and coupling procedures between these two models are yet not so well explored.

The next steps will be followed to achieve the objectives: (a) to implement a detailed framework for soot prediction based on the Discrete Sectional Method considering advanced thermal radiation models and detailed chemical kinetics, (b) to investigate the CO_2 effects on soot formation processes and on thermal radiation heat losses based on the framework previously implemented and (c) to explore the coupling between the soot Sectional Method with the Flamelet-Generated Manifold technique.

1.5 Thesis outline

Following the Introduction chapter, the manuscript is organized in more six chapters. Chapter 2 describes the formalism for modelling laminar non-premixed flames considering detailed chemical kinetics and thermal radiation. The FGM technique is also presented. Chapter 3 focus in a review of soot formation phenomenological processes and models and describes in details the Discrete Sectional soot model considered in this work. The peculiarities of CO_2 addition in the fuel and in the oxidizer mixtures on the soot formation processes are explored in Chapter 4. Following this context, Chapter 5 studies the effect of CO_2 addition on the thermal radiation and evaluate the superposition WSGG model against the LBL spectral integration. Chapter 6 explores the capabilities of the FGM technique in predicting soot formation considering the discrete sectional method. Chapter 7 concludes this thesis and present some guides for future works.

2 MODELLING OF LAMINAR NON-PREMIXED FLAMES

In this chapter, conservation equations and constitutive relations for modelling laminar non-premixed flames are presented. This study considers that the combustion occurs at atmospheric conditions with the gravitational force being the only body force acting on the flame. Reactive flows are governed by a set of equation that considered the conservation of total mass, of individual chemical species, momentum and energy. This equation system is closed with the equations of estate. Additionally, thermodynamic relations and models for transport properties are required.

2.1 Conservation and balance equations

Total mass conservation equation

The conservation equation of total mass is expressed as

$$\frac{\partial \rho}{\partial t} + \vec{\nabla}.(\rho \vec{v}) = 0, \tag{2.1}$$

where ρ is the mixture density and $\vec{v}$ is the flow velocity vector.

Momentum balance equation

The conservation of the momentum is represented by the Navier-Stokes equation in the compressible form

$$\frac{\partial (\rho \vec{v})}{\partial t} + \vec{\nabla}.(\rho \vec{v} \vec{v}) = -\vec{\nabla} p + \rho \vec{g} + \vec{\nabla}.\hat{\tau}, \tag{2.2}$$

where p is the static pressure and $\vec{g}$ represents the gravitational acceleration. In this equation, the term in parenthesis in the L.H.S. represents the material derivative of the velocity field, i.e., the acceleration of one fluid particle that moves in this field. The R.H.S. of the equation is the summation of the forces (per unit volume) that act on the fluid particle, with the first two terms being the pressure and body forces, respectively, while the remaining terms represent viscous forces.

Balance equation for individual chemical species

The balance equation of the chemical species i in terms of mass fraction (Y_i), is given by

$$\frac{\partial(\rho Y_i)}{\partial t} + \vec{\nabla}.\left(\rho Y_i\left[\vec{v} - \vec{V}_i\right]\right) = \dot{\omega}_i, \tag{2.3}$$

where $\vec{V}_i$ is the diffusion velocity and $\dot{\omega}_i$ is the the net rate of production/consumption of the specie i . The first term in the L.H.S. of the equation represents the time evolution of species i mass fraction, $Y_i = \rho_i/\rho$, with ρ_i being the partial density of species i. The second term in the L.H.S. represents the divergent of the mass flux of the species i. The term on the right hand side is the rate of reaction of species i, which takes into account all elementary reactions where species i is produced or consumed.

Energy Conservation equation

The energy conservation equation can be written in terms of the specific enthalpy of the mixture h, as

$$\frac{\partial(\rho h)}{\partial t} + \vec{\nabla}.(\rho\vec{v}h) = \frac{Dp}{Dt} + \hat{\tau} : \vec{\nabla}\vec{v} - \vec{\nabla}.\vec{q} + \dot{q}_R. \tag{2.4}$$

The L.H.S represents the time evolution of the mixture enthalpy h and its advective transport, respectively. The R.H.S. terms represents the pressure material derivative, the viscous dissipation ($\hat{\tau} : \vec{\nabla}\vec{v}$), the divergent of the heat flux ($\vec{\nabla}.\vec{q}$) and the radiative source term ($\dot{q}_R$) that accounts for thermal radiation emissions from the gas-phase ($\dot{q}_{R,g}$) and the solid-phase ($\dot{q}_{R,s}$). The pressure material derivative is assumed null ($Dp/Dt \simeq 0$) since temporal and spatial variations are negligible for atmospheric flames. The viscous dissipation term is usually neglected since it is very small when compared with the heat released from de flame.

2.2 Constitutive relations

To solve the Equations 2.2 to 2.4 the stress tensor $\hat{\tau}$, the diffusion velocity $\vec{V}_i$, the chemical source term $\dot{\omega}_i$, the heat flux vector $\vec{q}$ and the radiative source term $\dot{q}_R$ must be defined. The chemical source term and the thermal radiation source term are defined in

Section 2.5 and 2.6, respectively.

Stress Tensor

Assuming the Stokes hypothesis for a Newtonian fluid, the viscous stress tensor $\hat{\tau}$ is given by

$$\hat{\tau} = \mu \left[\vec{\nabla}\vec{v} + (\vec{\nabla}\vec{v})^T \right] - \frac{2}{3}\mu(\vec{\nabla}.\vec{v})\hat{I} \tag{2.5}$$

where μ is the dynamic viscosity, $\hat{I}$ is the identity tensor, $\vec{\nabla}\vec{v}$ is the velocity gradient tensor with components $(\partial/\partial x_i)v_j$, $(\vec{\nabla}\vec{v})^T$ is the transpose of the velocity gradient tensor with components $(\partial/\partial x_j)v_i$ and $(\vec{\nabla}.\vec{v})$ is the divergent of the veloctу vector. This term accounts for diffusion of linear momentum.

Diffusion velocity

This study considers that the combustion occurs in atmospheric conditions. In this way, the pressures gradients are small and the diffusion caused by pressure gradients can be neglected. The Soret effect (mass diffusion due to temperature gradients) is only important for species with low molecular weight as in hydrogen combustion. Thus it will also be neglected in the present study. As the body force accounts only for the gravitational force, the influence in the diffusion velocity by the body force term vanishes. With those assumptions, species diffusion occurs solely by concentration gradients. To avoid heavier computations of the Stefan-Maxwell equations, species diffusion in multicomponent mixtures are modelled by the Fick's Law for binary diffusion [Law, 2006]. In this assumption, the diffusion velocity is directly proportional to the concentration gradient of the species i, and it is given by

$$\vec{V_i} = -\frac{\mathcal{D}_{i,M}}{Y_i}\vec{\nabla}Y_i. \tag{2.6}$$

In these expressions, $\mathcal{D}_{i,M}$ is the average mass diffusion coefficient of species i in the mixture, which may be obtained by employing the Hirschfelder and Curtiss approximation [Hirschfelder et al., 1954]:

$$\mathcal{D}_{i,M} = \frac{1 - Y_i}{\sum_{i=1, i\neq j}^{\mathcal{N}_s} \dfrac{X_j}{\mathcal{D}_{i,j}}}. \tag{2.7}$$

where $\mathcal{D}_{i,j}$ can be determined considering the relation for binary mixtures of the Chapman-Enskog theory employing the molecular parameters of Lennard-Jones [Turns, 2000], tabulated as function of the temperature in a polynomial form.

Finally, the species conservation equation (Equation 2.3) is solved for all $\mathcal{N}_s$ species. Thus, the mass conservation ($\sum_{i=1}^{\mathcal{N}_s} Y_i \vec{V_i} = 0$) is guaranteed employing the diffusion velocity correction ($\vec{V_c} = -\sum_{i=1}^{\mathcal{N}_s} Y_i \vec{V_i}$) and assuming that the updated diffusion velocity vector of the species i is equal to

$$\vec{V_i'} = \vec{V_i} + \vec{V_c}, \; i = 1 ... \mathcal{N}_s. \tag{2.8}$$

Usually the diffusion velocity is corrected solely to the abundant species in the mixture (N_2)

Heat Flux

The heat flux vector can be expressed as:

$$\vec{q} = -\lambda \vec{\nabla} T + \sum_{i=1}^{\mathcal{N}_s} \rho \vec{V_i} Y_i h_i, \tag{2.9}$$

where λ is the thermal conductivity and h_i is the specific enthalpy of the chemical species i. The heat flux vector accounts for the conduction heat flux caused by temperature gradients (Fourier's Law, first term in the R.H.S.), and the heat flux through mass diffusion due to the different heat content of the various species (second term in the R.H.S.). The second-order heat flux due to concentration gradients (Dufour effect) is usually neglected in combustion processes.

2.3 Closure models

The equations system formed by the conservation and balance equations plus the constitutive relations is only complete with the following closure models:

Closure of the conservation equations system

The set of differential conservation equations is closed by two state equations (Equations 2.10 and 2.11). The thermal equation of state is given by the ideal gas law in the limit of low-Mach number, so that pressure $p \cong p_0$ is assumed constant and, as consequence, density is only a function of temperature:

$$\rho = \frac{pMW}{R_u T} \cong \frac{p_0 MW}{R_u T} \tag{2.10}$$

where R_u is the universal gas constant.

The calorific equation of state relates the enthalpy to the temperature according to

$$\vec{\nabla} h = c_p \vec{\nabla} T. \tag{2.11}$$

The mixture specific heat at constant pressure, c_p, reads

$$c_p = \sum\nolimits_{i=1}^{\mathcal{N}_s} c_{p,i} Y_i, \tag{2.12}$$

where $c_{p,i}$ is the specific heat at constant pressure of the chemical species i, which is calculated through a polynomial expression as function of temperature.

The effects of chemical reactions in the energy equations are accounted for by the specific enthalpy of the mixture, which is function of the mixture composition according to

$$h = \sum_{i=1}^{\mathcal{N}_s} Y_i h_i, \tag{2.13}$$

with each chemical species enthalpy, h_i, given by

$$h_i = h_{i,f}^0 + \int\limits_{T_{ref}}^{T} c_{p,i}(T)\mathrm{d}T, \tag{2.14}$$

where $h_{i,f}^0$ is the formation specific enthalpy at the reference temperature T_{ref}.

Transport and thermodynamic properties

The mixture's dynamic viscosity (μ) follows from the approximate expression of Wilke, 1950:

$$\mu = \sum_{i=1}^{\mathcal{N}_s} \frac{X_i \mu_i}{\sum_{j=1,j\neq i}^{\mathcal{N}_s} X_j \Phi_{i,j}}, \tag{2.15}$$

where $\Phi_{i,j}$ is dimensionless and defined as

$$\Phi_{i,j} = \frac{1}{\sqrt{8}} \left(1 + \frac{MW_i}{MW_j}\right)^{-1/2} \left[1 + \left(\frac{\mu_i}{\mu_j}\right)^{1/2} \left(\frac{MW_j}{MW_i}\right)^{1/4}\right]^2, \tag{2.16}$$

In this expressions μ_i is the dynamic viscosity of the species i, which is obtained in terms of the Lennard-Jones parameters.

The thermal conductivity (λ) is based on the the semi-empiric formulation of Mathur et al., 1967:

$$\lambda = \frac{1}{2} \left[\sum_{i=1}^{\mathcal{N}_s} X_i \lambda_i + \left(\sum_{n=1}^{\mathcal{N}_s} X_i / \lambda_i\right)^{-1}\right], \tag{2.17}$$

where the species conductivity (λ_i) is obtained from the kinetic theory.

Species transport coefficients

Transport properties can be obtained through the Chapman-Enskog theory [Hirschfelder et al., 1954]. This theory defines transport properties in terms of intermolecular potential energies of collisional molecules, and they are tabulated as a function of temperature in polynomial form:

$$\ln(\mathcal{D}_{i,j}) = \sum_{n=1}^{\mathcal{N}_{pc}} a_{n,ij} (\ln T)^{n-1}, \; i = 1...\mathcal{N}_s - 1, \; j = i+1...\mathcal{N}_s, \tag{2.18}$$

$$\ln(\mu_i) = \sum_{n=1}^{\mathcal{N}_{pc}} b_{n,ij} (\ln T)^{n-1}, \; i = 1...\mathcal{N}_s, \tag{2.19}$$

$$\ln(\lambda_i) = \sum_{n=1}^{\mathcal{N}_{pc}} c_{n,ij} (\ln T)^{n-1}, \; i = 1...\mathcal{N}_s, \tag{2.20}$$

where $\mathcal{N}_{pc}$ is the number of stored values, with $a_{n,ij}$, $b_{n,ij}$ $c_{n,ij}$ being the tabulated values.

2.4 Further approximation: the Lewis number assumption

Alternatively, the diffusive terms can be modelled through the Lewis number. The constant Lewis number approach simplifies significantly the diffusion terms calculation through relating species mass diffusivity to the mixture thermal conductivity. With this approximation, species mass diffusion flux becomes independent of species concentration and of diffusive coefficients, so that the calculation of binaries diffusion coefficients is unnecessary. The Lewis number is defined as

$$Le_i = \frac{\lambda}{\rho c_p \mathcal{D}_{i,M}}, \tag{2.21}$$

Substituting the Lewis number expression in the Equation 2.3, the species mass conservation equation reads

$$\frac{\partial(\rho Y_i)}{\partial t} + \vec{\nabla}.(\rho \vec{v} Y_i) = \frac{1}{Le_i}\vec{\nabla}.\left(\frac{\lambda}{c_p}\vec{\nabla}Y_i\right) + \dot{\omega}_i,\ i = 1...\mathcal{N}_s - 1, \tag{2.22}$$

The species diffusion flux can be rewritten in two parts:

$$\vec{\nabla}\cdot\left(\frac{\lambda}{Le_i c_p}\vec{\nabla}Y_i\right) = \vec{\nabla}\cdot\left(\frac{\lambda}{c_p}\vec{\nabla}Y_i\right) + \vec{\nabla}\cdot\left(\frac{\lambda}{c_p}\left(\frac{1}{Le_i} - 1\right)\vec{\nabla}Y_i\right) \tag{2.23}$$

where the terms in the right-hand side indicates, respectively, the non-preferential diffusion contribution and the preferential diffusion explicitly, i.e. the contribution when $Le_i \neq 1$. Inserting it in Equation 2.22 yields:

$$\frac{\partial(\rho Y_i)}{\partial t} + \vec{\nabla}\cdot(\rho \vec{v} Y_i) = \vec{\nabla}\cdot\left(\frac{\lambda}{c_p}\vec{\nabla}Y_i\right) + \vec{\nabla}\cdot\left(\frac{\lambda}{c_p}\left(\frac{1}{Le_i} - 1\right)\vec{\nabla}Y_i\right) + \dot{\omega}_i. \tag{2.24}$$

Substituting Equation 2.21 in Equation 2.4 and invoking Equation 2.11, the energy conservation equation, after neglecting the pressure variation and the viscous term, becomes

$$\frac{\partial(\rho h)}{\partial t} + \vec{\nabla}.(\rho \vec{v} h) = \vec{\nabla}.\left(\frac{\lambda}{c_p}\vec{\nabla}h\right) + \vec{\nabla}.\left[\sum_{i=1}^{\mathcal{N}_s}\left(\frac{1}{Le_i} - 1\right)\frac{\lambda}{c_p}h_i\vec{\nabla}Y_i\right] + \dot{q}_R''' \tag{2.25}$$

Assuming unity Lewis number ($Le_i = 1$), mass and heat diffuse at the same rate making the heat diffusion in the energy conservation equation to occur only by the Fourier law. The $Le = 1$ approximation does not consider preferential diffusion.

In detriment of the calculation of μ and λ for multicomponent mixtures, it is assumed the approximation proposed by Smooke and Giovangigli, 1991, (for combustion of methane and air) to reduce the computational time. This approximation considers that the mixture dynamic viscosity and conductivity are both functions of the temperature and the specific heat at constant pressure of the mixture according

$$\frac{\mu}{c_p} = 1.67 \times 10^{-8} \left(\frac{T}{298}\right)^{0{,}51} \tag{2.26}$$

$$\frac{\lambda}{c_p} = 2.58 \times 10^{-5} \left(\frac{T}{298}\right)^{0{,}69} \tag{2.27}$$

2.5 Detailed chemical kinetics modelling

This section describes the production and consumption of chemical species in the source term of the conservation equation of chemical species (Equation 2.3). Many elementary chemical reactions occur simultaneously in flame front. In general, those reactions are reversible and both directions have to be accounted for.

One generic chemical reaction j can be written as

$$\sum_{i=1}^{\mathcal{N}_s} \nu'_{i,k} \mathcal{M}_i \rightleftharpoons \sum_{i=1}^{\mathcal{N}_s} \nu''_{i,k} \mathcal{M}_i \tag{2.28}$$

where $\mathscr{M}_i$ represents the molecular formula of the species i, $\nu_{i,j}$ are the stoichiometric coefficients (that indicates how many number of moles of the species i are part of the reaction j), and the indexes $'$ and $''$ indicate the presence of the species in the reactants or in the products, respectively.

Following this notation, the net reaction rate for the j^{th} reaction is

$$\bar{\dot{\omega}}_j = k_{f,j} \prod_{i=1}^{\mathcal{N}_s} [\mathscr{M}_i]^{\nu'_{i,j}} - k_{r,j} \prod_{i=1}^{\mathcal{N}_s} [\mathscr{M}_i]^{\nu''_{i,j}}, \tag{2.29}$$

where the concentration of the species $\mathscr{M}_i$ is given by $[\mathscr{M}_i] = (Y_i MW/MW_i)(p_0/R_u T)$, and k represents the reaction rate coefficient. The subscripts f and r indicates the direct and the reverse ways of reactions, respectively.

The reaction rate coefficient k is given by the modified form of the Arrhenius expression:

$$k = AT^b \mathrm{e}^{-E_a/R_u T}. \tag{2.30}$$

where A is the pre-exponential factor, b is the temperature exponent and E_a is the activation energy. These parameters are determined empirically by adjusting procedures to recover experimental results, or theoretically from fundamental principles (*ab-initio*).

The reverse reaction rate coefficient k_r can be calculated from the equilibrium constant K_c through the Equation 2.31 [Turns, 2000]. In the equilibrium, the rate of change of any species concentration is zero. It results that the ratio between the direct and the reverse rate of reaction is equal to the equilibrium constant $K_{c,j}$ of reaction j.

$$K_{c,j}(T) = \frac{k_{f,j}(T)}{k_{r,j}(T)} = \frac{\prod_{i,j} [\mathcal{M}_i]^{\nu''_{i,j}}}{\prod_{i,j} [\mathcal{M}_i]^{\nu'_{i,j}}}, \tag{2.31}$$

where $K_{c,j}$, in the equilibrium, is calculated by the ratio of the product of products concentration and the product of reactants concentration, and tabulated as function of the temperature.

Lastly, the source term $\dot{\omega}_i$ of Equation 2.3 accounts all $\mathcal{N}_r$ reactions of the chemical kinetic mechanism containing the species i, and is given by

$$\dot{\omega}_i = MW_i \sum_{j=1}^{\mathcal{N}_r} (\nu''_{i,j} - \nu'_{i,j}) \bar{\dot{\omega}}_j. \tag{2.32}$$

Detailed chemical kinetics describes the elementary system of gas-phase interactions in reactive flows. In addition to that, soot is a particulate solid-phase that strongly depends on the chemical-species pool. The mechanisms of soot generation and its interaction with the gas-phase will be described in the Chapter 3.

2.6 Thermal radiation modelling

The radiation heat transfer is calculated by the Radiative Transfer Equation (RTE) [Modest, 2003; Dorigon et al., 2013; Cassol et al., 2014]. It describes the variation of the spectral radiation intensity I_η, for a given wavenumber (η) and direction (Ω), along a path x in the medium. For an absorpting, emitting and non-scattering medium the RTE is written as

$$\frac{\partial I_\eta(x)}{\partial x} = \kappa_\eta(x) I_{\eta b}(x) - \kappa_\eta(x) I_\eta(x), \tag{2.33}$$

where κ_η is the mixture spectral absorption coefficient and $I_{\eta b}$ is the blackbody spectral intensity at local temperature, given by the Plank's distribution law.

The spectral radiation properties (as the spectral absorption coefficient) present a complex dependence with the thermodynamic state (i.e., temperature, pressure and composition) and with the wavenumber, whereas the radiative intensities depend on the absorption and the scattering integration over all directions. Therefore, the RTE needs to be spectrally and spatially integrated to solve the radiative heat transfer problem.

The spectral solution requires the knowledge of the spectral absorption coefficient, which in turn, is dependent on the participating compounds (type and concentration). In combustion processes, CO_2 and H_2O are the main participant species followed by CH_4 and CO. But C_2H_2 and C_2H_4 may also contribute to thermal radiation emissions (up to 30%) at fuel-rich high temperature region of ethylene flames [Qi et al., 2017]. Soot particles also act as a participating compound in thermal radiation processes. Furthermore, gas-phase radiation is limited to specific bands of the spectrum while soot radiative properties are more homogeneous along the wavelength range. Therefore, the presence of soot or higher concentration of participating species, such as H_2O and CO_2, can easily enhance radiation heat transfer in combustion processes.

With the solution of the RTE, the radiative heat fluxes and the volumetric radiative heat source that interacts with the energy conservation equation and the net radiative heat transfer rate can be computed. The volumetric radiative heat source $\dot{q}_R$, present in the energy equation, is computed as the divergent of the radiative flux ($\vec{q_R}$) over the path s

$$\dot{q}_R(x) = -\nabla \cdot \vec{q_R}(x) = \int_\Omega \int_\eta \left(\kappa_\eta(x) I_\eta(x) - \kappa_\eta(x) I_{\eta b}(x)\right) \mathrm{d}\eta \mathrm{d}\Omega \tag{2.34}$$

There are several approaches to solve the radiation heat transfer problem [Modest, 2003]. These models are classified according to the spectral dependency of the absorption coefficient, the spatial integration and the detailing of the thermal radiation phenomena (only emission, emission and absorption, or complete modelling including scattering). The spatial dependence of radiation intensities is commonly solved by means of the Discrete Ordinates Method (DOM) [Thynell, 1998], which discretizes a solid angle in several angular directions over which the radiation intensities are integrated. On the other hand, several methods have been proposed to solve the spectral part of the radiative problem with different degrees of accuracy and computational requirements. A brief description of some of those models can be found in [Modest, 2003; Cassol et al., 2014; Kez et al., 2016]. The line-by-line (LBL) approach consists in integrating the spectral lines of participating compounds over the entire spectrum. This approach can provide solutions with high level of accuracy and can deal with local variation in the thermodynamic state (temperature and concentration of participating species). Nonetheless, it is excessively costly and not feasible for practical applications. In this way, LBL integration of spectral lines is commonly restricted to be the reference for the development of global radiation models in standard benchmark problems. On the other hand, the global weighted-sum-of-gray-gases (WSGG) method [Hottel and Sarofim, 1967] is particularly straightforward for practical engineering applications. Owing to its robustness and simplicity, it presents a high computational efficiency and good accuracy. In the WSGG method, the spectrum is replaced by a few gray-gases (with constant pressure absorption coefficients) plus a transparent window. Thus, the RTE has to be solved only for the gray-gases instead of all spectral lines. The WSGG (standard) relies on fixed mole concentration ratio of H_2O/CO_2, which can limit its application to flames were the global mole concentration ratio of H_2O/CO_2 is not in accordance with the fitted coefficients. Further developments proposed generalizations in the WSGG model to account for non-homogeneities of participating species concentration [Johansson et al., 2011; Kangwanpongpan et al., 2012; Bordbar et al., 2014; Cassol et al., 2014; Centeno et al., 2018]. Particularly, the superposition WSGG method introduced by Cassol *et al.* [Cassol et al., 2014] can be generalized for any arbitrary concentration and combination of participating species because it is based on correlations for each individual participating species. Details about the RTE solution employing the DOM together with the LBL or the WSGG approaches can be found in [Dorigon et al., 2013; Cassol et al., 2014; Centeno et al., 2014; Cassol et al., 2015]. The simplest model is the optically-thin approximation (OTA) [Chen et al., 1993; Barlow, 2020; Modest, 2003; Smooke et al., 1999]. It considers only emissions from gray-gases with Planck mean absorption coefficients (there is no dependence on the wave number) in the limit of an optically-thin medium, i.e., the medium does not scatter nor absorb radiation. The simplicity of this model relies in the fact than the RTE does not have to be solved.

2.6.1 Solution of the Radiative Transfer Equation

The spatial dependency of the radiation intensities is solved by means of the Discrete Ordinates Method (DOM) [Thynell, 1998]. This method discretizes a total solid angle of 4π in several $\mathcal{N}_l$ angular directions over which the radiation intensities are integrated. This work assumes 30 directions following [Dorigon et al., 2013; Cassol et al., 2014]. Based on the DOM, the RTE can be recast for positive and negative directions according to

$$\begin{aligned} +\gamma_l \frac{\mathrm{d}I^+_{\eta,l}(x)}{\mathrm{d}x} &= \kappa_{\eta,m}(x) I_{\eta b}(x) - \kappa_{\eta,m}(x) I^+_{\eta,l}(x) \\ -\gamma_l \frac{\mathrm{d}I^-_{\eta,l}(x)}{\mathrm{d}x} &= \kappa_{\eta,m}(x) I_{\eta b}(x) - \kappa_{\eta,m}(x) I^-_{\eta,l}(x), \end{aligned} \tag{2.35}$$

where γ_l is the directional cosine towards the l direction ($1 \leq l \leq \mathcal{N}_l$). For a one-dimensional slab bounded by black walls, for example, Equation 5.1 are subjected to the following boundary conditions: $I^+_{\eta,l}(x = -L) = I_{\eta b}(x = -L)$ at the left boundary and $I^-_{\eta,l}(x = +L) = I_{\eta b}(x = +L)$ at the right boundary.

After the solution of the spectral radiation intensities for each position s and direction l, the radiation heat flux can be determined by

$$q_R^{''} = \sum_{l=1}^{\mathcal{N}_l} \int_\eta 2\pi w_l \gamma_l \left[I^+_{\eta,l} - I^-_{\eta,l} \right] \mathrm{d}\eta, \tag{2.36}$$

with w_l being the integration weight since the continuous integral over the solid angle is computed by a Gauss-Legendre quadrature scheme. The volumetric radiative heat source corresponds to the divergence of the radiative heat flux with opposite sign, $\dot{q}_R(x) = -\nabla \cdot \vec{q_R}^{''}$, such that:

$$\dot{q}_R = \sum_{l=1}^{\mathcal{N}_l} \int_\eta \left(2\pi \kappa_{\eta,m}(x) w_l \left[I^+_{\eta,l} + I^-_{\eta,l} \right] - 4\pi \kappa_{\eta,m}(x) I_{\eta b}(x) \right) \mathrm{d}\eta. \tag{2.37}$$

In the present work, it is assumed that the medium is formed by a mixture of CO_2, H_2O and soot. Thus, the mixture spectral absorption coefficient $\kappa_{\eta,m}$ is given by a summation of the spectral absorption coefficient of the participating compounds

$$\kappa_{\eta,m}(x) = \kappa_{\eta,H2O}(x) + \kappa_{\eta,CO2}(x) + \kappa_{\eta,soot}(x) \tag{2.38}$$

The solution of Equations 5.2 and 5.3 requires also the integration over the wavenumber η. In this study this is done in two ways: using the line-by-line integration and by means of the superposition weighted-sum-of-gray-gases model.

2.6.1.1 Line-By-Line (LBL) Integration

In the LBL integration, the RTE is solved for each spectral absorption coefficient, and this approach can be considered exact unless for minor numerical approximations in the integration of the lines. The HITEMP 2010 database [Rothman et al., 2010] is used to generate the spectral absorption coefficients for CO_2 and H_2O in a wavenumber range between 0 and 10000 cm^{-1}, with spectral resolution of 0.333 cm^{-1}. It results in a total of 30000 spectral lines that were computed from the Lorentz profile [Modest, 2003]. The H_2O spectral database was generated for partial pressures of 0.01, 0.1, 0.2, 0.6 and 1 atm, and a linear interpolation is used for intermediate partial pressures. On the other hand, the CO_2 database was generated only for 1 atm since it does not present a self-broadening effect, thus a simple linear relation is assumed for other partial pressures [Dorigon et al., 2013; Cassol et al., 2014]. In addition, to avoid excessively high computational time without introducing significant errors, the spectra were generated for the range of 400 K to 2500 K with a temperature interval of 100 K. Finally each database is stored independently of the species partial pressures. Thus, the spectral absorption coefficient of each participating species i (CO_2 and H_2O) is given by $\kappa_{\eta,i} = \kappa_{p,\eta,i} p_i$, where p_i is the partial pressure and $\kappa_{p,\eta,i}$ the pressure absorption coefficient. Due to its small size and concentration, soot can be considered at the same temperature of the flame, emitting thermal radiation in a continuous spectrum in the infrared region. Soot absorption coefficient is frequently represented by a simple linear relation with the wavenumber [Modest, 2003; Abid et al., 2009; Yapp et al., 2015]:

$$\kappa_{\eta,soot}(x) = c_f f_v(x) \eta \tag{2.39}$$

with c_f being a dimensionless constant dependent on the fuel.

2.6.1.2 Weighted-Sum-of-Gray-Gases (WSGG) model

For a participating medium formed by gas-phase species, the WSGG is characterized by representing the entire spectrum by only few $\mathcal{N}_j$ gray-gases with uniform pressure absorption coefficients, $\kappa_{p,i,j}$, plus the transparent windows. The indexes indicate that it is computed for each medium component i and for each gray-gas j. In addition, it is assumed that the pressure absorption coefficient of each gray-gas is independent of the temperature and the participating species partial pressures p_i. Therefore, the absorption coefficient (in units of cm^{-1}) is computed as $\kappa_{i,j} = \kappa_{p,i,j} p_i$.

The WSGG relies on fitting the computed total emittance with the one obtained from the LBL integration of the spectrum, which is done for a set of temperatures and partial pressures path length ($p_i s$). The pressure absorption coefficients and the temperature dependent coefficients, $a_{i,j}(T)$, are obtained from de fitting. The latter one, also known as emission weighting factor, represents the fraction of black body energy that is emitted by each gray-gas, and it is computed by the polynomial function:

$$a_{i,j}(T) = \sum_{n=1}^{\mathcal{N}_{pc}} b_{i,j,n} T^{n-1}, \tag{2.40}$$

where $b_{i,j,n}$'s are the polynomial coefficients of $\mathcal{N}_{pc}$th order for the jth gray-gas. Finally, the radiation energy is conserved assuming the existence of a transparent window, for which the temperature dependent coefficient is computed as $a_{i,0}(T) = 1 - \sum_{j=1}^{\mathcal{N}_j} a_{i,j}(T)$, where $\mathcal{N}_j$ is the number of gray-gases for each participating compound. It is worth noting that the absorption coefficient of the transparent window is null, $\kappa_{i,0} = 0$. The temperature dependent coefficient $a_{i,j}$ is interpreted as the probability of the blackbody energy emitted in the region of the spectrum where the absorption coefficient is $\kappa_{p,i,j}$ [Cassol et al., 2014].

Soot treatment is quite similar to that used for the gas-phase participating species. The soot volume fraction absorption coefficients, $\kappa_{f_v,soot,j}$ and the temperature dependent coefficients, $a_{soot,j}(T)$, are fitted values given in [Cassol et al., 2014], but the soot absorption coefficient is computed by $\kappa_{soot,j}(x) = c_f f_v(x) \kappa_{f_v,soot,j}(x)$. It is worth mentioning that there is no transparent window for soot, therefore $a_{soot,0} = 0$.

The WSGG model [Cassol et al., 2014] for a non-isothermal and non-homogeneous medium with arbitrary concentration of CO_2, H_2O and soot is applied in this work. For each mixture compound it was assumed a total of $\mathcal{N}_j = 4$ gray-gases and a 4th order polynomial temperature dependent coefficient. The fitting coefficients of Equation 2.40 are provided in [Cassol et al., 2014]. This approach relies on the spectral absorption coefficients of the participating species being statistically uncorrelated. Therefore, the mixture absorption coefficient (κ_{m,j_m}) and the emission factor of the mixture (a_{m,j_m}) are given by

$$\begin{aligned} \kappa_{m,j_m}(x) &= \kappa_{H_2O,j_{H_2O}}(x) + \kappa_{CO_2,j_{CO_2}}(x) + \kappa_{soot,j_{soot}}(x), \\ a_{m,j_m}(x) &= a_{H_2O,j_{H_2O}}(x) \times a_{CO_2,j_{CO_2}}(x) \times a_{soot,j_{soot}}(x). \end{aligned} \tag{2.41}$$

The index m, in this case, identifies that the constants are related to the mixture of participating compounds. After combining all the participating compounds, the total number of gray-gases $\mathcal{N}_{j_m}$ would be the product between each individual compound gray-gases plus their transparent windows (soot does not have a transparent window): $\mathcal{N}_{j_m} = (\mathcal{N}_j + 1)_{H_2O} \times (\mathcal{N}_j + 1)_{CO_2} \times (\mathcal{N}_j)_{soot} = 100$. In this way, the radiation energy is conserved, i.e., $\sum_{j_m=1}^{\mathcal{N}_{j_m}} a_{m,j_m}(T) = 1$.

The RTE for the WSGG is given by

$$\begin{aligned} +\gamma_l \frac{\mathrm{d}I^+_{m,j,l}(x)}{\mathrm{d}x} &= \kappa_{m,j}(x) a_{m,j}(x) I_b(x) - \kappa_{m,j}(x) I^+_{m,j,l}(x), \\ -\gamma_l \frac{\mathrm{d}I^-_{m,j,l}(x)}{\mathrm{d}x} &= \kappa_{m,j}(x) a_{m,j}(x) I_b(x) - \kappa_{m,j}(x) I^-_{m,j,l}(x), \end{aligned} \tag{2.42}$$

where $I_b = \sigma T^4/\pi$ is the total blackbody intensity and σ is the Stefan-Boltzmann constant. The one-dimensional RTE is solved after the mixture absorption coefficients and weighting factors are obtained. It leads to the following expressions for the net radiation heat flux and the volumetric heat source, respectively:

$$\begin{aligned} q''_R &= \sum_{l=1}^{\mathcal{N}_l} \sum_{j_m=1}^{\mathcal{N}_{j_m}} 2\pi w_l \gamma_l \left[I^+_{m,j_m,l} - I^-_{m,j_m,l} \right], \\ \dot{q}_R &= \sum_{l=1}^{\mathcal{N}_l} \sum_{j_m=1}^{\mathcal{N}_{j_m}} 2\pi \kappa_{m,j_m}(x) w_l \left(\left[I^+_{m,j_m,l} + I^-_{m,j_m,l} \right] - 2 a_{m,j_m}(x) I_b(x) \right). \end{aligned} \tag{2.43}$$

2.6.2 The Optically-Thin Approximation - OTA

In addition to the detailed solution of the radiative transfer problem, the Optically Thin Approximation [Modest, 2003; Chen et al., 1993] is also considered for comparison. The Optical Thin Approximation (OTA) is largely employed in combustion modelling due to its simplicity and lower computation time [Bedir et al., 1997]. In this model only emission is responsible for the radiative heat transfer (absorption and scattering are neglected). The OTA assumes that the radiation is isotropic and that the participating medium does not interfere in the radiative heat transfer among the hot gases and the neighbor (which is considered a black body). As the radiative heat transfer depend solely on the local conditions of the flame and on the neighbor temperature, the RTE does not need to be solved.

In this approach, the source term of the gas-phase is defined by

$$\dot{q}_{R,g} = -4\sigma\kappa_p(T^4 - T_\infty^4), \tag{2.44}$$

where $\sigma = 5.670 \times 10^{-12}$ (W cm^{-2}K^{-4}) is the Stefan-Boltzmann constant, T and T_∞ are the local and the neighbor temperature, respectively.

The Plank mean absorption coefficient for a mixture of gases $\mathtt{k}_p$ is given by

$$\kappa_p = p_{CO_2}\kappa_{p,CO_2} + p_{H_2O}\kappa_{p,H_2O} + p_{CH_4}\kappa_{p,CH_4} + p_{CO}\kappa_{p,CO}, \tag{2.45}$$

where p_i and $\kappa_{p,i}$ are, respectively, the partial pressure and the Plank absorption coefficient for the chemical species i. For combustion process, it is usually assumed CO_2, H_2O, CH_4 and CO as radiating species.

The Planck mean absorption coefficient of the radiative species are calculated from adjusting a polynomial curve according to Equation 2.46 (for CO_2 and H_2O) and Equation 2.47 (for CH_4 and CO). The polynomials coefficients are presented in the Table 2.1 for CO_2 and H_2O (given in [Chen et al., 1993]) and for CH_4 and CO (given in [Barlow, 2020]).

$$\log_{10}\left(\frac{\kappa_{p,i}}{\kappa_{p,i,ref}}\right) = \sum_{n=0}^{\mathcal{N}_{pc}} a_{i,n}\left(\frac{T}{300}\right)^n, \; i = CO_2 \text{ and } H_2O \tag{2.46}$$

$$\kappa_i = \sum_{n=0}^{\mathcal{N}_{pc}} a_{i,n}T^n, \; i = CH_4 \text{ and } CO \tag{2.47}$$

where $\kappa_{p,i,ref} = 1/(m.atm)$ and $\mathcal{N}_{pc}$ is the number of polynomials coefficients.

The broad band soot thermal radiation is calculated following the formalism presented in [Smooke et al., 1999]. In addition to the fact that soot scattering can be neglected in low to moderate sooting flames, the absorption term may be insignificant when soot takes place only at the higher temperature region of the flame. Based on these premises, the simplest approach to model soot radiation heat losses is to consider a gray-gas approximation in an optically thin limit $\dot{q}_{R,s} = -Cf_vT^5$, with the constant $C = 4.243 \times 10^{-10}$ (W cm^{-3}K^{-5}) taken from Smooke et al., 1999.

Table 2.1 – Polynomial coefficients for the Planck mean absorption coefficient calculation of the emitting chemical species.

	CO_2	H_2O	CH_4	$CO \leq 750$ K	$CO > 750$ K
$a_{i,0}$	0,22317E+01	0,38041E+01	6,6334E+00	4,7869E+00	1,009E+01
$a_{i,1}$	-0,15829E+01	-0,27808E+01	-3,5686E-03	-6,953E-02	-1,183E-02
$a_{i,2}$	0,13296E+01	0,11672E+01	1,6682E-08	2,95775E-04	4,7753E-06
$a_{i,3}$	-0,50707E+00	-0,28491E+00	2,5611E-10	-4,25732E-07	-5,87209E-10
$a_{i,4}$	0,93334E-01	0,38163E-01	-2,6558E-14	2,02894E-10	-2,5334E-14
$a_{i,5}$	-0,83108E-02	-0,26292E-02	-	-	-
$a_{i,6}$	0,28834E-03	0,37774E-04	-	-	-

2.7 The Flamelet-Generated Manifold technique

The Flamelet-Generated Manifold (FGM) is a chemical reduction technique that lies in the assumption that multi-dimensional flames can be represented by a set of one-dimensional flames (*flamelets*). Like others flamelet based models, the FGM is based on the observation that the chemical kinetic process of a multi-dimensional flame can be decoupled from the main flow and mixing process and be represented by several flamelets in a flame-adapted coordinate system according to [Peters, 1984] and [de Goey and ten Thije Boonkkamp, 1999a]. Then, a manifold representing the thermophysical and chemical space is constructed through parametrizing variables of interest by some control variables. The number of control variables define the manifold dimension. Usually two or three dimensions are sufficient to adequately solve most combustion processes, however, manifolds with higher dimensions may be needed for more complex cases.

For adiabatic non-premixed flames the control variables are the mixture fraction (Z) and the progress variable ($\mathcal{Y}$). So, each thermo-chemical variable of interest, φ, becomes a function of the control variables $\varphi = \varphi(Z, \mathcal{Y})$. The enthalpy ($h$) becomes and additional control variable if heat losses would be accounted for, so that $\varphi = \varphi(Z, \mathcal{Y}, h)$. It is important to emphasize that the control variables must result in an unique mapping of the thermal-chemical composition for each combustion process. A more detailed description of the FGM technique is given in the next sections. Figure 2.1 represents the implementation of the FGM technique for the variable φ for a generic adiabatic non-premixed flame. First, hypothetical unidimensional counterflow solutions of the variable φ along position x for several strain rates a are shown. Then, these solutions are stored in the manifold together with transport and thermodynamic properties as function of the control variables. During FGM computations only the total mass, the momentum and the control variables conservation equations are solved and the manifold is constantly accessed to retrieve variables needed for the solution of the equations (such as mixture density, viscosity, conductivity and specific heat at constant pressure). With the convergence of the system, the multi-dimensional flames can be reconstructed by retrieving variables of interest from the manifold based on the control variables solution.

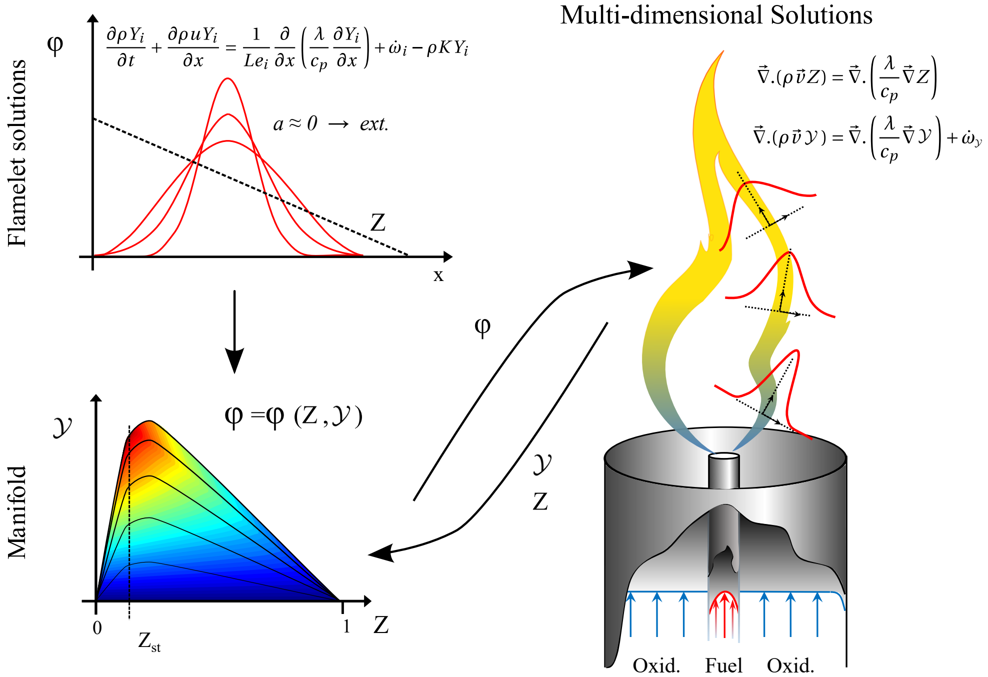

Figure 2.1 – Scheme of the FGM methodology for adiabatic non-premixed flames assuming unity Lewis number.

Flamelets will be created only for one-dimensional counterflow flames in this thesis. Counterflow burners are formed by two opposed nozzles with impinging reactant streams (Figure 2.2). In this case, along the coordinate x, it is assumed that fuel is inject in the left side at the position $-L$ while the oxidant is injected in the right side at the position $+L$. This configuration produces an axi-symmetric flow with an stagnation plane between the injection tubes. The stagnation plane depends on the flow linear momentum from each injection stream. For this flow configuration, radial gradients can be neglected in transport equations since they are much lower than the axial gradients. Therefore, the combustion variables only depend on the coordinate x perpendicular to the flame surface.

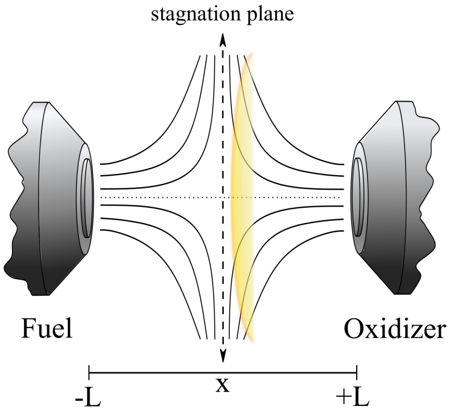

Figure 2.2 – Scheme of a non-premixed counterflow burner.

2.7.1 Flamelet equations

This section summarizes the derivation of the flamelet equation system presented in [de Goey and ten Thije Boonkkamp, 1999a; van Oijen and de Goey, 2000; van Oijen et al., 2016].

The reaction progress variable $\mathcal{Y}$ indicates the progress of the global chemical reaction. It can be defined as a linear combination of species mass fraction:

$$\mathcal{Y} = \sum_{i=1}^{N_s} \alpha_i Y_i, \tag{2.48}$$

where the weighting coefficients α_i are arbitrarily chosen constants.

First, a "flame surface" is defined as an iso-surface of $\mathcal{Y}$, $\mathcal{Y}(x,t) = constant$, and its motion is described by the kinematic equation

$$\frac{\mathrm{d}\mathcal{Y}}{\mathrm{d}t} : \frac{\partial \mathcal{Y}}{\partial t} + (\mathbf{u}_f \cdot \nabla)\mathcal{Y} = 0, \tag{2.49}$$

which states that a point on the flame surface stays on this surface for all t. The local velocity of a flame surface $\mathbf{u}_f$ is given by a balance between the local fluid velocity $\mathbf{u}$ and the local burning velocity s_L:

$$\mathbf{u}_f = \mathbf{u} + s_L \mathbf{n}. \tag{2.50}$$

The burning velocity is defined as the velocity at which the flame surface propagates normal to itself and relative to the flow in the unburnt mixture. Thus, the normal vector

$\mathbf{n}$ is determined from the progress variable field directed to the unburnt gas mixture:

$$\mathbf{n} = -\frac{\nabla \mathcal{Y}}{|\nabla \mathcal{Y}|}. \tag{2.51}$$

Combining Equations 2.49 to 2.51, the kinematic equations of $\mathcal{Y}$ becomes

$$\frac{\partial \mathcal{Y}}{\partial t} + \mathbf{u} \cdot \nabla \mathcal{Y} = s_L |\nabla \mathcal{Y}|. \tag{2.52}$$

Then, de Goey and ten Thije Boonkkamp, 1997, introduced a stretch rate term K as the relative rate of change of mass $M(t)$ (given by $M(t) = \int_{V(t)} \rho dV$) contained in an infinitesimal volume $V(t)$ in the flame moving with the local velocity of the flame surface $\mathbf{u}_f$:

$$K = \frac{1}{M} \frac{\mathrm{d}M}{\mathrm{d}t}. \tag{2.53}$$

Applying the Reynolds' transport theorem to $M(t)$ results in the following equation for K:

$$\rho K = \frac{\partial \rho}{\partial t} + \nabla \cdot (\rho \mathbf{u}_f). \tag{2.54}$$

The expression for the scalar field quantity K (Equation 2.54) can be used together with Equation 2.50 to rewrite the continuity equation (Equation 2.1) to the form

$$\nabla \cdot (\rho s_L \mathbf{n}) = \rho K, \tag{2.55}$$

with the right-hand side term accounting for all deviations from unidimensional flames behavior (as flame curvature, flow straining and additional contributions, for instance due to flame thickness variation). Details about all these deviations can be found in [de Goey and ten Thije Boonkkamp, 1997].

In the next step, based on its definition (Equation 2.48), a transport equation for the progress variable $\mathcal{Y}$ can be rigorously derived from a linear combination of species' conservation equation:

$$\frac{\partial (\rho \mathcal{Y})}{\partial t} + \nabla \cdot (\rho \mathbf{u} \mathcal{Y}) = \nabla \cdot \left(\frac{\lambda}{Le_{\mathcal{Y}} c_p} \nabla \mathcal{Y} \right) + \dot{\omega}_{\mathcal{Y}}. \tag{2.56}$$

Combining Equation 2.56 with Equations 2.50, 2.52 and 2.54 it becomes

$$-\nabla \cdot (\rho s_L \mathbf{n} \mathcal{Y}) - \nabla \cdot \left(\frac{\lambda}{Le_{\mathcal{Y}} c_p} \nabla \mathcal{Y} \right) - \dot{\omega}_{\mathcal{Y}} = -\rho K \mathcal{Y}, \tag{2.57}$$

where all transport contributions along the flame surface are gathered in the term $-\rho K\mathcal{Y}$. According to [de Goey and ten Thije Boonkkamp, 1999a], this equation can be written in quasi-1D form by introducing the arc-length perpendicular to the flame surface s, the measure ς for the area of the flame surface through which transport takes place and the mass burning rate $m = \rho s_L$. The flamelet equation for $\mathcal{Y}$ now reads:

$$\frac{\partial}{\partial s}\left(\varsigma m\mathcal{Y}\right) - \frac{\partial}{\partial s}\left(\varsigma\frac{\lambda}{Le_{\mathcal{Y}}c_p}\frac{\partial\mathcal{Y}}{\partial s}\right) = \varsigma(\dot{\omega}_{\mathcal{Y}} - \rho K\mathcal{Y}). \tag{2.58}$$

Recognizing that the derivative of ς is related to the flame surface curvature k through

$$k = \nabla\cdot\mathbf{n} = -\frac{1}{\varsigma}\frac{\partial\varsigma}{\partial s}, \tag{2.59}$$

Equation 2.58 can be recast to its final form:

$$\frac{\partial}{\partial s}\left(m\mathcal{Y}\right) - \frac{\partial}{\partial s}\left(\frac{\lambda}{Le_{\mathcal{Y}}c_p}\frac{\partial\mathcal{Y}}{\partial s}\right) - \dot{\omega}_{\mathcal{Y}} = -\rho K\mathcal{Y} + kF_{\mathcal{Y}}, \tag{2.60}$$

where the right-hand terms gather all distortions from 1D flat flame behavior. $F_{\mathcal{Y}}$ is introduced to represent the convective and diffusive fluxes of $\mathcal{Y}$:

$$F_{\mathcal{Y}} = m\mathcal{Y} - \frac{\lambda}{Le_{\mathcal{Y}}c_p}\frac{\partial\mathcal{Y}}{\partial s}. \tag{2.61}$$

Similarly to the derivation of Equation 2.60, now, flamelet equations are derived from the three-dimensional conservation equations Equations 2.1, 2.3 and 2.4 [de Goey and ten Thije Boonkkamp, 1999a]. The set of conservation equations in a quasi-1D form are:

$$\frac{\partial m}{\partial s} = -\rho K + km, \tag{2.62}$$

$$\frac{\partial F_i}{\partial s} - \dot{\omega}_i = -\rho K Y_i + kF_i + Q_i, \tag{2.63}$$

$$\frac{\partial F_h}{\partial s} = -\rho K h + kF_h + Q_h, \tag{2.64}$$

with the species mass fraction and enthalpy fluxes being written similar to Equation 2.61:

$$F_i = mY_i - \frac{\lambda}{Le_i c_p}\frac{\partial Y_i}{\partial s} \tag{2.65}$$

and

$$F_h = mh - \frac{\lambda}{c_p}\frac{\partial h}{\partial s} - \frac{\lambda}{c_p}\sum_{i=1}^{N_s}\left(\frac{1}{Le_i} - 1\right)h_i\frac{\partial Y_i}{\partial s}. \tag{2.66}$$

The terms Q_i and Q_h denotes the transport along flame surfaces that occurs because, generally, the local iso-surfaces of Y_i and h do not coincide with the ones of $\mathcal{Y}$:

$$Q_i = \rho \left(\mathbf{u}_{fi} - \mathbf{u}_f \right) \cdot \nabla Y_i + \nabla \cdot \left(\frac{\lambda}{Le_i c_p} \nabla_{||} Y_i \right), \tag{2.67}$$

$$Q_h = \rho \left(\mathbf{u}_{fh} - \mathbf{u}_f \right) \cdot \nabla h + \nabla \cdot \left(\frac{\lambda}{c_p} \nabla_{||} h + \frac{\lambda}{c_p} \sum_{i=1}^{N_s} \left(\frac{1}{Le_i} - 1 \right) h_i \nabla_{||} Y_i \right), \tag{2.68}$$

where $\mathbf{u}_{fi}$ and $\mathbf{u}_{fh}$ are the local velocity of the iso-surfaces of Y_i and h, and $\nabla_{||}$ denotes the nabla operator in tangential direction. In Equations 2.67 and 2.68, the first term characterizes the movement of iso-surfaces of Y_i in relation to the iso-surface of $\mathcal{Y}$, and the second term represents the diffusive transport of Y_i along iso-surfaces of $\mathcal{Y}$.

No approximations have been made and all perturbations from local 1D flat flame are gathered together in the right-hand side of the flamelet equations. The stretch term, for example, can be neglected when Karlovitz number is much smaller than unity ($K_a = K\delta_f/s_L \ll 1$, with δ_f being the flame thickness). When curvature radius k^{-1} of the flame surfaces is much larger than the flame thickness ($|k^{-1}| \gg \delta_f$) it can also be disregarded in the flamelet formalism. In case that the transient time scales are longer than the flame time scale $t_L = \delta_f/s_L$, the first term in Equations 2.67 and 2.68 can also be neglected. Finally, assuming that the length scales of the distortions along the flame surfaces are much larger than the flame thickness [de Goey et al., 1997] makes the second term in Equations 2.67 and 2.68 to be negligible.

For a counterflow burner, the stretch field K for a constant flame curvature is yet unknown and its quantities need to be defined to close the equation system. For this flame configuration, Dixon-Lewis, 1991, has shown that a differential equation for K can be derived from the momentum equation in transverse direction. For the current flamelets equation system, the conservation equation of K reads

$$\frac{1}{\varsigma} \frac{\partial}{\partial s} \left(\varsigma \rho u K \right) - \frac{1}{\varsigma} \frac{\partial}{\partial s} \left(\varsigma \right) \left(\mu \frac{\partial K}{\partial s} \right) = -\rho K^2 + \rho_o a^2, \tag{2.69}$$

in which, a is the linear strain rate $a = -\partial u/\partial s$ (s^{-1}) and ρ_o the density, both defined at the oxidant side in non-premixed counterflow flames. The variable K accounts for multidimensional deviations in unidimensional simulations.

The boundary conditions for the set of 1D partial differential equations for counterflow flamelets are depicted in Table 2.2.

Table 2.2 – Boundary conditions of the flamelet equation system for counterflow flames. The subscripts f and o represents the fuel and the oxidant, respectively. The position of the boundary conditions $-L$ (fuel side) and $+L$ (oxidant side) indicates.

Fuel side	Oxidant side
$u(x=0)=0$	
$Y_i(x \rightarrow -L) = Y_{i,f}$	$Y_i(x \rightarrow +L) = Y_{i,o}$
$h(x \rightarrow -L) = h_f$	$h(x \rightarrow +L) = h_o$
$K(x \rightarrow -L) = a\sqrt{\rho_f/\rho_o}$	$K(x \rightarrow +L) = a$

2.7.2 Manifold construction

Solution of the one-dimensional conservation equations (Equations 2.62-2.64 and 2.69), including thermodynamic and transport properties, are stored in a manifold as function of the control variables. For non-premixed adiabatic flames, the mixture fraction Z and the reaction progress variable $\mathcal{Y}$, as control variables, are sufficient to accurately reproduce the thermal-chemical composition space.

The mixture fraction represents the mass fraction of the material originating from the fuel stream in the reactants mixture. It is based on the local composition of chemical elements according to Bilger et al., 1990,

$$Z = \frac{2Z_C/MW_C + 0,5Z_H/MW_H + (Z_{O,2} - Z_O)/MW_O}{2Z_{C,1}/MW_C + 0,5Z_{H,1}/MW_H + Z_{O,2}/MW_O}. \tag{2.70}$$

In the above equation, $Z_j = \sum w_{i,j} Y_i$ is the elementary mass fraction with $w_{i,j}$ being the mass fraction of the element j in the chemical species i. Using these definitions, Z can be written as a linear combination of species mass fractions

$$Z = \sum_{i=1}^{Ns} w_i Y_i, \tag{2.71}$$

where w_i is the weight of species i in the mixture fraction. The mixture fraction is normalized in such a way that it only assumes values between 1 (in the pure fuel region) and 0 (in the pure oxidizer region).

The reaction progress variable $\mathcal{Y}$ is given by Equation 2.48 ($\mathcal{Y} = \sum_{i=1}^{N_s} \alpha_i Y_i$) and its definition is important for the method accuracy and need to be well established for each studied flame. Implicitly, $\mathcal{Y}$ presents informations of the mixture composition, reaction rates and transport properties. To adequately map the thermo-chemical composition space of a flame, the chosen progress variable should follow some rules [Ihme et al., 2012]: a) lead, in combination with Z, to a unique description of the mixture composition, b) be independent of other control variables, c) include reactive scalars with time scales of the same order while evolving along the chemical trajectories and d) result in a transport equation that can be solved.

In general, $\mathcal{Y}$ is arbitrarily defined as a linear combination of major chemical species of the combustion products. However optimization methods may be used to systematically define the most adequate progress variable definition [Ihme et al., 2012; Niu et al., 2013; Najafi-Yazdi et al., 2012] for each flame. The progress variable is frequently defined as a combination of major combustion products ($\mathcal{Y} = \alpha_{H_2O}Y_{H_2O} + \alpha_{CO_2}Y_{CO_2} + \alpha_{CO}Y_{CO} + \alpha_{H_2}Y_{H_2}$, with α_i being the inverse of the molar mass of the species i, $\alpha_i = 1/MW_i$) [van Oijen and de Goey, 2000; Verhoeven et al., 2012; Donini et al., 2015; van Oijen et al., 2016], but no universal definition of $\mathcal{Y}$ exists. In a recent study of our group [Hoerlle et al., 2017] about CO_2 diluted laminar non-premixed flames of methane, it was demonstrated that a single definition of $\mathcal{Y}$ may not represent flames with different levels of dilution. This is so not only because the progress variable plays an important role for correctly mapping the thermo-chemical space but also because it defines the resulting variable gradients in the manifold, which have to be small, otherwise it can lead to interpolation errors and consequently solution difficulties or poor results.

2.7.3 FGM simulations

In FGM (one- or multi-dimensional) simulations, conservation equations are solved for each control variable (Z, $\mathcal{Y}$) in addition to the conservation of total mass and momentum.

A transport equation for the reaction progress variable $\mathcal{Y}$ is derived from the species' conservation equation assuming that species diffusion flux is modeled based on the constant Lewis number approximation. Based on the definition of the reaction progress variable (Equation 2.48), a linear combination of the species conservation equation yields [de Goey and ten Thije Boonkkamp, 1999a; van Oijen and de Goey, 2000]:

$$\nabla \cdot (\rho \mathbf{u} \mathcal{Y}) - \nabla \cdot \left(\frac{\lambda}{c_p} \nabla \mathcal{Y} \right) = \nabla \cdot \left(\frac{\lambda}{c_p} \sum_{i=1}^{Ns} \alpha_i \left(\frac{1}{Le_i} - 1 \right) \nabla Y_i \right) + \dot{\omega}_{\mathcal{Y}}. \tag{2.72}$$

where $\dot{\omega}_{\mathcal{Y}}$ is the source term for the progress variable $\mathcal{Y}$, which includes the source terms

($\dot{\omega}_{\mathcal{Y}} = \sum_{i=1}^{N_s} \alpha_i \dot{\omega}_i$) of the chemical species that constitute the progress variable, and it is tabulated in the FGM manifold as function of the control variables.

Similarly, conservation of species can be rewritten into conservation of elements taking the proper linear combination of species' conservation equation, resulting in the following mixture fraction transport equation

$$\nabla \cdot (\rho \mathbf{u} Z) - \nabla \cdot \left(\frac{\lambda}{c_p} \nabla Z \right) = \nabla \cdot \left(\frac{\lambda}{c_p} \sum_{i=1}^{N_s} \beta_i \left(\frac{1}{Le_i} - 1 \right) \nabla Y_i \right) . \tag{2.73}$$

There is no source term in the mixture fraction transport equation. In Equations 2.72 and 2.73, the first term in the right-hand-side represents the preferential diffusion, which is yet dependent on species gradients.

The boundary conditions for the control variables transport equations assumes: $Z = 1$ and $\mathcal{Y} = 0$ for the fuel inlet and $Z = 0$ and $\mathcal{Y} = 0$ for the oxidant inlet. The remaining boundary conditions (such as walls and outlets) are usually defined as having fluxes equal to zero.

During multidimensional simulations, the values of the control variables are read for each cell of the computational domain and the manifold is accessed after each iteration to retrieve the variables needed to solve the conservation equation system (e.g. source-terms, thermodynamic and transport properties). Then, the control variables are updated after each iteration until the convergence of the equation system is achieved. At the end of the computation, the final fields of the control variables are used together with the manifold data to reconstruct the multidimensional flame. The retrieval from the FGM manifold is based on biliniar interpolations [van Oijen, 2002].

3 SOOT PHYSICS AND MODELLING

Soot formation is a complex process that associate particle to particle interaction, heterogeneous chemical reactions at soot surface and gas-phase homogeneous reactions. The many gaps in the knowledge of physical and chemical processes of soot formation has led to the proposition of several models. These models differ on the processes considered, the mathematical approach in which soot is modeled and in the required computational effort. This chapter presents a brief description of soot formation processes and several soot models available in the literature. Additionally, the soot model implemented in this thesis is presented in detail.

3.1 Brief description of the soot formation mechanism

This section briefly describes general physics involved in the soot formation processes and some of the models available in the literature.

Gas-phase and polycyclic aromatic hydrocarbons (PAHs) growth

Detailed soot modelling requires the prediction of PAHs, which are regarded as the main soot precursor [Richter and Howard, 2000; Wang, 2011]. Adequate chemical kinetic mechanisms should be able to describe the formation and growth of polyciclic-aromatic hydrocarbon (PAH) over the broad range of conditions typical of practical combustion devices. These mechanisms are constructed incorporating sub-mechanisms for prediction of light molecular weight species, the formation of one-ring aromatics and the growth to larger aromatics. There are many pathway leading to PAH formation and there is no consensus in the literature about all the species that participate on soot inception.

The first step in the PAH mechanism is the formation of the first aromatic ring from fuel pyrolysis. As briefly described in [Frenklach, 2002b], the main reactions leading to the formation of the first ring are:

- The first path leading to the formation of benzene ($A1$) and phenyl (C_6H_5) are the addition of C_2H_2 to $n-C_4H_3$ and $n-C_4H_5$:

$$
\begin{gathered}
n-C_4H_3+C_2H_2 \rightarrow C_6H_5 \\
n-C_4H_5+C_2H_2 \rightarrow A1+H
\end{gathered}
$$

- A second path is the recombination of two propargyl (C_3H_3) into benzene and phenyl:

$$C_3H_3 + C_3H_3 \rightarrow A1$$
$$C_3H_3 + C_3H_3 \rightarrow C_6H_5 + H$$

- Another path is the addition of a methyl (CH_3) group on cyclo-pentadiene (C_5H_5) to the formation of benzene, and the cyclo-pentadiene recombination to the formation of naphthalene ($C_{10}H_8$) :

$$C_5H_5 + CH_3 \rightarrow A1 + H + H$$
$$C_5H_5 + C_5H_5 \rightarrow C_{10}H_8 + H + H$$

- The forth path consists of a reaction between acetylene and propargyl to form a cyclo-pentadienyl radical ($c - C_5H_5$):

$$C_3H_3 + C_2H_2 \rightarrow c - C_5H_5$$

  Once $c - C_5H_5$ is produced it forms benzene. This reaction is addressed as the most probably path to the formation of the first aromatic.

The growth of the aromatics proceeds through the H-abstraction-C_2H_2-addition (HACA) mechanism exemplified in Figure 3.1. In this mechanism the first aromatics grow by reactions with C_2H_2 where an H atom is abstracted from the aromatic ring and a ($-C_2H$) group is added. Over consecutive H-abstraction and C_2H_2-addition, new aromatic radical rings are formed. The growth of PAHs proceeds as described until pyrene ($C_{16}H_{10}$ a four ring PAH) is formed.

After pyrene is formed, the molecules are more probable to condensate on each other forming small clusters. These clusters continue to grow by surface condensation of PAHs and HACA reactions. The clusters may also grow by collision and coagulation forming larger clusters. At some point the soot particle is formed in a step called particle inception. Johansson et al., 2017, observed that some larger PAHs are formed through combination reactions between moderately sized radicals, instead the traditional sequential growth through addition of small hydrocarbon species.

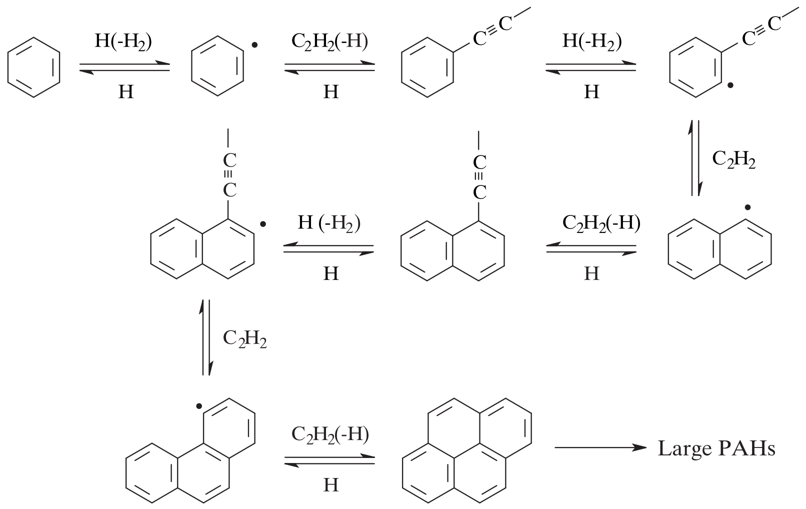

Figure 3.1 – The H-abstraction-C_2H_2-addition (HACA) mechanism of polycyclic aromatic hydrocarbon formation [Adapted from Law, 2006].

Nucleation and condensation

The inception of soot primary particles is due to the nucleation process, which is considered the least well-understood step in the soot formation process [Richter and Howard, 2000; Frenklach, 2002b; Kholghy et al., 2018]. The nucleation takes place by the evolution of PAH clusters into solid particles. This evolution consists of simultaneous accumulation of particles mass by chemical reaction with gas-phase precursors and by collisions among PAHs.

The coalescence of PAHs is the most commonly adopted nucleation mechanism. Although a unique soot precursor has not been identified, pyrene is the most widely used and validated PAH precursor [Kazakov and Frenklach, 1998; Mauss et al., 2006; Roy, 2014; Zhang, 2009; Appel et al., 2000; Charest et al., 2014]. Pyrene is a PAH molecule with chemical formula $C_{16}H_{10}$ arranged in four aromatic rings. Detailed soot modellings usually assumed that the dimer formed by the sticking of two pyrene molecules represents the first primary particle. In reality, bigger PAHs are involved in soot nucleation. Dobbins et al., 1998 found that soot particle precursors are formed by PAHs from 16 to 30 carbon atoms, and that higher PAH concentrations in those particles are of PAH formed with 20 to 24 carbon atoms (PAHs of approximately five-member rings).

The condensation of PAH into soot particle surface is a physical process. It increase soot mass by the sticking of PAH on soot surface but without altering the particle number.

Condensation is usually modeled as a collisional phenomenon between PAH and soot particles due to Brownian motion. Its rates depend on the soot surface area and on the number density of soot particles and PAH molecules in the combustion system. Similarly to the nucleation process, pyrene condensation is the most widely used and validated model although various PAH of different sizes and structures may condensate on soot surface [Wang et al., 2015b; Veshkini et al., 2016b; Eaves et al., 2017]. Moreover, only a certain percentage of such PAHs effetively remain attached onto the soot particle surface after collision. In this way, several authors also accounted for a condensation efficiency in their models [Wen et al., 2006; Blanquart and Pitsch, 2009; Zhang et al., 2009b; Saffaripour et al., 2014; Wang et al., 2015b; Veshkini et al., 2016b; Eaves et al., 2017].

Some studies investigated the thermodynamic stability of physically bonded dimers at flames temperature ($>$ 1000 K) [Raj et al., 2010; Sabbah et al., 2010; Totton et al., 2012; Mercier et al., 2019]. It was found that relatively small PAHs, with 4- and 5-rings, are not well favoured to dimerize since their binding energies are considered too weak to allow them to survive in this environment. Therefore, it was observed that a very small efficiency takes place for dimerization of small PAHs. The dimerization efficiency became higher only when the molecular mass of the colliding PAHs increase [D'Anna and Kent, 2008]. Thus, sticking after collision between small PAHs, small-large PAHs or small PAHs with particles are unlikely to occur. The collision efficiency of PAHs is an important parameter to soot particle inception and it depends on the mass and collision diameter of the smaller of the two colliding PAH. Chung and Violi, 2011 determined that not only the PAH's size but also the addition of aliphatic chains influence whether or not a dimerization was favored. It was asserted that the dimerization efficiency should be a function of equilibrium ratios. Several studies investigated the equilibrium properties for the dimerization of several PAHs [Rapacioli et al., 2007; Wang, 2011; Totton et al., 2012; Elvati and Violi, 2013; Lowe et al., 2015] in terms of defining their binding energies and vibration modes (magnitude and frequency) during the process of dimerization, heterogeneous dimer pair stability and the addition of aliphatic chains. All those works suggested that dimmerization of relatively small PAHs is a highly reversible process. Recent studies [Eaves et al., 2015, 2017; Veshkini et al., 2016b; Aubagnac-Karkar et al., 2018; Mercier et al., 2019] brought to light the importance of the reversible nucleation and condensation processes.

As noted, PAH clustering by physical forces (e.g., van der Waals interactions) is unlikely for relatively small PAHs at high temperatures since they are not thermodynamically stable at this condition [Sabbah et al., 2010; Totton et al., 2012]. Thereby pyrene dimerisation cannot play a role in soot particle inception and much larger PAHs, such as circumcoronene ($C_{54}H_{18}$) [Totton et al., 2012] or circumpyrene ($C_{42}H_{16}$) [Adkins and Miller, 2015], would be needed for PAH attraction. Yet, small PAHs of approximately 5-rings are abundantly found at nascent soot particles [Dobbins et al., 1998; Teini et al., 2011; Johansson et al., 2017; Mercier et al., 2019] and even at more mature soot particles [Dobbins et al., 1998], which contradicts the results of these thermodynamic investigations. Therefore, it has been suggested that nucleation and condensation are kinetically controlled processes (for which reversibility would be important) [Eaves et al., 2017; Kholghy et al., 2018, 2019; Mercier et al., 2019], rather than solely equilibrium controlled processes. So that, strong chemical bonds between small PAHs molecules are needed to maintain dimer stability at high temperature inception. Chemical bonds formation between PAHs are important for sustaining soot inception by reducing the nucleation reversibility. Trough reversible PAH clustering models with chemical bond formation Eaves et al., 2017, and Kholghy et al., 2019, observed that smaller PAHs are most important for the nucleation, while both small and large PAHs are important for the condensation. This is due to the relatively lower reversibility of condensation compared to the nucleation process.

While much effort have been done in this subject, the transition between gas- to solid-phase is still not well understood. Very recently, Johansson et al., 2018, proposed a new mechanism to explain the high-temperature gas-to-particle conversion based on chain reactions of resonance-stabilized hydrocarbon radicals that may form covalently bound clusters of PAHs. Since those small clusters would not be favored to condense at high temperatures, this mechanism provides a key step for the rapid particle formation. Additional discussion about this mechanism can be found in [Thomson and Mitra, 2018].

The gradual inclusion of all those processes taking place on soot inception and PAHs condensation improved prediction capabilities and generality (lower tuning parameters) for the detailed soot models. Previously it was discussed that not all PAHs' collisions form a dimer neither stick onto the particle surface. In fact, PAH-PAH and PAH-particle iteraction are usually assumed irreversible processes, therefore, constant collision efficiencies have been introduced in the nucleation and condensation rates as a simple way to take into account this simplification [Zhang et al., 2009a; Saffaripour et al., 2014; Aubagnac-Karkar et al., 2015; Wang et al., 2015b]. The inclusion of dimerization efficiencies tends to improve the prediction of primary particle diameters and the number of primary particles per aggregate with experiment data. Saffaripour et al., 2014, reported that considering benzopyrene ($C_{20}H_{12}$, a PAH with five aromatic rings) as inception species instead of pyrene, reduced the over-prediction of soot concentration on the wings at lower flame heights and improved the prediction in the central region of the flame. Later on, several researchers demonstrated the participation of multiple PAHs bigger than pyrene in soot inception [Wang et al., 2015b; Veshkini et al., 2016b; Eaves et al., 2017]. For example, Wang et al., 2015b, considered that soot nucleate through reactions between eight PAH molecules from pyrene up to coronene ($C_{24}H_{12}$ with 7 aromatic rings). Homogeneous reactions represent interaction between same PAH ($PAH_i + PAH_i$), while heterogeneous reactions involve two different PAHs ($PAH_i + PAH_j$). In those works, a proper collision efficiency was assumed for each PAH. The inclusion of the interaction between multiple PAHs in those works improved the predictions of soot volume fraction and particle properties respective to their experimental data. Studies [Eaves et al., 2015; Veshkini et al., 2016b; Eaves et al., 2017; Aubagnac-Karkar et al., 2018; Mercier et al., 2019] of soot modelling including reversible nucleation and condensation with further inclusion of chemical bounds formation [Eaves et al., 2017; Kholghy et al., 2019] reported an improved prediction of all relevant soot morphological parameters (including particle size distributions) determined experimentally for both burner stabilized stagnation premixed and non-premixed laminar coflow flames configuration.

Surface growth and oxidation

Particles growth and size distribution are also subjected to chemical phenomena that involve heterogeneous surface reactions. The change of soot size due to surface reaction depends on the gas-phase composition, the thermodynamic state of the system, the total particle surface area and the surface reactivity. It is recognized that acetylene is the principal species that increases particle size by attaching itself on soot surface, while reduction of particle size occurs due to carbon removal by oxidative effects of O_2, O and OH.

Frenklach and Wang, 1994, described the heterogeneous surface reactions based on elementary chemical reactions of surface active sites. Active sites represent the parcel of surface radicals (sites) available for chemical reactions. This approach assumes that particle surface is formed by aromatic basal planes (edges of large PAH covered by $C-H$ bounds) [Frenklach, 2002b] that reacts with gaseous species, losing hydrogen atoms and becoming a surface radical. Thus, soot surface chemistry is controlled by Hydrogen-Abstraction-C_2H_2-Addition (HACA), similarly as what occurs for PAH grow, plus reactions with O_2 and OH to account for soot oxidation. This HACA-based mechanism represents a set o elementary reactions that considers interaction of active sites with hydrogen, hydroxyl radicals, water vapor, acetylene and oxygen. However, the reaction paths and constants of the HACA-based mechanism are still not known precisely. In addition to the well known model of Appel et al., 2000, additional variants of the HACA-based mechanism have been proposed [Blanquart and Pitsch, 2009; Wang et al., 2015b; Aubagnac-Karkar et al., 2015]. The global mechanism for surface reactions presented by Appel et al., 2000, is:

$$
\begin{gathered}
C_{soot,n} + H \rightleftharpoons C^*_{soot,n} + H_2, \\
C_{soot,n} + OH \rightleftharpoons C^*_{soot,n} + H_2O, \\
C^*_{soot,n} + H \rightarrow C_{soot,n}, \\
C^*_{soot,n} + C_2H_2 \rightarrow C_{soot,n+2} + H, \\
C^*_{soot,n} + O_2 \rightarrow C^*_{soot,n-2} + 2CO, \\
C_{soot,n} + OH \rightarrow C^*_{soot,n-1} + CO
\end{gathered}
$$

where $C_{soot,n}$ is a soot particle with n carbon atoms bounded with hydrogen and $C^*_{soot,n}$ is a soot particle with dehydrogenated sites on its surface.

Oxidation reactions presented in the HACA-based mechanism are also global reactions. Although these global reactions are widely used in detailed soot models, soot oxidation is a much more complex process. In[Frenklach et al., 2018; Frenklach, 2019] it was demonstrated that global reactions are not able to reproduce accurately the effects of a more detailed surface oxidation mechanism, which depends on the formation of oxy-radicals and their decomposition and on the formation of five-member rings that are oxidized by O atoms.

The surface growth rate reduces as soot particle size evolves when travelling to the post-flame region [Appel et al., 2000; Frenklach, 2002b]. The soot surface is formed by graphitic edges (surface radicals susceptible to chemical reactions) with some parts of basal aromatic planes (non-reactive). In the maturing of soot primary particles, graphitic shell structures are formed principally by PAHs nano-rearrangements due to dehydrogenation/-carbonization and aromatization reactions that reduce the H/C ratio on soot particles surface [Kholghy et al., 2016]. In other words, PAHs on soot surface change configuration from edge-on-surface (for nascent particles and low temperatures) to face-on-surface as soot particles mature (at high temperature regions). Dehydrogenation/carbonization represents the loosing of hydrogen atoms without the formation of a radical site. The radical formed by the H-atom attack cyclize and form a closed aromatic ring [Sirignano et al., 2013]. This maturing process is called ageing and it limits the surface growth of soot primary particles by reducing surface reactivity [Smooke et al., 2005]. Soot particles may increase in size only by aggregation after that surface growth limit is reached. This process is also related to the transition from the "liquid-like" to rigid particle structure. Therefore, a more comprehensive modelling of particle surface reactivity would require the track of soot dehydrogenation and the evolution of internal nano-structures to correctly describe the H/C ratio of soot particles and, consequentely, to produce radicals and chemicaly growth [Sirignano et al., 2013; Saggese et al., 2015; Kholghy et al., 2016].

As is comprehensively discussed in Veshkini et al., 2014, a steric-factor α was embedded to the HACA-based surface mechanism to account for the surface ageing effect in a simplified way. Thus, the steric factor indicates the fraction of those surface sites that are available for chemical reactions and accounts for the difference between the soot surface growth rates at low and high-temperature flames and with the primary particles diameter. Different formalism for α have been used in literature (from constant values to functions dependent on temperature and the mean particle size). Since the α functions are usually obtained by fitting experimental soot volume fraction, the steric factor becomes intrinsically dependent on the reaction mechanism. Other works attempted to include the effect of particle ageing in the global oxidation process [Khosousi and Dworkin, 2015a] as a function of the soot surface reactivity.

Particles coagulation and fragmentation

Particles coagulation is a collisional phenomenon between two soot particles in Brownian motion that stick together forming larger particles or aggregates. It is modeled based on aerosol dynamics. The coagulation process changes soot morphology, increases particle size and decreases particle number density without changing soot mass. Therefore, it plays an important role in the evolution of particle size distribution.

Spherical growth takes place for small coagulated particles while a fractal-like growth takes place for large coagulated particles. This behavior characterize, respectively, two limiting cases of coagulation: the coalescence and the agglomeration/aggregation. In the coalescence limit, particles are treated as spherical liquid-like structures. When two of this particles collide, they merge together forming a larger particle but reducing number density and destroying particle surface area. On the opposite limit, soot particles are treated as rigid spheres and a fractal-like aggregate structure is formed when rigid primary particles/clusters collide and stick together in a point-contact bond. The exact transition between the two coagulation limits is still debated.

Between these two limits, particles can collide and partially merge forming a neck region. According to Frenklach, 2002b, several studies suggested that nucleation and surface growth play a role together with the coagulation for the spherical shape of soot particles. In an environment with intense nucleation it is more likely that PAH clusters collide. Among collisions they may stick together (and form a larger PAH) or not, but in both cases the PAH clusters deform themselves and rearrange their internal structures assuming a more spheroidal-like shape. In this way, nucleation contributes to the formation of spheroidal primary particles. The role of surface growth is as follows: once particles collide and stick together through a contact point, a sufficiently fast surface growth covers the gap between attached particles with mass deposition. For large particles the growth may not be sufficient and a neck region appears between colliding particles.

No robust coagulation model exists that can deal with all these phenomenon at the same time [Zhang, 2009]. Usually the coagulation models assume just the coalescence limit [Gelbard et al., 1980; Aubagnac-Karkar et al., 2015; Roy, 2014; Mauss et al., 2009; Wang et al., 2015b; Mehta et al., 2009] or the aggregation limit [Park and Rogak, 2004; Dworkin et al., 2011; Zhang, 2009; Bhatt and Lindstedt, 2009]. While the knowlendge of one soot property, as the volume fraction, is sufficient to model particles coalescence, to model aggregates the number of primary particles and particle clusters [Zhang, 2009], or particles volume and surface area [Blanquart and Pitsch, 2009] need to be tracked simultaneously.

Models for soot formation that describe simutaneously the morphology of both primary particles coalescence and aggregatetion are still incipient. A common approach is to assume an approximate treatment where a critical particle diameter is assumed as a boundary between the two limits like a step function [Kazakov and Frenklach, 1998; Smooke et al., 2005; Mauss et al., 2006; Netzell et al., 2007; Saggese et al., 2015], whereas Saffaripour et al., 2014, implemented a characteristic coalescence time to associate the reduction of surface area due to coalescence to the change in the number of primary particles per aggregate. Veshkini et al., 2016a, investigated the coagulation mechanism of soot particles by two different approaches: one approach assumes that the transition from pure coalescence to pure aggregation occurs instantaneously based on a cutoff diameter; the other approach assumes a transition from spherical particles to aggregates based on a sintering process between the colliding particles with a finite residence time. Sirignano et al., 2013, considered both coagulation limits, but soot formation process was modelled through a chemical representation. In this approach soot particles are treated similarly as gaseous species and not as a dispersed phase. Then both coalescence and aggregation are treated as chemical reactions. Similar approach was considered by Saggese et al., 2015.

An important additional process is the particle fragmentation. Bigger particles or agregates may break-up into smaller ones due to particle-particle collisions or reactions with oxidative species, increasing the total number of primary particles or smaller aggregates. The fragmentation due to particles collision are described somehow similar to particles coagulation but with appropriate rates [Gelbard et al., 1980; Kumar and Ramkrishna, 1996; Zhang, 2009]. In the oxidation-induced fragmentation, the oxidizing specie may penetrate deep into the particle to remove C-atoms [Sirignano et al., 2013; Saggese et al., 2015; Sirignano et al., 2016], breaking-up primary particles or aggregates into fragments.

3.2 Soot models

In general, soot models are categorized as empirical, semi-empirical and detailed [Kennedy, 1997]. These three different types of models are briefly presented in this section.

Empirical methods represents the soot formation at specific combustion conditions based on empirical correlations for experimental data [Takahashi and Glassman, 1984; Olson et al., 1985]. Because this type of model does not describe any phenomenological soot formation sub-process it is computationally fast and easy to implement.

Semi-empirical models [Leung et al., 1991; Liu et al., 2002; Wen et al., 2003; Demarco et al., 2013] are based on empirical correlations, but incorporates some phenomenological soot formation process such as precursors prediction, nucleation, surface growth, surface oxidation and coagulation. This type of model is not dependent of the combustion equipment but is limited inherently to specific conditions for which their rates were adjusted. In addition, semi-empirical models assume that all particles have the same structure (a mono-dispersed approximation).

In contrast to the previous models, detailed methods account for poly-dispersed particles including more sophisticated soot formation processes. This category of soot models deals with the dynamics and the distribution of different particle sizes and with different soot structures, what makes them computationally demanding and more difficult to implement. However, it is expected that they present better soot predictions over a wide range of combustion conditions.

The more accurate soot formation models are based on stochastic and chemical representation approaches. The stochastic method [Balthasar and Kraft, 2003; Singh, 2006; Morgan et al., 2007; Patterson, 2013] solves the dynamics and the particles distribution trough Monte-Carlo simulations. Soot formation sub-processes are treated probabilistically, i.e., soot structure changes following probabilistic assumptions for abstraction or addition of atoms. This method is the most computationally demanding but it may provide a full detail about particles structure. However, a drawback is that the method is difficult to couple with gas-phase chemistry solvers, thus most of its usage was limited to frozen field analysis. Soot can also be predicted in terms of kinetic molecular dynamics [Pope and Howard, 1997; Richter et al., 2005; D'Anna and Kent, 2008; Sirignano et al., 2013; Saggese et al., 2015]. In this approach, soot formation sub-processes are considered as elementary gas-phase reactions for each particle size class. Thus, the gas and solid-phase are solved simultaneously trough a kinetic mechanism. The set of dozens elementary reactions describing the formation of each particle class results in soot kinetic mechanisms that can easily reach thousands of elementary reactions. Both the stochastic and the kinetic molecular dynamics approaches brings detailed insights of soot formation processes in molecular levels and of the shape of the particle size distribution function (PSDF), but these methods cannot be used for engineering problems due to high demand of computational resources.

Detailed soot models more accessible for engineering problems are the Method of Moments and the Discrete Sectional methods. These methods assumes a dispersed phase interacting with the gaseous phase based on aerosol dynamics. The Method of Moments describes the dynamics of particles size distribution in terms of soot moments. The particle size distribution is fully represented by solving all the moments, however, the solution of only the first few moments is sufficient to well describe the evolution of soot properties in practical applications. In the univariate Method of Moments, for example, the zeroth moment is the total particle number density, while the first moment is related to the total mass or volume of soot, and the second moment is proportional to the soot surface area. These first moments present physical interpretation of soot properties. Moments of higher-order lack simple physical interpretations but are necessary to improve accuracy. One equation describing the transport of each soot moment is solved in this approach, however, their source terms are unclosed when complex physical and chemical models are considered because their dependency on the moments that are not solved. To overcome this mathematical issue, several variants of the method were proposed to deal with the closure of the source terms [McGraw, 1997; Kazakov and Frenklach, 1998; Wright et al., 2001; Frenklach, 2002a; Marchisio and Fox, 2005; Mueller et al., 2009; Yuan and Fox, 2011; Mueller et al., 2011; Yuan et al., 2012; Salenbauch et al., 2015]. In general, the Method of Moments determines the average properties of the PSDF with accuracy and computational efficiency, but its implementation can be difficult due to the closure problems and its applications might be limited because a priori assumption of the shape of the particle size distribution. The Discrete Sectional Method [Gelbard et al., 1980; Park and Rogak, 2004] assumes that the continuous particle size distribution is divided in sections representing different size classes, so that particles/clusters are assigned to different sections according their mass or volume. It means that all particles within a section can be described by a single scalar that represents the particle size class. In this approach a particle balance equation is solved for each section, thus, it is able to adequately solve the particle size distribution function with a sufficient number of sections. The computation cost of the Section Method still might be high because the large number of equations to be solved, but its implementation is relatively simple and it offers the advantage of not requiring assumptions about the shape of the particle size distribution.

3.3 General soot aerosol dynamic model

The Smoluchowsky equation is a population balance equation (PBE) that describes the variation of the size distribution of a population of particles due to Brownian collisions among these particles (i.e., physical interaction between different particles) in time [Friedlander, 2000]. It is based on the theory of aerosol dynamics of particles in a gaseous medium. Despite the Smoluchowsky equation only describes particles coagulation, analogous versions of the equation can be extended to model other physical processes of soot formation (such as particles nucleation and condensation) [Frenklach, 2002a; Roy, 2014], since most of them are dominated by interaction between particles moving in Brownian motion. Further, the Smoluchowsky equation can be can be incorporated in a balance equation and generalized to take into account surface growth/oxidation processes. This balance equation (commonly called general population balance equation, GPBE) describes the evolution of the particle size distribution (PSD) with time and positions. In the continuous form it reads [Friedlander, 2000; Zhang, 2009]:

$$\begin{aligned}\frac{\partial n(v,t)}{\partial t} + \vec{v}.\vec{\nabla} n(v,t) - \vec{\nabla}.D\vec{\nabla} n(v,t) = \\ &+ \frac{1}{2}\int_0^v \beta(v-v',v')n(v',t)n(v-v',t)dv' \\ &- n(v,t)\int_0^\infty \beta(v,v')n(v',t)dv' \\ &- \frac{\partial I(v,t)}{\partial v} + Nu(v,t) \qquad (3.1)\end{aligned}$$

where $n(v,t)$ is the number density function of particles with volume v and time t, D is the diffusion coefficient, $I(v,t)$ is the current of particles due to surface processes defined as $I(v,t) = n(v,t)dv/dt$ (with dv/dt being the net surface growth/oxidation rate), $N_u(v,t)$ is the nucleation rate and $\beta(v,v')$ is the collision frequency factor (collision/s) between particles of size v and v'. The first term in the L.H.S. of the equation represents the time evolution of the size distribution, while the second and third terms in the L.H.S. are respectively the divergent of the particles advective flux and the divergent of the particles diffusive flux. The first term in the R.H.S. determines the formation of particles with size v' through the collision of particles with lowers sizes, and the second term in the R.H.S. represents the loss of particles with size v' as a consequence of collision with particles of other size. The third term in the R.H.S. is associated to surface processes (condensation, growth and oxidation). The last term in the R.H.S., $Nu(v,t)$, represents the nucleation source term.

An accurate solution of the Equation 3.1 requires the knowledge of $n(v,t)$ for an infinite number of particle sizes, thus leaving this equation unclosed. One way to solve this problem is to formulate the GPBE in terms of a discrete particle size distribution for a particle property (such as number density or volume fraction). The conservation of this property is achieved from the balance among all events described by Equation 3.1. In this case, soot particles are assigned to different sections according to their volume or mass [Gelbard et al., 1980; Kumar and Ramkrishna, 1996; Park and Rogak, 2004]. Thus, the discretized form of the GPBE describes the time evolution of a particle population by a finite set of partial differential equations representing different particles size classes. For a more detailed description of population balance equation and for a review of its different solution methodologies, the reader is refereed to the work of Kumar and Ramkrishna, 1996.

Collision frequency factor

The collision frequency factor, β, is defined for the free-molecular, the transition and the continuum regimes as a function of the particle size and the local gas thermodynamic state [Frenklach and Wang, 1994; Kazakov and Frenklach, 1998; Mauss et al., 2009]. The limits of each regime is given by the Knudsen number, $K_n = 2\lambda/D_p$, which is defined as the ratio of the gas molecular mean free path λ and the particle radius $D_p/2$, with λ given by

$$\lambda = \frac{k_B T}{\sqrt{2}\pi D_{gas}^2 p}, \tag{3.2}$$

which is a function of the temperature T, the pressure p and the gas molecule diameter

$$D_{gas} = (6MW_{gas}/(\pi\rho_{gas}\mathcal{N}_A))^{1/3},$$

where MW_{gas}, ρ_{gas} and $\mathcal{N}_A$ are respectively the molecular weight and the density of the gas, and the Avogadro's number. k_B is the Boltzmann constant. For air, the mean free-path is $\lambda = 2.3701 \times 10^{-3} T/(1.103 \times 10^5 p)$.

Considering that collisions occur between particles with size class i and j, the collision regimes are defined as follows:

- Free-molecular regime, $K_n >> 1$: applied when a particle is small relative to the mean free-path of the gas molecules.

  $$\beta_{i,j}^{fm} = k_{fm} \left(v_i^{1/3} + v_j^{1/3} \right)^2 \left(\frac{1}{v_i} + \frac{1}{v_j} \right)^{1/2}, \tag{3.3}$$

  $$k_{fm} = \epsilon_{i,j} \left(\frac{3}{4\Pi} \right)^{1/6} \left(\frac{6k_B T}{\rho_s} \right)^{1/2}, \tag{3.4}$$

  where v_i is the volume of particle with size class i, ρ_s is the density of a soot particle (assumed to be equal to solid carbon), $\epsilon_{i,j}$ is the Van der Waals coagulation enhancement factor.

  Harris and Kennedy, 1988, obtained mean Van der Waals coagulation enhanced factor, $\epsilon_{i,j}$, for several particles size class. Thus they determined values of $\epsilon_{i,j}$ varying from 1.2 to 2.4 depending on the size of the particle. For flames at atmospheric conditions where particles interaction occurs mostly in the free-molecular regime, it is more likely that small-larger soot particle collide than small-small or large-large particles. For this situation, the enhanced factor vary between 1.2 to 1.8 to collisions between small and larger particles. Nonetheless, it is usually assumed a constant conservative value equal to 2.2 [Frenklach and Wang, 1994; Frenklach, 2002a; Zhang, 2009; Roy, 2014; Mehta et al., 2009], which is an average over the range of soot particle sizes studied in [Harris and Kennedy, 1988].

- Continuum regime, $K_n << 1$: applied when the size of a particle is large relative to the mean free path of the gas molecules:

  $$\beta_{i,j}^{c} = k_c \left(v_i^{1/3} + v_j^{1/3} \right) \left(\frac{C_{S_i}}{v_i^{1/3}} + \frac{C_{S_j}}{v_j^{1/3}} \right), \tag{3.5}$$

  where C_{S_i} is the Cunningham slip factor for the size class i (related to the Knudsen number by $C_{S_i} = 1 + 1.257K_{n_i}$ [Kazakov and Frenklach, 1998]) and k_c is a function of the temperature and the gas dynamic viscosity μ:

$$k_c = \frac{2k_B T}{3\mu}. \tag{3.6}$$

The gas dynamic viscosity is approximated by the Sutherland's law:

$$\mu = \frac{C_1 T^{3/2}}{T + C_2}, \tag{3.7}$$

where $C_1 = 1.4558 \times 10^{-5}$ g.cm^{-1}.s^{-1}.K$^{-1/2}$ and $C_2 = 110.4$ K are the Sutherland's coefficients for air.

- Transition regime, $0.1 < K_n < 10$: defined as an harmonic mean between the continuum and the free-molecular regime:

$$\beta^t_{i,j} = \frac{\beta^{fm}_{i,j}\beta^c_{i,j}}{\beta^{fm}_{i,j} + \beta^c_{i,j}}. \tag{3.8}$$

For common combustion systems at low pressures (atmospheric or lower), the soot size is usually not sufficient to reach the continuum regime [Kazakov and Frenklach, 1998]. For example, it was demonstrated that for particulate carbon of approximately 100 nm [Singh, 2006], the transition regime is attained for pressures greater than approximately 10 atm while the continuum regime is reached with pressures in order of 100 atm.

3.4 The Discrete Sectional Method (DSM)

Aerosol dynamics consists of solving the particle population balance equation continuously over a infinite number of particle sizes. However, solving this system of equations even for one-dimensional flames is not possible due to computational constraints. In this way, the Discrete-Sectional method is considered to describe the particle size distribution in terms of discrete number of sections.

In the discrete sectional model implemented in this work, one transport equation is solved for each section to describe the soot evolution in the combustion system. The transport equation of soot mass fraction $Y_{s,i}$ of section i is given by

$$\frac{\partial(\rho Y_{s,i})}{\partial t} + \vec{\nabla}.(\rho\vec{v}Y_{s,i}) = -\vec{\nabla}.(\rho v_T Y_{s,i}) + \vec{\nabla}.(\rho\mathcal{D}_{s,i}\nabla Y_{s,i}) + \dot{\omega}_{s,i},\ \ i = 1, ..., \mathcal{N}_{sec}, \tag{3.9}$$

where $\mathcal{D}_{s,i}$ is the diffusion coefficient of the soot particles of class i^{th}, v_T is the thermophoretic velocity, $\dot{\omega}_{s,i}$ is the net rate of soot production/destruction and $\mathcal{N}_{sec}$ is the total number of sections. The soot source term $\dot{\omega}_{s,i}$ (in units of $\mathrm{g}_i\mathrm{cm}^{-3}\mathrm{s}^{-1}$) is given by the soot formation and oxidation models. Once soot diffuses much slower than the gas-phase species, it is assumed that $\mathcal{D}_{s,i}$ is approximately equal to 1% of the average gas diffusivity due to numeric stability reasons [Kennedy et al., 1990; Zimmer et al., 2017], the value of $\mathcal{D}_{s,i}$ is set to 1×10^{-6} $\mathrm{cm}^2\mathrm{s}^{-1}$. The thermophoretic velocity is calculated as follows [Friedlander, 2000; Roy, 2014; Wang et al., 2015b]:

$$v_T = -\frac{3}{4}\left(1 + \frac{\pi\alpha_{acc}}{8}\right)^{-1} \frac{\nu}{T}\nabla T \tag{3.10}$$

where ν is the kinematic viscosity and $\alpha_{acc} = 0.9$ is the accommodation factor. Ono et al., 2002, demonstrated that the thermophoretic velocity scarcely depends on particles morphology in the free-molecular regime.

In this work, soot particles are considered to be formed by pure solid carbon with constant density and modeled as a distinct dispersed phase that interacts with the gaseous phase. In addition, for atmospheric flames it is assumed that soot is formed only in the free-molecular regime and that coagulation occurs only in the coalescence limit. The soot particles and gas-phase species are fully coupled following Zimmer et al., 2017. The interaction between soot particles and gas-phase molecules is considered for the conservation equation of total mass, individual chemical species and energy. Additional source terms for chemical species involved in soot formation/oxidation processes are included to conserve chemical elements. Furthermore, soot is accounted for the correction of diffusion fluxes to guarantee mass conservation and for the computations of the mixture density, the mixture enthalpy and in the total heat capacity. It is assumed that mixture viscosity and thermal conductivity are not affected by the presence of soot.

The implemented Discrete Sectional method is based on the works of [Gelbard et al., 1980; Mauss et al., 2009; Mehta et al., 2009; Roy, 2014; Vervisch, 2012; Aubagnac-Karkar et al., 2015; Roy and Haworth, 2016]. Details of the discretization of the particle-size distribution, the physical and chemical soot formation processes and the definition of source terms of the soot transport equations are given in the next sections. First, the particle volume discretization and model variables that represent soot in each sections are presented. Then, the soot formation models are described by collisional source terms (particle inception, condensation and coagulation) and surface chemistry source terms (surface growth and oxidation).

3.4.1 Discretization of the Particle Size-Distribution

In the Sectional Method, the continuous PSD is discretized into a finite number of sections, $\mathcal{N}_{sec}$, between the volume of the smallest particle (v_{MIN}) and the volume of the largest particle (v_{MAX}) considered in the model. The particle minimum volume v_{MIN} is equal to the carbon-equivalent volume of the number of carbon atoms of the soot precursors (incipient molecules). The carbon-equivalent volume is defined for two atoms of carbon as being

$$v_{C_2} = \frac{2MW_C}{\mathcal{N}_A \rho_s} \tag{3.11}$$

where MW_C is the molecular weight of carbon, $\mathcal{N}_A$ is the Avogadro number and ρ_s is the soot density (equivalent to solid carbon). Assuming pyrene ($C_{16}H_{10}$) as the aromatic precursor and its dimer as the first particle size, $v_{_{MIN}}$ becomes equal to $16v_{C_2} = 3.428$E-28 m^3, which is equivalent of a sphere with approximately 0.9 nm of diameter. The biggest particle volume in the system, $v_{_{MAX}}$, is assumed to be 5.236E-18 m^3, which is equivalent of a 10 μm diameter sphere.

Figure 3.2 presents a hypothetical bi-modal PSDF in terms of particles volume. In this approach, a given section i is defined by its lower boundary v_{i-1} and upper boundary v_i, so that the biggest particle volume of section i is the same of the smallest particle volume of section $i+1$ and so on for the remaining sections.

A common approach to discretize the PSDF is to assume that sections sizes growth linearly on a logarithmic scale [Gelbard et al., 1980]. Thus, the discretization of the PSDF is given by [Netzell et al., 2007; Roy, 2014]

$$v_i = v_{_{MIN}} \left(\frac{v_{_{MAX}}}{v_{_{MIN}}} \right)^{i/\mathcal{N}_{sec}} . \tag{3.12}$$

In the literature it is commonly used around 25 to 35 sections to represent the PSDF [Veshkini et al., 2014; Aubagnac-Karkar et al., 2015] but higher number of sections may be used [Netzell et al., 2007; Naseri et al., 2017]. The number of sections depend of the maximum particle size of the flame. However, it should conciliate the computational

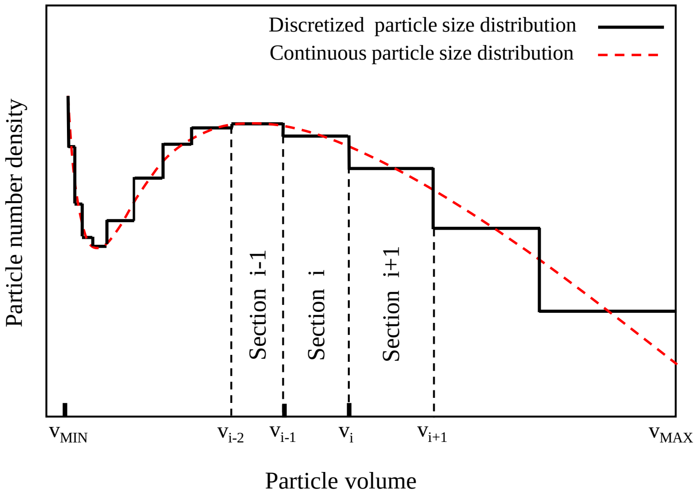

Figure 3.2 – Scheme for the continuous and the discretized particle size distribution.

cost and the solution accuracy.

Since section discretization varies linearly in the logarithmic scale, a mean particle diameter for each section $\bar{v}_i = (v_i - v_{i-1})/(\ln(v_i) - \ln(v_{i-1}))$ may be assumed for numerical simplifications of the collision rates β (Equations 3.3-3.8).

3.4.2 Model variables

In the current approach, soot source terms are calculated in terms of the soot volume fraction rates, $\dot{Q}_i$ ($\mathrm{cm}_i^3\ \mathrm{cm}^{-3}\ \mathrm{s}^{-1}$), of section i. The soot mass fraction of section i is directly correlated to the volume fraction, Q_i, by the ratio between the density of soot and the mixture density (ρ):

$$Y_{s,i} = \frac{\rho_s}{\rho} Q_i. \tag{3.13}$$

Similarly, the source terms ($\dot{\omega}_{s,i}$) in the transport equations (Equation 3.9) are given by $\dot{\omega}_{s,i} = \rho_s \dot{Q}_i$.

The Sectional Method considered in this study assumes that all particles within a section are represented by a single soot parameter, which was chosen to be the soot volume fraction density q_i. The soot volume fraction of each section comes from the integral of the soot volume fraction density $Q_i = \int_{v_{i-1}}^{v_i} q_i(v)dv$. Assuming a constant soot volume fraction density within the section one arrives at

$$q_i(v) = \frac{Q_i}{v_{i,max} - v_{i,min}} = \frac{Q_i}{v_i - v_{i-1}}, \tag{3.14}$$

where $v_{min,i}$ and $v_{max,i}$ are respectively the lower and upper volume boundaries of section i. Thus, a distribution of the soot volumetric fraction exists within each section volume. The type of the soot parameter function (constant, linear, logarithmic) does not affect the final result for sufficient number of sections [Roy, 2014]. Since particle's size varies from $v_{min,i}$ to $v_{max,i}$ in section i, the number density distribution ($n_i(v)$) within each section is defined by Gelbard et al., 1980, as

$$n_i(v) = \frac{q_i(v)}{v}, \tag{3.15}$$

with v comprehending the volume between section boundaries. This formalism leads to the calculation of the section i number density, N_i, according to

$$N_i = \int_{v_{i-1}}^{v_i} n_i(v)\mathrm{d}v. \tag{3.16}$$

For the constant profile of sectional size distribution (Equation 3.14), the number density becomes

$$N_i = \frac{Q_i}{v_i - v_{i-1}} \ln\left(\frac{v_i}{v_{i-1}}\right). \tag{3.17}$$

Finally, the total soot volume fraction (f_v) and the total number density (N_{total}) are given by the summation of Q_i and N_i over all sections:

$$f_v = \sum_{i=1}^{\mathcal{N}_{sec}} Q_i, \tag{3.18}$$

$$N_{total} = \sum_{i=1}^{\mathcal{N}_{sec}} N_i. \tag{3.19}$$

The steps for the solution of those variables for the section i can be summarized as follows. First the transport equation solves the field of the soot mass fraction, $Y_{s,i}$, from which the soot volume fraction, Q_i is calculated. Then, q_i is defined and together with the relation for n_i they are used to calculate the soot number density of the section, N_i. At the end, total quantities are achieved by summing the number density and the soot volume fraction of all sections.

3.4.3 Soot formation processes

Processes describing soot formation/oxidation are accounted for as source terms in Equation 3.9. These processes are detailed explained below.

3.4.3.1 Nucleation

The nucleation process connects the gaseous species with the incipient solid soot particles. Despite several advances in understanding the soot formation, the nucleation process is still one of the least understood. There are various approaches descriing the particle inception pathways from gas-phase in combustion systems. Most comprehensive models are based on soot nucleation from multiple PAHs considering that not all collisions are succesful. However, the most used model assumes that soot nucleates through Brownian collision of two pyrene molecules ($A4$, with molecular formula $C_{16}H_{10}$) as in [Frenklach and Wang, 1994; Appel et al., 2000], resulting in incipient soot particles made up of 32 carbon atoms according

$$A4 + A4 \rightarrow Particle_1 + 10H_2.$$

With an expression analogous to the Smoluchowsky equation, the nucleation term is modeled as

$$\dot{N}_1 = \beta_{A4,A4} N_{A4}^2, \tag{3.20}$$

where N_{A4} is the number density of $A4$ ($N_{A4} = [A4]\mathcal{N}_A$) and $\beta_{A4,A4}$ is the collision frequency of PAH molecules. In terms of unit volume basis, the change in soot volume fraction due to nucleation in the first section (given in $\mathrm{cm}^3_{soot}\mathrm{cm}^{-3}\mathrm{s}^{-1}$) became:

$$\dot{Q}_{1,nuc} = 2 v_{A4} \beta_{A4,A4} N_{A4}^2, \tag{3.21}$$

where v_{A4} is the volume of the $A4$ molecule. This process adds volume to the first section only, and intrinsically assumes that the volume of the first particle is equal of the volume of carbon atoms present in the two precursors. The collision between two $A4$ molecules occurs in the free-molecular regime and its frequency is

$$\beta_{A4,A4} = 4\sqrt{2} k_{fm} (v_{A4})^{1/6}. \tag{3.22}$$

with the van der Waals enhancement factor ($\epsilon_{i,j}$) equal to 2.2 following the literature [Frenklach and Wang, 1994; Frenklach, 2002a; Zhang, 2009; Roy, 2014; Mehta et al., 2009].

To couple the solid phase with the gas-phase, production of H_2 and consumption of $A4$ by the nucleation process need to be accounted for. Considering the rate of soot nucleation, the $A4$ consumption and the H_2 production rates (in units of mol/(cm^{3}s), are respectively

$$\frac{d[A4]}{dt} = -2\frac{\dot{Q}_{1,nuc}}{2v_{A4}\mathcal{N}_A} = -2\beta_{A4,A4}\mathcal{N}_A[A4]^2 \tag{3.23}$$

$$\frac{d[H_2]}{dt} = -5\frac{d[A4]}{dt} \tag{3.24}$$

3.4.3.2 PAH condensation

Condensation is modeled as Brownian collision of PAH molecules and soot particles for all sections. Soot particles of section i growth due to PAH addition and migrate to the next higher section $i+1$. Solely pyrene molecules are allowed to condense onto soot particles surface.

The total soot volume growth rate due to $A4$ condensation $\Delta\dot{Q}_{i,cond}$ in section i is given by:

$$\Delta\dot{Q}_{i,cond} = v_{A4}N_{A4}\int_{v_{i-1}}^{v_i}\beta_{i,A4}n_i(v)\mathrm{d}v. \tag{3.25}$$

The numerical integration need to be performed for each section together with the complexity of $\beta_{i,A4} \sim f(v, v_{A4})$. Since this numerical integration is computationally demanding, a simple approach is to assume a mean particle volume, $\bar{v}_i$, for each section to estimate the collision rate ($\beta_{i,A4} \sim f(\bar{v}_i, v_{A4})$). In this way, $\beta_{i,A4}$ can be moved out of the integral and the total soot volume growth rate due to $A4$ condensation reduces to

$$\Delta\dot{Q}_{i,cond} = v_{PAH}\beta_{i,PAH}N_{PAH}\frac{Q_i}{v_i - v_{i-1}}\ln\left(\frac{v_i}{v_{i-1}}\right). \tag{3.26}$$

Unless explicitly described, the current formulation assumes a unity condensation probability. In other words, all collision among PAH and soot particles leads to soot surface growth due to condensation. Condensation also increase soot size in relatively low temperatures regions of flames rich in PAH.

Finally, considering the rate of soot condensation in section i, the $A4$ consumption and the H_2 production (in units of mol cm^{-3}s^{-1}), are respectively

$$\frac{d[A4]_i}{dt} = -\frac{\Delta \dot{Q}_{i,cond}}{v_{A4}\mathcal{N}_A} \tag{3.27}$$

$$\frac{d[H_2]_i}{dt} = 5\frac{\Delta \dot{Q}_{i,cond}}{v_{A4}\mathcal{N}_A} \tag{3.28}$$

3.4.3.3 Growth and oxidation by surface reactions

Heterogeneous surface reactions also play an important role on the soot surface growth. The kinetic mechanism required to model the heterogeneous gas-soot surface reactions is based on the Hydrogen-Abstraction-C_2H_2-Addition (HACA) plus reactions with O_2 and OH to account for soot oxidation [Appel et al., 2000]. This mechanism is hereafter mentioned as HACA-based mechanism. The constants of the heterogeneous soot-gas surface reactions are detailed in Table 3.1. The rate of surface reactions is given in terms of the particle surface area and of the number of surface sites (armchair sites on the particle surface), except for the reaction SR6 which is defined in terms of collision efficiency $\gamma_{OH} = 0.13$ [Neoh et al., 1981]. Variation of the HACA-based mechanism might also be employed for modelling non-premixed flames. One is the proposal of Wang et al., 1996, that assumes that surface radicals are conserved during surface growth and consist in substituting reaction SR4a by reaction SR4b but maintaining the reaction constants. This affect only the calculation of the active sites concentration as described below. Another possibility is to include additional reactions of H-abstraction, SR7-SR9, related to hydrocarbon radicals as proposed by Hwang and Chung, 2001. The latter authors discussed that surface activation by reaction SR1 dominates reactions SR7-SR9 when H is abundant in the sooting region as in premixed flame, however, reaction SR7-SR8 should not be neglected in flames where H is hardly present. This extended HACA-based mechanism was employed for modelling soot growth in counterflow diffusion flames in [Wang et al., 2015b; Wang and Chung, 2016a,b].

It should be noted that soot particles are assumed to be formed only by carbon atoms and that the hydrogen conservation is generally neglected without any serious

Table 3.1 – Heterogeneous soot-gas surface reactions mechanism. Where $\rightleftharpoons$ denotes a reversible reaction and $\rightarrow$ denote a irreversible reaction.

No.	Reaction	$k = AT^b exp(-E_a/RT)$		
		A (cm^{3}mol^{-1}s^{-1})	b	E_a (kcal/mol)
$SR1_f$	$C_{soot,n} + H \rightleftharpoons C^*_{soot,n} + H_2$	4.2×10^{13}	0.0	13.0
$SR1_r$		3.9×10^{12}	0.0	11.0
$SR2_f$	$C_{soot,n} + OH \rightleftharpoons C^*_{soot,n} + H_2O$	1.0×10^{10}	0.734	1.43
$SR2_r$		3.68×10^8	1.139	17.1
$SR3$	$C^*_{soot,n} + H \rightarrow C_{soot,n}$	2.0×10^{13}	0.0	0.0
$SR4a$	$C^*_{soot,n} + C_2H_2 \rightarrow C_{soot,n+2} + H$	8.0×10^{10}	1.560	3.8
$SR4b$	$C^*_{soot,n} + C_2H_2 \rightarrow C^*_{soot,n+2} + H$	8.0×10^{10}	1.560	3.8
$SR5$	$C^*_{soot,n} + O_2 \rightarrow C^*_{soot,n-2} + 2CO$	2.2×10^{12}	0.0	7.5
$SR6$	$C_{soot,n} + OH \rightarrow C^*_{soot,n-1} + CO$	$\gamma = 0.13$		
$SR7_f$	$C_{soot,n} + CH_3 \rightleftharpoons C^*_{soot,n} + CH_4$	3.99×10^{-1}	3.933	11.771
$SR7_r$		4.48×10^{-2}	4.248	4.277
$SR8_f$	$C_{soot,n} + C_3H_3 \rightleftharpoons C^*_{soot,n} + C_3H_4$	9.538×10^0	3.529	24.449
$SR8_r$		1.36×10^0	3.761	1.088
$SR9$	$C_{soot,n} + C_2H \rightarrow C^*_{soot,n} + C_2H_2$	2.0×10^{13}	0.0	0.0

error in the formulation. In reality, soot particles are formed by both C and H and gain or loss of hydrogen atoms occurs due to heterogeneous surface reactions, changing the C/H ratio as soot particles age. More fundamental approaches ensuring the hydrogen conservation would require the explicit track of H atoms and surface sites [Kholghy et al., 2016; Frenklach et al., 2018] or the solution of particles bins with different C/H ratios [Saggese et al., 2015]. Those approaches result in the solution of additional transport equations that lead to an increased computational time. Despite that, it is expected that assuming the transfer of hydrogen atoms between particles and H_2 do not exacerbate any lack of hydrogen conservation since the concentration of H_2 is much higher than the concentration of H atoms involved in the soot formation processes.

Surface sites presented in reactions SR1 to SR9 can be carbon atoms either saturated (C_{soot}) or dehydrogenated (C^*_{soot}). The concentration of saturated sites $[C_{soot}]_i$ on section i is calculated by

$$[C_{soot}]_i = \frac{\chi_{C_{soot}} S_i}{\mathcal{N}_A} \tag{3.29}$$

where $\chi_{C_{soot}}$ represent the number of sites per unit soot surface area and is estimated to be equal to 2.3×10^{15} sites/cm^2 [Frenklach and Wang, 1991, 1994; Appel et al., 2000];

S_i is the surface density of soot particles ($\mathrm{cm^2cm^{-3}}$) in section i, which is given by the surface area of soot particles times the number density in the respective section ($A_i \times N_i$). In terms of volume of particles with size class i, S_i is written by

$$S_i = \pi \left(\frac{6}{\pi}\right)^{2/3} \int_{v_{i,min}}^{v_{i,max}} v^{2/3} n_i(v) \mathrm{d}v,$$

where $n_i(v) = q_i/v$. Performing the integral for the constant profile of particles distribution inside section i, S_i become:

$$S_i = \pi \left(\frac{6}{\pi}\right)^{2/3} \frac{Q_i}{v_i - v_{i-1}} \frac{3}{2} \left(v_i^{2/3} - v_{i-1}^{2/3}\right).$$

The concentration of dehydrogenated (radical) active sites $[C^*_{soot}]_i$ is calculated assuming that a fraction of the radical sites per unit surface area on the soot are active:

$$[C^*_{soot}]_i = \frac{\alpha \chi_{C^*_{soot}} S_i}{\mathcal{N}_A}, \tag{3.30}$$

where α is the steric factor, $\chi_{C^*_{soot}}$ is the number of radical sites per unit surface area. $\chi_{C^*_{soot}}$ is obtained assuming a steady-state approximation for C^*_{soot} in the heterogeneous soot-gas surface reactions of the HACA-based mechanism according to

$$\chi_{C^*_{soot}} = k_{ss} \chi_{C_{soot}}, \tag{3.31}$$

with k_{ss} being the steady-state constant from SR1 to SR5 (Table 3.1) defined as

$$k_{ss} = \begin{cases} \text{for depleted surface radicals (SR4a):} \\ \dfrac{k_{1,f}[H] + k_{2,f}[OH]}{k_{1,r}[H_2] + k_{2,r}[H_2O] + k_{3,f}[H] + k_{4,f}[C_2H_2] + k_{5,f}[O_2]} \\ \\ \text{for conserved surface radicals (SR4b):} \\ \dfrac{k_{1,f}[H] + k_{2,f}[OH]}{k_{1,r}[H_2] + k_{2,r}[H_2O] + k_{3,f}[H] + k_{5,f}[O_2]} \end{cases} \tag{3.32}$$

$k_{j,f}$ and $k_{j,r}$ are, respectively, the forward and the reverse rate coefficients for reaction j.

In the case of the extended HACA-based mechanism (reactions SR1 to SR9) the steady-state constant k_{ss} is given by

$$k_{ss} = \begin{cases} \text{for depleted surface radicals (SR4a):} \\ \dfrac{k_{1,f}[H] + k_{2,f}[OH] + k_{7,f}[CH_3] + k_{8,f}[C_3H_3] + k_{9,f}[C_2H]}{k_{1,r}[H_2] + k_{2,r}[H_2O] + k_{3,f}[H] + k_{4,f}[C_2H_2] + k_{5,f}[O_2] + k_{7,r}[CH_4] + k_{8,r}[AC_3H_4]} \\ \\ \text{for conserved surface radicals (SR4b):} \\ \dfrac{k_{1,f}[H] + k_{2,f}[OH] + k_{7,f}[CH_3] + k_{8,f}[C_3H_3] + k_{9,f}[C_2H]}{k_{1,r}[H_2] + k_{2,r}[H_2O] + k_{3,f}[H] + k_{5,f}[O_2] + k_{7,r}[CH_4] + k_{8,r}[AC_3H_4]} \end{cases} \tag{3.33}$$

The steric factor, α, quantify the changes in soot surface morphology as dependent of particle size and the local temperature [Appel et al., 2000] and is given by

$$\alpha = \tanh\left(\frac{a}{\log \bar{n}_{C_{atoms}} + b}\right), \tag{3.34}$$

where $a(T) = 12.65 - 0.00563T$ and $b(T) = -1.38 + 0.00068T$ are fitted functions of the local temperature. The number of carbon atoms $\bar{n}_{C_{atoms}}$ of the average particle size of section i is given by the ratio of the average soot particle volume and the volume of one carbon atom v_C:

$$\bar{n}_{C_{atoms}} = \frac{\int_{v_{i,min}}^{v_{i,max}} v n_i(v) \mathrm{d}v}{\int_{v_{i,min}}^{v_{i,max}} n_i(v) \mathrm{d}v} \frac{1}{v_C}.$$

With the previous definitions, the rate of soot surface growth due to C_2H_2 addition and oxidation by O_2 and OH in section i given, respectively, by reactions SR4, SR5 and SR6 are

$$\Delta\dot{Q}_{i,sg} = +2 v_C k_4 [C_2H_2][C^*_{soot}]_i \mathcal{N}_A, \tag{3.35}$$

$$\Delta\dot{Q}_{i,ox,O_2} = -2 v_C k_5 [O_2][C^*_{soot}]_i \mathcal{N}_A, \tag{3.36}$$

and

$$\Delta\dot{Q}_{i,ox,OH} = -1 v_C \gamma [OH] \mathcal{N}_A \int_{v_{i,min}}^{v_{i,max}} \beta_{i,OH} n_i(v) \mathrm{d}v. \tag{3.37}$$

Since a mean particle size is assumed for each section, the collision rate between OH molecules and soot particles of section i becomes $\beta_{i,OH} \sim f(\bar{v}_i, v_{OH})$ and the numerical integration is simplified. This approach is similar to the one assumed for the $A4$

condensation.

In a similar way, the rate of production/consumption of gas-phase specie G_l due to surface reaction j for each soot section can be written as

$$\dot{\omega}_{l,j} = \pm n_{G_l} k_j \prod [G_l]_j \tag{3.38}$$

where k_j is the rate of reaction j in Table 3.1, n_{G_l} is the number of mole produced/consumed of specie G_l with ± representing production + or consumption −. This general formulation is valid for all surface reactions with except for SR6, which is based on the collision efficiency between OH and particles in section i:

$$\dot{\omega}_{l,6} = \pm n_{G_l} \gamma [OH] \int_{v_{i,min}}^{v_{i,max}} \beta_{i,OH} n_i(v) \mathrm{d}v \tag{3.39}$$

3.4.3.4 Coagulation

Coagulation source terms involve a direct integration of the Smoluchowsky equation over all sections. It describes the particle-particle interactions in the limit of pure coalescence. Unless explicitly described, unity collisions efficiency are assumed. Two coagulation models were implemented in this thesis and are described below:

- Gelbard et al., 1980, model:

In the formalism of Gelbard et al., 1980, the coagulation source term of section i is defined as:

$$\begin{aligned} \dot{Q}_{i,coag} = & \sum_{r=1}^{i-1} \sum_{p=1}^{i-1} \beta^1_{r,p,i} Q_{s,r} Q_{s,p} - Q_{s,i} \sum_{r=1}^{i-1} \beta^2_{r,i} Q_{s,r} \\ & - \frac{1}{2} \beta^3_{i,i} Q^2_{s,i} - Q_{s,i} \sum_{r=i+1}^{\mathcal{N}_{sec}} \beta^4_{r,i} Q_{s,r}, \end{aligned} \tag{3.40}$$

where $\beta^{1 \dots 4}$ are the sectional coagulation coefficients

$\beta^1_{r,p,i}$ is valid in the limit $2 \leq i \leq \mathcal{N}_{sec}$ for $r < i$ and $p < i$,
$\beta^2_{r,i}$ is valid in the limit $2 \leq i \leq \mathcal{N}_{sec}$ for $r \leq i$,
$\beta^3_{i,i}$ is valid in the limit $1 \leq i \leq \mathcal{N}_{sec}$,
$\beta^4_{r,i}$ is valid in the limit $1 \leq i \leq \mathcal{N}_{sec}$ for $i < r$.

calculated by

$$\beta^1_{r,p,i} = \int_{l=v_r-1}^{v_r} \int_{m=v_p-1}^{v_p} \frac{\delta_{(v_{i-1}<l+m\leq v_i}(l+m)\beta_{l,m})}{lm(v_r - v_{r-1})(v_p - v_{p-1})} \mathrm{d}m\mathrm{d}l \tag{3.41}$$

$$\beta^2_{r,i} = \int_{l=v_r-1}^{v_r} \int_{m=v_i-1}^{v_i} \frac{\left[\delta_{(l+m>v_i)}m - \delta_{(l+m\leq v_i)}l\right]\beta_{l,m}}{lm(v_r - v_{r-1})(v_i - v_{i-1})} \mathrm{d}m\mathrm{d}l \tag{3.42}$$

$$\beta^3_{i,i} = \int_{l=v_i-1}^{v_i} \int_{m=v_i-1}^{v_i} \frac{\delta_{(l+m>v_i)}(l+m)}{lm(v_i - v_{i-1})(v_i - v_{i-1})} \mathrm{d}m\mathrm{d}l \tag{3.43}$$

$$\beta^4_{r,i} = \int_{l=v_r}^{v_r} \int_{m=v_i-1}^{v_i} \frac{m\beta_{l,m}}{lm(v_r - v_{r-1})(v_i - v_{i-1})} \mathrm{d}m\mathrm{d}l \tag{3.44}$$

The reader is refereed to the original work of Gelbard et al., 1980, for a detailed description of this formalism.

To avoid the expensive numerical integration of the double integrals of the collision coefficients ($\beta^{1...4}$), its computation is done in terms of the mean particle size of each section ($\bar{v}_i$). For a sufficient number of sections it is expected that any mass loss arising from the current simplification is negligible. The size range of section i may be divided into small sub-sections j to enhance the coagulation predictions [Netzell et al., 2007; Mauss et al., 2009]. Each sub-section presents a representative size $\bar{v}_{i,j}$ with a proportional q_i value (since it is assumed a constant q_i profile for each section). Then, the sectional coagulation source term is computed by directly accounting the collision between all the subsections. However, Mauss et al., 2009, pointed out that the inclusion of these sub-sections do not improve expressively the particle size distribution.

- Kumar and Ramkrishna, 1996, model:

The particle population in each section is described by a number of particles N_i with representative volume $\bar{v}_i$. Thus the evaluation of the double integrals of the coagulation coefficients is not necessary. The soot coagulation source term of section i derived by Kumar and Ramkrishna, 1996, is given by

$$\frac{\mathrm{d}N_i}{\mathrm{d}t} = \sum_{\bar{v}_{i-1}\leq(\bar{v}_j+\bar{v}_k)\leq\bar{v}_{i+1}}^{k\leq j\leq i} \left(1 - \frac{\delta_{j,k}}{2}\right)\theta\beta_{j,k}N_jN_k - N_i\sum_{k=1}^{\mathcal{N}_{sec}}\beta_{i,k}N_k \tag{3.45}$$

where $\delta_{j,k}$ is the collision efficiency between particles with representative size of section j and k, which is assumed to be unity, and θ is the splitting factor of the new particles given by

$$\theta = \begin{cases} \dfrac{\bar{v}_{i+1} - (\bar{v}_j + \bar{v}_k)}{\bar{v}_{i+1} - \bar{v}_i}, & \bar{v}_i \leq (\bar{v}_j + \bar{v}_k) \leq \bar{v}_{i+1} \\ \dfrac{\bar{v}_{i-1} - (\bar{v}_j + \bar{v}_k)}{\bar{v}_{i-1} - \bar{v}_i}, & \bar{v}_{i-1} \leq (\bar{v}_j + \bar{v}_k) \leq \bar{v}_i \end{cases} \tag{3.46}$$

One particularity of this model is that collision of two particles my result in the generation of particles that lay in between two adjacent representative sizes. Therefore, the splitting scheme η is devised to assign the new particle to the two adjacent representative sizes, leading to the conservation of both mass and number density.

It is worth noting that Equation 3.45 is described in terms of the particles number density. Since source terms of the sectional equations are given in terms of the volume fraction, the conversion from number density to volume fraction is done evoking Equation 3.16, which results in

$$\dot{Q}_{i,coag} = \frac{\mathrm{d}N_i}{\mathrm{d}t} \frac{(v_{i,max} - v_{i,min})}{\ln(v_{i,max}/v_{i,min})} \tag{3.47}$$

3.4.4 Inter-sectional dynamics

An inter-sectional model is needed to account for the migration of particles from one section to their neighboring sections [Netzell et al., 2007; Mauss et al., 2009; Vervisch, 2012; Roy, 2014]. The distribution of the rate of change in soot volume $\Delta\dot{Q}_i$ for section i is constrained by the number density conservation, so that

$$\Delta\dot{Q}_i = \Delta\dot{Q}_i^{out} + \Delta\dot{Q}_i^{ins}. \tag{3.48}$$

$\Delta\dot{Q}_i^{out}$ represents soot volume that moves to the lower or higher neighbor section after the surface process, whereas $\Delta\dot{Q}_i^{ins}$ is the net soot volume of section i such that $\Delta\dot{Q}_i^{ins} = \Delta\dot{Q}_i - \Delta\dot{Q}_i^{out}$.

The inter-sectional dynamics are crucial for the evaluation of source terms for a given section. They are required for surface processes because these processes alter the soot particle size but not the number density. On the other hand, soot coagulation models already incorporate particle dynamics into their formalism. Thus, $\Delta\dot{Q}_i^{out}$ and $\Delta\dot{Q}_i^{ins}$ are defined for $A4$ condensation, growth by C_2H_2 and oxidation by O_2 and OH.

For growing particles, the number density conservation across sections assuming an evenly distributed $\Delta\dot{Q}_i$ within the section gives:

$$-\Delta N_i = \Delta N_{i+1}. \tag{3.49}$$

Which can be rewritten using Equations 3.15 and 3.16 as

$$\frac{\Delta \dot{Q}_i^{ins}}{v_{i,max} - v_{i,min}} \int_{v_{i,min}}^{v_{i,max}} \frac{1}{v} \mathrm{d}v = \frac{\Delta \dot{Q}_i^{out}}{v_{i+1,max} - v_{i+1,min}} \int_{v_{i+1,min}}^{v_{i+1,max}} \frac{1}{v} \mathrm{d}v. \tag{3.50}$$

Finally, combining Equation 3.50 with Equation 3.48 it is found:

$$\Delta \dot{Q}_{i,(sg)}^{out} = \frac{\Delta \dot{Q}_{i,(sg)}}{1 - \dfrac{v_{i,max} - v_{i,min}}{v_{i+1,max} - v_{i+1,min}} \dfrac{\ln(v_{i+1,max}/v_{i+1,min})}{\ln(v_{i,max}/v_{i,min})}}, \tag{3.51}$$

$$\Delta \dot{Q}_{i,(sg)}^{ins} = \frac{\Delta \dot{Q}_{i,(sg)}}{1 - \dfrac{v_{i+1,max} - v_{i+1,min}}{v_{i,max} - v_{i,min}} \dfrac{\ln(v_{i,max}/v_{i,min})}{\ln(v_{i+1,max}/v_{i+1,min})}}. \tag{3.52}$$

where the subscript *sg* stands for surface growth.

Similarly, for particles reducing in size due to oxidation

$$-\Delta N_i = \Delta N_{i-1}, \tag{3.53}$$

it is found:

$$\Delta \dot{Q}_{i,(ox)}^{out} = \frac{\Delta \dot{Q}_{i,(ox)}}{1 - \dfrac{v_{i,max} - v_{i,min}}{v_{i-1,max} - v_{i-1,min}} \dfrac{\ln(v_{i-1,max}/v_{i-1,min})}{\ln(v_{i,max}/v_{i,min})}}, \tag{3.54}$$

$$\Delta \dot{Q}_{i,(ox)}^{ins} = \frac{\Delta \dot{Q}_{i,(ox)}}{1 - \dfrac{v_{i-1,max} - v_{i-1,min}}{v_{i,max} - v_{i,min}} \dfrac{\ln(v_{i,max}/v_{i,min})}{\ln(v_{i-1,max}/v_{i-1,min})}}, \tag{3.55}$$

where the subscript *ox* stands for oxidation.

3.4.5 Source terms

The source terms in soot volume basis, $\dot{Q}_{i,sg}$ ($\mathrm{cm}^3_{soot}\mathrm{cm}^{-3}\mathrm{s}^{-1}$), can be defined in the section i after the inter-sectional dynamics computation. The first and last sections require special treatments in the constraints. There is no soot growing out from the last section $\mathcal{N}_{sec}$, thus, $\Delta \dot{Q}^{out}_{\mathcal{N}_{sec},(sg)} = 0$ and $\Delta \dot{Q}^{ins}_{\mathcal{N}_{sec},(sg)} = \Delta \dot{Q}_{\mathcal{N}_{sec},(sg)}$. On the other side, the first section can still lose particles for the gas-phase by oxidation but not for any other section, so that, $\Delta \dot{Q}^{out}_{(ox)} = 0$ and $\Delta \dot{Q}^{ins}_{(ox)} = \Delta \dot{Q}_1$. The source terms for surface growth can be written as

$$\dot{Q}_{i,sg} = \Delta\dot{Q}^{out}_{i-1,sg} + \Delta\dot{Q}^{ins}_{i,sg}, \tag{3.56}$$

where $\Delta\dot{Q}^{ins}_{i,sg}$ represent the growth rate of soot particles that remain in the same section i, and $\Delta\dot{Q}^{out}_{i-1,sg}$ represent the growth rate of soot particles that moves out of section $i-1$ to i. However, there is no soot growing from section lower than the first and there is no soot growing out of the last section, in this way, the source term for $A4$ condensation and carbon addition by C_2H_2 become

$$\dot{Q}_{i,(sg)} = \begin{cases} \Delta\dot{Q}_{i,(sg)} & \text{for } i = 1 \\ \Delta\dot{Q}^{out}_{i-1,(sg)} + \Delta\dot{Q}^{ins}_{i,(sg)} & \text{for } 1 < i < \mathcal{N}_{sec} \\ \Delta\dot{Q}^{out}_{i-1,(sg)} + \Delta\dot{Q}_{i,(sg)} & \text{for } i = \mathcal{N}_{sec} \end{cases} \tag{3.57}$$

The source terms for surface oxidation $\dot{Q}_{i,ox}$ process is formed by oxidation rate of soot particles that stays in the section i, $\Delta\dot{Q}^{ins}_{i,ox}$, and by the oxidation rate of soot particles that moves from section $i+1$ to i, $\Delta\dot{Q}^{out}_{i+1,ox}$, according to

$$\dot{Q}_{i,ox} = \Delta\dot{Q}^{out}_{i+1,ox} + \Delta\dot{Q}^{ins}_{i,ox}. \tag{3.58}$$

As there is no soot coming by oxidation from sections greater than the last one, $\mathcal{N}_{sec}$, and there is no soot moving out the first section, the source term for oxidation by O_2 and OH become

$$\dot{Q}_{i,(ox)} = \begin{cases} \Delta\dot{Q}^{out}_{i+1,(ox)} + \Delta\dot{Q}_{i,(ox)} & \text{for } i = 1 \\ \Delta\dot{Q}^{out}_{i+1,(ox)} + \Delta\dot{Q}^{ins}_{i,(ox)} & \text{for } 1 < i < \mathcal{N}_{sec} \\ \Delta\dot{Q}_{i,(ox)} & \text{for } i = \mathcal{N}_{sec} \end{cases} \tag{3.59}$$

3.5 Gas-phase kinetic mechanism

Two principal gas-phase reaction mechanisms were employed in the numerical modelling along this work. The C2 chemistry of Appel et al., 2000, (namely ABF) consists of 101 chemical species and 544 reactions describing the pyrolysis and oxidation of C1-C2 hydrocarbons including PAH growth beyond pyrene ($A4$). The mechanism was originally created for predicting sooting characteristics in premixed flames, but it also performed reasonably well in predicting sooting characteristics of non-premixed flames [Zhang, 2009; Mehta et al., 2009; Dworkin et al., 2011; Liu et al., 2015]. However, recent studies demonstrate that PAH concentration was underpredicted in the fuel rich region of ethylene laminar coflow flames [Dworkin et al., 2011] and in counterflow flames of ethylene and ethane [Wang et al., 2015b]. The C4 reaction mechanism of Wang et al., 2013, (namely KM2) comprises of 202 species and 1351 reactions including PAH growth up to coronene ($A7$). The KM2 mechanism was validated for ethylene premixed flames at low and atmospheric pressures and was also successfully used to study the effects of mixing propane and benzene in the fuel stream on counterflow ethylene flames. This mechanism was further employed to simulate soot formation in both premixed [Naseri et al., 2017] and non-premixed counterflow flames [Wang et al., 2015b; Wang and Chung, 2016a]. Other kinetic mechanisms include the reaction mechanism of Slavinskaya and Frank, 2009, (which PAHs routes formation were further updated by Chernov et al., 2014) that predicts PAHs formation up to five-rings and the Blanquart et al., 2009, reaction mechanism with PAHs predictions up to pyrene. These mechanisms distinguish significantly among them not only regarding the coefficients of the Arrhenius's equation but also in the chemical pathways. A comparison between all these mechanisms is performed in Appendix A for a incipient sooting counterflow flame of ethylene experimentally studied by Carbone et al., 2015. From the comparison it was observed that the chemical prediction of lightweight species are much more consolidated while significant discrepancies can be found for large aromatic species.

3.6 Assessment of the DSM in laminar non-premixed counterflow flames

The main difficulty in soot modelling is that all the physical and chemical processes are not yet fully understood. This leads to the proposal of models of varying complexity degrees. Even for detailed soot models, several parameters are still experimentally defined and, in this way, dependent on the combustion process. Therefore, the basic implementation of the DSM is verified in Appendix B with the data provided in [Roy, 2014] for the reference soot model. The implemented DSM is explored in Appendix C for modelling the soot formation of non-premixed counterflow flames. A sensitivity study of the number of sections and of the coagulation models are performed in Appendix C followed by a evaluation of the effects of several DSM variants on the soot predictions.

4 EFFECTS OF CO2 ADDITION ON SOOT FORMATION OF ETHYLENE NON-PREMIXED FLAMES UNDER OXYGEN ENRICHED ATMOSPHERES

This section was fully published at: Journal Combustion and Flame, 2019, Vol. 203, pp. 407-423.

4.1 Introduction

Regulations related to soot emissions are becoming more stringent due to the negative impact of soot on the environment and human health [Lighty et al., 2000; Seaton and Donaldson, 2005; Kum, 2009; Shrestha et al., 2010; Kim et al., 2013]. Soot exists as individual spherical particles (of the order of 10 nm) or in the form of agglomerated particles (with size up to 1 μm). These nano-particles can easily escape out from post-combustion cleaning devices of exhaust systems [Lighty et al., 2000] and may be dispersed long-range through the air. Soot contaminates soils and water basins, and contributes to the global warming and climate change [Shrestha et al., 2010] in two ways: atmospheric soot particles absorb solar radiation, directly heating the atmosphere, and soot deposits decrease the Earth's surface albedo. Moreover, soot particles are toxic, carcinogenic and mutagenic, and once inhaled, they may travel from the lungs to the blood and can easily penetrate human cells [Lighty et al., 2000; Seaton and Donaldson, 2005; Kim et al., 2013], causing many respiratory and heart illnesses. Thus, it is not sufficient to control only the total amount of soot released from hydrocarbon combustion, but the particle size is also a matter of concern.

New combustion technologies have demonstrated to be good strategies in reducing pollutants while improving combustion efficiency. Such technologies include oxygen-enriched flames [Baukal Jr, 2010; Escudero et al., 2016] and oxyfuel flames [Nemitallah et al., 2017; Zhang et al., 2018], which can be allied with flue gas recirculation. In oxy-combustion technologies, the high oxygen concentration accelerates the fuel consumption and increases the flame temperature. This condition is very favorable to the formation of soot, but at some level the oxygen enrichment can also promote soot oxidation in the post flame region [Zhang et al., 2018; Hwang and Chung, 2001; Kalvakala et al., 2018]. Therefore, higher local peaks of soot volume fraction can be achieved while the release of soot to the atmosphere may be suppressed. Complementary, the recirculation of combustion products, principally dry CO_2, helps to control flame temperature, enhances radiation heat transfer and drops the generation of NO_x by reducing both the temperature and the nitrogen content of the mixture. Moreover, oxy-combustion technologies, allied to flue gas recirculation, facilitate the carbon dioxide capture and storage [Boot-Handford et al., 2014; Underschultz et al., 2016]. Significant amounts of CO_2 are also frequently found in renewable fuels such as biogas or syngas. Despite the peculiarities of each combustion process and fuel composition, in all of them CO_2 plays an important role. The amount of CO_2 influences the combustion process by limiting the concentration of reactants, by participating in elementary reactions, by changing the thermodynamic properties (mainly to its higher heat capacity when compared to N_2) and by modifying the transport properties of the mixture [Du et al., 1991; Liu et al., 2001]. The CO_2 also reduces the soot volume fraction by limiting the formation of soot precursors and species responsible for surface growth [Wang and Chung, 2016a; Naseri et al., 2017] and by acting as a participating species in radiative heat transfer [Dorigon et al., 2013; Cassol et al., 2014].

The multiple effects of CO_2 concentration on flame behavior has been explored by many investigators. Du et al., 1991, demonstrated that CO_2 addition in the fuel or in the oxidizer can suppress soot formation due to chemical effects, and not just through the influence of decreased reactant concentrations and flame temperature reduction, with thermal effect exerting a strong influence on soot particle inception limit. Liu et al., 2001, observed a reduction of the maximum temperature and a dramatic decrease of C_2H_2 concentration with CO_2 addition on both fuel and oxidizer sides. Additionally, it was found that the chemical effect is associated to the reaction $CO_2 + H \rightleftharpoons CO + OH$ which increases the concentration of hydroxyl radicals (OH) and decreases the H-radicals. Hence, the increased OH concentration would enhance the oxidative attack on soot precursors. On the other hand, for fuel dilution, Guo and Smallwood, 2008 found a negligible chemical effect of the CO_2 addition on soot oxidation process because, although the formation of OH is intensified by the last reaction, its formation by reaction $H + O_2 \rightarrow O + OH$ is reduced. They also observed that the consumption of H-radicals, by the former reaction, suppresses the formation of higher size PAHs (leading to lower soot inception) and also suppresses the soot surface growth rate. Oh and Shin [Oh and Shin, 2006] observed a reduction in primary particle number concentration and soot volume fraction with CO_2 addition in the oxidizer stream. The suppression was attributed to a short residence time in the inception region and to a small surface growth region. Similarly, Wang and Chung, 2016a, observed a reduction in the soot volume fraction and number density in fuel diluted ethylene counterflow non-premixed flames. They also found that the CO_2 addition chemically reduces the soot precursors formation (lowering inception rates and soot number density, which in turn results in lower surface area for soot mass addition) and reduces H, CH_3 and C_3H_3 concentrations (limiting the H-abstraction rate and making, consequently, less active sites per unit surface area to be available for soot growth). Comparing the effect of fuel dilution with hydrogen and carbon dioxide on soot formation of ethylene coflow flames, Gu et al., 2016, showed that the addition of H_2 is more effective in the soot inception suppression while the addition of carbon dioxide is more effective in suppressing the soot surface growth, and that the chemical interactions between these two diluents on soot formation are weak. The effect of changing the stoichiometric mixture fraction (Z_{st}) on flame structure and soot formation was analyzed by Lou et al., 2019. Using CO_2 as diluent they demonstrated that high temperature flames with reduced soot formation are obtained by increasing Z_{st} via the combination of fuel dilution and oxygen enrichment. It was also found that, for a constant Z_{st}, reducing the CO_2 addition enhances soot formation due to higher flame temperature while reducing thermal radiation emissions.

Recently, studies about the influence of dilution with carbon dioxide on soot formation were carried out in premixed laminar ethylene burner stabilized stagnation flames. Tang et al., 2016, studied the particle size distribution and showed that, CO_2 addition decreases soot nucleation and mass growth rates. They argued that the inhibition of soot formation was caused predominantly by chemical effects. The same observations were made by Naseri et al., 2017. They found, from sensitivity analysis, that the reaction $CH_2^* + CO_2 \rightarrow CH_2O + CO$ is one of the most sensitive reactions to the addition of carbon dioxide. The rise in consumption of CH_2^* with dilution would lead to a further reduction in C_2H_2, C_3H_3 and benzene (species that are the main responsible for the growth of higher PAHs). They argued that CO_2 affects soot formation primarily trough PAH suppression since soot growths via HACA is not noticeable in this type of flames. As a consequence of the decline in nucleation rate and surface growth, the particle size distribution presents a reduction in the particle number density and a shift towards smaller particles.

It is clear that CO_2 suppresses the soot formation. It is also widely recognized that the reaction $CO_2 + H \rightarrow CO + OH$ is one of the main pathways for the CO_2 chemical effect, which results in the suppression of species related to the soot formation. However, there is still room for further clarification on the detailed mechanisms through which the CO_2 influences the sooting flame structure. Particularly for non-premixed flames, the effect of CO_2 on the particle size distribution is a subject that is rarely explored, and the differences on the mechanism by which CO_2 influences flame structure when added to the fuel or to the oxidizer mixtures are not clearly demonstrated. Furthermore, a direct comparison of CO_2 addition on the fuel or on the oxidizer side has to be carefully interpreted because the same CO_2 molar fraction on the fuel or oxidizer streams represents two very distinct flame conditions. A better comparison between fuel/oxidant dilution can be obtained by considering flames with the same amount of CO_2 in a stoichiometric mixture of fuel and oxidant, according to Hoerlle et al., 2017.

Thus, the aim of this paper is to analyze the role of CO_2 addition on soot formation in oxygen-enriched non-premixed flames exploring the CO_2 effect on the particle size distribution while clarifying the peculiarities of fuel and oxidant dilution. The study will be conducted numerically for one-dimensional counterflow flames. Specifically, this work intend to contribute to a further comprehension of the mechanisms by which a systematic addition of CO_2 on reactants influence (1) the general flame structure, (2) the soot inception and further growth/oxidation process and, consequently, (3) the particle size distribution. To the author best knowledge, such a comprehensive study has not yet been reported for laminar non-premixed flames.

4.2 Numerical model

Steady-state one-dimensional flames were solved with the CHEM1D [Somers, 1994] code. The code solves the system of conservation equations for reactive flows based on the finite volume method with a fully implicit modified Newton technique. A computational domain of 2.0 cm length is initially discretized with 400 equidistant points and the code employs a grid refinement algorithm to increase the number of control volumes in regions with steep gradients. The advective terms of the conservation equations were treated by the exponential discretization scheme, while the diffusive ones were treated by the central difference scheme.

The conservation equations describe the conservation of total mass, stretch rate, chemical species and enthalpy. The derivation of this set of equations can be found in [de Goey and ten Thije Boonkkamp, 1999b] and will not be repeated here. The mixture density is only a function of temperature due to the Low Mach number approximation. The stretch rate is understood as a relative rate of change of mass, and contemplates all local deviations from the one-dimensional approximation. In the current formalism, the velocity boundary is treated as a potential flow. The energy equation is solved in terms of the total specific enthalpy of the mixture. Species diffusivities are modeled by the Fick's Law, while the Soret and Duffor effects are neglected. The conservation of total mass is guaranteed employing a velocity correction for all species. In the current code, the flow stagnation plane is imposed to be located at $x = 0$ cm. The details of the soot model are given in the following sections.

Reaction rates are modeled by the Arrhenius equation and the KAUST Mechanism 2.0 [Wang et al., 2013]. Formed by 203 species and 1346 reactions to describe C1-C4 oxidation including chemical path up to coronene, the mechanism was validated for premixed and counterflow flames. Wang et al., 2013, reported an improved agreement of the KM2 mechanism with experimental data of PAHs for counterflow flames when compared to other kinetic mechanisms. Moreover, the KM2 mechanism was successfully employed in modelling soot formation in counterflow [Wang and Chung, 2016a] and premixed [Naseri et al., 2017] ethylene flames diluted with CO_2.

The Radiative Transfer Equation (RTE) describes the radiative intensities considering emission, absorption and neglecting scattering for a participating medium formed by CO_2, H_2O and soot. The spatial dependence of the RTE was solved by the Discrete Ordinate method and the spectral dependence of the absorption coefficient is treated by solving the RTE with the superposition Weighted-Sum-of-Gray-Gases (WSGG) following [Cassol et al., 2015].

4.2.1 Soot model

The present approach considers that soot particles are solid spheres, modeled as a distinct dispersed phase interacting with the gaseous phase. The gas-phase and the particulate-phase are fully coupled following Zimmer et al., 2017. Soot is assumed to have a specific mass equal to 1.86 g/cm^3 (graphite).

The soot formation follows a Discrete Sectional method based on the models of [Gelbard et al., 1980; Netzell et al., 2007; Mauss et al., 2009; Roy, 2014; Vervisch, 2012; Aubagnac-Karkar et al., 2015]. This method assumes that the continuous particle size distribution is discretized in a finite number of sections, each one representing a range (or class) of soot particle sizes. Thus, a standard transport equation for the soot mass fraction is solved for each section. The thermophoretic velocity for round particles in the free-molecular regime is assumed to be the same for all soot size classes and is computed as indicated in [Friedlander, 2000]:

$$v_T = -\frac{3}{4}\left(1+\frac{\pi\alpha_{acc}}{8}\right)^{-1}\frac{\nu}{T}\nabla T, \tag{4.1}$$

where ν is the kinematic viscosity , $\alpha_{acc} = 1.0$ is the accommodation factor and T the local temperature. A very small particle diffusivity (1% of the average gas diffusivity) is retained following [Zimmer et al., 2017] solely for numerical stability, but does not effectively contribute to particle diffusion.

4.2.1.1 Discretization of the particle-size distribution

The particle size range is discretized based on soot particle volume following a geometric progression [Roy, 2014]:

$$v_{i,max} = v_0 \left(\frac{v_{_{MAX}}}{v_0}\right)^{i/\mathcal{N}_{sec}}, \tag{4.2}$$

where $v_{i,max}$ is the maximum particle volume of section i, $v_{_{MAX}}$ is the volume size of the biggest soot particle, v_0 the size of the smallest particle and $\mathcal{N}_{sec}$ the total number of sections. Considering that the first particle is formed from the collision of two pyrene molecules ($C_{16}H_{10}$ or $A4$ for a short reference), v_0 becomes equal to 3.43E-22 cm^3 which corresponds approximately to the volume of a sphere with diameter of 0.9 nm. The maximum particle volume is assumed to be $v_{_{MAX}} = 5.30\text{E-}12$ cm^3, which corresponds to a particle with diameter of approximately 2163 nm. The maximum soot volume size was defined so that the particle-size distribution of the flames under analysis would be entirely covered by the model (no soot particles are present in the last section). Preliminary studies indicated that 50 sections ($\mathcal{N}_{sec} = 50$) present a good compromise between computational efficiency and accuracy.

4.2.1.2 Model variables

The soot mass fraction of section i ($Y_{s,i}$) can be directly correlated to the volume fraction of section i (Q_i) by the ratio between the density of soot (ρ_s) and the density of gas mixture (ρ): $Y_{s,i} = \rho_s Q_i/\rho$. Similarly, the source terms ($\dot{\omega}_i$) in the transport equations are given by $\dot{\omega}_{s,i} = \rho_s \dot{Q}_i$, where $\dot{Q}_i$ is the rate of volume fraction creation/destruction by a given process. The soot parameter representing soot particles within a section is the soot volume fraction density q_i, which is assumed to be a constant distribution within each section as

$$q_i = \frac{Q_i}{v_{i,max} - v_{i,min}}, \tag{4.3}$$

where $v_{i,min}$ and $v_{i,max}$ are respectively the lower and upper volume boundaries of section i. The number density distribution ($n_i(v)$) within each section is $n_i(v) = q_i/v$, with v being the particle volume. This formalism leads to the calculation of the section i number density, N_i, according to

$$N_i = \int_{v_{i,min}}^{v_{i,max}} n_i(v)dv = \frac{Q_i}{v_{i,max} - v_{i,min}} \ln\left(\frac{v_{i,max}}{v_{i,min}}\right). \tag{4.4}$$

Finally, the total soot volume fraction (f_v) and the total number density (N) are given by the sum of Q_i and N_i over all sections. The type of the soot parameter function (constant, linear, logarithmic) does not affect the final result for sufficient number of sections [Roy, 2014].

4.2.1.3 Physical and chemical process of soot formation

All processes that describe the volumetric rate of soot production in the transport equations are formulated in terms of the volume fraction. Soot dynamics are accounted for by physical (nucleation, condensation and coagulation) and chemical (reactions with C_2H_2, O_2, and OH) processes. Their contributions are computed for each section.

The physical processes are represented by the Smoluchowski equation. This equation describes the interaction between soot particles moving in Brownian motion as a function of particle size, collision efficiency and the thermodynamic estate. Collisions, may occur at different regimes (from free-molecular to continuum regime) according to the Knudsen number (K_n). For atmospheric low to moderate sooting flames it is unlikely that soot particles interaction reach the continuum regime ($K_n < 0.1$) or the transition regime ($0.1 \leq K_n \leq 10$) [Kazakov and Frenklach, 1998]. In this work it is assumed that collisions occur solely in the free-molecular regime ($K_n > 10$). The collision frequency, β, between particle-particle or particle-molecule, is defined as a function of the particle size and the local gas temperature following [Mauss et al., 2009; Kazakov and Frenklach, 1998; Frenklach and Wang, 1994], with a constant Van der Waals enhancement factor of 2.2 [Harris and Kennedy, 1988]. For the flames studied in this work (presented in Section 4.4), the local Knudsen number for the average diameter is in general larger than 10 while the Knudsen number for the section with the largest volume fraction varies between 4 and 10. Thus, the free-molecular regime approximation is not expected to introduce significant errors.

The knowledge of polycyclic-aromatic hydrocarbons (PAHs) formation and growth and their role in soot formation processes has deepened during the last decades [Richter and Howard, 2000; Frenklach, 2002b; Wang, 2011]. Several researchers demonstrated the participation of PAHs of multiple size in soot inception and condensation [Wang et al., 2015b; Eaves et al., 2017]. It was found that bigger PAHs (up to 20 carbon atoms) are more likely to stick together after collision. Hence, they are more prone to form the first particles and to condense onto the particle surface than smaller PAHs as benzene. Not all PAHs' collisions form a dimer neither stick onto the particle surface [D'Alessio et al., 2005; Raj et al., 2010]. PAH-PAH and PAH-particle iteration are usually assumed irreversible processes, therefore, collision efficiencies have been introduced in the nucleation and condensation rates as a simple way to take into account this simplification [Aubagnac-Karkar et al., 2015; Wang et al., 2015b; Zhang et al., 2009a]. Other studies attempt to describe the nucleation and condensation processes in more detail by considering their reversibility [Eaves et al., 2017, 2015; Veshkini et al., 2016b]. For models based on pyrene as the only PAH interacting with soot, however, taking the collision efficiency or the reverse direction into account may lead to reaction rates that are too low to compensate for the absence of additional PAHs or even the reverse rate may be dominant [Aubagnac-Karkar et al., 2018]. While much effort have been done in this subject, the transition between gas- to solid-phase is still not well understood. Very recently, in [Johansson et al., 2018] it is reported important advances in this point, but the consequences for modelling are still to be developed. Therefore, to assume pyrene ($A4$) as the unique PAH that interacts with the solid phase is the most widely used and validated approach [Roy, 2014; Kazakov and

Frenklach, 1998; Zhang et al., 2009a; Aubagnac-Karkar et al., 2018; Mauss et al., 2006; Appel et al., 2000; Charest et al., 2014] and it is used in this work with unity collision efficiency.

The nucleation source term is, then, given by

$$\dot{Q}_{1,nuc} = 2 v_{A4} \beta_{A4,A4} N_{PAH}^2, \tag{4.5}$$

where v_{A4} is the volume of the $A4$ molecule, $\beta_{A4,A4}$ is the collision frequency between $A4$ molecules in the free-molecular regime and N_{A4} is the $A4$ number density. Once the first particles are formed, additional pyrene molecules might condense on their surface. It results in soot growth due to Brownian collision, with the change in soot volume being the same of the PAH molecule. Hence, the volume change in section i by this process is described as

$$\Delta \dot{Q}_{i,cond} = v_{A4} N_{A4} \int_{v_{i,min}}^{v_{i,max}} \beta_{A4,i} n_i(v) dv. \tag{4.6}$$

Surface reactions are due to interaction of soot particles with the surrounding gas-phase species. The importance of the H-Abstraction-C-Addition (HACA) based mechanism is well recognized to describe soot surface growth and oxidation [Appel et al., 2000]. The HACA-based mechanism used is this study for surface growth/oxidation is given in Table 4.1, with reaction rates taken from [Wang et al., 2015b; Appel et al., 2000]. The mechanism assumes that C_2H_2 (for surface growth) and O_2 (for surface oxidation) react with active sites present on the soot particle surface, while oxidation by OH occurs with bulk carbon atoms. Active sites, C_{soot}^*, represent the parcel of surface radicals (dehydrogenated sites) available for chemical reactions. In addition to the HACA-based mechanism, Hwang and Chung, 2001, incorporated three additional reactions related to hydrocarbon radicals (CH_3, C_3H_3 and C_2H) for the activation of soot surface for non-premixed flames. The authors discussed that surface activation by reactions involving these species and saturated sites, C_{soot}, should not be neglected in regions of the flames where H-atoms are hardly present.

Oxidation reactions presented in the HACA mechanism are global reactions. Although these global reactions are widely used in detailed soot models, it is worth remembering that soot oxidation is a much more complex process. Recently, Frenklach et al., 2018, demonstrated that global reactions are not able to reproduce accurately the detailed surface oxidation mechanism, which depends on the formation of oxy-radicals and their

Table 4.1 – Heterogeneous soot-gas surface reaction mechanism. $C_{soot,n}$ represents the saturated sites with n carbon atoms and $C^*_{soot,n}$ the number of active sites present on the soot surface.

		$k = AT^b exp(-E_a/RT)$		
No.	Reaction	A (cm^{3}mol^{-1}s^{-1})	b	E_a (kcal/mol)
$SR1_f$	$C_{soot,n} + H \rightleftharpoons C^*_{soot,n} + H_2$	4.2×10^{13}	0.0	13.0
$SR1_r$		3.9×10^{12}	0.0	11.0
$SR2_f$	$C_{soot,n} + OH \rightleftharpoons C^*_{soot,n} + H_2O$	1.0×10^{10}	0.734	1.43
$SR2_r$		3.68×10^8	1.139	17.1
$SR3$	$C^*_{soot,n} + H \rightarrow C_{soot,n}$	2.0×10^{13}	0.0	0.0
$SR4a$	$C^*_{soot,n} + C_2H_2 \rightarrow C_{soot,n+2} + H$	8.0×10^{10}	1.560	3.8
$SR4b$	$C^*_{soot,n} + C_2H_2 \rightarrow C^*_{soot,n+2} + H$	8.0×10^{10}	1.560	3.8
$SR5$	$C^*_{soot,n} + O_2 \rightarrow C^*_{soot,n-2} + 2CO$	2.2×10^{12}	0.0	7.5
$SR6$	$C_{soot,n} + OH \rightarrow C^*_{soot,n-1} + CO$	$\gamma_{OH} = 0.13$		
$SR7_f$	$C_{soot,n} + CH_3 \rightleftharpoons C^*_{soot,n} + CH_4$	3.99×10^{-1}	3.933	11.771
$SR7_r$		4.48×10^{-2}	4.248	4.277
$SR8_f$	$C_{soot,n} + C_3H_3 \rightleftharpoons C^*_{soot,n} + C_3H_4$	9.538×10^0	3.529	24.449
$SR8_r$		1.36×10^0	3.761	1.088
$SR9$	$C_{soot,n} + C_2H \rightarrow C^*_{soot,n} + C_2H_2$	2.0×10^{13}	0.0	0.0

decomposition, and the formation of five-member rings that are oxidized by O atoms. Other works attempted to include the effect of particle ageing in the global oxidation process [Khosousi and Dworkin, 2015a] as a function of the soot surface reactivity.

In soot formation counterflow non-premixed flames, soot is formed on the oxidizer side in the region delimited by the gas-phase stagnation and the stoichiometric mixture fraction planes. For such flames, Wang et al., 1996, showed that the reaction SR4a is inadequate to describe the surface growth process. The main reason is that SR4a assumes that each C_2H_2 reaction destroys a radical site, which cannot be easily regenerated because both temperature and H-atoms concentration diminished significantly in the soot-forming zone away from the stoichiometric mixture fraction region. Consequently, the surface growth process stops. On the contrary, the assumption of reaction SR4a is adequate for premixed flames since soot is formed in an environment that is very favorable for surface radical regeneration. Therefore, Wang et al., 1996, suggested that surface radicals would remain conserved after reacting with C_2H_2 in soot formation counterflow flames, which is represented by reaction SR4b. In this specific case, surface growth is sustained even at low temperature and low H-atoms concentration. Wang, 2011, argued that, regardless the origin of such conserved radicals (or persistent free radicals), there are various experimental and numerical evidences that supports their existence. Very recently, Johansson et al., 2018, reported important advances in this subject. Reactions SR4a and SR4b represent the two extremes in the surface growth process. In reality, these concepts should be conciliated [Wang et al., 1996] such that the role of surface radicals in the generation of soot would lay in between these extremes. However, this is still an open subject to be studied [Mehta et al., 2009; Roy and Haworth, 2016].

The total rate of change in soot volume due to surface reactions SR4 and SR5 are modeled as

$$\Delta\dot{Q}_i = n_C v_C k_{g,j}[G_j]\alpha\chi_{C^*_{soot}} \int_{v_{i,min}}^{v_{i,max}} A_i(v)dv, \tag{4.7}$$

where n_C is the number of carbon atoms gained or lost in the surface growth or oxidation reactions, v_C is the volume of one carbon atom, α is the steric factor, $\chi_{C^*_{soot}}$ is the number density of active sites on the soot surface area, $k_{g,i}$ is the kinetic rate coefficient of reaction j, G_j is the gas-phase species present in reaction j and A_i is the total soot surface area in section i.

Soot oxidation by the OH-radical (SR6) is modeled assuming collisions of OH molecules with soot particles as

$$\Delta\dot{Q}_i = \gamma_{OH} n_C v_C N_{OH} \int_{v_{i,min}}^{v_{i,max}} \beta_{OH,i} n_i(v)dv, \tag{4.8}$$

with γ_{OH} being the collision probability presented in Table 4.1.

The number of carbon atoms gained or lost due to surface reactions are $n_c = 2$ and $n_c = -2$, respectively for SR4 and SR5 (Equation 4.7), and $n_c = -1$ for SR6 (Equation 4.8).

In Equation 4.7, the steric factor indicates the fraction of surface radical sites available for chemical reactions as being dependent of temperature and particle size following Appel et al., 2000. The number of radical sites is determined from the number density of total surface sites $\chi_{C_{soot}}$ (estimated to be 2.3×10^{15} cm^{-2} [Frenklach and Wang, 1994]) as $\chi_{C^*_{soot}} = k_{ss}\chi_{C_{soot}}$, with k_{ss} representing a steady-state relation calculated from the

HACA-based mechanism. For the current HACA-based mechanism, k_{ss} becomes:

$$k_{ss} = \begin{cases} \dfrac{k_{1,f}[H] + k_{2,f}[OH] + k_{7,f}[CH_3] + k_{8,f}[C_3H_3] + k_{9,f}[C_2H]}{k_{1,r}[H_2] + k_{2,r}[H_2O] + k_{3,f}[H] + k_{4,f}[C_2H_2] + k_{5,f}[O_2] + k_{7,r}[CH_4] + k_{8,r}[C_3H_4]}, \\ \text{for depleted surface radicals (SR4a).} \\ \\ \dfrac{k_{1,f}[H] + k_{2,f}[OH] + k_{7,f}[CH_3] + k_{8,f}[C_3H_3] + k_{9,f}[C_2H]}{k_{1,r}[H_2] + k_{2,r}[H_2O] + k_{3,f}[H] + k_{5,f}[O_2] + k_{7,r}[CH_4] + k_{8,r}[C_3H_4]}, \\ \text{for conserved surface radicals (SR4b).} \end{cases} \tag{4.9}$$

One limitation of Equation 4.9 is that k_{ss} is not bounded to ≤ 1. In this way, $\chi_{C^*_{soot}}$ may be overestimated, which would directly enhance the surface growth by the HACA mechanism. Eaves et al., 2016, introduced a correction to Equation 4.9 to ensure that k_{ss} does not exceed unity. A comparison between the k_{ss} values computed with Equation 4.9 and the corrected formalism following Eaves et al., 2016, was conducted for the flames studied in this work and only small differences in the sooting region were observed.

It is important to note that, several processes take place at the soot surface and influence surface reactivity, in addition to the soot surface radicals being depleted or conserved. As is comprehensively discussed in Veshkini et al., 2014, the steric-factor α was embedded to the HACA surface mechanism to account for the surface ageing effect (i.e., the experimentally observed decrease in the surface site reactivity with increasing particle growth and age). Different formalism for α have been used in literature (from constant values to functions dependent on temperature and the mean particle size). Since the α functions are usually obtained by fitting experimental soot volume fraction, the steric factor becomes intrinsically dependent on the reaction mechanism. Moreover, most of the current soot modelling approaches lack of correct predictions of H/C ratio of soot particles and make no distinction between nascent and mature soot primary particles. The maturing of soot primary particles is characterized by PAHs nano-rearrangements forming graphitic shell structures principally due to dehydrogenation/carbonization of soot particles [Kholghy et al., 2016]. Therefore, a more comprehensive modelling of particle surface reactivity would require the track of soot dehydrogenation and the evolution of internal nano-structures.

Finally, coagulation rates have to be considered. When two particles collide and coalesce into a single particle, this process changes the soot number density, the particle volume and the soot total area, resulting in a significant impact on the surface processes of soot formation. For brevity, this model will not be described here. The coagulation model implemented in the present work describes the Brownian collision of all particles in the limit of pure coalescence (only spherical particles). By assuming a representative particle size $\bar{v}_i$ for each section (instead of a distribution as in [Gelbard et al., 1980], the coagulation is computed based on the model proposed by Kumar and Ramkrishna, 1996.

The representative particle size, $\bar{v}_i$, simplifies the computation of collision frequencies (β), avoiding their computationally intensive double integration over the particle size space in the coagulation model. The section representative size is also assumed for the computation of the pyrene condensation (Equation 4.6) and oxidation by OH (Equation 4.8). A preliminary study indicated that additional representative sizes per section presented only small changes in the final results. The same observation was made in [Mauss et al., 2009]. The usage of the representative volume, $\bar{v}_i$, is a simplistic approach that may deviate from the exact collision rate β (that is a function of the colliding particle volumes) but its effect on the predictions of soot volume fraction and number density is reduced for a significant number of sections.

4.2.1.4 Source terms and the inter-sectional dynamics

It should be noted that the change in soot particle size due to PAH condensation, particle growth and oxidation is not restricted to the parent section. The process of carbon addition/abstraction may result in particles with size outside the boundaries of the section being evaluated, implying in the movement of those particles across adjacent sections. In other words, particles may growth out of section i to section $i+1$ or they can migrate from section i to section $i-1$ due to oxidation. The particle migration from the parent section is not directly accounted for by Equation 4.6 to 4.8 and a special formalism is required to conserve volume and particle number [Mauss et al., 2009]. Then, there is a balance among the total rate of carbon addition/abstraction ($\Delta\dot{Q}_i$), the rate of soot volume that will be moved to the neighboring section ($\Delta\dot{Q}_i^{out}$) and the rate of soot volume change in the same section ($\Delta\dot{Q}_i^{in}$):

$$\Delta\dot{Q}_i = \Delta\dot{Q}_i^{out} + \Delta\dot{Q}_i^{in}. \tag{4.10}$$

Assuming that each $\Delta\dot{Q}_i$ is evenly spread over its section, the two quantities $\Delta\dot{Q}_i^{out}$ and $\Delta\dot{Q}_i^{in}$ are found by applying a scheme that conserves both volume and number density [Netzell et al., 2007]. Therefore, the decrease of number density of section i due to surface growth is the same of the increase of section $i+1$ and result in $-\Delta N_i = \Delta N_{i+1}$. For surface oxidation the dynamics is similar but in opposite direction, $-\Delta N_i = \Delta N_{i-1}$. A full description of the particle's migration formalism can be found elsewhere [Netzell et al., 2007; Mauss et al., 2009; Roy, 2014; Vervisch, 2012]. Finally, the source term for surface growth process (pyrene condensation and C_2H_2 addition) reads

$$\dot{Q}_{i,sg} = \begin{cases} \Delta\dot{Q}_{i,sg}^{in} & \text{for } i = 1 \\ \Delta\dot{Q}_{i-1,sg}^{out} + \Delta\dot{Q}_{i,sg}^{in} & \text{for } 1 < i < \mathcal{N}_{sec} \\ \Delta\dot{Q}_{i-1,sg}^{out} + \Delta\dot{Q}_{i,sg} & \text{for } i = \mathcal{N}_{sec} \end{cases} \tag{4.11}$$

and the source terms for oxidation (by O_2 and OH) reads

$$\dot{Q}_{i,ox} = \begin{cases} \Delta\dot{Q}_{i+1,ox}^{out} + \Delta\dot{Q}_{i,ox} & \text{for } i = 1 \\ \Delta\dot{Q}_{i+1,ox}^{out} + \Delta\dot{Q}_{i,ox}^{in} & \text{for } 1 < i < \mathcal{N}_{sec} \\ \Delta\dot{Q}_{i,ox}^{in} & \text{for } i = \mathcal{N}_{sec} \end{cases} \tag{4.12}$$

Contrarily to the surface processes, the coagulation model intrinsically incorporates the inter-sectional dynamics since it is based on the direct integration of the Smoluchowski equation. In the coagulation model, when two particles collide, a new birthed particle is often of a volume that does not match the representative volume of any of the sections. This is why, a splitting scheme devised to conserve volume and number density is introduced to split the new formed particle into adjacent sections [Kumar and Ramkrishna, 1996] (the reader is referred to the original article for more details).

The total source term of each soot section is achieved by combining the source terms respective to each process involved in the generation of soot: $\dot{Q}_i = (1 - \delta_{i1})\dot{Q}_{i,nuc} + \dot{Q}_{i,sg} + \dot{Q}_{i,ox} + \dot{Q}_{i,cond} + \dot{Q}_{i,coag}$, where δ_{i1} is the Kronecker delta function.

4.3 Model validation and limitations

First, a quantitative agreement of the model predictions with some experimental data from literature is achieved assuming that radical sites in the surface reaction SR4 are neither depleted nor conserved. This implies in adjusting the steady-state relation (Equation 4.9) such that $k_{ss} = \xi_{dc} k_{ss,cons.} + (1 - \xi_{dc}) k_{ss,dep.}$, with ξ_{dc} being an adjusted constant while the indexes *dep.* and *cons.* represent depleted and conserved reactive sites, respectively. The constant ξ_{dc} was calibrated to achieve good predictions of soot volume fraction when compared to experimental results for soot formation ethylene flames at atmospheric conditions from [Hwang and Chung, 2001; Wang and Chung, 2016a; Wang et al., 2015b, 1996; Vandsburger et al., 1984; Axelbaum et al., 1988; Hwang et al., 1998; Choi et al., 2011].

Figure 4.1.a brings the obtained values of ξ_{dc} as a function of the maximum f_v, showing a significant dispersion among all analyzed flames. A constant average value equal to 0.7 is assumed as a first modelling approximation. In Figure 4.1.b the computed soot volume fraction profile is compared for three different treatments of the surface radicals, for a pure ethylene flame burning in a mixture of 24% O_2 + 76% N_2 at a strain rate of 40 s^{-1} (the flow stagnation plane is defined to be axially located at $x = 0$ cm in the current model). For this soot formation flame, it is observed a difference of approximately one order of magnitude between the extremes of the treatment for soot surface radicals (conserved vs. depleted). On the other hand, a much better result was achieved assuming $\xi_{dc} = 0.7$. This value will be used for the rest of the counterflow simulations of this article. It is important to note, however, that the parameter ξ_{dc} does not have a general validity. For example, it was found that a ξ_{dc} in order of 0.15 is more adequate to reproduce the experimental data of the soot formation/oxidation (25% C_2H_4+75% N_2/90% O_2+10% N_2) counterflow flames studied by Hwang and Chung, 2001, (not shown).

Validation of the model, in terms of f_v distribution, is presented in Figure 4.2. Figure 4.2.a presents the comparison with the data from [Axelbaum et al., 1988] for C_2H_4 flames diluted with N_2; Figure 4.2.b present the data from [Wang and Chung, 2016a] for pure C_2H_4 and $C_2H_4{-}CO_2$ flames, and Figure 4.2.c presents the comparison with the data from [Vandsburger et al., 1984] and [Hwang and Chung, 2001] for pure C_2H_4 at three levels of oxygen concentration in the oxidizer stream. Predictions are in reasonable agreement with the experiments. Although important quantitative differences exist between model and experimental results, the qualitative tendencies of the soot volume fraction and their order of magnitude are well captured with the present implementation for a wide range of flame conditions.

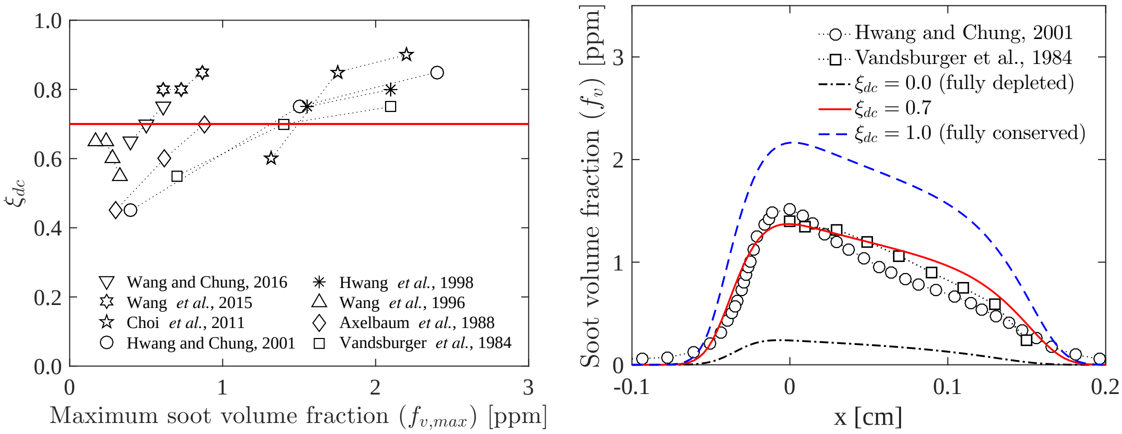

(a) (b)

Figure 4.1 – Calibration of the treatment for the soot surface radicals: (a) parameter ξ_{dc} obtained for the set of simulated flames as a function of maximum soot volume fraction ($f_{v,\ max}$); and (b) comparison between treatment options and experiments by Hwang and Chung, 2001, and Vandsburger et al., 1984, for a counterflow flame of 100% $C_2H_4/(24\%\ O_2 + 76\%\ N_2)$.

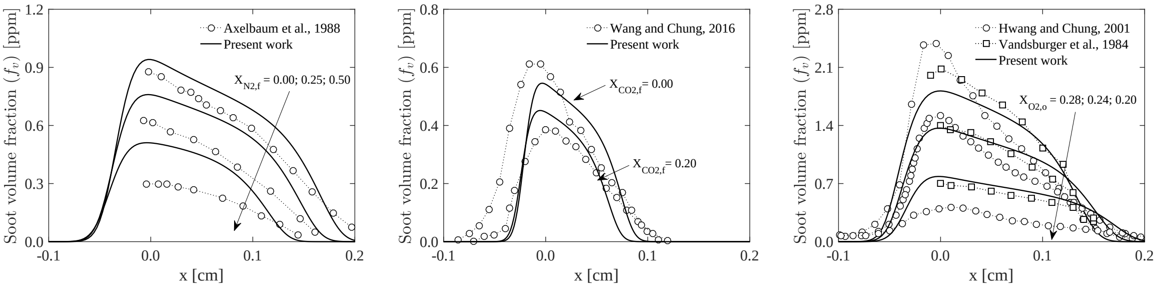

(a) (b) (c)

Figure 4.2 – Validation of the discrete sectional method with experimental data: (a) Axelbaum et al., 1988, (b) Wang and Chung, 2016a, and (c) Vandsburger et al., 1984, and Hwang and Chung, 2001.

Additional verification of the present soot sectional method is conducted with recent experimental data of Wang et al., 2015b, for pure C_2H_4 combustion in air. Distribution of soot volume fraction (f_v), number density and average particle diameter D_{63} are shown in Figure 4.3. A good qualitative and quantitative agreement is found between the present numerical simulation and the experimental data.

The present soot model was also compared to the experimental results of Du et al., 1991. In their study, Du *et al.* evaluated the strain rate at the soot inception limit for

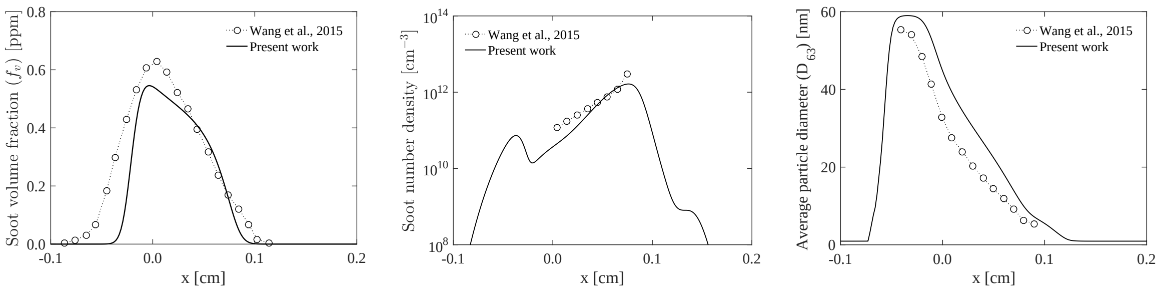

(a) (b) (c)

Figure 4.3 – Validation of the discrete sectional method with the experimental data of Wang et al., 2015b, in terms of: (a) soot volume fraction f_v, (b) number density and (c) average particle diameter D_{63}.

CO_2 addition on the fuel and on the oxidizer sides for ethylene counterflow flames. Soot was detected based on the light scattered by soot particles. The limiting strain rate for which no signal was obtained was considered as the soot inception limit (see Figure 4.4). The same procedure was employed with the present numerical model, but the control parameter was changed to the maximum volume fraction or a parameter proportional to the average scattering cross section of the particle distribution [Santoro et al., 1983]. The values of these parameters for the pure ethylene case are used as reference. The experimental soot signal is influenced by scattering and absorption along the light path, therefore, only a qualitative comparison between the model and experiments is possible. Figure 4.4 shows that the present model is able to qualitatively capture a more intense decrease of the inception limit when CO_2 is added on the oxidant side. Moreover, the effect of CO_2 on the fuel side tends to follow a parabola, whereas it is linear on the oxidant side for both model and experiments.

To further verify the implemented soot sectional method, the model is used to simulate a burner-stabilized premixed flame of $C_2H_4/CO_2/O_2/Ar$ studied experimentally by Tang et al., 2016, and numerically by Naseri et al., 2017, (employing a state-of-the-art soot sectional method). Simulations were performed for two mixture compositions of $16\%C_2H_4 + 00\%CO_2 + 24\%O_2 + 60\%Ar$ and $16\%C_2H_4 + 18\%CO_2 + 24\%O_2 + 42\%Ar$ subjected to a burner to stagnation plate distance (H_p) of 1.0 cm. The temperature profiles (numerical and experimental) presented by Tang *et al.* for the two cases were imposed for the simulations. As previously discussed, the ξ_{dc} parameter approaches the fully depleted surface radical treatment for premixed flames, therefore, a value of $\xi_{dc} = 0.25$ was found

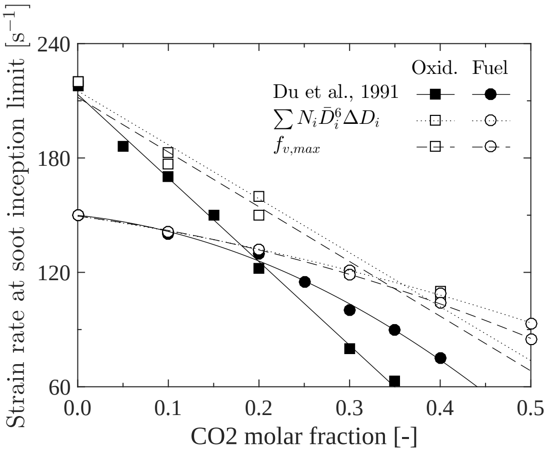

Figure 4.4 – Comparison of the predicted strain rate at the inception limit with experimental data of Du et al., 1991, for CO_2 addition on the fuel and on the oxidizer sides for ethylene counterflow flames.

suitable for the current flames. The predicted $f_{v,max}$ obtained with the current model (employing the numerical temperatures from [Tang et al., 2016]) and from the two references are presented in Table 4.2. Compared to the experiments, a reasonable prediction of f_v is obtained for the flame with 00% of CO_2 addition, but a difference of one order of magnitude is found for the 18% of CO_2 addition. Nonetheless, the $f_{v,max}$ predictions are in a close agreement with the more sophisticated soot model of Naseri et al., 2017. The computed particle size distribution is presented in Figure 4.5 with the predictions of Naseri *et al.* and the experimental results of Tang *et al.* It is possible to see that the present model and the model of Naseri *et al.* present a qualitative agreement. However, both models present significant quantitative discrepancies relative to the experiments.

Table 4.2 – Validation of the computed maximum soot volume fraction (in ppm) against the experimental data of Tang et al., 2016, and the numerical data of Naseri et al., 2017. Results obtained with the imposed numerical temperature profiles from [Tang et al., 2016].

Soot volume fraction f_v (ppm)			
Cases $H_p = 1.0$ cm	Present work	Naseri *et al.* [Naseri et al., 2017]	Tang *et al.* [Tang et al., 2016]
00% CO_2	1.5E-02	1.6E-02	8.3E-03
18% CO_2	4.0E-03	3.1E-03	2.6E-04

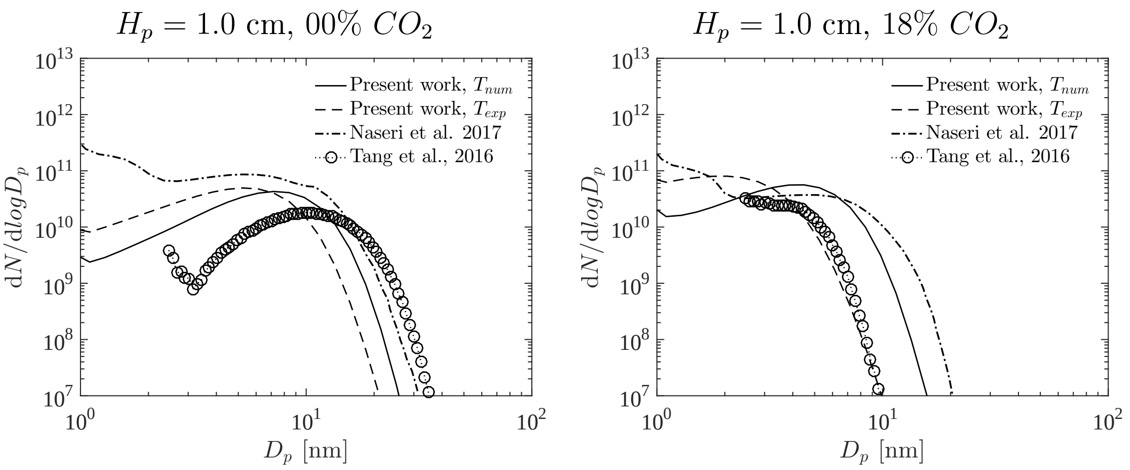

Figure 4.5 – Comparison of the computed particle size distribution with the experimental data of Tang et al., 2016 and the numerical data of Naseri et al., 2017.

Although the implemented soot section method is much more complete than semi-empirical soot models in describing soot dynamics, several processes are still not accounted for. Therefore, the use of the ξ_{dc} parameter, and the associated concept of deplete or conserved active sites, may be accounting for the lack of more fundamental models as a consistent track of H atoms and soot surface sites [Wang et al., 2015b; Frenklach et al., 2018; Kholghy et al., 2016], the soot particle carbonization and change in internal structure [Kholghy et al., 2016] and a fundamental description of particle oxidation [Frenklach et al., 2018; Khosousi and Dworkin, 2015a]. A more detailed nucleation/condensation model considering multiple PAHs including proper collision efficiencies [D'Alessio et al., 2005; Raj et al., 2010] or the reversibility of these processes [Eaves et al., 2017, 2015] are also important since they are limiting agents on the C/H ratio of soot particles.

4.4 Problem definition

The studied cases are ethylene counterflow non-premixed flames with CO_2 addition at atmospheric pressure and strain rate of 20 s^{-1}. The reference flame consists of a fuel mixture composed of 50% of C_2H_4 and 50% of N_2 reacting with an oxidizer formed by 28% of O_2 and 72% of N_2, in molar basis. The temperature of reactants is equal to 300 K. The content of C_2H_4 in the fuel and the content of O_2 in the oxidant are kept constant for all flames analyzed. The effect of CO_2 on soot formation is studied by replacing a parcel of the nitrogen of the fuel or of the oxidizer mixtures by an equivalent amount of CO_2.

In this way, the effect of pure dilution (reduction of reactant concentrations) is isolated, and differences between flames with CO_2 addition and the reference are attributed only to the effects of chemical kinetics and thermophysical properties.

To directly compare the CO_2 effect when added on the fuel or on the oxidizer sides, the addition level is evaluated in terms of the CO_2 molar fraction of the reactants for a stoichiometric mixture, i.e. the ratio of the number moles of CO_2 in the fuel or in the oxidizer to the total moles of reactants ($X^*_{CO2} = n_{CO_2}/n_{reactants}$), as in [Hoerlle et al., 2017]. With this approach, the amount of CO_2 in the reaction layer is expected to be equal for the nitrogen substitution taking place on the fuel or on the oxidizer side. Then, three different conditions are considered:

- The flame in which the nitrogen content of the fuel is replaced by CO_2 is referred to as SF (substitution on the fuel side).
- The flame in which the nitrogen content of the oxidizer is replaced by CO_2, without any reference to the SF case, is referred to as SO (substitution on the oxidizer side).
- The flame in which the nitrogen content of the oxidizer is replaced by CO_2 with an amount that results in the same CO_2 molar fraction in a stoichiometric mixture as that obtained for the SF case is referred to as ESO (equivalent substitution on the oxidizer side).

Table 4.3 shows the variation of some flame parameters with the CO_2 addition for the three dilution conditions.

4.5 Results

First, the CO_2 effect on the gas-phase species and reactions is presented (Section 4.5.1). Then, its effect on soot parameters is explored (Section 4.5.2). Lastly, the effect of CO_2 addition at higher strain rates is briefly discussed (Section 4.5.3).

4.5.1 Effects of CO_2 addition on soot precursors for adiabatic conditions

Flame structure is presented for the pure N_2-diluted case ($Ref - N_2$) and the cases with 50% Vol. of CO_2. To clearly assess the chemical and thermodynamic contributions of

Table 4.3 – CO_2 molar fraction at the boundaries ($X_{CO_2,f}$ on the fuel and $X_{CO_2,o}$ on the oxidizer sides), for a stoichiometric mixture of reactants (X^*_{CO2}) and the stoichiometric mixture fraction (Z_{st}) for the studied cases. The O_2 molar fraction on the oxidizer side ($X_{O2,o} = 0.28$) and the ethylene molar fraction on the fuel side ($X_{C2H2,f} = 0.50$) are maintained constant for all cases.

CO_2 level	*SF* flames			*SO* flames			*ESO* flames		
% Vol.	$X_{CO2,f}$	X^*_{CO2}	Z_{st}	$X_{CO2,o}$	X^*_{CO2}	Z_{st}	$X_{CO2,o}$	X^*_{CO2}	Z_{st}
10	0.1	0.0094	0.1596	0.1	0.0843	0.1455	0.0104	0.0094	0.1510
20	0.2	0.0209	0.1668	0.2	0.1685	0.1393	0.0233	0.0209	0.1497
30	0.3	0.0353	0.1738	0.3	0.2528	0.1336	0.0400	0.0353	0.1484
40	0.4	0.0538	0.1808	0.4	0.3371	0.1284	0.0622	0.0538	0.1472
50	0.5	0.0787	0.1876	0.5	0.4213	0.1235	0.0933	0.0787	0.1459

CO_2 addition, the flame structure in this section is presented only for adiabatic condition, i.e., thermal radiation is neglected.

Table 4.3 reveals the increase of the stoichiometric mixture fraction for the *SF* flames with CO_2 addition and a slight reduction for the *ESO* flames. The former condition shifts the flame front towards the fuel side and closer to the gas-phase stagnation plane ($x = 0.0$ cm) while the shift of the temperature profile for the *ESO* flames relative to the reference is negligible. The change in Z_{st} for the *SO* flames promotes a considerable shift of the temperature profile towards the oxidizer side. Thus, for a better comparison, the results in this section (species molar fractions, source terms and elementary reaction rates) are shifted so that the positions of their maximum values are coincident with the reference ($Ref - N_2$).

4.5.1.1 General flame structure

Temperature profiles are presented in Figure 4.6.a. A reduction of the maximum value and a narrowing of the thermally affected region occurs with the N_2 substitution by CO_2. The maximum temperature of the reference-flame is 2404 K, with the stoichiometric mixture fraction of $Z_{st} = 0.1523$ located at $x = 0.31$ cm. A difference of 11 K in the maximum temperature was found between the *SF* and the *ESO* flames (their maximum temperatures are respectively 2236 K and 2225 K). The *SF* and *ESO* flames are quite similar with respect to temperature because the differences between their thermophysical properties are small. Thus, these flames are well suited for studying the chemical effect of CO_2 addition. Clearly the effect of CO_2 is much more important for the SO flame, which presents a maximum temperature of 2082 K. The major difference between the SF or ESO flames and the SO flame can be attributed primarily to the fact that the amount of CO_2 in the latter case is much higher than the other two flames, such that the effect of its higher thermal capacity compared to N_2 and its participation in chemical reactions become more expressive. Complementary, Figure 4.6.b shows the temperature as a function of the residence time for the oxidizer side. The residence time is calculated by integrating the inverse of the axial velocity component along the burner axis from the edge of the thermally affected region on the oxidizer side towards the stagnation plane. As will be shown later, chemical reactions and soot formation take place on the right side of the flow stagnation plane. Thus, Figure 4.6.b shows the thermal history that a fluid particle is subjected within the reactive layer. It is observed that the temperature history remains nearly similar between the SF and the ESO flames, with differences at higher residence times (from the maximum temperature position), where a nearly constant difference of approximately 100 K is found (the processes of soot formation takes place from $\sim$ 0.050 s to $\sim$ 0.075 s). The differences between the SF and ESO flames are attributed to combined effects of chemical kinetics and thermophysical properties due to CO_2 addition. As one can note, the temperature history experienced in the SO flame differs significantly from the other two cases. As will be seen later, the temperature history on the left side of the stagnation plane is less relevant since the flame chemistry is much less active in that region.

4.5.1.2 The influence of CO_2 addition on key chemical species for soot formation

The influence of CO_2 addition on some chemical species directly related to the soot formation/oxidation is presented in Figure 4.7. While H-radical concentration influences soot formation by determining the amount of radical sites at the soot particle surface, the C_2H_2 and OH-radical (not shown) are the major species responsible, respectively, for surface carbon addition (reaction SR4) and abstraction (reaction SR6). C_2H_2 also plays a role of precursor to the first aromatic ring and its subsequent growth. Furthermore, pyrene ($A4$) concentration limits soot inception and consequently the number of soot particles. The influence of adding CO_2 is more visible for radicals. The reduction in the H-radical

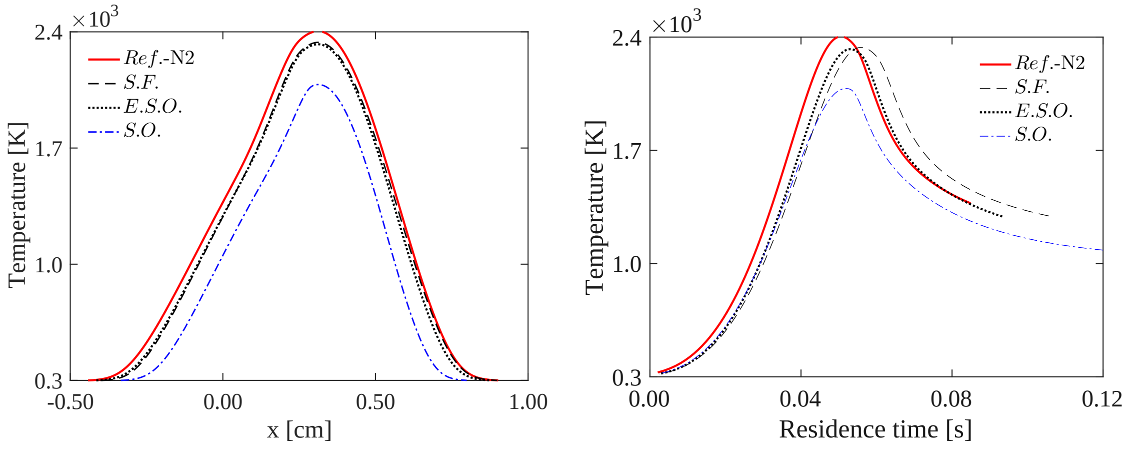

(a) (b)

Figure 4.6 – Temperature profile for adiabatic flames with CO_2 addition level equal to 0.5 according to Table 4.3 as function of: (a) the spatial position and (b) the residence time on the left side of the burner.

is about 20% when CO_2 is added to the SF or ESO flames. The behavior of OH-radical is very similar to the H-radical with a molar fraction approximately three times higher with a slightly increased peak for the SF case. C_2H_2 is more affected when CO_2 is added to fuel rather than by an equivalent proportion on the oxidizer, presenting a reduction in its maximum values. The same conclusions can be drawn for the $A4$ main molar fraction peak. Only negligible differences are found between the SF and the ESO cases for the secondary peak because acetylene and the species leading to PAHs are formed on the fuel-rich side of the flame. As expected, the increased amount of CO_2 in the SO flame presents a greater impact on species molar fractions. As stated in [Gu et al., 2016], the addition of CO_2 weakens all parameters for PAH formation and growth (temperature, H and C_2H_2) from $A1$, following the PAH's HACA growth mechanism. The suppression of key species for the soot formation processes with CO_2 addition is in accordance with the findings of [Liu et al., 2001; Wang and Chung, 2016a; Naseri et al., 2017; Guo and Smallwood, 2008; Gu et al., 2016; Liu et al., 2015] for both non-premixed and premixed flames.

A more detailed insight about the mechanisms by which carbon dioxide affects chemical species, and consequently soot, can be achieved by looking at the species source terms. As can be seen in Figure 4.8.a, the consumption rate of H-radical is only slightly affected, while its formation in the flame front decreases when CO_2 is added. Once again

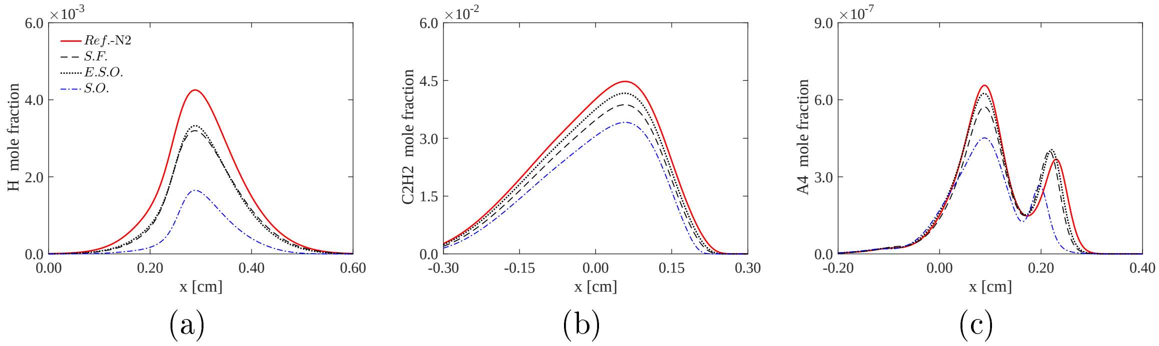

(a) (b) (c)

Figure 4.7 – Molar fraction profiles of species related to soot formation for adiabatic flames with CO_2 addition level equal to 0.5 according to Table 4.3: (a) hydrogen, (b) acetylene and (c) pyrene.

this behavior is more pronounced for the SF flame. The OH-radical source term presents a similar trend to the H-radical. Total rates of formation/destruction of C_2H_2 and $A1$ (benzene) are also presented in Figure 4.8.b and 4.8.c. Acetylene is the main species that contributes to the growth of soot and PAHs. For both C_2H_2 and $A1$, the production rate reduces and the consumption rate increases when CO_2 is added to the flame, and this behavior is more pronounced for the SF flame. The same is observed in the formation of CH_2^* (not shown). The activated methylene CH_2^* is recognized as being important in flames rich in CO_2 [Wang and Chung, 2016a; Naseri et al., 2017]. It not only reacts with CO_2 to form CO but also reacts with C_2H_2 to form propargyl (C_3H_3) - which in turns, is recognized as one of the main routes to the formation of the first aromatic ring ($A1$) due to self combination ($C_3H_3 + C_3H_3 \rightleftharpoons A1$) [Frenklach, 2002b]. So, the CO_2 addition also tends to suppress the propargyl formation and, as a consequence, the propargyl contribution to the formation of benzene is more restricted for the SF than for the ESO case. In fact, the $A1$ production remains only marginally affected in the ESO case. There are negligible differences between the SF and the ESO flames for the consumption of the aforementioned species. Figure 4.8 made clear the slightly higher suppression in the formation of chemical species leading to PAHs and subsequently growth for the SF case.

For completeness, chemical and thermophysical effects of N_2 substitution by CO_2 are quantified. Chemical effect is isolated by running adiabatic simulations assuming the addition of a fictitious carbon dioxide (FCO_2) that presents the same thermodynamic and transport properties of CO_2, but that is not allowed to participate in chemical re-

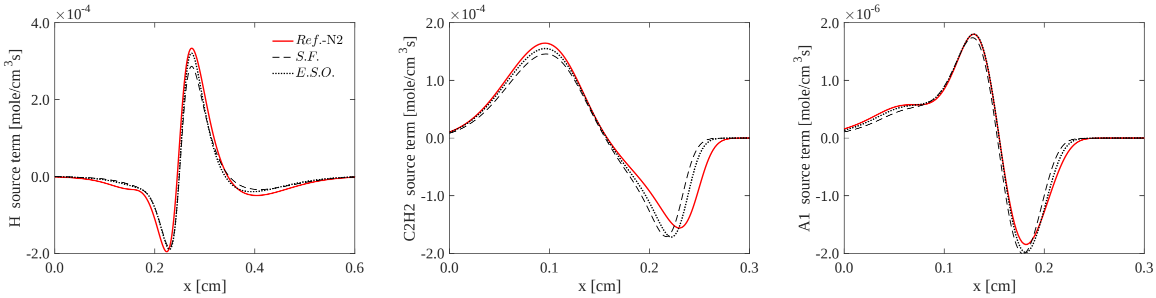

(a) (b) (c)

Figure 4.8 – Source terms of species related to the formation of precursors for adiabatic flames with CO_2 addition level equal to 0.5 according to Table 4.3: (a) hydrogen-radical, (b) acetylene and (c) benzene.

actions. Thus, the differences between the CO_2 and the FCO_2 results represent the chemical effect, while the differences between the FCO_2 and the reference case represent the thermophysical effect of CO_2 addition relative to N_2.

Figure 4.9 shows the change of the integrated source of C_2H_2 relative to the reference $(Ref - N2)$. This figure evidences the monotonic decrease in C_2H_2 formation with CO_2. As previously discussed, the suppression of C_2H_2 is higher for the SF flames than for the ESO flames. Results obtained with the fictitious species FCO_2 suggest that the contribution of chemical effects of CO_2 addition (relative to its total decrease) are much more important than the thermophysical effects for both the ESO and the SO flames. In [Liu et al., 2001] a high chemical effect on the oxidizer side has also been reported. For the SF flames, both effects are of the same order with the thermophysical effect being higher. The same trend is observed for C_3H_3, $A1$ and $A4$. This behavior is expected since those species occur only on the fuel-rich side of the flames, and therefore, are more exposed to the thermophysical effects of CO_2 addition on the fuel mixture.

4.5.1.3 Effect of CO_2 addition on key chemical reactions

It is widely recognized in the literature [Liu et al., 2001; Guo and Smallwood, 2008; Liu et al., 2015; Wang and Chung, 2016a] that the primary pathway for the chemical effect of CO_2 dilution is through the reverse direction of the reaction $CO + OH \rightleftharpoons CO_2 + H$ (R1). Examination of the sensitivity to CO_2 for reaction rates revels that the same finding is valid for the present work. The reverse direction of R1 is important once it takes

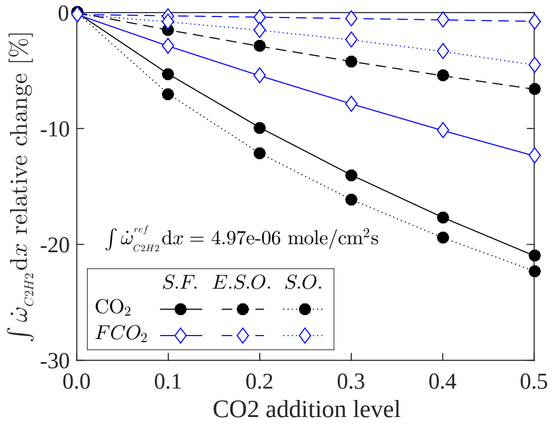

Figure 4.9 – Relative change of the integrated source term of C_2H_2 in respect to the non-diluted simulation (reference) as a function of the CO_2 addition. The CO_2 molar fractions for the ESO case are defined according to Table 4.3.

place in the same region of soot formation on the fuel-rich side of the high temperature region. A secondary path of the chemical effect of CO_2 was found to be the reaction $CO_2 + CH \rightarrow HCO + CO$, which is consistent with the findings of [Liu et al., 2001], but with rates one order of magnitude lower than the rates of R1. Reaction rates of R1 are presented in Figure 4.10. It can be seen that the rates of reaction R1 are intensified in the direct and reverse directions with the CO_2 addition in relation to the base-flame. In terms of whether CO_2 is added to the fuel or to the oxidizer side it is observed that the rate of reaction R1 becomes much more intense for the SF case than for the ESO case in both direct and reverse directions. This implies in increased consumption of H-radical towards the fuel-rich side of the flame. The rate of reaction R1 is much more pronounced for the SO case due to the higher carbon dioxide concentration in this type of flame. An analysis similar to the one made in Figure 4.9 showed that the major contribution to the enhancement of the reaction rate in the $CO_2 + H \rightarrow CO + OH$ direction is due to chemical effects. The results for the FCO_2 addition remained very close to the base-flame even for higher addition levels.

Reaction R1 reduces the acetylene formation principally by the route $C_2H_4 \rightarrow C_2H_3 \rightarrow C_2H_2$. It occurs because the reaction R1 competes with the reaction $C_2H_4 + H \rightarrow C_2H_3 + H_2$ for H-radicals. The lower concentration of C_2H_3, in turns, influences the reaction $C_2H_3(+M) \rightarrow C_2H_2 + H(+M)$ (R2) presented in Figure 4.11.a. It is observed that the rate of $C_2H_3 \rightarrow C_2H_2$ dissociation of the SF flame is lower than the ESO flame

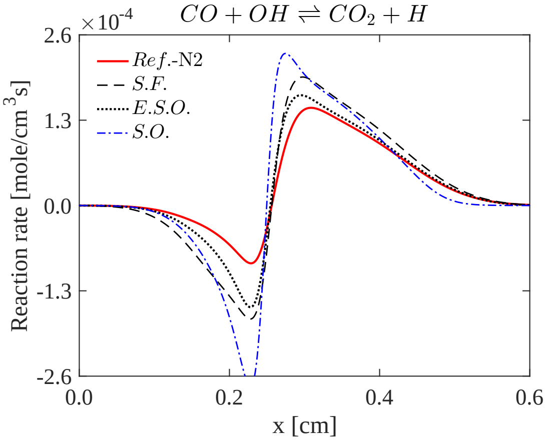

Figure 4.10 – Effect of CO_2 addition on the rates of the elementary reaction $CO + OH \rightleftharpoons CO_2 + O$ (R1) for the CO_2 addition level equal to 0.5 according to Table 4.3.

because of the higher CO_2 concentration on the fuel rich-side of the flame. Besides the role of acetylene in the soot formation process and PAH's growth, this species has a major contribution in the methylene (CH_2 and CH_2^*) formation trough the $C_2H_2 \rightarrow HCCO \rightarrow CH_2^*$ and $C_2H_2 \rightarrow CH_2$ branches. Therefore, a lower formation of methylene occurs in the SF flame (not shown). Those species are important since they are precursors of propargyl (C_3H_3). Furthermore, Wang and Chung, 2016a (for non-premixed counterflow flames) and Naseri et al., 2017 (for premixed ethylene burner-stabilized flames) also identified the reaction $CH_2^* + CO_2 \rightleftharpoons CH_2O + CO$ (R3) as being sensitive to the CO_2 addition. This reaction is relevant since it tends to diminish the concentration of CH_2^* that would act in the route of propargyl formation. Its rate is presented in Figure 4.11.b. The augmented consumption of methylene by reaction R3 is more significant in the SF flame than in the ESO flame. Reaction R3 is intensified in approximately 35% for the SF and 30% for the ESO flames. Although not shown, the rate of C_2H_2 formation and CH_2^* consumption in the SO are significantly lower. Addition of CO_2 suppresses the formation of acetylene, methylene and activated methylene more to the fuel-rich side of the flame ($x \lesssim 0.2$ cm), which influences the formation of propargyl principally via the reaction $C_2H_2 + CH_2^* \rightleftharpoons C_3H_3 + H$ (R4), presented in Figure 4.11.c. Another path of propargyl formation present in the KM2 mechanism [Wang et al., 2013] is $C_2H_2 \rightarrow C_3H_4 \rightarrow C_3H_3$. It was found that the effect of CO_2 on the latter route to propargyl formation is only secondary since the C_3H_4 molar fraction remains nearly constant for the three types of flames analyzed. Thus, the lower content of acetylene and the hydrocarbon radicals (CH_2^* and CH_2) contribute to a lower formation of propargyl, principally when CO_2 is added to the fuel mixture.

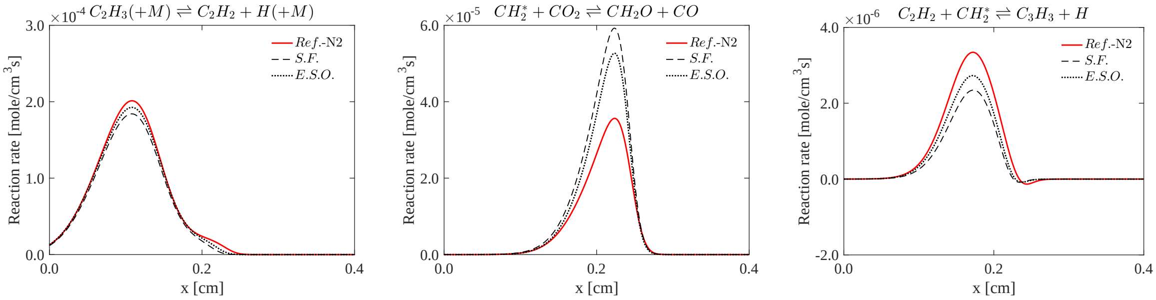

(a) (b) (c)

Figure 4.11 – Elementary reactions affected by the CO_2 addition for the adiabatic flames with CO_2 addition level equal to 0.5 according to Table 4.3: (a) reaction R2, (b) reaction R3 and (c) reaction R4.

Acetylene and progargyl are the precursors of the first aromatic ring and the main building blocks of the growth to larger PAHs. In this way, the effect of CO_2 addition is extended for PAHs of higher size like pyrene ($A4$). Figure 4.12 shows the net source of pyrene from the gas-phase (consumption by soot nucleation and condensation is not accounted for). The reduction in the formation of $A4$ is clearly stronger for the SF flame than for the ESO flame based on the reasons previously discussed. The suppression of PAH precursors is even stronger for the SO flame. The $A4$ source term has a secondary peak close to $x = 0.23$ cm. Looking at the chemical reactions involved in the process of $A4$ formation present in the KM2 mechanism, it was found that at the first peak ($x \simeq 0.09$ cm) the reactions $A3^- + C_2H_2 \rightarrow A4 + H$ and $A3C_2H_2 \rightarrow A4 + H$ are the main formation reactions. For the second peak, there is a balance between the production reactions $A4^- + H \rightarrow A4$ and $A4^- + H_2O \rightarrow A4 + OH$ with consumption reactions of the type $A4 + H \rightarrow A4^- + H_2$. Other reactions involved in the formation/oxidation of $A4$ present maximum rates at least one order of magnitude lower. When consumption by soot related reactions is accounted for, these two peaks of the $A4$ source term becomes of the same order of magnitude. This is why pyrene molar fraction presents the double peak (Figure 4.7.c).

Summarizing, the CO_2 addition suppresses the formation of the main building-

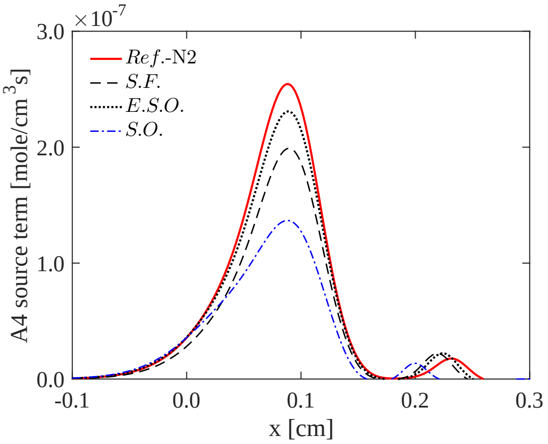

Figure 4.12 – Pyrene source term from the gas-phase for the adiabatic flames with CO_2 addition level equal to 0.5 according to Table 4.3. Pyrene consumption by soot process are not accounted for in this source term.

block species of PAH formation and subsequent growth. Those species (including C_2H_2, C_3H_3, and hydrocarbon radicals such as CH_2) are generated on the fuel rich side of the reaction layer. Their suppression is induced by the change in thermophysical properties of the mixture and by chemical reactions, principally by reaction R1, that influences the radical pool. Therefore, the suppressing effects of CO_2 addition are more pronounced for the SF flame than for the ESO flame. Of course the suppression is stronger for the SO flame, for which the level of CO_2 at the reaction layer is much larger.

4.5.2 Effects of CO_2 addition on soot formation for non-adiabatic conditions

This section intends to explore the influence of CO_2 on the soot formation mechanism and to identify the contribution of thermal radiation heat losses. Therefore, non-adiabatic simulations were performed. For a clear comparison of the sooting behavior, all profiles were shifted so that the position of the maximum soot volume fraction is the same as the $Ref - N_2$ flame.

4.5.2.1 General flame structure

The effect of thermal radiation on flame temperature is shown in Figure 4.13.a. The adiabatic $Ref - N_2$ flame temperature profile is included to reveal the narrowing of the thermally affected region and the reduction of the maximum temperature with the inclusion of the thermal radiation modelling. The relative change of maximum temperature with respect to the adiabatic reference flame ($Ref - N_2$) is presented in Figure 4.13.b. Comparing adiabatic and non-adiabatic curves, it can be seen that radiation heat losses are nearly constant for all studied flames and are responsible for a reduction of the maximum temperature of about 5%. This trend is indifferent whether CO_2 is added on the fuel or on the oxidizer stream (ESO case). This result makes clear that the contribution of chemical effects (given by the difference between CO_2 and FCO_2 curves) and thermodynamic effect on temperature of the SF and the ESO flames are approximately of the same magnitude. On the other hand, the reduction of maximum temperature in the SO flames is primarily due to thermodynamic properties of the CO_2. In general, differences in maximum temperature between SF and ESO flames are lower than 1% even with heat losses.

Computed soot volume fraction is presented in Figure 4.14.a. In soot formation counterflow flames soot is formed at the fuel rich side of the reaction layer (still at the oxidant side relative to the gas stagnation plane) and is convected towards $x = 0.0$ cm (the gas stagnation plane for the reference flame). For the present flames, soot is principally formed in a region between $x = 0.05$ cm and $x = 0.15$ cm where relatively high temperature and high concentration of species related to soot formation (e.g. C_2H_2, H, CH_3, C_3H_3 and $A4$) are found. Once soot particles are formed and grow to larger particles they are transported towards the gas-phase stagnation plane as a result of combined effect of convection and thermophoretic velocity, which is sufficiently high (in comparison with the flow velocity) to make soot particles to diffuse across this plane. For the reference case, the maximum soot volume fraction of 2.1 ppm for the adiabatic condition drops to 1.7 ppm for the non-adiabatic condition. At the complete nitrogen substitution by CO_2 on the fuel mixture (SF flame), the maximum soot volume fraction is approximately 1.45 ppm while the equivalent oxidant dilution (ESO flame) shows a slightly wider f_v profile but with the same maximum value As one should expect the SO flame presents the lowest soot volume fraction.

The relative change of the integrated soot volume fraction ($\int f_v \mathrm{d}x$) as a function of the CO_2 addition is shown in Figure 4.14.b. For the adiabatic cases at the maximum nitrogen substitution, the integrated soot volume fraction was reduced in 17% and 9%, respectively, for the SF and the ESO cases in respect to the reference (no CO_2 addition),

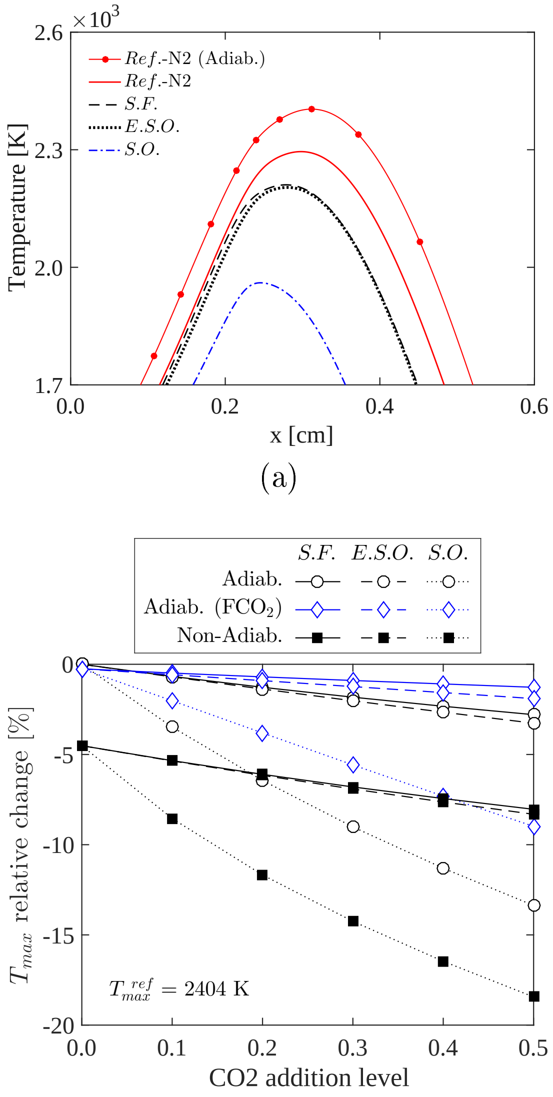

(a)

(b)

Figure 4.13 – Computed flame temperature for the non-adiabatic flames: (a) profiles for CO_2 addition level of 0.5 according to Table 4.3; (b) relative change of maximum flame temperature in respect to the non-diluted adiabatic simulation (reference) as function of CO_2 addition. The CO_2 molar fractions for the ESO case are defined according to Table 4.3.

while a reduction of 30% was found for the SO case. Although the SF and ESO flame temperature profiles are very similar for adiabatic and non-adiabatic conditions (Figure 4.13.a), the total soot content of the flame, i.e., the integrated f_v, presents significant differences for both heat loss conditions, with the SF case being more affected by CO_2 addition. For the adiabatic cases, the addition of FCO_2 instead of CO_2 revels again that chemical effects are important in the soot formation mechanism. At the maximum sub-

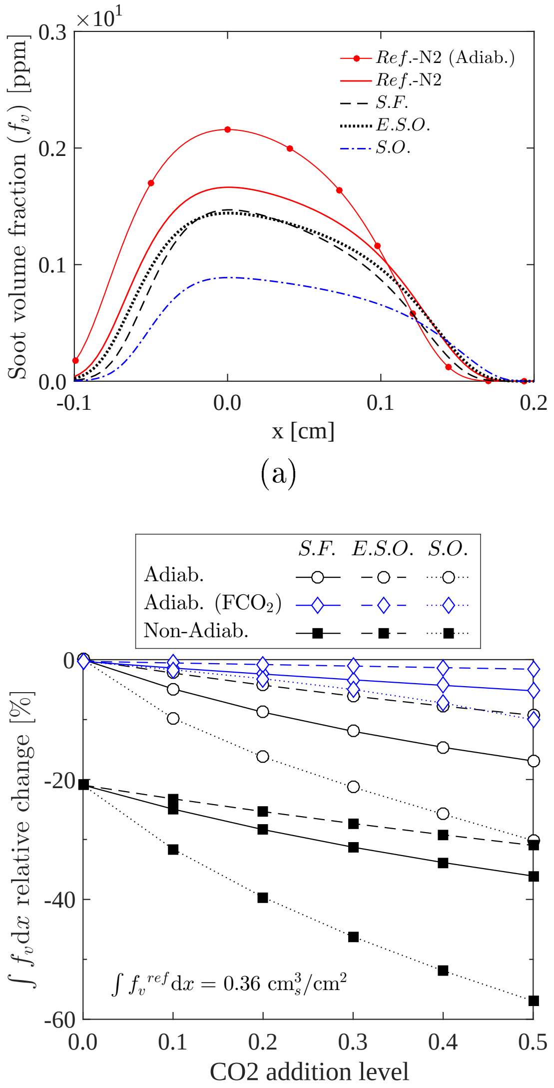

(a)

(b)

Figure 4.14 – Computed soot volume fraction (f_v) for the non-adiabatic flames: (a) profile for CO_2 addition level of 0.5 according to Table 4.3; (b) relative change of the integrated soot volume fraction in respect to the non-diluted adiabatic simulation (reference) as function of CO_2 addition. The CO_2 molar fractions for the ESO case are defined according to Table 4.3.

stitution level, the addition of FCO_2 reduces the integrated soot volume fraction only by 6%, 2% and 10%, respectively, for the SF, the ESO and the SO cases, making clear that the chemical effect of CO_2 addition significantly overcomes the thermophysical effects on the soot generation processes. The thermal radiation effect, on the other hand, reduces the integrated soot volume fraction in approximately 19%, 22% and 27% respectively for the SF, the ESO and the SO cases. Thus, both radiative heat losses and chemical effects are important for soot suppression, with the radiative effect being larger.

Particle number density and mean diameter are quite similar for all studied flames in the soot formation region (Figure 4.15). The high number density at $x \simeq -0.1$ cm is consistent with the existence of very tiny particles in this location, since soot volume fraction tends to zero. The monotonously decrease of number density from $x \simeq 0.10$ cm to $x \simeq -0.05$ cm indicates that particle coalescence is taking place as soot grows and diffuses to the fuel side, which is confirmed by the mean particle diameter indicated in Figure 4.15.b. While the mean particle diameter remains nearly equal for all flames from $x \gtrsim 0.0$ cm, the same is not true for $x \simeq -0.05$ cm where particles with distinct diameters are present. The smaller mean diameter for the SF case when compared to the ESO case is compensated by a higher number density, and both cases reach approximately the same f_v levels in this region.

The number density profile presents a secondary peak at $x = -0.1$ cm due to a local particle nucleation. It was found that the KM2 mechanism predicts a (third) very small local peak of $A4$ molar fraction at this position. It results in a secondary nucleation peak of soot particles of the order of 1E-08 g/cm^{3}s (as will be shown in Figure 4.16.a, this rate is very small in comparison to the maximum nucleation rate of the flame). However, it is important to point out that this local higher number density is inexpressive in terms of soot volume fraction (Figure 4.14.a).

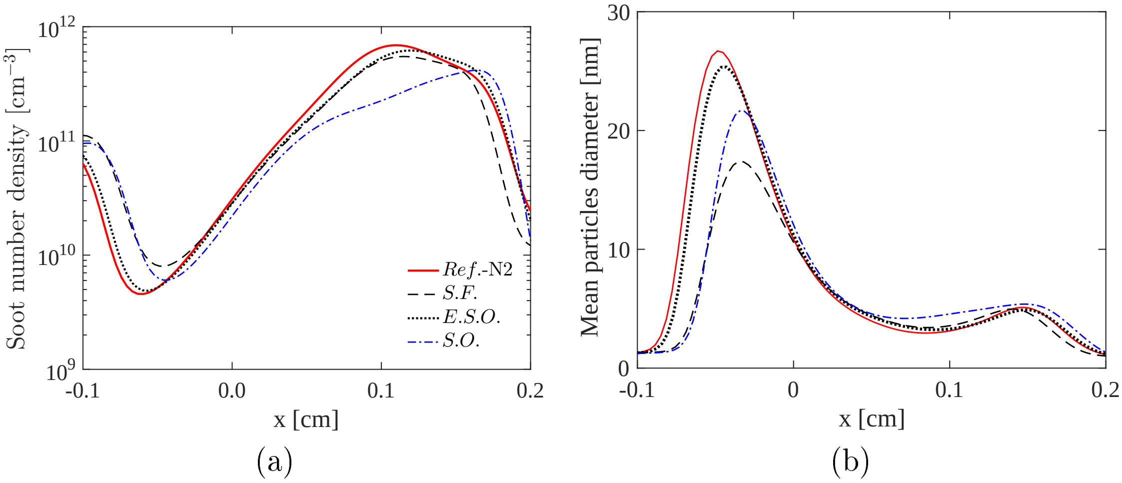

Figure 4.15 – Profile of number density (a) and average particle diameter (b) for the non-adiabatic flames with CO_2 addition level of 0.5 according to Table 4.3.

4.5.2.2 Soot formation rates

A better understanding about the process of soot formation can be obtained from its production and consumption rates. Figure 4.16.a presents the rates of soot generation for the reference flame ($Ref-N_2$). Soot nucleates on the fuel-rich side of the reaction layer around $x \simeq 0.1$ cm, where the maximum concentration of pyrene is present (Figure 4.7.c). Once the first particles are formed, they undergo pyrene condensation. Since condensation rate is directly proportional to the concentration of pyrene, its peak tends to be in the same location of nucleation. The growth rate represents the carbon addition by reaction SR4, thus, the major growth occurs in the region of concomitant presence of C_2H_2, C_3H_3, CH_3 and H. Propargyl and CH_3-radical are important for the process of formation of surface radical sites since their molar fraction is of the same order of magnitude of the H-radical molar fraction in the sooting region. The new born soot particles are immediately exposed to an atmosphere rich in H and hydrocarbon radicals. These species, in turns, act on the armchair structures on the soot surface removing an H-atom and turning a local structure into a radical site. A parcel of these sites will be effectively active to the carbon addition, as a consequence, the elevated concentration of C_2H_2 makes this process to give a major contribution to the soot growth, with its rate being one order bigger than condensation. The nature of the soot formation flame tends to minimize the soot oxidation by convecting soot particles away from the higher temperature position (region where chemical species related to reaction SR5 and SR6 occur). Some works [Hwang and Chung, 2001; Wang and Chung, 2016a; Wang et al., 2015b, 1996] suggests that oxidation may be neglected in this type of flame, but in the present study this process could not be neglected. According to Figure 4.16.a, the maximum oxidation rates correspond to approximately 25% of the HACA surface growth. Oxidation occurs mainly due to OH-radicals since the contribution of O_2 is minimal. Once soot moves towards the stagnation plane, coagulation of particles becomes more important. In early stages, soot particles are small and it is unlikely that they will collide and coalesce into bigger particles, but collisions become more probable with the growth of particle volume. This is clearly observed in Figure 4.15 from the existence of a lower number of particles with bigger size.

The total soot mass growth rate is shown in Figure 4.16.b. The total growth rate accounts for the contribution of all processes involved in soot generation (nucleation, condensation and surface growth/oxidation from the HACA-based mechanism). The higher suppression of chemical species involved in the soot formation mechanisms for the SF flame provides a lower and narrower soot mass growth rate relative to the ESO flame. This is in accordance with the f_v profile and the integrated soot volume fraction presented in Figure 4.14. Relative to the reference flame, the CO_2 addition tends to suppress the formation of new particles and limits the mass growth more than the carbon removal by oxidation. Peak rates decline approximately 35%/21%/75% for particle nucleation and 29%/18%/66% for PAH condensation, while the rate of surface growth by carbon deposition decreases approximately 16%/9%/36% for the $SF/ESO/SO$ flames. Such behavior could be expected since C_2H_2 and radicals act not only on the HACA-base mechanism but also on the chemical pathways to the formation of PAHs. On the other hand, the oxidation rates are only marginally altered ($\lesssim$ 5%) for CO_2 addition in the fuel and for its equivalent addition in the oxidizer. For the SO flame, 50% of N_2 substitution by CO_2 leads to a decrease of 30% of the oxidation process. Some studies [Du et al., 1991; Liu et al., 2001] suggested that CO_2 addition may enhance soot oxidation since reaction R1 promotes the formation of OH. However, consistently with the studies of Liu et al., 2015, and Guo and Smallwood, 2008, it was observed that the consumption of H-radical by R1 also weakens the chain branching reaction $H + O_2 \rightarrow O + OH$, resulting in lower OH concentrations in the sooting region, therefore, reducing soot oxidation.

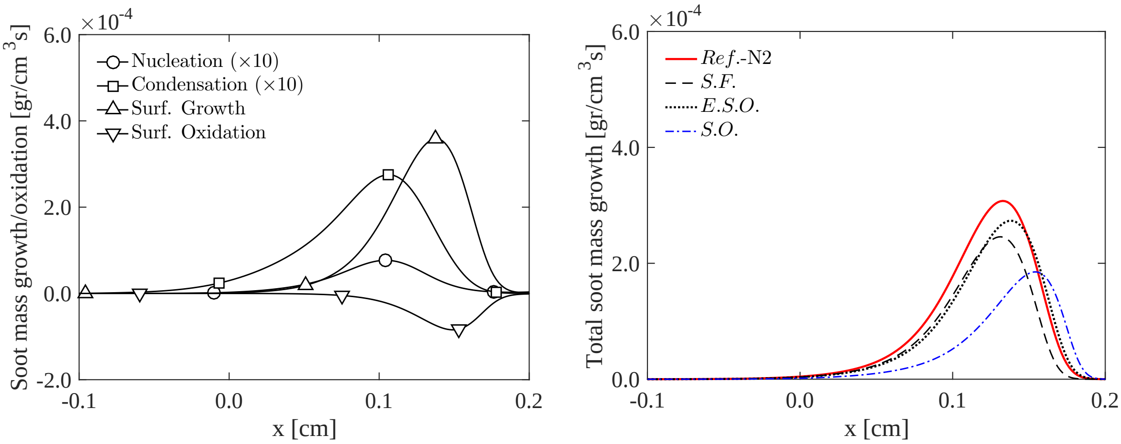

(a) (b)

Figure 4.16 – Rates of soot generation for the non-adiabatic flames: physical and chemical rates of soot generation for the $Ref - N_2$ flame; (b) profiles of soot total mass growth rate for CO_2 addition level of 0.5 according to Table 4.3.

4.5.2.3 Particle size distribution function

Dynamics of particle size can be interpreted in terms of the particle size distribution function (PSDF). A sensitivity analysis demonstrates that the shape of the PSDF is strongly influenced by various parameters of the soot model [Singh et al., 2006; Abid et al., 2008; Yapp et al., 2015]. Hence, the shape of the PSDF becomes dependent of local flame characteristics. A competition between particle nucleation and coagulation leads the PSDF to change from an unimodal to a bimodal distribution. In the later case, the first mode represents a power-law type function whereas the second mode is characterized by a log-normal distribution. The region between the two modes is usually referred to as trough. In the bimodal PSDF, both the nucleation and coagulation rates tend to make the trough deeper and wider [Abid et al., 2008], while the coagulation also reduces the peak of the log-normal mode and moves the PSDF to bigger particles [Yapp et al., 2015]. In addition, Singh et al., 2006, found that carbon addition by C_2H_2 tends to shift the PSDF to bigger particles while increasing the trough, and Blacha et al., 2012 showed that PAHs condensation presents only a minor influence on the shape of the trough.

At this point, it is instructive to explore how the CO_2 addition affects the particle size distribution. However, it is important keep in mind the model limitations (no aggregation is considered, for example) and the lack of a detailed validation against experimental results. Therefore, the effect of CO_2 addition presented in this section is of a speculative nature, especially for larger particle sizes. Experimental determination of PSDF in counterflow flame remains a challenge.

Figure 4.17 presents PSDFs taken from positions, on the oxidizer side, where the soot volume fraction is equal to 10%, 50%, 75% and 100% of its maximum value ($f_{v,max}$). Initially the PSDF presents an unimodal decay, around the position of 10% of $f_{v,max}$ on the oxidant side of the stagnation plane (at $x \gtrsim 0.13$ cm), in a region with reduced inception rates but significant carbon addition and abstraction rates. The region from 10% to 50% of $f_{v,max}$ corresponds, approximately, to the transition from an unimodal to a bimodal PSDF, which takes place at temperatures around 1650 K. As those particles grow and move towards $x = 0.0$ cm, the PSDF evolves to a bimodal shape and shifts the trough towards lower particle sizes. The trough of the bimodal PSDF indicates that small particles tend to collide and coalesce onto the surface of bigger particles, reducing the number of particles but increasing their diameter. This evolution of the PSDF is in accordance with the experimental measurements in premixed ethylene flames of [Abid et al., 2008; Zhao et al., 2005], whose findings indicate the existence of bimodal PSDF only for temperatures lower than 1800 K and that the trough deepens with the increase in particles residence time within the flame. Similar particle diameters ($\sim$ 4 nm) were found at the trough.

From transmission electron microscopy it was also shown by Abid et al., 2008, that a bimodal PSDF occurs even when only spherical particles exist, reinforcing that bimodality occurs because particles undergo size growth and not as an unique result of the formation of fractal-like aggregates. The maximum particle diameter predicted by Abid *et al.* was approximately 30 nm, which is in the transition limit from spherical to aggregated particles. The present model, which assumes only spherical particles coagulating in the coalescence limit, is qualitatively consistent with those findings. The transition from spherical to aggregates is likely to happen for particles with diameter from 20 to 30 nm [Kazakov and Frenklach, 1998; Smooke et al., 2005; Veshkini et al., 2016a], which is approximately the diameter of the maximum values of $\mathrm{d}N/\mathrm{d}(\log D_p)$ in the log-normal part. Thus, in the current approach, bigger particles could be understood as having equivalent volume of aggregates. Nonetheless, neglecting particles aggregation will affect the correct prediction of the particles size and number density.

The particle's distribution is weakly sensitive to the CO_2 addition on the current flames. Looking first at the behavior of the trough ($D_p \lesssim$ 10 nm), from the PSDFs taken at the positions of 50% and 75% of $f_{v,max}$ (which are closer to the position of maximum nucleation) it can be seen that the SF and the SO flames present a lower number of particles and that the particle diameter at the trough tends to be smaller as the CO_2 effects on the flame get stronger (i.e., $SO > SF > ESO > Ref - N_2$). As soot particles mature, from 75% of $f_{v,max}$, the shape of the trough tends to be quite similar for all analyzed cases. For the log-normal type distributions, the results for the SO flame become more distinct from the others with the existence of smaller particles, especially in the right-end of the PSDF where it is also observed a significant reduction of particle number. The shape of the PSDF in the log-normal type distribution obtained for the SF and the ESO cases are very close to the reference ($Ref - N_2$), with some differences closer to the trough at 75% of the $f_{v,max}$. The behavior observed in the PSDF of the SO case can be attributed to a combined effect of the diminished pyrene concentration and

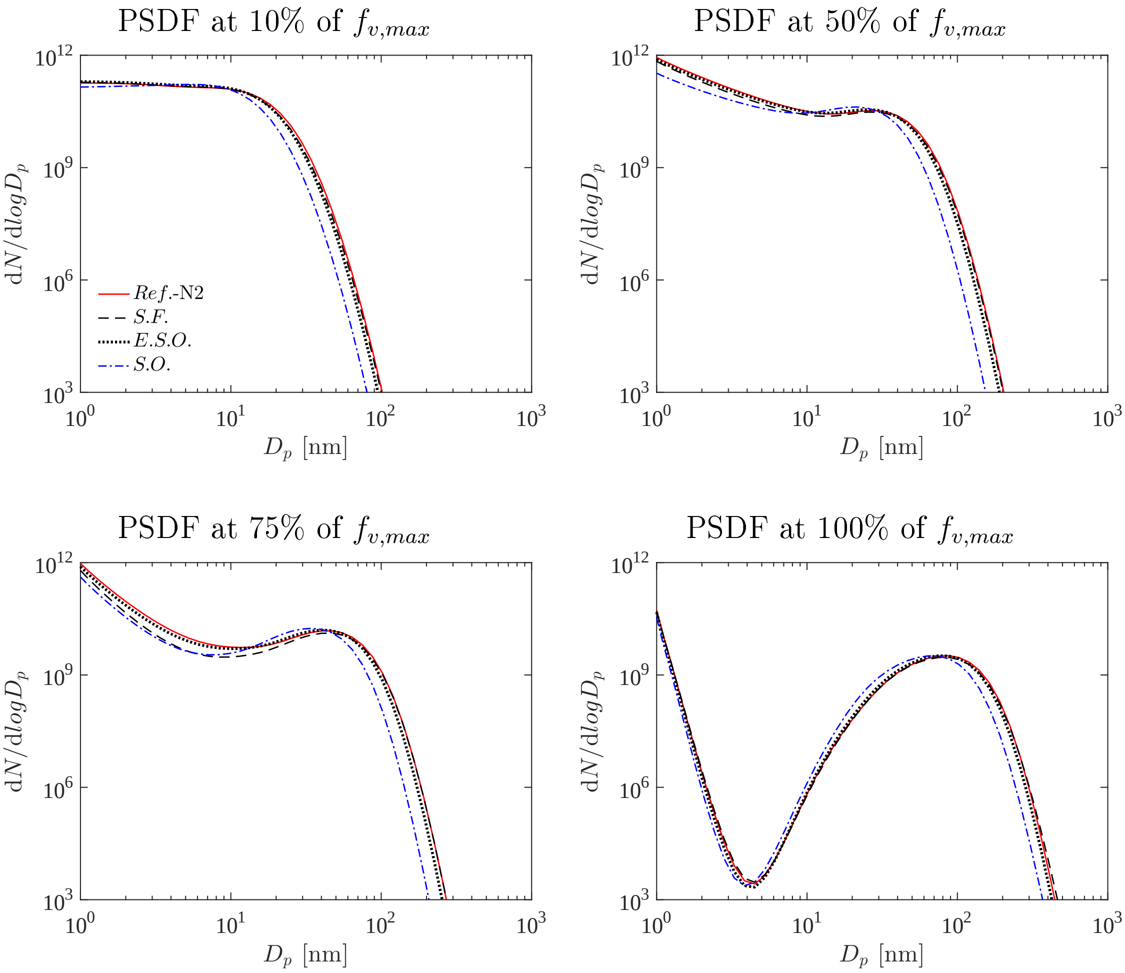

Figure 4.17 – Particle size distribution function for the non-adiabatic flames with CO_2 addition level equal to 0.5 according to Table 4.3.

surface growth [Singh et al., 2006; Yapp et al., 2015], which tends to shift the PSDF toward particles with lower diameters. The peak of the log-normal type distribution of the PSDF being nearly equal for all cases indicates that coagulation rates between bigger particles are minimum. In fact, a closer look in the coagulation rates reveals that, for sections with particle diameters larger than 100 nm, the reduction in volume due to collision with bigger particles is very low compared to the gain of volume due to collision with smaller particles. In this way, CO_2 acts on the PSDF principally by reducing the number of small younger particles and by limiting the growth to higher size particles with this trend being stronger for the SO flames.

4.5.3 CO_2 addition effects at higher strain rates

Complementary simulations were performed for the strain rate $a = 120$ s^{-1}. At this low residence time condition, the influence of thermal radiation is reduced. Thus, the flame structure at higher strain rates depends basically on chemical and thermophysical effects of CO_2 addition. Zimmer et al., 2017, showed that thermal radiation presents a major influence in the prediction of soot properties only for small strain rates ($a \lesssim 25$ s^{-1}) in counterflow flames. In fact, thermal radiation grows in importance with the reduction of the strain rate until the flame extinguishes due to excessive heat losses. At higher strain rates the flame shortens, temperature drops and a lower conversion of intermediate species is found, which directly impacts the soot tendency of the flame.

At $a = 120$ s^{-1}, a significant reduction of f_v was observed as a consequence of the lower soot number density and mean diameter. This is in accordance with the work of Wang and Chung, 2016b, who demonstrated that this behavior occurs due to the decrease in PAH's concentration (which lowers the soot inception rate) along with the decrease in the residence time for soot undergoing surface growth. Despite differences in magnitude, a trend similar to the results at $a = 20$ s^{-1} is observed for the f_v profile principally comparing the SF and the ESO flames. On the other hand, the $f_{v,max}$ predicted by the SO flame becomes significantly lower. Analysis of the chemical, thermophysical and radiation effects conducted for the flames at $a = 120$ s^{-1} (Figure 4.18) presents, in general, the same pattern observed for the case at $a = 20$ s^{-1}, but with an increased suppression of the integrated soot volume fraction. This was found to be principally due to an enhancement of the thermophysical effect. For the SO flame, at the maximum CO_2 addition, this effect changed from approximately 10% to 40% when the strain rate was increased. A proportional enhancement was also observed for the ESO flame. The chemical and thermophysical effects of the SF flame, on the other hand, were less sensitive to the increase in the strain rate. As expected, the thermal radiation drops from approximately 20% to 7% with the increase of the strain rate. These findings suggest that the soot formation at higher strain rates are more sensitive to thermophysical effects of CO_2 addition.

For the high strain rate of $a = 120$ s^{-1}, the particle size distribution also evolved consistently with the findings at $a = 20$ s^{-1}. Due to a reduced particle nucleation, mass growth and coagulation, it presents a shift towards smaller particles and a formation of smaller trough as the PSDF evolves, principally for the SO flames.

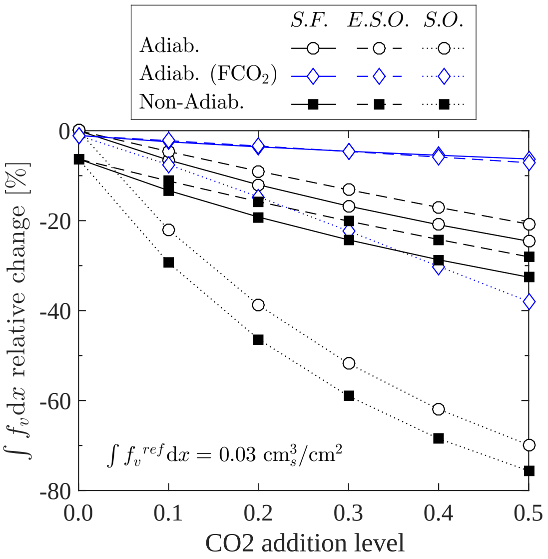

Figure 4.18 – Relative change of the integrated soot volume fraction in respect to the non-diluted adiabatic simulation (reference) as a function of CO_2 addition at $a = 120$ s^{-1}. The CO_2 molar fractions for the ESO case are defined according to Table 4.3.

4.6 Conclusion

This work addresses the role of CO_2 addition on flame structure and soot formation processes for ethylene counterflow non-premixed flames under oxygen enriched conditions, while clarifying the peculiarities of CO_2 addition on the fuel or oxidizer mixtures. The addition of CO_2 on the fuel (SF) or on the oxidizer (ESO) sides are compared based on the same amount of CO_2 for a stoichiometric mixture of fuel and oxidizer. A standard dilution at the oxidizer side (SO) is also evaluated. With this criterion, the comparison is made with approximately the same level of CO_2 at the reaction region (SF vs. ESO cases). Furthermore, the total fuel and oxidizer dilutions are kept constant for all investigated flames. A detailed Sectional Method is implemented for soot modelling, and thermal radiation is accounted for by solving the RTE with the WSGG/DOM approach. The soot model was verified against soot measurements from literature with a good qualitative agreement. Furthermore, chemical and thermophysical effects of CO_2 addition were isolated by assuming a fictitious FCO_2 species, and thermal radiation effects were obtained by comparing adiabatic and non-adiabatic results.

First, the influence of CO_2 addition on soot precursors formation was determined based on adiabatic simulations. The results showed that the general flame structure remains similar when comparing CO_2 addition on the fuel or on the oxidizer sides provided that approximately the same CO_2 concentrations are found in the reaction layer. A higher CO_2 effect for the SF flame, in comparison to the ESO flame, pointed out to a higher consumption of the H-radical on the fuel-rich side of the reaction layer by reaction $CO_2 + H \rightarrow CO + OH$, leading to a suppression of species (such as hydrocarbon radicals, C_2H_2 and PAHs) responsible for the formation and growth of soot precursors and soot particles. In addition, it was found that chemical and thermophysical properties have almost an equivalent effect on chemical species related to soot generation. This suppression is induced primarily by chemical effects for both the ESO and the SO flames while thermophysical effects are slightly more important for the SF flames.

Then the effect of CO_2 addition on soot formation process was investigated for non-adiabatic simulations. The results showed that the general flame structure of the SF and the ESO flames remained very similar when thermal radiation was accounted for in the simulations, with negligible differences in the temperature profiles and in the maximum soot volume fractions. However, the slightly narrow f_v profile towards the fuel-rich side computed for the SF case confirmed the tendency of suppressing soot formation when CO_2 is added on the fuel side. Finally, the role of chemical, thermophysical and radiation heat losses on soot formation were also quantified. It was observed that thermophysical and chemical effects contributed distinctly for different aspects of the flames. While the former effect is the main responsible for the temperature reduction, the later has a more important influence on the total amount of soot within the flame. The radiation effect contributed significantly for temperature and soot volume fraction reductions for all CO_2 addition cases. So that, both radiative heat losses and chemical effects are important for soot suppression, with the radiative loss effect being larger. When a direct comparison is made in terms of the CO_2 level on the fuel (SF) and on the oxidizer (SO) sides, clearly the flame structure was more affected for the SO flame due to a combined effect of thermodynamic properties, chemical reactions and radiation emissions due to the elevated concentration of CO_2 in the flame.

Results for the particle size distribution were also presented, despite the lack of aggregates modelling. In general, the PSDF was only slightly sensitive to the carbon dioxide addition for the SF and the ESO flames. The PSDF showed a higher deviation for SO in respect to the reference flame. For this case, the PSDF shifted towards smaller particles due to the reduced surface growth and the reduced number of small particles (caused by the suppressed nucleation rates) in comparison to the SF and the ESO cases.

5 EFFECTS OF RADIATION MODELLING ON NON-PREMIXED SOOTING FLAMES SIMULATIONS UNDER OXYFUEL CONDITIONS

This section was published at: Journal Combustion and Flame, 2020, Vol. 217, pp. 294-305.

5.1 Introduction

Previous studies [Hwang and Chung, 2001; Zimmer et al., 2017; Hoerlle and Pereira, 2019] have shown that the radiative heat modelling has a central role for the simulation of soot formation in flames. Thus, it is of primary importance that simplified models, usually employed for predicting radiative heat losses, are able to reproduce detailed simulations at conditions found in flames of interest.

Commonly, simplified spectral radiative models are validated by comparison with the detailed line-by-line (LBL) integration approach in idealized (benchmark) problems [Kangwanpongpan et al., 2012; Dorigon et al., 2013; Bordbar et al., 2014; Cassol et al., 2014; Orbegoso et al., 2016; Chu et al., 2017; Coelho and França, 2018]. Such problems, although consisting of temperatures and compositions relevant for combustion applications, usually do not take into account the intense gradients found in real flames. Only few studies have compared different radiation models with the LBL approach in two dimensional flames [Centeno et al., 2015, 2016, 2018; Rodrigues et al., 2019], consequently with gradients relevant for combustion processes, but it was assumed that temperature and composition fields were frozen for the LBL computations. This method is convenient for comparing radiative models, but cannot quantify the impact of simplifications since coupling effects are not taken into account.

Multi-dimensional simulations coupling the LBL radiation approach with detailed chemical kinetics and soot models are still beyond standard computational powers in research groups. In these cases, the radiative-transfer equation (RTE) has to be computed for each cell of the computational domain, to take into account local variations of temperature and species concentration, and has to be integrated over dozens of angular directions. In addition, the LBL approach performs a direct integration over hundreds of thousands of spectral lines for each participating gas. These intensive computations frequently make the LBL approach too expensive, even for research applications.

Therefore, the canonical one-dimensional counterflow flame is a good candidate for studies which aim to coupled detailed radiation, chemical kinetics and soot models. This simplified configuration allows the simultaneous consideration of these models for a wide range of conditions (different residence times and fuel/oxidant composition). Additionally, the counterflow flame can be experimentally accessed, which is a big advantage for validation purposes. This configuration may also be a good candidate for a fine-tunning of radiative models that has not been explored yet.

In a flame, the optical thickness increases with the increase of participating species concentrations due to radiation self-absorption effects. This feature can be used to create a wide range of conditions for studying radiaion in flames. Additionally, some fuels and processes are characterized by variable levels of participating species. New combustion processes such as oxygen-enriched technologies allied to dry or wet flue gas recirculation are characterized by high concentrations of CO_2 species [Boot-Handford et al., 2014; Escudero et al., 2016; Nemitallah et al., 2017; Zhang et al., 2018]. Biogas and syngas also present high amounts of participating species (principally CO_2) in their composition [Hosseini and Wahid, 2014].

Some studies explored the influence of CO_2 on thermal radiation phenomena. Extinction characteristics of counterflow non-premixed flames of methane were investigated by Maruta et al., 2007, for pressures from 0.1 MPa to 0.7 MPa. Simultaneous CO_2 addition to fuel and oxidizer under oxygen-enrichment were considered. They found an extended extinction limit at lower stretch rates for high pressures. They pointed out the importance of radiation reabsortion in extending the extinction limits. Extinction limits at higher strain rates of counterflow non-premixed methane flames were investigated for oxygen-enriched oxidizer by Li et al., 2014. The influence of CO_2 addition in the fuel ($CH_4 + CO_2$) or in the oxidizer ($O_2 + CO_2$), and high temperature oxidizer were explored. In general it was observed an increase of the extinction strain rate with the increase of O_2 concentration and oxidizer temperature. This trend was more expressive for fuels with low dilution levels. They also demonstrated that radiative heat losses were minimum at high strain rates due to reduced residence times, even with a high CO_2 content in the reactants.

Additional studies investigated the importance of soot concentrations on the thermal radiation heat transfer. Liu et al., 2004, explored the role of soot radiative heat loss for counterflow non-premixed flames with oxidizer enriched with O_2 and observed that its contribution was equivalent to the gas-phase for a soot volume fraction of approximately 2.5 ppm. Zimmer et al., 2017, investigated the mass-energy coupling on the soot formation for non-premixed counterflow flames. Among others findings, they showed that both soot and gas radiation are of primary importance for predicting the flame structure. Katta et al., 2009, explored the importance of soot thermal radiation in the transition from steady to unsteady non-premixed coflow flames, and their results demonstrated that soot radiation tends to suppress flame oscillations caused by buoyancy-induced instabilities. In an extensive study of the effect of thermal radiation on soot production in laminar coflow diffusion flames conducted by Demarco et al., 2013, it was found that gas-phase emission dominates the radiation heat transfer for weakly-sooting flames, whereas soot radiation was enhanced with the sooting propensity of the flame.

An extensive study of CO_2 effect on flame structure and soot formation was conducted by Zhang et al., 2018, in laminar coflow non-premixed ethylene flames. The oxidizer was composed of O_2/N_2 and O_2/CO_2 mixtures with O_2 mole fraction varying from 21% to 50% in molar basis. The increase of O_2 concentration lead to a significant enhancement of the maximum temperature and soot loading, and those maximum values are higher for ethylene burning in O_2/N_2 atmospheres than in O_2/CO_2 atmospheres. Such tendency was attributed to thermodynamic and chemical effects of CO_2. Although an extensive analysis of O_2 enrichment over soot generation was presented, no discussion about radiative heat losses was provided by the authors. However, as discussed in [Wang and Chung, 2014], soot propensity changes with fuel structure, flame temperature, residence time and fuel dilution among other factors, which directly influences the radiation heat transfer. For this reason, this work will investigate the effect of CO_2 addition on the flame response employing different radiation models.

Most of the reviewed studies pointed out that thermal radiation is required for adequate predictions of flame characteristics. Radiation reabsorption is important to capture soot formation and limiting processes as flame extinction. It was also shown that radiation reabsorption should not be neglected when high concentrations of CO_2 or soot are present. This is a problem because simplified models, based solely on emissions (optically thin approximation - OTA) or on global spectral approximation (weighted-sum-of-gray-gases or wide/narrow band models), are frequently employed in practical engineering applications. It was observed that none of the reviewed studies compared the capabilities of simplified radiation models with the line-by-line integration approach in order to quantify the expected discrepancies.

The objective of the present work is to explore the effects of different radiation models, including the detailed LBL approach, on the flame response due to CO_2 addition. The canonical one-dimensional counterflow flame is chosen as a convenient target since it allows the coupling of detailed radiation, soot formation (sectional method) and chemical kinetic models. The detailed sectional method presented in a previous work [Hoerlle and Pereira, 2019] will be considered. It describes a poly-disperse particle distribution assuming nucleation and condensation from large polycyclic aromatic hydrocarbons, surface reactions for growth and oxidation and particles coagulation. To our best knowledge, there are no studies in the literature coupling such detailed soot formation model with the LBL radiation integration, even for one-dimensional flames. Additionally, the flame optical thickness will be varied by the addition of CO_2 on the fuel and on the oxidant sides to create different heat loss conditions.

5.2 Problem description and numerical model

The influence of the radiative heat loss on the flame structure and soot formation is evaluated for ethylene counterflow flames burning in oxygen enriched atmospheres for a variety of CO_2 addition in the fuel or in the oxidizer mixtures. The reference flame, $Ref. - N_2$, consists of burning a mixture of 50% of ethylene and 50% of N_2 in an oxidizer formed by 28% of O_2 and 72% of N_2, in molar basis. The influence of CO_2 addition is evaluated for a partial substitution of N_2 by CO_2 in the fuel (SF flames) and oxidizer (SO flames) mixtures. The ethylene mole fraction at the fuel and the oxygen mole fraction at the oxidizer are kept equal for all studied cases. Upstream temperature and pressure are equal to 300 K and 1 atm. The simulations were conducted for a strain rate equal to 20 s^{-1} applied to the oxidizer side. It is important to point out that thermal radiation presents significant influence in the prediction of soot global properties (as volume fraction, for example) only at low strain rates ($a \lesssim 25$ s^{-1}) [Zimmer et al., 2017], i.e., at high residence times.

Some results of the present flames have already been presented in [Hoerlle and Pereira, 2019], employing the WSGG model. There, it was showed that CO_2 addition on the fuel or on the oxidizer mixtures play different roles on the process of soot formation. The study has also explored a condition of equivalent dilution on the oxidizer side (ESO) that results in approximately the same amount of CO_2 concentration at the reaction region as in the SF case. A preliminary study on the thermal radiation showed that differences between SF and ESO are minimum in terms of radiative heat flux and radiative volumetric source term. Therefore, this work considers solely the cases SF and SO cases, as defined in Section 5.2.

5.2.1 Numerical method

Steady-state one-dimensional flames were solved with the CHEM1D [Somers, 1994] code. The code solves the system of conservation equations for reactive flows based on the finite volume method with a fully implicit Newton technique. In this work the fuel inlet is located at $x = -0.5$ cm while the oxidizer is injected at $x = 1.5$ cm. In the current formalism the velocity boundary is treated as a potential flow with the strain rate defined as boundary condition in the stretch rate equation at the oxidizer side. The strain rate at the fuel side is computed in order to balance the momentum flux of both streams. The position of the flames is defined so that $x = 0$ cm is located at the stagnation plane. The computational domain of 2.0 cm length was discretised with 400 equidistant points. Additionally, the code employs a grid refinement algorithm to increase the number of control volumes in regions with steeper gradients. This discretization was sufficient to guarantee mesh independence. The advective terms of the conservation equations were treated by the exponential discretization scheme, while the diffusive ones were treated by the central difference scheme.

The conservation equations describe the conservation of total mass, stretch rate, chemical species and enthalpy. The derivation of this set of equations can be found in [de Goey and ten Thije Boonkkamp, 1999a] and will not be repeated here. It is assumed that the mixture density is a function of temperature only, due to the Low Mach number approximation. The stretch rate is understood as a relative rate of change of mass and contemplates all local deviations from one-dimensional flames. Reaction rates are modelled by the Arrhenius equation, and the KAUST Mechanism 2.0 [Wang et al., 2013] (formed by 203 species and 1346 reactions) was considered to describe the chemical path up to larger PAHs. The energy equation is solved in terms of the total specific enthalpy of the mixture. Species diffusivities were modeled by the Fick's Law, while the Soret and Duffor effects were neglected. The set of conservation equations is closed by the ideal gas law and the caloric equation of state. The conservation of total mass is guaranteed employing a velocity correction for all species. Details of radiation heat transfer models are described in the following sections.

The soot model is only briefly described. For a complete description the reader is referred to Hoerlle and Pereira, 2019. The present approach considers that soot particles are solid spheres modeled as a distinct dispersed phase interacting with the gaseous phase. Soot dynamics, modeled considering the Discrete Sectional method [Gelbard et al., 1980; Mauss et al., 2009; Mehta et al., 2009; Roy, 2014; Roy and Haworth, 2016], accounted for physical (nucleation, condensation and coagulation) and chemical processes (surface growth and oxidation). It is assumed that nucleation takes place from collisions of two pyrene molecules, forming the first particles. Once the first particles are formed, additional pyrene molecules might condense on their surface. The carbon addition/abstraction by chemical reactions are described by an H-Abstraction-C-Addition (HACA) based mechanism [Wang et al., 2015b]. The mechanism assumes that C_2H_2 (for surface growth) and O_2 and OH (for surface oxidation) react with active sites in the soot surface area. The steric factor considered for surface growth follows [Appel et al., 2000]. In addition, the model assumes that surface radicals are neither completely depleted or conserved during the process of C_2H_2 addition. Instead, an average between these two extremes is assumed following [Hoerlle and Pereira, 2019]. Finally, the coagulation process describes the collision of two particles in the limit of pure coalescence based on the formalism proposed by [Park and Rogak, 2004].

Although the present soot model describes the major processes of soot formation, several simplifications are still assumed. Pyrene dimerization is the most widely used and validated PAH precursor for soot models, but in reality soot inception occurs from many PAHs with larger size [Dobbins et al., 1998], principally from 5-ring PAHs [Teini et al., 2011; Johansson et al., 2017]. Similarily to nucleation, larger PAHS also condensate onto the particle surface. Moreover, it has been suggested that nucleation and condensation are kinetically controlled processes, for which reversibility is important [Kholghy et al., 2018; Eaves et al., 2017; Mercier et al., 2019; Kholghy et al., 2019]. Trough reversible PAH clustering models with chemical bond formation, Eaves et al., 2017, and Kholghy et al., 2019, reported an improved prediction of all relevant soot morphological parameters (including particle size distributions) determined experimentally for both burner stabilized stagnation premixed flame and non-premixed laminar coflow flame configurations. As is comprehensively discussed in Veshkini et al., 2014, a steric-factor, α was embedded to the HACA-based surface mechanism to account for the surface ageing effect in a simplified way. α functions are usually obtained by fitting experimental soot volume fraction [Appel et al., 2000], however, research has been done on the matter to establish realistic variation in the parameter by Dworkin and coworkers [Veshkini et al., 2014; Khosousi and Dworkin, 2015b]. Moreover, the present soot model assumes that coagulation occurs solely in the limit of pure coalescence. Neglecting particles aggregation may affects the correct prediction of the particles size and number density [Veshkini et al., 2016a], which changes the total surface area and, consequently, the total surface growth. What should be emphasized is that, besides these several simplifications, the verification conducted in [Hoerlle and Pereira, 2019] revealed a reasonable capability of the present model for predicting soot formation for counterflow non-premixed flames and the model can be considered adequate for the purposes of the present study.

5.2.2 Thermal radiation model

The radiation heat transfer is calculated by the Radiative Transfer Equation (RTE) [Modest, 2003]. It describes the variation of the spectral radiation intensity (I_η), for a given wavenumber (η) and direction (Ω), along a path x in the medium. The volumetric radiative heat source corresponds to the divergent of the radiative heat flux. In this work, the RTE is solved for an emitting/absorbing and non-scattering participating medium. Only a brief description of the thermal radiation modelling is provided. The reader is referred to [Dorigon et al., 2013; Cassol et al., 2014; Centeno et al., 2018; Ziemniczak et al., 2019] for a complete description of these methods since the LBL and the WSGG one-dimensional codes for the RTE solution used in [Dorigon et al., 2013; Cassol et al., 2014] were coupled to the flame code used in the present study.

The spatial dependency of the radiation intensities is solved by the discrete ordinates method (DOM) [Thynell, 1998]. The total solid angle is discretized in 30 angular directions over which the radiation intensities are integrated. In [Dorigon et al., 2013; Cassol et al., 2014] it was verified that 30 directions present sufficient resolution for independence of 1D radiation transfer calculations with the number of directions. For one-dimensional counterflow flame, the radiative domain is similar to a slab bounded by black walls at the same temperature of the reactants. Based on the DOM, the RTE can be recast for positive and negative directions according to:

$$\begin{aligned} +\gamma_l \frac{\mathrm{d}I^+_{\eta,l}(x)}{\mathrm{d}x} &= \kappa_{\eta,m}(x) I_{\eta b}(x) - \kappa_{\eta,m}(x) I^+_{\eta,l}(x) \\ -\gamma_l \frac{\mathrm{d}I^-_{\eta,l}(x)}{\mathrm{d}x} &= \kappa_{\eta,m}(x) I_{\eta b}(x) - \kappa_{\eta,m}(x) I^-_{\eta,l}(x), \end{aligned} \tag{5.1}$$

where γ_l is the directional cosine towards the l direction ($1 \leq l \leq \mathcal{N}_l$). For a one-dimensional slab bounded by black walls, for example, Equation 5.1 are subjected to the following boundary conditions: $I^+_{\eta,l}(x = -L) = I_{\eta b}(x = -L)$ at the left boundary and $I^-_{\eta,l}(x = +L) = I_{\eta b}(x = +L)$ at the right boundary.

After the solution of the spectral radiation intensities for each position s and direction l, the radiative heat flux can be determined by:

$$q_r^{''} = \sum_{l=1}^{\mathcal{N}_l} \int_\eta 2\pi w_l \gamma_l \left[I^+_{\eta,l} - I^-_{\eta,l} \right] \mathrm{d}\eta, \tag{5.2}$$

with w_l being the integration weight since the continuous integral over the solid angle is computed by a Gauss-Legendre quadrature scheme. The volumetric radiative heat source corresponds to the divergence of the radiative heat flux with opposite sign, $\dot{q}_r(x) = -\nabla \cdot \vec{q_r}^{''}$, such that:

$$\dot{q}_r = \sum_{l=1}^{\mathcal{N}_l} \int_\eta \big(2\pi \kappa_{\eta,m}(x) w_l \left[I^+_{\eta,l} + I^-_{\eta,l} \right] - 4\pi \kappa_{\eta,m}(x) I_{\eta b}(x) \big) \mathrm{d}\eta. \tag{5.3}$$

In the present work, it is assumed that the participating medium is formed by a mixture of CO_2, H_2O and soot. Thus, the mixture spectral absorption coefficient $\kappa_{\eta,m}$ is given by a summation of the spectral absorption coefficient of the participating species and soot

$$\kappa_{\eta,m}(x) = \kappa_{\eta,H2O}(x) + \kappa_{\eta,CO2}(x) + \kappa_{\eta,soot}(x). \tag{5.4}$$

Two methods for the spectral solution of the RTE are considered in this work: the line-by-line integration and the superposition weighted-sum-of-gray-gases model.

5.2.2.1 Line-By-Line (LBL) Integration

The LBL integration consists in solving the RTE computing the spectral absorption coefficient for all spectral lines of each participating gas. Since radiation properties of participating species depend on local temperature, partial pressure and wavenumber, a detailed computation over all spectral lines is not straightfoward. Thus, simplified databases are generated for specific range of wavenumber and temperature and stored independently of the species partial pressures. A complete description of the generation of the database of participating the species used in this work (CO_2 and H_2O) is found in [Dorigon et al., 2013]. This approach can be considered exact from the spectral point of view unless for minor numerical approximations in the generation of the spectral lines database. This work assumes spectral integrations on wavenumber range between $\eta = 0$ and η = 10,000 cm^{-1} which is discretized in 30,000 intervals, resulting in a spectral resolution of $\Delta\eta = 0.333$ cm^{-1}. For the same wavenumber range, Ziemniczak et al., 2019, evaluated the LBL database with spectral resolution from $\Delta\eta = 1.0$ cm^{-1} (10,000 lines) to $\Delta\eta = 0.067$ cm^{-1} (150,000 lines) and found an average deviation of around 5% between the least refined to the most refined resolution. The limitation of the spectral resolution was imposed to due to computational power restrictions to solve the detailed LBL model coupled to the soot sectional method and the gas-phase detailed chemical kinetics.

5.2.2.2 Weighted-Sum-of-Gray-Gases (WSGG) model

The WSGG superposition model [Cassol et al., 2014] for a non-isothermal and non-homogeneous medium with arbitrary concentration of CO_2, H_2O and soot is applied in this work. In general, the WSGG is characterized by representing the entire spectrum of one participating species by a few gray-gases with uniform pressure absorption coefficient plus some transparent windows.

The WSGG lies on fitting the computed total emittance with the one provided from the LBL integration of the spectrum, which is done for a set of temperatures and pressure path lengths, $p_i x$, in benchmark problems. From this fitting procedure it is obtained pressure absorption coefficients and temperature dependent coefficients. The later ones, also known as weight factors, represent the fraction of black body energy that is emitted by the gray-gas and is given by polynomial functions of temperature.

Finally, the radiation energy is conserved assuming the transparent windows, for which the absorption coefficient is null. The absorption coefficients of participating species are computed based on the correlations for individual species (H_2O or CO_2) and soot. For all mixture compounds it was assumed a total of 4 gray-gases and a 4th-order polynomial temperature dependent coefficients provided by Cassol et al., 2014.

5.2.2.3 Optically-Thin Approximation

In addition to the detailed solution of the radiative transfer problem, the Optically Thin Approximation [Modest, 2003; Chen et al., 1993] is also considered for comparison. The Optical Thin Approximation (OTA) is largely employed in combustion modelling due to its simplicity and lower computational time [Bedir et al., 1997]. In this model only emission is responsible for the radiative heat transfer (absorption and scattering are neglected). Thus, the RTE is not needed for calculating the heat losses by radiation, which is an important advantage. Following [Zimmer et al., 2017], the absorption coefficients (modeled with a gray gas approximation) for CO_2 and H_2O are taken from [Chen et al., 1993] and for CH_4 and CO from [Barlow, 2020].

5.2.2.4 Soot radiation

Spectral radiative properties of soot depend on particle characteristics (concentration, shape and size distribution) and on its optical properties [Chippett and Gray, 1978; chia Chang and Charalampopoulos, 1990; Smyth and Shaddix, 1996; Sorensen, 2001; Williams et al., 2007]. Due to its small size and concentration, soot can be considered in thermal equilibrium with the local temperature, emitting, absorbing and scattering thermal radiation in a continuous spectrum of the infrared region. In fact, radiative scattering by solid particles grows in importance only for very high soot content. It was shown [Modest, 2003] that the emission and absorption of radiation are much higher than scattering for soot volume fractions below 10^{-3}, thus, the later phenomenon is frequently neglected. Furthermore, gas-phase radiation is limited to specific bands of the spectrum while soot radiative properties are more homogeneous along the wavelength range. Therefore, radiation emissions are easily enhanced in combustion processes with significant amounts of soot.

Soot radiation is frequently assumed linearly proportional to the total soot volume fraction [Solovjov and Webb, 2001; Modest, 2003]. In this case, the spectral soot absorption coefficient is modeled as $\kappa_{\eta,soot} = C_{\kappa,s} f_v \eta$, where η is the wavenumber (in cm^{-1}). This formalism is directly applicable to the LBL spectral integration approach. For the superposition WSGG model, soot treatment is quite similar as for the other participating species [Cassol et al., 2014]. The soot volume fraction absorption coefficients, $\kappa_{f_v,j}$, and the temperature dependent coefficients are fitted values and the soot absorption coefficient is computed as $\kappa_{soot} = \sum_j C_{\kappa,s} f_v \kappa_{f_v,j}$ over all j gray-gases. It is worth mentioning that there is no transparent window for soot. For gray-gases in the optically thin limit, the soot radiation source term is given by $\dot{q}_{r,soot} \sim 4\sigma\kappa_{soot}T^4$, where the Plank mean absorption coefficient of soot particles may be expressed as $\kappa_{soot} = 3.83 f_v C_{\kappa,s} T/C_{P2}$ [Modest, 2003], with $C_{P2} = 1.4388$ (cm K) being the second Plank's constant. In all those models, $C_{\kappa,s}$ is a dimensionless constant depending on the soot complex refractive index.

It is generally assumed that soot primary particles are spherical Rayleigh scattering objects and that aggregates are formed by point contact between primary particles. Thus, the dimensionless constant can be determined from the Rayleigh's theory for small particles as:

$$C_{\kappa,s} = \frac{36\pi nk}{(n^2 - k^2 + 2)^2 + 4n^2k^2} = 6\pi \; E(m), \tag{5.5}$$

with n and k being the refractive and absorptive indexes, respectively. $E(m)$ is the soot refractive index absorption function.

A wide range of the soot refractive index absorption function $E(m)$ is reported in literature [Chippett and Gray, 1978; chia Chang and Charalampopoulos, 1990; Smyth and Shaddix, 1996; Sorensen, 2001; Williams et al., 2007]. The value of $E(m) = 0.26$ discussed by [Smyth and Shaddix, 1996], which results in $C_{\kappa,s} = 4.9$, was more recently used in [Abid et al., 2009; Yapp et al., 2015]. On the other hand, values of $E(m)$ around 0.4 were found by [Snelling et al., 2004; Williams et al., 2007], which would result in $C_{\kappa,s} \sim 7.0$. All these $E(m)$ values resulted from very distinct complex refractive index (n and k) which are dependent on the wavelength. A more state-of-the art approach was proposed by chia Chang and Charalampopoulos, 1990, which assumes polynomial functions of the wavelength for n and k. Due to significant uncertainties related to the values of the soot refractive index absorption function $E(m)$, it is frequently assumed $C_{\kappa,s} = 5.5$ [Zhang et al., 2009a; Dworkin et al., 2011; Veshkini et al., 2014; Saffaripour et al., 2014; Eaves et al., 2017; Naseri et al., 2017]. This value is an average dimensionless constant over all the experimental measurements of Buckius and Tien, 1977, and it will be used in the current work as reference. For gray-gases in the optically thin limit, Smooke et al., 1999, proposed the soot radiation as being $\dot{q}_{r,soot} = 4.243 \times 10^{-10} f_v T^5$, which is equivalent of assuming $C_{\kappa,s} = 7.0$ in the Rayleigh's theory. The assumption of $C_{\kappa,s} = 4.9$ results in $\dot{q}_{r,soot} \sim 2.958 \times 10^{-10} f_v T^5$, while $C_{\kappa,s} = 5.5$ results in $\dot{q}_{r,soot} \sim 3.321 \times 10^{-10} f_v T^5$.

5.3 Results and discussions

Results are presented in three parts. In the first part some basic aspects of the flame structure are presented. In the second part, the role of thermal radiation on soot predictions with CO_2 addition are discussed. In the last part the effect of thermal radiation absorption and the capabilities of the optically-thin approximation are evaluated for a variety of CO_2 addition levels. Otherwise stated, soot radiation is computed assuming the dimensionless absorption constant $C_{\kappa,s} = 5.5$ for all thermal radiation formalisms used in this work. It is worth to point out that LBL simulations are conducted solely for the cases of 0% and 50% of CO_2 addition due to the higher computational time required to solve the equation system. The one dimensional fully coupled counterflow simulation with the LBL approach took approximately 72 hours to converge running in serial in a Intel i-7 3.6 GHz processor. The same case takes roughly 1 hour to converge for the WSGG model.

5.3.1 Effect of thermal radiation on the reference flame

Adiabatic and non-adiabatic results of the reference flame ($Ref - N_2$) are presented in Figure 5.1.a-c. Temperature profile and species related to soot formation are shown in physical space. The stoichiometric mixture fraction is located in the oxidizer side at $x = 0.31$ cm. It is possible to observe that radiation heat transfer is important for the flame simulation at this lower strain rate. The flame becomes narrower and the maximum values of temperature and chemical species are reduced. Major chemical species as H_2O, CO_2 and radicals peak closer to the high temperature position, while C_2H_2 and PAHs (as benzene - $A1$) are formed in the rich side of the flame. Although thermal radiation slightly affected the formation of major species, intermediate species and radicals are more sensitive to the flame temperature reduction. The reduction of maximum temperature due to radiative heat losses influences significantly the chemical kinetics and consequently the formation of soot due to the strong coupling between them. The radiative source term gives an idea about this coupling. The energy withdraw by radiation presents two peaks where the maximum values of soot and participating species are present. Such effect becomes more intense for lower strain rates [Zimmer et al., 2017] and increased CO_2 addition (as will be shown later). At lower strain rates (higher flame residence times) the total radiative heat loss is enhanced due to: the increased production of soot, increased conversion of intermediate species into H_2O and CO_2 and the increased residence time at the hot region of the flame.

Results for the two thermal radiation approaches are also included in Figure 5.1.a-c. Small discrepancies were found for the WSGG results relative to the detailed LBL integration only in the radiative source term. This discrepancy was not sufficient to change the overall performance of the computations. The WSGG coefficients were well validated for benchmark solutions with variable temperature and participating species concentration [Cassol et al., 2014]. The agreement of f_v with the reference LBL simulations shows that the WSGG is adequate for predicting the flame structures, where steep gradients of temperature and participating species concentration are present.

5.3.2 Structure of the radiating sooting flame with CO_2 addition

In this section the influence of thermal radiation on flame structure will be discussed for ethylene sooting flames with CO_2 addition in the fuel (SF) or in the oxidizer (SO) mixtures. In both flames, 0.5 mole fraction of N_2 is substituted by CO_2 in the respective stream.

The CO_2 acts in different ways on the flame structure whether it is added in the fuel or in the oxidizer mixtures [Hoerlle and Pereira, 2019]. The effect of CO_2 addition (i.e., chemical and thermophysical properties effects) were detailed discussed in [Hoerlle and Pereira, 2019]. Briefly, the increased heat capacity of CO_2 tends to reduce flame temperature and consequently affects the chemical kinetics. In addition, CO_2 participates in chemical reactions favoring the formation of CO and limiting the concentration of H-radicals. The formation of C_2H_2 and hydrocarbon radicals (as CH_2 and C_3H_3) is also suppressed. These species act as limiting agents in the pathway to the formation of the first Polycyclic-Aromatic-Hydrocarbon (PAH) and its successive growth. In the end, the formation of soot is restricted by the lower concentration of precursors (PAH

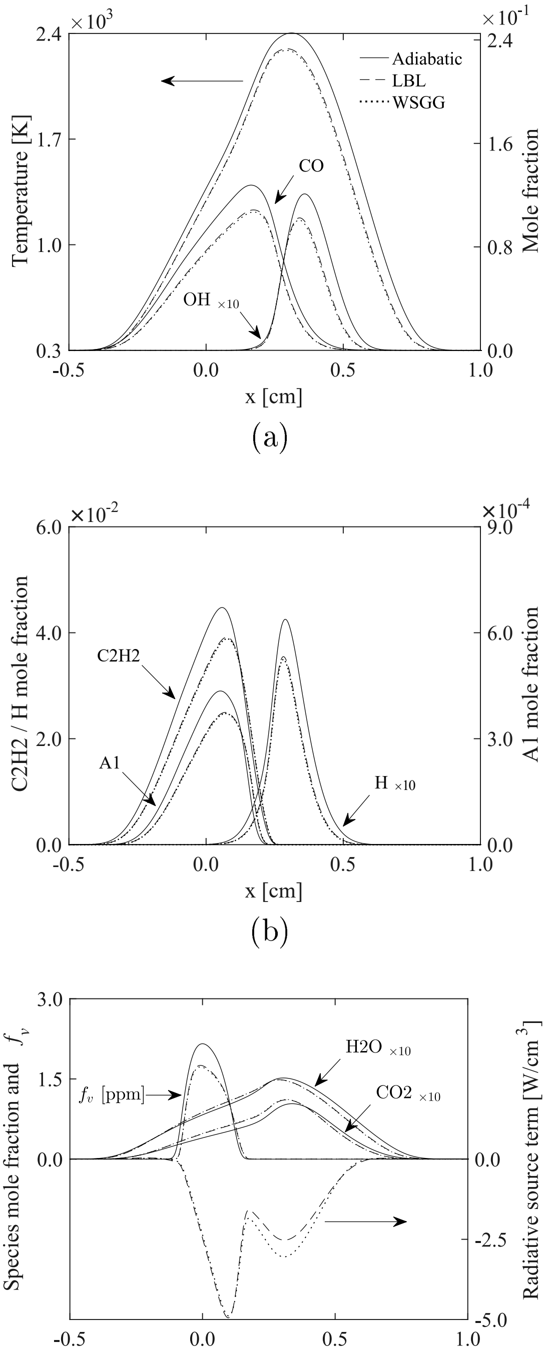

(a)

(b)

(c)

Figure 5.1 – Flame structure of the reference flame ($Ref - N_2$) for adiabatic and non-adiabatic (LBL and WSGG) simulations. Adiabatic and WSGG results from Hoerlle and Pereira, 2019.

of higher size) and by the reduced superficial growth from the H-abstraction-C-addition based mechanism. This suppression is higher when CO_2 is added on the fuel side when compared to an equivalent substitution on the oxidizer side (same CO_2 content for a stoichiometric mixture, ESO in [Hoerlle and Pereira, 2019]). When the comparison is made with the direct substitution on the oxidant side (SO) at the same levels found in the fuel side (SF), the suppression effect becomes more pronounced for the SO case due to the higher amounts of CO_2 at the reaction region.

Figure 5.2 presents the profiles of temperature and soot volume fraction (f_v) for the three flames analyzed in this work. It can be seen that the increased amount of CO_2 available in the flame front for the SO case changes more significantly the flame structure, relative to the reference flame, than the SF case. Previous work [Hoerlle and Pereira, 2019] made clear that this monotonic decrease is caused by equivalent contribution of chemical and thermophysical effects of CO_2 addition (being the latter effect slightly larger for the SF flame). The suppression of soot formation is mostly due to chemical effects [Hoerlle and Pereira, 2019]. Negligible differences are found between the two radiation approaches indicating that the WSGG model can effectively deal with the variations of the CO_2 and H_2O concentration across the flame.

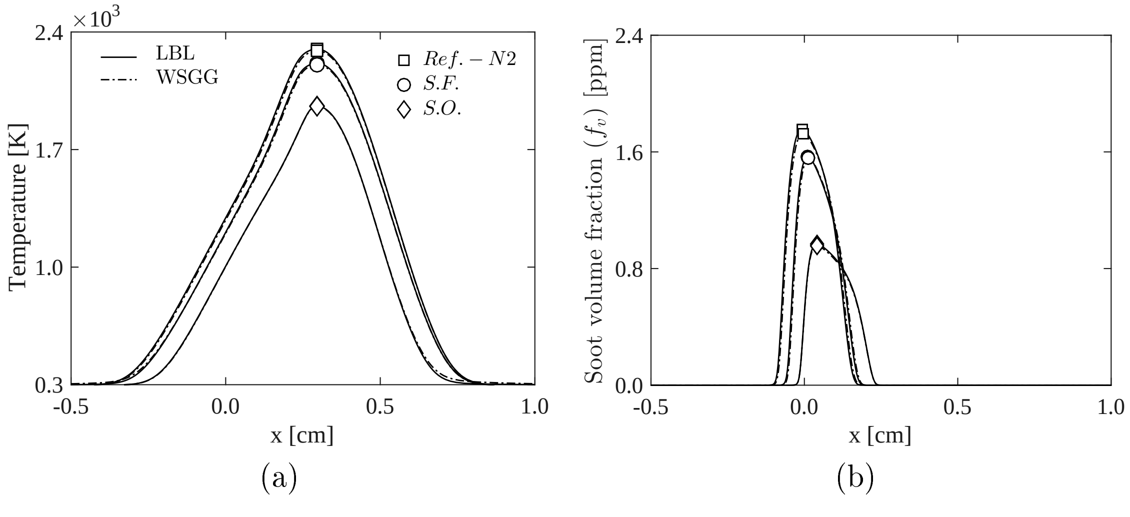

(a) (b)

Figure 5.2 – Comparison of (a) temperature and (b) soot volume fraction profiles for 0.5 mole fraction of CO_2 addition on the fuel (SF) and on the oxidizer (SO) mixtures in relation to the reference ($Ref - N_2$). WSGG results from Hoerlle and Pereira, 2019.

The radiative heat flux ($q_r^{"}$) and the radiative source terms ($\dot{q}_r$) in the energy equation computed by the LBL and by the WSGG approaches are shown in Figure 5.3. For the LBL spectral integration, the contribution of solid- and gas-phase are shown separately so that the importance of each phase can be quantified. Separate contributions of each phase are not possible for the WSGG due to the correlate contribution between all gray-gases in the computation of the absorption coefficient. The radiative heat fluxes are depicted in Figures 5.3-left, where the negative flux indicates that energy is propagating to the left while the positive flux indicates that energy is propagating to the right. The radiative heat flux increases in magnitude in both directions out of the flame inside the maximum temperature region (between $x \simeq 0.0$ cm and $x \simeq 0.5$ cm), then it becomes constant towards the reactant inlet. The radiative source terms ($\dot{q}_r$) are shown in Figures 5.3-right. As mentioned previously, the source term presents two peaks indicating the emission from the solid- and the gas-phase. For the $Ref - N_2$ case, the radiative heat fluxes leaving the thermally affect region to both sides are equivalent and the peak radiative source term from the solid-phase is approximately twice as higher as the gas-phase (one should note, however, that the gas-phase source term is significantly wider). For the SF case, the total radiative heat flux closer to the fuel inlet is lower than the reference whereas the total radiative heat flux is higher than the reference close to the oxidant inlet. Figure 5.3 (middle-right) shows that radiation emissions are enhanced due to the higher concentration of CO_2 (relative to the reference) within the high temperature region of the flame. This figure also shows that radiation reabsorption overcomes emissions at low temperatures of the thermally affected region in the fuel rich side of the flame due to the presence of CO_2. As consequence, the peak radiative source term from both phases became equivalent for this case. Similar trends are observed for the SO flame (bottom of Figure 5.3) but now the radiative heat losses decreases towards the oxidant side and increases towards the fuel side and the maximum radiative source term becomes more expressive than the other two flames (with the heat loss being predominantly from the gas-phase). The radiative heat flux from the solid-phase represents approximately 40% of the total radiative heat flux in the reference flame ($Ref - N_2$) and 25% in the SF flame. Soot presents only a minor contribution to the total radiative heat flux in the SO flame ($\sim$ 13%). Clearly, the radiative heat flux is attenuated for the SF and the SO flames towards the reactant inlet subjected to the CO_2 addition as consequence of the enhanced radiation reabsoption due to the elevated CO_2 concentration at low temperatures.

Moreover, the higher amount of CO_2 in the reaction region for flames SF and SO suppresses soot formation and, consequently, soot radiative heat losses drop proportionally to the volume fraction reduction. On the other hand, the contribution of the gas-phase to

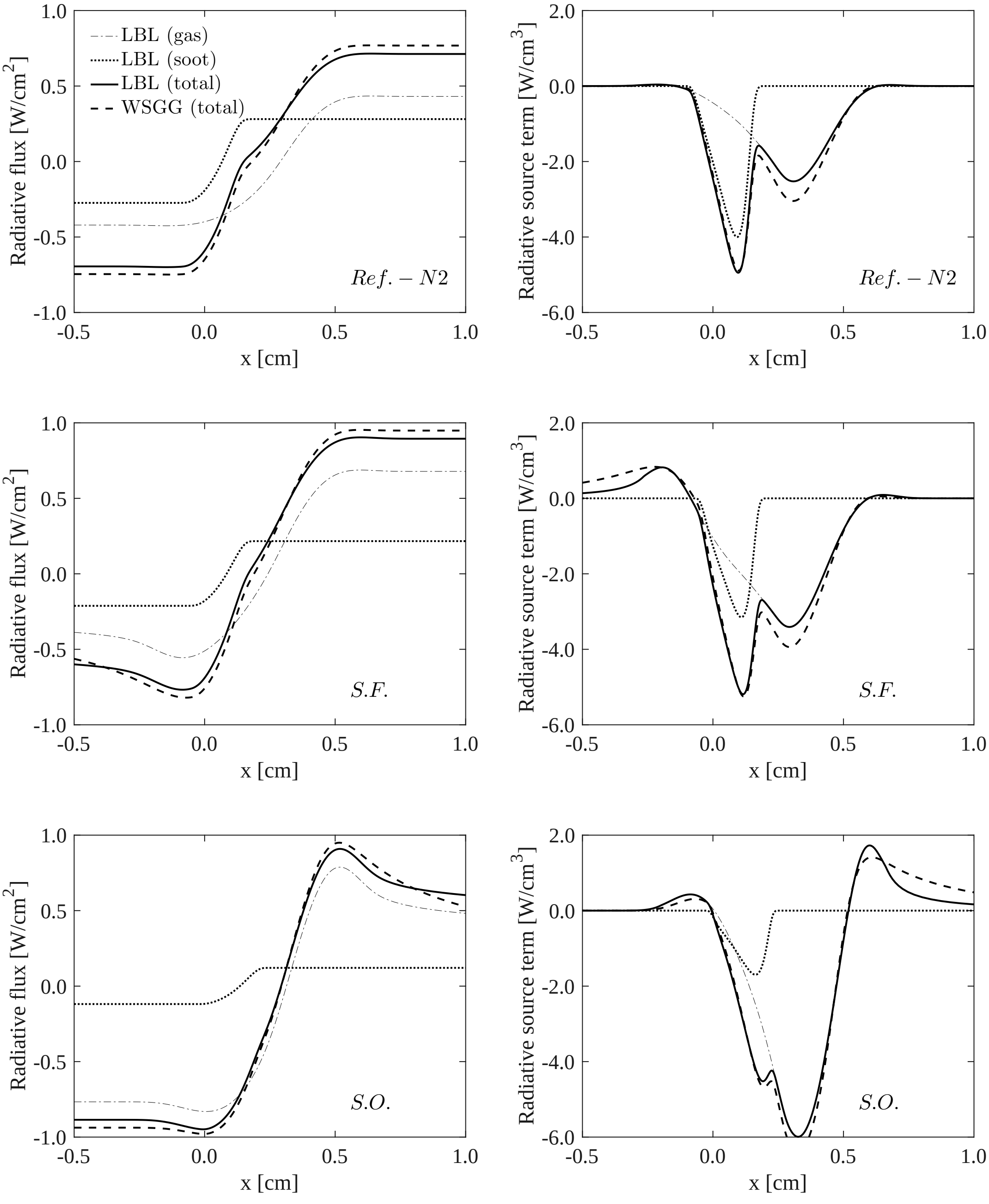

Figure 5.3 – Comparison of radiative heat flux (left) and source term (right) for the reference ($Ref - N_2$, top) and 0.5 mole fraction of CO_2 addition on the fuel (SF, middle) and on the oxidizer (SO, bottom).

the overall radiative heat losses enhances proportionally to the CO_2 concentration. For these reasons, the SO flame presents the lower heat loss by the solid-phase and the higher heat losses by the gas-phase resulting in the highest total radiative heat loss among the three flames. The increased contribution of the gas-phase in the radiative heat losses of such flames are attributed solely to the increase in carbon dioxide concentration once the water vapor remains nearly similar for all flames.

Figure 5.3 also compares results obtained with the LBL and the WSGG computations. In general, there is a good agreement between the two approaches in the high temperature region, principally where the radiative source term is dominated by soot emissions. On the other hand, the WSGG model predicted a slightly higher heat transfer out of the flame (closer to $x \simeq 0.3$ cm where the maximum concentration of the participating species occurs) and overpredicts the radiation reabsoption closer to the reactant stream where CO_2 is added. However, these discrepancies are not sufficiently to affect the overall structure of the analysed flames, as shown in Figure 5.2.

According to Centeno et al., 2018, possible source of errors of the WSGG approach could be the assumption that the gray-gases of participating species are perfectly uncorrelated, or the steeper gradients of the flame in relation to the benchmark solution for which the correlations were evaluated, indicating a potential for improvements of the WSGG coefficients, using the canonical 1D flame models.

The superposition WSGG model [Cassol et al., 2014] was able to reproduce all the main features of the sooting flames considered in this study, dealing sufficiently well with the change of participating species concentration along the flame. In addition, the superposition WSGG model used in this work can be easily extended to include more participating species as CO, but with increased computational time [Cassol et al., 2014].

5.3.3 Influence of the optical thickness of the medium

The importance of the radiation reabsorption is first evaluated by the dimensionless optical thickness of the medium. If the dimensional optical thickness is much lower than one, radiation absorption is negligible and the participating medium is said to be optically thin. Conversely, the participating medium is said to be optically thick [Modest, 2003]. Here, it is defined as the integral of the absorption coefficient on the path along the thermal affected region of the flame and the absorption coefficient is computed based on the WSGG model for convenience. The medium optical thickness of 0.24, 1.10 and 1.64 is obtained respectively for the reference and for 0.5 mole fraction of CO_2 addition in the fuel (SF) and in the oxidizer (SO) mixtures.

The influence of radiation absorption is also quantified by solving the WSGG model neglecting the absorption term in the RTE (called hereafter as WSGG-NA). Results obtained with two variations of the optically thin approximation are also included for comparison: one assuming only $CO2$ and H_2O (OTA) and another assuming four-gray gases (OTA*) as described in Section 5.2.2.3.

Figure 5.4 presents the relative change of the peak temperature (T_{max}) and the maximum soot volume fraction ($f_{v,max}$) in respect to the reference ($Ref. - N_2$ assuming the LBL approach) as function of N_2 substitution by CO_2. The agreement between the WSGG model and the detailed LBL approach is again very good for both T_{max} and $f_{v,max}$ in both flames, even at 50% of CO_2 addition. Other simplified models presented important discrepancies. Figure 5.4.a shows that the reduction of maximum temperature with CO_2 addition becomes higher for the WSGG-NA than the WSGG. Such trend occurs for SF and SO flames, but it is more intense in the later case. The difference between the two approaches, that is approximately 1% for the reference case, becomes 2% and 5%, respectively for the SF and SO cases at 0.5 mole fraction of CO_2 addition. Despite the fundamental differences in their formalism, principally due to different soot absorption coefficients, the OTA and the WSGG-NA temperature predictions are very close. The change in flame temperature presents a direct effect on the soot formation mechanism (Figure 5.4.b). Therefore, the maximum soot volume fraction is very susceptible to the effect of neglecting radiation absorption. The difference of 4% between the WSGG and the WSGG-NA approaches for the non-diluted flame rises to 15% and 22%, respectively for the SF and the SO cases at 0.5 mole fraction of CO_2 addition. The maximum f_v computed with the OTA is slightly lower than the WSGG-NA, for both flames, as a direct consequence of the slightly lower temperature of the former case. Finally, OTA and OTA* results indicate an insignificant importance of CO and CH_4 on radiation emissions for all range of CO_2 addition.

The computed radiative fraction (X_r) is presented in Figure 5.5. It indicates the parcel of the total heat generated in the combustion process that is lost by the radiation heat transfer. Here it is defined as the ratio between the integral of the radiative source term and the integral of the chemical heat release rate. The radiative fraction computed by the LBL approach presents only a minor increase from 8% (reference) to approximately 10% at 0.5 mole fraction of CO_2 addition for both SF and SO flames. The small influence

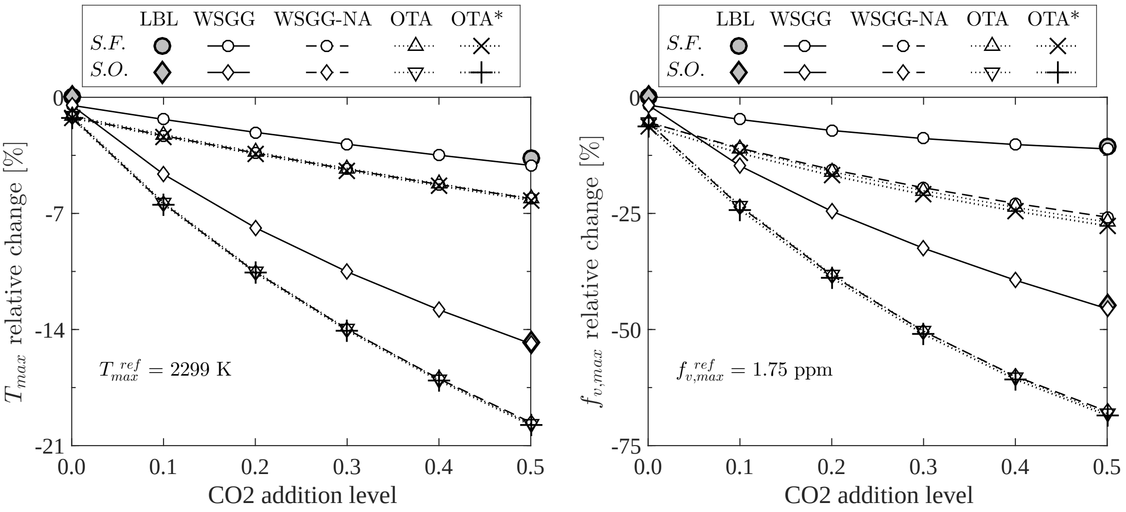

(a) (b)

Figure 5.4 – Effect of systematic CO_2 addition on the fuel (SF) and on the oxidizer (SO) mixtures on the (a) maximum temperature, T_{max}, and (b) maximum soot volume fraction, $f_{v,max}$. Results are presented in terms of the relative change respective to the reference ($Ref. - N_2$). WSGG results were partially presented in [Hoerlle and Pereira, 2019].

of CO_2 addition on the X_r obtained with the LBL approach can be understood analysing the combined effect of soot and gas-phase radiation. The soot volume fraction is higher at lower CO_2 mole fractions but decreases significantly with the CO_2 addition, so that the reduction of soot radiation is balanced by the higher CO_2 contribution. The WSGG results computed a radiative fraction that remained around 9% for all studied flames. Small variations are observed, with the SF flame presenting a minimum X_r at 0.2 mole fraction of CO_2 addition whereas the SO flame presented a maximum at 0.1 mole fraction of CO_2 addition. Respective to the LBL results, the WSGG slightly overpredicted the radiation emission for the undiluted case while a lower X_r is obtained at the maximum CO_2 addition due to the higher radiation reabsortion (as can be seen in Figure 5.3). This effect is due to CO_2 since the contribution of soot radiation is similar between the WSGG and the LBL approaches (Figure 5.3). These results reveal the potential of the 1D canonical flames to be used as benchmark for a fine tuning of radiation models. On the other hand, the radiative fraction increases expressively with CO_2 addition for the WSGG-NA and OTA models for all studied flames since only radiation emission is taking place. As expected, the optically thin approaches result in the higher X_r among all radiation models analyzed. The effect of radiation emission or absorption is merely due to the different concentrations of CO_2 because the H_2O concentration profiles are quite similar for all studied cases.

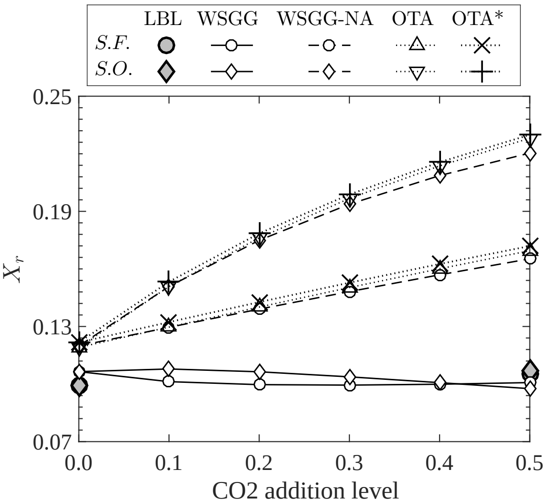

Figure 5.5 – Effect of systematic CO_2 addition on the fuel (SF) and on the oxidizer (SO) mixtures on the radiative fraction (X_r). Results are presented in terms of the relative change respective to the reference ($Ref - N_2$).

The higher concentration of CO_2 in SF and SO flames enhances not only the radiation emission but also the radiation absorption. Hence a more fundamental modelling of the thermal radiation including absorption is required, for example, for adequate modelling of oxyfuel combustion and soot predictions. The increased discrepancies when absorption is neglected made clear its importance for correctly modelling sooting flames at higher CO_2 addition. Furthermore, the use of simplified models, such as the OTA approximation, should be avoided when high fidelity solutions are required or when the soot formation is of concern.

5.3.4 Soot radiation coefficient

Influence of the dimensionless constant $C_{\kappa,s}$, of the soot absorption coefficient, on the maximum soot volume fraction ($f_{v,max}$) is evaluated in Figure 5.6. Simulations were performed with the WSGG model for three values of $C_{\kappa,s}$ (4.9, 5.5 and 7.0). The results show that the soot radiation treatment presents a slightly higher effect for the undiluted case (higher soot volume fraction) and tends to reduce with the increase of

CO_2 addition. Bigger $C_{\kappa,s}$ values clearly increase the radiative heat loss of the flame, reducing temperature and $f_{v,max}$. Moreover, the influence of the dimensionless constant is more significant for the SF case than for the SO case for all CO_2 addition levels. This happens because the suppression of soot formation is enhanced in the latter case due to the higher CO_2 amount within the flame. The maximum differences of $f_{v,max}$ obtained between results assuming $C_{\kappa,s} = 5.5$ and $C_{\kappa,s} = 7.0$ are approximately 5%. Although the influence of $C_{\kappa,s}$ is not so expressive in the flames under analysis, it may influence the flame extinction limit at lower strain rates or general flame structure in these sooting flames (as laminar coflow ethylene flames).

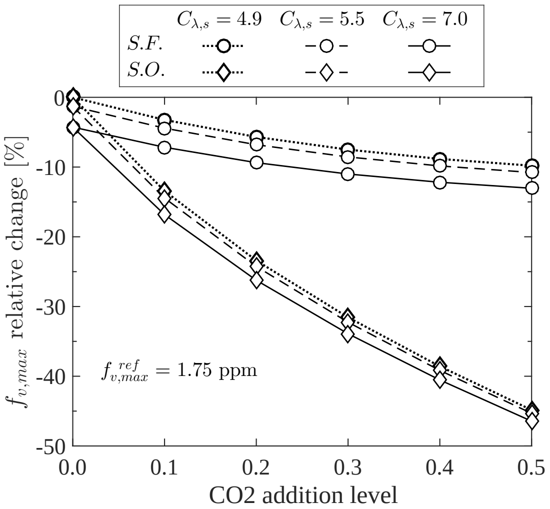

Figure 5.6 – Influence of the dimensionless soot absorption coefficient $C_{\kappa,s}$ on the maximum soot volume fraction ($f_{v,max}$). Results were computed with the WSGG approach are presented in terms of the relative change respective to the reference ($Ref - N_2$ computed with the LBL assuming $C_{\kappa,s} = 5.5$).

5.3.5 Radiation effect at lower strain rates

Simulations were also conducted for a lower strain rate $a = 5$ s^{-1}, for 0.5 mole fraction of CO_2 addition. This condition is much closer to the extinction limit due to radiative heat losses. Figure 5.7.a evidences the reduction of maximum flame temperature for lower strain rates due to increased thermal radiation. However, the increased residence time enhances the production of soot formation related species (principally the precursors) leading to a higher soot content on the flame (Figure 5.7.b). Although the WSGG model still keeps a good agreement with the LBL integration, some non-negligible discrepancies in T_{max} and $f_{v,max}$ start to appear, mainly for the reference flame, when it approaches the extinction limit.

The radiative fraction presented in Figure 5.8 shows an expressive increase with the reduction of the strain rate. Whereas all studied cases presented X_r approximately equal to 11% for $a = 20$ s^{-1}, for $a = 5$ s^{-1}, the LBL results presented X_r values of approximately 23% for the $Ref. - N2$ and the SO flames and 28% for the SF flame. The higher X_r value for the latter case occurs due to the relatively high temperature and soot volume fraction of the flame. Since the SO flame presents much more CO_2 at the flame, it has a lower temperature and soot volume fraction (due to the thermodynamic and soot suppression effects of CO_2 addition) leading to a reduction in the radiative heat loss. For the lower strain rate, the WSGG approach clearly tends to overestimate the radiative fraction of the reference flame and to underestimate it for flames with CO_2 addition. This behavior is explained by the increased radiation absorption observed in Figure 5.3 for the WSGG model.

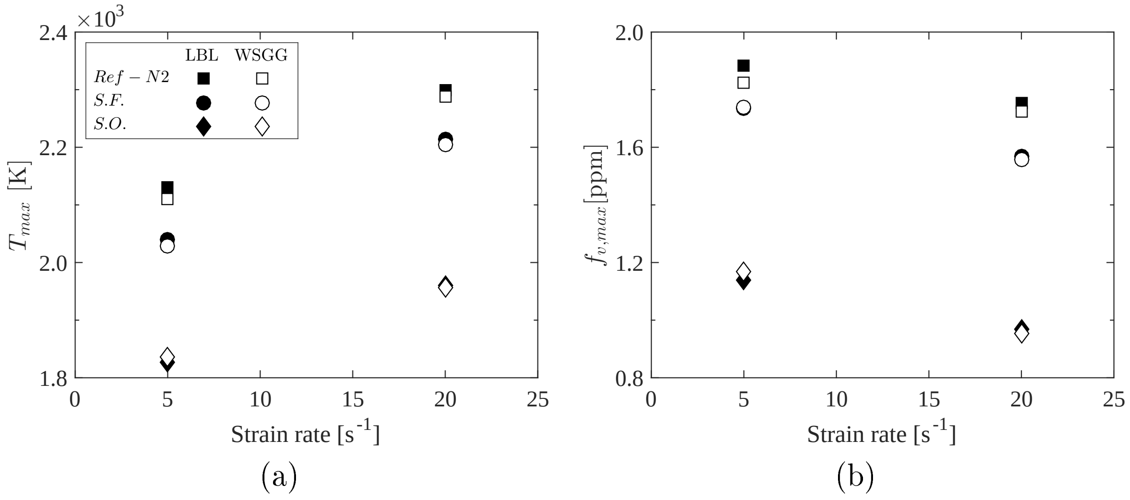

Figure 5.7 – Effect of the strain rate on the (a) maximum temperature, T_{max}, and (b) maximum soot volume fraction, $f_{v,max}$, for the reference ($Ref. - N2$) and the 0.5 mole fraction of CO_2 addition on the fuel (SF) and on the oxidizer (SO) mixtures.

5.4 Conclusion

This work explored the influence of thermal radiation models on soot formation. Simulations were conducted for counterflow non-premixed flames of ethylene under oxygen

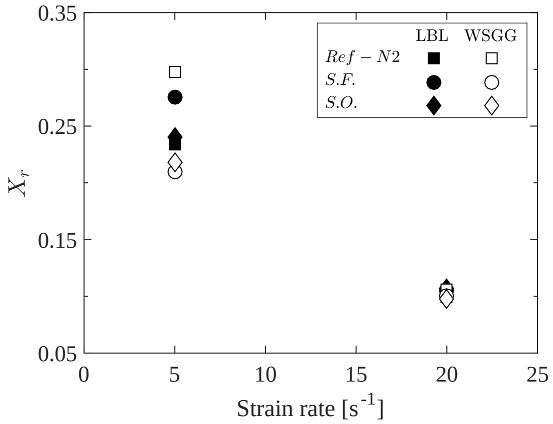

Figure 5.8 – Effect of the strain rate on the radiative fraction (X_r) for the reference ($Ref. - N2$) and the 0.5 mole fraction of CO_2 addition on the fuel (SF) and on the oxidizer (SO) mixtures.

enriched conditions with CO_2 addition in either the fuel or oxidizer mixtures. A detailed Sectional Method is used for soot modelling, and thermal radiation is accounted for by solving the RTE with the superposition WSGG/DOM approach and with the LBL/DOM integration method. The OTA model is also included for comparison. The canonical 1D counterflow flame allows for the detailed solution of gas-phase kinetics, soot formation and thermal radiation in a coupled manner. Thus the effects of inaccuracies introduced by simplified models can be studied and quantified.

Results showed that the spectral superposition WSGG model is able to accurately describe the general flame structure and to achieve good soot predictions relative to the LBL integration model. A good agreement was obtained for the reference flame and for the cases of CO_2 addition in the fuel and in the oxidizer mixtures. Small discrepancies were found for the radiative flux, and consequently, for the radiative source term. For the CO_2 addition flames, the WSGG model tends to overestimate the radiation emission at high temperature regions and to overestimate the radiation absorption at low temperatures towards the reactant with CO_2 addition. For moderate strain rates, these discrepancies were not high enough to influence the flame structure, thus the superposition WSGG, even being a global radiation model, demonstrated to be robust for modelling thermal radiation in a typical flame.

The importance of thermal radiation reabsoption was determined performing simulations with the WSGG-NA model and a standard OTA approach. The WSGG-NA is very similar to the WSGG but neglects the absorption terms. These results showed an increasing importance of radiation reabsorption with CO_2 addition. The non-absorbing models were able to capture the main flame characteristics (with discrepancies in the soot volume fraction lower than 10%) only for the reference flame. Expressive reductions of soot volume fraction were obtained when 50% of CO_2 was added to the fuel side (SF) and to the oxidant side (SO). In this way, simplified models based on pure emissions should be avoided when high fidelity solutions are required or when soot predictions are crucial for the study.

The evaluation of the soot spectral radiation coefficient reveled a major influence in the soot volume fraction for low levels of CO_2 addition, principally for the reference flames. The soot radiation contribution for the SO flame becomes much lower since the CO_2 concentration in the SO flame is very high, leading to an increased soot suppression. It was observed a maximum difference of approximately 7% in the soot volume fraction between the cases assuming $C_{\kappa,s} = 4.9$ and $C_{\kappa,s} = 7.0$, which occurs for the reference flame. Although the influence of $C_{\kappa,s}$ is not so expressive in the flames under analysis, it may influence the flame extinction limit at lower strain rates or general flame predictions of higher sooting flames (as laminar coflow ethylene flames).

At lower strain rates, discrepancies between the radiative fraction, X_r, predictions from the LBL and WSGG approaches become more expressive. As the CO_2 addition increases, the X_r predicted by the WSGG model goes from larger to lower values relative to the LBL approach due to over estimation of CO_2 reabosorption by the WSGG model.

6 MODELLING OF SOOTING OXYFUEL NON-PREMIXED ETHYLENE FLAMES WITH THE FLAMELET-GENERATED MANIFOLD TECHNIQUE

6.1 Introduction

Detailed soot models require the prediction of the thermodynamic state of the system and gaseous species related to soot inception, growth and oxidation [Hoerlle and Pereira, 2019]. It is well known that polycyclic-aromatic-hydrocarbons (PAH) are the main soot precursors. Thus, the necessity to model the growth of hydrocarbon aromatic compounds up to several rings results in large kinetic mechanism that can easily reach hundreds of species and thousands of reactions. However, theoretical studies using large kinetic mechanisms are computationally challenging, principally when dealing with the complexity of detailed soot models. Flamelet techniques has been proposed to overcome these limitations. In those flamelet models, a set of one-dimensional solutions are pre-tabulated into a manifold (a flamelet look-up table) as function of some control variables to map the thermal-composition space. Therefore, to describe a combustion process in multidimensional simulations, the solution of transport equations for all chemical species is replaced solely by the solution of the control variables. For non-premixed and partially-premixed flames, the control variables are usually the mixture fraction Z (that describes the state of the mixing) and a second control variable describing the chemistry evolution. For premixed flames, only a control variable describing the chemistry evolution may be sufficient. The enthalpy becomes and additional control variable for cases including heat losses.

One of the most used flamelet methods to solve non-premixed flames is the Steady Laminar Flamelet Model (SLFM) [Peters, 1984]. In this context, the second control variable is the scalar dissipation rate χ_{st} that describes the non-equilibrium chemistry. Since this approach was developed based on fast chemistry it may be limited and not accurate for modelling slow process as soot or NOx formation. Thus, Unsteady/Interative Flamelet Models (ULFM) [Pitsch et al., 1998; Barths et al., 1998] were proposed as an evolution of the SLFM to handle these limitations.

There are, however, many different forms of flamelet models, such as the Flamelet/Progress

Variable Model (FPV) [Pierce and Moin, 2004], the Flame-Prolongation of ILDM (FPI) [Gicquel et al., 2000] and the Flamelet-Generated Manifold (FGM) [van Oijen and de Goey, 2000]. This group of flamelet techniques were first conceived to model premixed flames, but were successfully employed for modelling non-premixed flames with the inclusion of the mixture fraction in the tabulation methodology. For this group of flamelet techniques, instead of the the scalar dissipation rate, the second control variable is the reaction progress variable that indicates how the reaction evolves (i.e., to describe the advancement of the chemical reactions). According to van Oijen and de Goey, 2000, the FGM technique, for example, is able to reduce computational time of multidimensional simulations up to 100 times with good quality results.

Flamelet techniques have been widely used to simulate sooting flames with a relatively good accuracy, but there is still no consensus about the best practices. Most of the studies about soot formation with flamelet techniques were conducted for Steady [Balthasar et al., 1996; Bai et al., 1998; Demarco et al., 2013; Xuan and Blanquart, 2013, 2014] and Unsteady/Interactive [Mauss et al., 2006; Netzell et al., 2007; Carbonell et al., 2009; Kim and Kim, 2015] Laminar Flamelet models. The latter concept presents good accuracy in relation to experiments or detailed transport solutions but requires more computational resources than pre-tabulated methods. Soot modelling through the FPV/FPI approaches are limited to a reduced number of studies [Ihme and Pitsch, 2008; Mueller and Pitsch, 2012; Lecocq et al., 2014; Yen and Abraham, 2016; Xuan and Blanquart, 2015]. The author is aware of solely a few studies with the FGM technique on soot [Zimmer, 2016] and PAHs [Verhoeven et al., 2013] formation, both for non-premixed coflow flames. Furthermore, majorily of the studies of soot formation with flamelet techniques implemented semi-empiric models or the Method of Moments for soot formation and only a reduced number of them implemented a soot Sectional Method as in the works of [Mauss et al., 2006; Netzell et al., 2007].

However, modelling soot formation with flamelet techniques is not straightforward. Those flamelet techniques are usually employed based on several assumptions that are not truly valid in the context of soot formation, viz.: the assumption of fast-chemistry, the assumption of equal mass and thermal diffusion (i.e., $Le = 1$) for all species and the consideration of only planar flamelets for the construction of the manifolds. Moreover, the coupling between the gas- and the solid-phases due to the mass transfer between these two phases usually requires special treatments, principally regarding soot precursors modelling. Those limitations/assumptions are briefly described in the next sections in the context of soot formation employing flamelet techniques.

6.1.1 Solid- and gas-phase coupling

Soot formation is a relatively slow process compared to the time-scales at which gas-phase reactions take place. Because flamelet tabulations are often based on fast chemistry assumption, the direct retrieval of soot concentration from the database (manifold) results in erroneous values since the characteristic time-scales of the soot formation processes are not well captured [Zimmer, 2016]. This problem was further addressed by solving the transport equations of soot particles with the source terms describing the phenomenological soot formation processes being retrieved from the manifold [Balthasar et al., 1996; Carbonell et al., 2009]. Moreover, it is usually assumed that soot formation is fully uncoupled from the gas-phase chemistry. Based on detailed one-dimensional laminar counterflow ethylene flames, Zimmer et al., 2017, showed that this assumption would be valid for low to moderate soot concentrations (i.e., $f_v \lesssim 5.0$ ppm) without introducing much error in the soot prediction.

Although the uncoupled treatment of soot formation does not introduce major difficulties for soot models based on acetylene as precursor (as the semi-empirical Two-Equation models), the same is not trivial for more advanced multi-physics soot models based on PAHs as precursors (as the Discrete Sectional method or the Method of Moments). It occurs because the consumption of acetylene by soot formation processes is relatively low (due to its higher concentration) in comparison to PAHs consumption. PAHs are involved in both nucleation and condensation onto particle surface. Condensation rates are linearly dependent of the PAHs concentration while nucleation presents a quadratic dependence on the precursor concentration.

Furthermore, PAH's chemistry is reversible and relatively slow compared to the major combustion products [Bisetti et al., 2012], in the same way as for soot particles formation. Since PAHs are recognized as the main soot precursor, a good prediction of their chemical evolution along the flame is crucial for the soot model success. In this way, an adequate prediction of PAH's concentration, accounting for its formation/consumption by both the gas- and the solid-phase, is of fundamental importance.

Two ways to contour the soot-gas coupling limitation respective to the precursor modelling with flamelet thecniques are: to assume that all precursors production and consumption processes are in steady state [Aubagnac-Karkar et al., 2015], resulting in an equivalent concentration of the precursor; or by solving transport equations for lumped PAHs as a link between the two phases and to better capture the precursors chemical-scales [Mueller and Pitsch, 2012; Xuan and Blanquart, 2014].

6.1.2 Influence of preferential diffusion

Preferential diffusion effects also play an important role on the flame structure and, therefore, on the soot formation. Preferential diffusion effects occurs for species with Lewis number (L_e) different from unity. Guo and Smallwood, 2010, demonstrated that preferential diffusion effects are crucial for correct predictions of PAHs in non-premixed laminar flames. The simplified assumption of $L_e = 1$ for all chemical species reduces the diffusion rates of the H-radical from the main reaction zone to the PAH formation and soot growth region that takes place at the fuel-rich side of the flame. Since the H-radical is a key species in the route of PAHs formation and growth and in the soot particles surface carbon deposition (due to the Hydrogen-Abstraction-Carbon-Addition mechanism), less PAHs are formed and lower particle surface growth is found. Owing to their higher Lewis number, preferential diffusion reduces the diffusion of PAHs towards the flame sheet.

6.1.3 Influence of curvature effects

Recent works demonstrated that both flame curvature and tangential diffusion play a role in the structure of non-premixed laminar coflow flames [Kortschik et al., 2005; Xuan and Blanquart, 2014; Scholtissek et al., 2015; Gierth et al., 2018; Han et al., 2019; Schlup and Blanquart, 2019]. Flame curvature is important when the radius of curvature is comparable or smaller than the local flame thickness. In these case, flame curvature might enhance species mass flux towards lower/higher mixture fraction values for species with Lewis number very small/large than unity. Flame curvature is commonly defined as positive when the center of curvature lies on the rich side of the mixture whereas negative curvature indicates that the center of curvature lies on the lean side of the mixture. As detailed by Xuan and Blanquart, 2014, positive (convex) curvatures induces species mass flux towards large mixture fractions when $Le > 1$ and towards lower mixture fraction when $Le < 1$, while the exact opposite behavior occurs for negative (concave) curvatures. Therefore, curvature effects are strongly related to differential diffusion effects. For multidimensional non-premixed reacting flows, flame curvature, stretch or scalar dissipation may not be uniform along a mixture fraction (Z) iso-surface. These non-uniformities introduce a variation of the thermochemical variables causing, thereby, a tangential diffusion flux along the Z iso-contours. This phenomenon is also referred to as multidimensional effects. Theredore, flame curvature induce a normal transport in the Z-direction but it might also induce a differential diffusion in flame-tangential direction along the Z iso-contours.

The relevance of curvature and tangential diffusion effects has been identified for non-premixed coflow laminar flames in the constext of flamelet techniques [Verhoeven et al., 2012; Xu et al., 2013; Xuan and Blanquart, 2014; Scholtissek et al., 2015; Han et al., 2019]. In general, it was confirmed the presence of strong curvature and tangential diffusion effects near the tip and on the axis of the flame, presenting a transition further upstream up the region near the nozzle exit where those effects becomes much less relevant because of the rather flat flame front. Around the flame tip, it was noted that the scalar fields (mixture fraction, species mass fraction and temperature) are more influenced by curvature on radial directions (with the largest curvatures near the axis) while tangential diffusion is more relevant along flame axis. Those works also emphasize the impact of differential diffusion on the curvature and tangential diffusion effects. In simulations assuming non-unity Lewis number for all species, Verhoeven et al., 2012, observed discrepancies between detailed and FGM simulations principally in the centerline of the flame that were attributed to the lack of the curvature and tangential diffusion effects in their flamelet formalism (for the unity Lewis case those discrepancies were reduced significantly). It was also identified that although curvature effects were important at the centerline, they were only secondary effects compared to tangential diffusion. In the work of Xuan and Blanquart, 2014, it was found an important improvement in the flame structure predictions by the SLMF at flame centerline when curvature-induced normal transport in the Z-direction was included. Their study suggested that tangential diffusion was only a secondary effect. A similar study conducted later by Scholtissek et al., 2015, SLFM extended the model to account for both effects asserted that tangential diffusion effects surpass curvature effects. Results obtained by Han et al., 2019, indicated that tangential diffusion, compared to curvature induced normal transport, is more important in the flame centerline but that it may also play an important role in the entire mixture fraction space. They also compared the capabilities of the SLFM and the FPV methods in predicting curvature and tangential diffusion effects. It was interestingly observed that the FPV method was most likely able to predict those two effects even if only conventional (planar) flamelets were used. This was attributed to a superior potential of the progress variable in capturing the chemical time-scales compared to a passive scalar as the scalar dissipation rate. In the work of Xuan and Blanquart, 2014, where it was identified from an scale analysis that curvature may influence PAHs' concentration even if curvature effects are negligible near the flame front due to their strong differential diffusion effects. It should be pointed out that although all those studies were conducted on non-premixed laminar coflow flames of methane/air, their flow characteristics and reactants mixture composition were different.

Curvature and tangential diffusion effects studies of non-premixed flame structure have focused mainly on the gas-phase. Their influence on soot formation was scarcely explored, except in [Lignell et al., 2008; Bisetti et al., 2012; Franzelli et al., 2017]. In the context of turbulent non-premixed coflow flames, Lignell et al., 2008, found that curvature strongly impacts transport of soot, but with the turbulent mixing of reactants still having a major effect. It was also noticed that the higher soot volume fraction occurs when soot particles move towards leaner mixtures and grow due to surface reaction with C_2H_2. This behavior is induced by negative curvatures while the opposite occurs for soot particles in regions of positive curvatures. Bisetti et al., 2012, observed a similar behavior of the soot particles movement with the local flame curvature, but with an increase of the soot volume fraction for both negative and positive (principally) curvatures. According to the authors, soot moving towards the flame sheet first grows by surface reactions but are quickly oxidized as they continue moving towards the lean mixture. On the other hand, soot particles moving away from the flame sheet experiences a more sustained growth by PAHs condensation (surface reactions barely contributing to the soot growth) with their morphology strongly dependent of coagulation. Differences in the findings of these two works may be twofold: the former authors used a more simplistic two-equation soot model and made their analysis in regions close to the flame sheet; the latter authors used a more detailed soot model and conducted their analysis at slightly richer mixture fraction values around the maximum soot volume fraction position. Similar findings were obtained by Franzelli et al., 2017, in their study of the vortex iterations on laminar coflow flames. It was ratified that, compared to flat flames, negative curvatures tends to enhance soot production, whereas positive curvatures have a negative effect on soot production. Although no details were provided for specific soot formation processes, it was clear the strong effect of curvature on larger PAHs. Negative curvatures increase the concentration of PAHs by enhancing the heat transport from the flame towards the preheated region, further increasing the soot formation.

6.1.4 Objectives

Differential diffusion of gas-phase species, the PAHs prediction and curvature effects are relevant for adequate soot predictions and flamelet techniques should be capable of dealing with all those effects. The combined influence of flame curvature and preferential diffusion on chemical species is well recognized in the literature. However, the form those effects interfere in the soot formation processes need further investigations.

The main goal of this work is to explore the coupling between the soot Sectional Method with the Flamelet-Generated Manifold technique based on the treatment of PAHs as a link between the solid- and gas-phase. The effects of transport properties including preferential diffusion and curvature effects on soot formation will also be addressed. Numerical simulation will be conducted for soot formation in one-dimensional counterflow non-premixed flames. Although literature works pointed out that tangential diffusion is important is multidimensional flames, it will not be considered in this work.

6.2 Numerical methodology

Simulations are performed for the combustion of ethylene in oxyfuel conditions at atmospheric pressure and constant inlet temperatures equal to 298 K. The reference flame consist of a fuel mixture formed by 50% of ethylene and 50% of nitrogen burning in an oxidizer composition of 28% of oxygen and 72% of nitrogen, with compositions in volume basis. This flame was extensively explored by our group in [Hoerlle and Pereira, 2019] and in Section 5. The oxyfuel flame is very similar to the reference flame, but with all nitrogen of the oxidizer replaced by carbon-dioxide. Steady-state simulations of laminar non-premixed flames are performed solving the system of conservation equations for one-dimensional counterflow flames assuming detailed chemical kinetics and the Flamelet-Generated Manifold methodology. Numerical assumption are described in [Hoerlle and Pereira, 2019]. The detailed kinetic mechanism of Appel et al., 2000, is considered in this work. Radiation heat transfer is neglected and soot formation is modeled assuming the detailed sectional method employed in [Hoerlle and Pereira, 2019]. FGM simulations are performed solely for the oxyfuel flame.

6.2.1 Detailed one-dimensional simulations

Detailed one-dimensional flames (flamelets) are solved with the specialized CHEM1D [Somers, 1994] code as described in [Hoerlle and Pereira, 2019]. The flamelet equation system (total mass, chemical species, enthalpy and stretch rate equations) was derived from the three-dimensional conservation equations to describe the flame in a quasi-one-dimensional framework perpendicular to the flame front. Assuming that the length scales of the distortions along the flame surfaces are much larger than the flame thickness [de Goey et al., 1997; de Goey and ten Thije Boonkkamp, 1999a] makes the tangential diffusion of chemical species to be negligible. In other words, it is assumed that the transport along the flame surface is small compared to the stretch effects in most situations. Therefore, tangential diffusion is not considered in this work. In addition, realizing that curvature radius k^{-1} of the flame surfaces can be disregarded in the flamelet formalism only if it is much larger than the flame thickness ($|k^{-1}| \gg \delta_f$), the 1D partial differential equations for the laminar flames describing the conservation of total mass, mass of species and enthalpy can be recast as

$$\frac{1}{\varsigma}\frac{\partial}{\partial x}\left(\varsigma\rho u\right) = -\rho K, \tag{6.1}$$

$$\frac{1}{\varsigma}\frac{\partial}{\partial x}\left(\varsigma\rho u Y_i\right) = -\frac{1}{\varsigma}\frac{\partial}{\partial x}\left(\varsigma\rho Y_i V_i\right) - \rho K Y_i + \dot{\omega}_i, \text{ from } i = 1 \text{ to } \mathcal{N}_s, \tag{6.2}$$

$$\frac{1}{\varsigma}\frac{\partial}{\partial x}\left(\varsigma\rho u h\right) = -\frac{1}{\varsigma}\frac{\partial}{\partial x}\left(\varsigma\left(-\frac{\lambda}{c_p}\frac{\partial h}{\partial x} + \sum_{i=1}^{\mathcal{N}_s} h_i \rho Y_i V_i\right)\right) - \rho K h, \tag{6.3}$$

where x, u, ρ, Y_i, $\dot{\omega}_i$, h, h_i and V_i are, respectively, the spatial coordinate normal to the flame surface, flow velocity, mixture density, species i mass fraction, species i chemical source term, mixture enthalpy, species i enthalpy and the species i diffusion velocity. Mixture conductivity and specific heat are given by λ and c_p, respectively. The diffusion velocity is given by $V_i = -(\mathcal{D}_{i,M}/Y_i)\nabla Y_i$, where $\mathcal{D}_{i,M}$ is the average mass diffusion coefficient of specie i in the mixture. In Equation 6.1-6.3 the local stretch rate K and the surface area function ς have been introduced to model the relative rate of change in mass in the normal direction of the flame surface and flame curvature, respectively. Thus, flame stretch and curvature are the only multi-dimensional perturbations considered in this work. The derivative of ς is related to the curvature k of the flame surface via

$$k = \nabla \cdot \vec{n} = -\frac{1}{\varsigma}\frac{\partial \varsigma}{\partial x}, \tag{6.4}$$

where $\vec{n}$ is the flame surface normal coordinate.

The stretch field K for a constant flame curvature is yet unknown and its quantities are obtained from the following conservation equation to close the equation system:

$$\frac{1}{\varsigma}\frac{\partial}{\partial x}\left(\varsigma \rho u K\right) = \frac{1}{\varsigma}\frac{\partial}{\partial x}\left(\varsigma\right)\left(\mu \frac{\partial K}{\partial x}\right) - \rho K^2 + \rho_o a^2, \tag{6.5}$$

in which, μ is the viscosity, ρ_o is the oxidizer density a is the linear strain rate $a = -\partial u/\partial x$ (in units of s^{-1}) defined at the oxidant side.

Finally, the set of differential equations was accompanied by two state equations: the ideal gas law and the caloric equation of state. A complete description of the formalism is found in [de Goey and ten Thije Boonkkamp, 1997, 1999a; van Oijen and de Goey, 2000].

Soot formation is modeled assuming a Discrete Sectional method presented and extensively validated in [Hoerlle and Pereira, 2019]. The soot model considers nuclearion based on the collision of two pyrene ($A4$) molecules, the condensation of pyrene onto particles surface, the surface growth by an extended HACA mechanism and surface oxidation by O_2 and OH and particles coagulation in the limit of pure coalescence. It is assumed that all collisions occurs in the free-molecular regime. The soot model was updated in the present study by including the pyrene condensation efficiency of 0.5 and the averaged particles coagulation efficiency of 0.2 following [Zhang, 2009] and by bounding the surface radicals ratio to be ≤ 1 [Eaves et al., 2016]. In relation to the reference model of [Hoerlle and Pereira, 2019], adjustments on the soot model were required in the present work due to the reduced $A4$ concentration, that leads to a lower number of incipient particles, and increased surface growth predicted predicted by the Appel et al., 2000, mechanism. The adjusted model is verified in Section 6.3.1. Moreover, since adiabatic simulations were performed at relatively low strain rates (resulting in increased particles diameters) the particle size distribution was discretized assuming 60 sections with maximum particle volume of $V_p = 5.236E - 10$ cm^3. Although the presented soot model is simpler than more advanced soot sectional methods [Wang et al., 2015b; Eaves et al., 2016; Veshkini et al., 2016b; Aubagnac-Karkar et al., 2018], it is adequate for the purpose of this study since it captures the main processes of soot formation. A more detailed description of the numerical approach is given in [Hoerlle and Pereira, 2019]. In the Discrete Sectional method, a transport equation for the soot mass fraction ($Y_{s,i}$) is solved for each representative particle size class i. Similarly to the flamelet equations, the transport equation of each soot particle size reads

$$\frac{1}{\varsigma}\frac{\partial}{\partial x}\left(\varsigma\rho\vec{v}Y_{s,i}\right) = -\frac{1}{\varsigma}\frac{\partial}{\partial x}\left(\varsigma\left(\rho v_T Y_{s,i} - \rho\mathcal{D}_{s,i}\frac{\partial Y_{s,i}}{\partial x}\right)\right) - \rho K Y_{s,i} + \dot{\omega}_{s,i}, \text{ from } i = 1 \text{ to } \mathcal{N}_{sec}, \tag{6.6}$$

where $Y_{s,i}$ and $\dot{\omega}_{s,i}$ are the mass fraction and the source term of soot particles with size i, $\mathcal{D}_{s,i}$ is the diffusion coefficient, v_t is the thermophoretic velocity and $\mathcal{N}_{sec}$ is the total number of particle size classes. It is assumed that $\mathcal{D}_{s,i}$ is approximately equal to 1% of the average gas diffusivity due to numeric stability reasons [Kennedy et al., 1990; Zimmer et al., 2017], the value of $\mathcal{D}_{s,i}$ is set to 1×10^{-6} cm^{2}s^{-1}.

Counterflow burners are formed by two opposed nozzles with impinging reactant streams along the coordinate x. The fuel is injected in the left side at the position $-L$ while the oxidant is injected in the right side at the position $+L$. The boundary conditions for the set of 1D partial differential equations for counterflow flamelets (Equations 6.1-6.6) are depicted in Table 6.1.

Table 6.1 – Boundary conditions of the flamelet equation system for counterflow flames. The subscripts f and o represents the fuel and the oxidant, respectively. The position of the boundary conditions $-L$ (fuel side) and $+L$ (oxidant side) indicates.

Fuel side	Oxidant side
$u(x=0)=0$	
$Y_i(x \to -L) = Y_{i,f}$	$Y_i(x \to +L) = Y_{i,o}$
$h(x \to -L) = h_f$	$h(x \to +L) = h_o$
$K(x \to -L) = a\sqrt{\rho_f/\rho_o}$	$K(x \to +L) = a$

6.2.2 Flamelet-Generated Manifold simulations

The Flamelet-Generated Manifold (FGM) technique [van Oijen and de Goey, 2000] lies on the assumption that multi-dimensional flames can be represented by a continuous set of one-dimensional flames (*flamelets*). Like other flamelet models, the FGM is based on the observation that the chemical kinetic processes of a multi-dimensional flame can be decoupled from the main flow and mixing process and be represented by several flamelets in a flame-adapted coordinate system according to [Peters, 1984] and [de Goey and ten Thije Boonkkamp, 1999a]. Then, a manifold is constructed through parametrizing flamelet solutions by some control variables which are used in FGM simulations. Those steps are explained in the following sections. A more comprehensive description of the FGM methodology is found in [van Oijen, 2002; Verhoeven et al., 2012; van Oijen et al., 2016; Hoerlle et al., 2017].

6.2.2.1 Flamelets solution and manifold Construction

Steady-state solution of the one-dimensional conservation equation system, Equations 6.1-6.3 and 6.5, describing flat counterflow flames are solved for varying strain rates from near equilibrium ($a \rightarrow 0$) to extinction due to lower residence time at higher strain rates. Beyond that point, transient solutions are computed until the mixing limit between reactants is reached. The lowest strain rate considered here is 0.1 s^{-1}. The higher strain rate flamelet is case dependent. From the oxyfuel flame, the transition from steady to unsteady regimes is reached at a strain rate of 1040 s^{-1}. Then the results of interest are stored in a manifold together with thermodynamic and transport properties as function of the control variables. For non-premixed adiabatic flames a 2D manifold is usually sufficient to accurately reproduce the thermo-chemical composition space. In this case, the appropriate control variables are the mixture fraction Z and the reaction progress variable $\mathcal{Y}$. Therefore, each thermo-chemical variable of interest, φ, is described as a function of the control variables $\varphi = \varphi(Z, \mathcal{Y})$. It is important emphasize that the control variables must result in an unique mapping of the thermal-chemical composition for each combustion process. The mixture fraction Z is based on the local composition of chemical elements according to Bilger et al., 1990.

The definition of the reaction progress variable $\mathcal{Y}$ is important for the method accuracy and need to be established for each studied flame. To adequately map the thermo-chemical composition space of a flame, it is recommended that the progress variable should follow some rules [Ihme et al., 2012]: a) lead, in combination with Z, to a unique description of the mixture composition, b) be independent of other control variables, c) include reactive scalars with time scales of the same order while evolving along the chemical trajectories and d) result in a transport equation that can be solved. In general, $\mathcal{Y}$ is arbitrarily defined as a linear combination of major chemical species of the combustion products:

$$\mathcal{Y} = \sum_{i=1}^{\mathcal{N}_s} \alpha_i Y_i, \tag{6.7}$$

with the weighting coefficients α_i being the inverse of the molar mass of the specie i ($\alpha_i = 1/MW_i$). The weighting coefficients are constants chosen to yield a smooth mapping of the variables with respect to the control variables. Optimization methods may be used to systematically define the most adequate progress variable definition [Ihme et al., 2012; Niu et al., 2013; Najafi-Yazdi et al., 2012] for each flame. The progress variable not only plays an important role for correctly mapping the thermo-chemical space but it also defines the resulting variable gradients in the manifold, which should be small, otherwise it can lead to interpolation errors and consequently solution difficulties or poor results. The chosen progress variable as well as the manifold validation are discussed in Section 6.4.

6.2.2.2 FGM simulations

In FGM simulations, conservation equations are solved for each control variable in addition to the conservation of total mass and momentum (or stretch rate for one-dimensional simulations). During the FGM simulations, the computed values of the control variables are read for each cell of the computational domain and the manifold is accessed for each iteration to retrieve the variables needed to solve the conservation equation system (e.g. source-terms, differential diffusion coefficients and thermal and transport properties). Then, control variables are updated after each iteration until the convergence of the equation system is achieved. At the end of the computation, the final fields of the control variables are used together with the manifold data to reconstruct the flame structure. The retrieval from the FGM manifold is based on biliniar interpolations following [van Oijen, 2002]. In the remainder of this section the conservation equations for the control variables are derived considering preferential diffusion.

Transport equations for generic control variables, Y_{cv}, including preferential diffusion were derived by de de Swart et al., 2010. The derivation of such equations results in the preferential diffusion term depending on the spatial gradients of species (which are not directly solved in FGM simulations). However, since species mass fractions are functions of the control variables, $Y_i = Y_i(Y_{cv,1}, \cdots, Y_{cv,\mathcal{N}_{cv}})$ (with $\mathcal{N}_{cv}$ being the total number of control variables), the preferential diffusion term may be written in terms of the control variables by applying the chain rule in ∇Y_i. In addition, it is further assumed that the control variable $Y_{cv,j}$ in the manifold is a function only of the first control variable. The first control variable is usually assumed to be the one with the biggest gradients. The mixture fraction Z is the first control variable for non-premixed flames such that $Y_{cv,1} = Z$ and $Y_{cv,j} = Y^{1D}_{cv,j}(Z)$, where $Y^{1D}_{cv,j}(Z)$ stands for control variable values stored in the database. Thus, the preferential diffusion terms is taken into account solely by the first control variable instead of using all species. Applying proper algebraic operations together with the mentioned assumptions, de Swart shows that transport equations of the control variables can be written as

$$\frac{\partial (\rho Z)}{\partial t} + \nabla \cdot (\rho \vec{u} Z) = \nabla \cdot \left(\frac{\lambda}{c_p} \nabla Z \right) + \nabla \cdot (d_Z \nabla Z), \tag{6.8}$$

$$\frac{\partial (\rho \mathcal{Y})}{\partial t} + \nabla \cdot (\rho \vec{u} \mathcal{Y}) = \nabla \cdot \left(\frac{\lambda}{c_p} \nabla \mathcal{Y} \right) + \nabla \cdot (d_{\mathcal{Y}} \nabla Z) + \dot{\omega}_{\mathcal{Y}}, \tag{6.9}$$

with the differential diffusion coefficient given by:

$$d_Z = \frac{\lambda}{c_p} \sum_{i=1}^{\mathcal{N}_s} w_i \left(\frac{1}{Le_i} - 1 \right) \left(\frac{\partial Y_i}{\partial Z} + \frac{\partial Y_i}{\partial \mathcal{Y}} \frac{\partial \mathcal{Y}^{1D}}{\partial Z} \right), \tag{6.10}$$

$$d_{\mathcal{Y}} = \frac{\lambda}{c_p} \sum_{i=1}^{\mathcal{N}_s} \alpha_i \left(\frac{1}{Le_i} - 1 \right) \left(\frac{\partial Y_i}{\partial Z} + \frac{\partial Y_i}{\partial \mathcal{Y}} \frac{\partial \mathcal{Y}^{1D}}{\partial Z} \right). \tag{6.11}$$

w_i and α_i are the weigth of the chemical species i in the mixture fraction ($Z = \sum_{i=1}^{\mathcal{N}_s} w_i Y_i$) and progress variable ($\mathcal{Y} = \sum_{i=1}^{\mathcal{N}_s} \alpha_i Y_i$). The the source term of the progress variable transport equation is computed similarly to the $\mathcal{Y}$ as $\dot{\omega}_{\mathcal{Y}} = \sum_{i=1}^{\mathcal{N}_s} \alpha_i \dot{\omega}_i$. Preferential diffusion effects are computed by Equations 6.10 and 6.11 from the flamelet solutions and tabulated into the manifold for each control variable together with the source term of the progress variable. The boundary conditions for the control variables transport equations assumes: $Z = 1$ and $\mathcal{Y} = 0$ for the fuel inlet and $Z = 0$ and $\mathcal{Y} = 0$ for the oxidant inlet.

6.3 Results of detailed one-dimensional simulations

This section explores basic aspects of modelling soot formation with the FGM technique, including the transport properties computation and the coupling of the soot precursor with the technique. The reference flame ($50\%C_2H_4$ + $50\%N_2$ / $28\%O_2$ + $72\%N_2$) studied in [Hoerlle and Pereira, 2019] is considered for this analysis. The stoichiometric mixture fraction of the reference flame is $Z_{st} = 0.152$. Then, the effect of flame curvature is studied comparing the reference flame with a oxyfuel flame consisting of $50\%C_2H_4$ + $50\%N_2$ / $28\%O_2$ + $72\%CO_2$, with $Z_{st} = 0.114$.

6.3.1 Validation of the soot model

First, the soot model described in Section 6.2.1 is validated against the soot model of [Hoerlle and Pereira, 2019] for the reference flame. The refereed soot model assumes that all collisions between particle-particle and particle-molecule are sucessfull (collisions efficiency equal to unity) with the gas-phase being solved with the KM2 mechanism [Wang et al., 2013]. The Appel *et. al* mechanism is used in this work since it present half the size of the KM2 mechanism, which results in lower computational requirements. However, it is worth noting that the Appel *et. al* mechanism tends to underpredicts the concentration of pyrene (which is the assumed the soot precursor) and overpredicts the concentration of acetylene (the main surface growth species) relative to the more recent KM2 mechanism, which influences the prediction of soot volume fraction (f_v) and number density. Here, computations were performed assuming a fully soot-gas coupling [Zimmer et al., 2017]. The comparison between the two models presented in Figure 6.1.a for a wide range of strain rates demonstrates a reasonable agreement for the present model in comparison to the reference model in terms of f_v. It is worth mentioning that the same is not valid for the remaining properties of soot (as number density and particles diameter) since the predictions of the chemical species pool differs significantly between the two kinetic mechanisms. Despite that, Figure 6.1.b shows that the shape of the particle size distribution is captured by the present simulations, although the curve is shifted towards larger particles. The particle size distribution is obtained at the maximum f_v position for the strain rate of $a = 50$ s^{-1}. Similar behavior was observed for the lower and the higher strain rates. Differences are attributed to different contributions of the two chemical kinetic mechanism on the soot model.

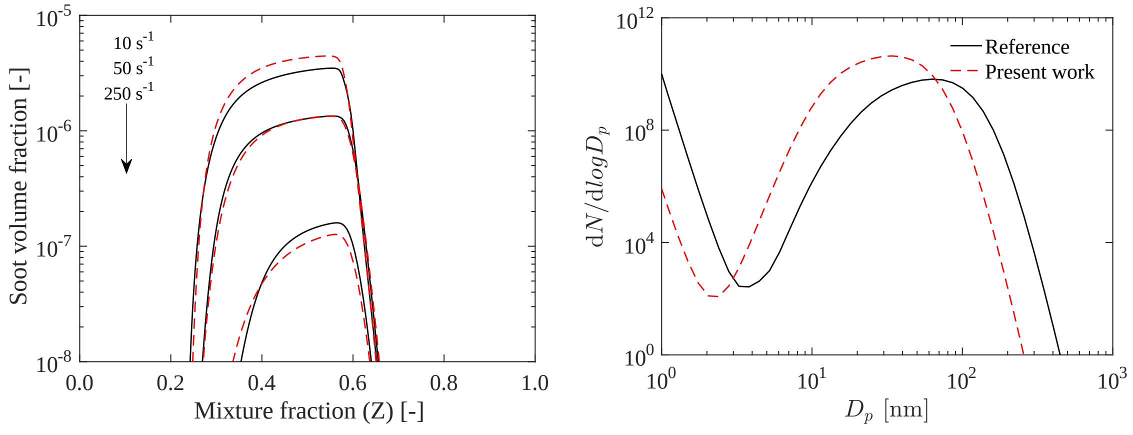

(a) (b)

Figure 6.1 – Validation of the present soot model for the 50%C_2H_4 + 50%N_2 / 28%O_2 + 72%N_2 flame: (a) soot volume fraction and (b) particle size distribution at the maximum f_v position for the strain rate of $a = 50$ s^{-1}. The reference soot model is presented in [Hoerlle and Pereira, 2019].

6.3.2 Evaluation of transport properties

Four different approaches are evaluated for the transport properties computation (diffusion coefficients and mixture conductivity and viscosity). Thermal mass diffusion was neglected since it marginally affects the soot formation [Dworkin et al., 2009].

- The first approach ($Mix.\ \ Average$) assumes a fully mixture averaged treatment. In this case, average mass diffusion coefficient ($\mathcal{D}_{i,M}$) of species are obtained by the Hirschfelder and Curtiss approximation [Hirschfelder et al., 1954], the mixture's dynamic viscosity (μ) follows from the approximate expression of Wilke, 1950, and the thermal conductivity (λ) is based on the the semi-empiric formulation of Mathur et al., 1967.

- In the second approach ($Mix.\ \ Le_i = c_i$) species diffusion coefficient is modeled using constant Lewis number (but not unity) whereas the mixture conductivity and viscosity are mixture-averaged and computed as the previous approach. The applied Lewis numbers are obtained by a least-squares fit on the mixture-averaged properties Smooke and Giovangigli, 1991.

- The third approach (*Simp.* $Le_i = c_i$) assumes constant Lewis number for species diffusion coefficient and simplified mixture properties. The simplified mixture conductivity and viscosity are modeled using polynomial functions dependent of the local temperature and mixture specific heat as in [Smooke and Giovangigli, 1991]. The simplified mixture conductivity and viscosity, respectively, reads:

$$\begin{aligned} \lambda/c_p &= 2.58 \times 10^{-4}(T/298)^{0.69}, \\ \mu/c_p &= 1.67 \times 10^{-4}(T/298)^{0.51}. \end{aligned} \tag{6.12}$$

- The fourth approach (*Simp.* $Le_i = 1$) assumes unity Lewis number for species diffusion coefficient and the simplified mixture properties (Equation 6.12).

6.3.2.1 Discussion

The influence of different transport properties formalisms are shown in Figure 6.2 for the strain rate of $a = 50$ s^{-1}. The same tendencies descussed below were observed for a wide range of strain rates. Computations were performed assuming a fully soot-gas coupling [Zimmer et al., 2017]. In general, a good agreement is observed between the simplified and the mixture-averaged approaches. Results obtained with the *Mix.* $Le_i = c_i$ approach are almost equal to with the results from the *Mix. Average* approach. More visible differences are found for the f_v profile computed with the *Simp.* $Le_i = c_i$, but lower than 0.2 ppm. Therefore, discrepancies are majorly due to the simplified mixture conductivity and the specific heat rather than the constant Lewis approximation for the diffusion coefficient computation.

On the other hand, to neglect the preferential diffusion (*Simp.* $Le_i = 1$) causes a major impact in the flame structure. This simplification tends do enhance the mass fraction of small radicals while it reduces the mass fraction of larger species such as PAHs. Consequently, the soot volume fraction is under-predicted in about two orders of magnitude (not visible in Figure 6.2.d scale). As detailed explored by Guo and Smallwood, 2010, the unity Lewis number assumption results in lower diffusion rates of the H-radical from the main reaction zone to the PAH formation and soot growth region, which takes place at the fuel-rich side of the flame. Since the H-radical is a key species in the route of PAHs formation and growth, less PAHs are formed. All these effects leads to a reduced inception rate and a smaller total surface area and, as consequence, to a lower surface growth rate. Guo and Smallwood also observed a higher OH-radical concentration due to the unity Lewis assumption, causing an increased soot oxidation rate. This was also found in the current flames, but not shown in Figure 6.2. In this way, it is crucial to include preferential diffusion for soot predictions in laminar non-premixed flames.

Based on the finding of this section, for convenience, all next simulations are conducted assuming the simplified transport properties with constant, but not unity, Lewis number for all chemical species.

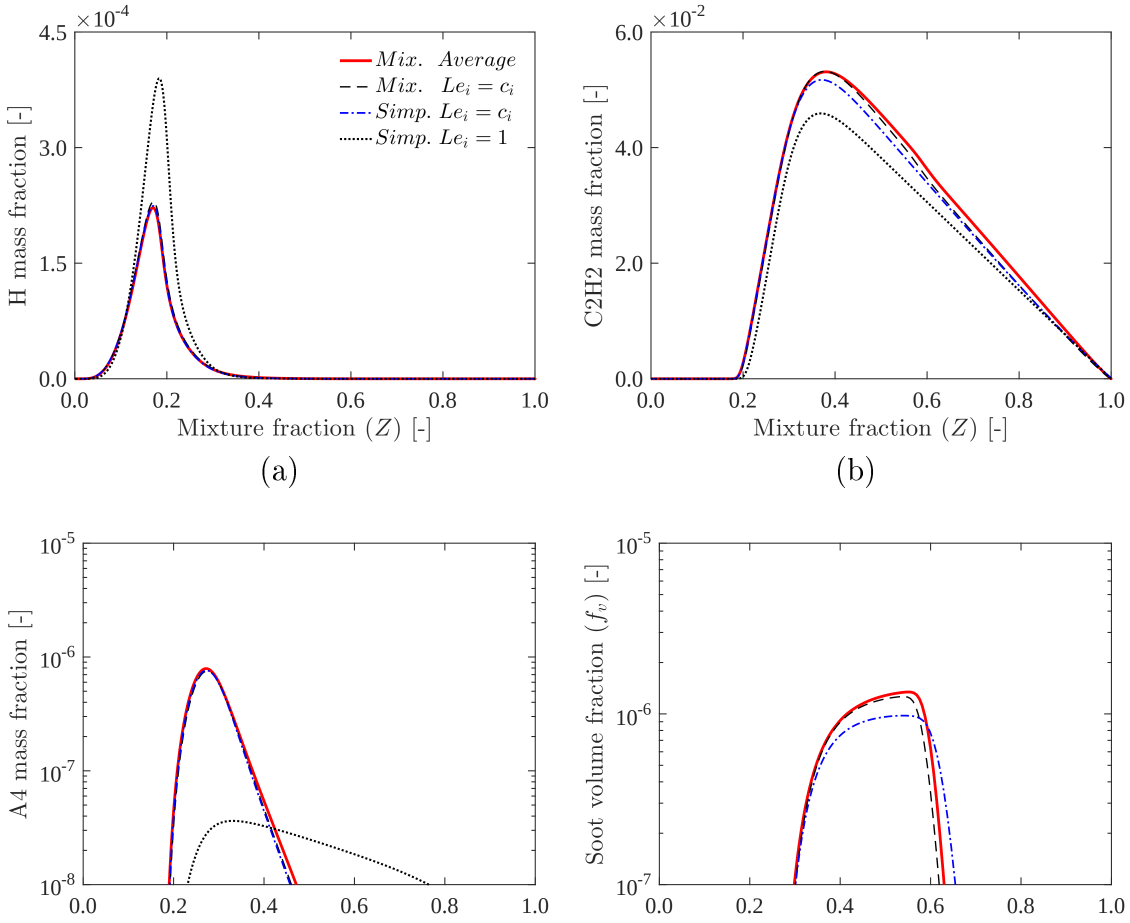

(a) (b)

(c) (d)

Figure 6.2 – Evaluation of the transport properties computation at the strain rate of $a = 50\ \mathrm{s}^{-1}$.

6.3.3 Evaluation of solid- and gas-phase coupling

The aim of this section is to investigate the capabilities of different coupling approaches for the subsequent implementation of the Flamelet-Generated Manifold technique. Two ways to solve the PAH's concentration to fully decouple the soot formation from the gas-phase chemistry are explored. Fully coupled and partially coupled cases are considered for comparison.

- The *Fully Coupled* approach consist in coupling the mass transfer between gas- and solid-phases for all species relevant for soot formation.
- The *Partially Coupled* approach assumes only the mass transfer from $A4$ to soot (the gas-phase species involved in the surface growth/oxidation processes remain uncoupled).
- The uncoupled *Lumped PAHs* apprach assumes the solution of additional standard transport equations for PAHs [Ihme and Pitsch, 2008; Mueller and Pitsch, 2012; Xuan and Blanquart, 2014]. In this case, the PAH's consumption by the soot formation processes is accounted for as source terms in the transport equation of the lumped precursor. The inclusion of a additional transport equation for the solution of chemical species with slow chemistry was introduced by Ihme and Pitsch, 2008, for nitric oxide predictions and was further extended for PAHs prediction [Mueller and Pitsch, 2012; Xuan and Blanquart, 2014], in the context of flamelet modelling. The idea raised from the observation that direct retrieval of mass fraction of those species from databases in flamelet models deviates significantly from detailed solutions due to their slow chemistry (long chemical time-scales compared to the major combustion products). In the context of flamelet techniques, it means that all other species except the PAHs relax within relatively short time scales, so that their concentrations are given by the corresponding steady state value.
- The uncoupled *Steady-State* approach consist in assuming a steady-state relation for the precursor ($A4$), accounting for its formation/consumption by the gas-phase chemistry and the consumption by soot nucleation and condensation as presented by [Aubagnac-Karkar et al., 2015].

The two fully decoupled models are detailed below.

6.3.3.1 Lumped PAHs transport approach

This approach consist in solving a transport equation for several PAHs. The standard steady transport equation for a generic PAH mass fraction, Y_{A_n}, with n aromatic rings is given by

$$\nabla.(\rho\vec{u}Y_{A_n}) - \nabla.\left(\frac{1}{Le_{A_n}}\frac{\lambda}{c_p}\nabla Y_{A_n}\right) = \dot{\omega}_{A_n}, \tag{6.13}$$

where $\dot{\omega}_{PAH}$ is the net mass reactions rate of the PAH (in units of g/cm^{3}s). In this approach, all reactions leading to the formation of A_n from A_{n-1} are lumped into a representative production reaction and all reactions consuming A_n are are grouped into a representative consumption reaction (which is proportional to its own mass fraction). Therefore, the source term of Eq.6.13 becomes

$$\dot{\omega}_{A_n} = \left(\frac{\dot{\omega}^{+}_{A_n}}{Y_{A_{n-1}}}\right)_{gas} Y_{A_{n-1}} - \left(\frac{\dot{\omega}^{-}_{A_n}}{Y_{A_n}}\right)_{gas} Y_{A_n}, \tag{6.14}$$

where the super-scripts + and − indicates production and consumption, respectively and *gas* stands for variables computed by the gas-phase chemistry. The source term is formed by the production ($\dot{\omega}^{+}_{A_n}$) and consumption ($\dot{\omega}^{-}_{A_n}$) of the PAH by the gas-phase chemistry. The terms in parenthesis in Equation 6.14 are independent of the species mass fraction and can be tabulated into a manifold of flamelet techniques.

Transport equations for lumped PAHs are solved from benzene ($A1$) to pyrene ($A4$). Since benzene is the first aromatic species formed by the gas-phase chemistry, the source term of its transported equation is simply the net chemical reaction between production and consumption. Equation 6.14 is applied for the lumped aromatics of two to four rings. For the soot precursor, $A4$, an additional term is included in Equation 6.14 to account for the mass transfer from the gas- to- solid-phases, which accounts for the consumption rates due to soot formation process of nucleation and condensation ($\dot{\omega}^{-}_{A_n,soot}$). The precursor number density required by the soot model is then computed from the results of Equation 6.13.

6.3.3.2 Precursor steady-state approach

This approach relies on assuming a steady-state relation among all the precursor ($A4$) production and consumption source terms accounting for the solid- and the gas-phases according to [Aubagnac-Karkar et al., 2015]. In terms of the precursor volume fraction rate $\dot{Q}_{A4}$ ($\mathrm{cm}^3_{A4}/\mathrm{cm}^3\mathrm{s}$), it means:

$$\dot{Q}^{+}_{A4,gas} \simeq \dot{Q}^{-}_{A4,gas} + \dot{Q}^{-}_{A4,nuc} + \dot{Q}^{-}_{A4,cond}. \tag{6.15}$$

The volume fraction reaction rate of $A4$ from the gas-phase are

$$\dot{Q}^{+}_{A4,gas} = v_{A4}\mathcal{N}_A \ \dot{\omega}^{+}_{A4,gas} \tag{6.16}$$

and

$$\dot{Q}^{-}_{A4,gas} = \left(v_{A4} \ \frac{\dot{\omega}^{-}_{A4,gas}}{[A4]} \right) N_{A4} = k_{cons} N_{A4}, \tag{6.17}$$

where $\dot{\omega}$ is the reaction rate in units of mole/cm^{3}s, v_{A4} is approximated as the volume of 16 carbon atoms, $\mathcal{N}_A$ is the Avogadro's number, $[A4]$ is the $A4$ concentration and N_{A4} is the $A4$ number density. The nucleation rate comes from the Smoluchowski equation:

$$\dot{Q}^{-}_{A4,nuc} = \left(2 v_{A4} \beta_{(A4,A4)} \right) N_{A4} N_{A4} = k_{nuc} N_{A4} N_{A4}, \tag{6.18}$$

where $\beta_{(A4,A4)}$ is the collision frequency between two precursors. The total amount of precursors colliding onto soot particles surface is expressed by:

$$\dot{Q}^{-}_{A4,cond} = \left(v_{A4} \sum_{i=1}^{\mathcal{N}_{sec}} \beta_{(A4,i)} \int_{V_{min,i}}^{V_{max,i}} n_i(v) dv \right) N_{A4} = k_{cond} N_{A4}, \tag{6.19}$$

where $\beta_{(A4,i)}$ is the collision frequency between the precursors and soot particles of section i.

Substituting Equations 6.16-6.19 in Equation 6.15 yields a second order polynomial equation with the positive root being the $A4$ number density:

$$N_{A4} = \frac{-(k_{cond} + k_{cons}) + \sqrt{(k_{cond} + k_{cons})^2 + 4\dot{Q}^{+}_{A4,gas} k_{nuc}}}{2k_{nuc}}. \tag{6.20}$$

6.3.3.3 Discussion

Results are presented for the the Fully Coupled, the Partially Coupled, the uncoupled Steady-State and the uncoupled Transported (lumped) PAHs approaches. The constant value of the particle surface radicals treatment $\xi_{dc} = 0.7$ for surface growth (detailed discussed in [Hoerlle and Pereira, 2019]) is retained for all cases otherwise explicitly described. One should note that the uncoupled approaches do not interfere in the gas-phase chemical species pool and neither on the thermodynamic properties.

Figure. 6.3 shows the profiles of the precursor and soot volume fraction for strain rates of a =10 and 250 s^{-1}. Small differences between the *Fully Coupled* and the *Partially Coupled* approaches suggest that, for the current flames, the soot model is more sensitive to the PAHs gas to solid mass transfer than other species (such as C_2H_2 and radicals) for adequate predictions of soot formation over a wide range of strain rates. It means that the uncoupled assumption for soot modelling with flamelet techniques is valid for soot predictions provided that the precursor concentration is well captured, at least for soot volume fractions in order of 1 ppm.

Major discrepancies are found between the uncoupled (*Steady-State* and *Lumped PAHs*) and the coupled approaches. For all strain rates, the fully uncoupled cases tend to overpredict the precursor mass fraction, and therefore, higher soot volume fractions are obtained. Moreover, the results show that the soot prediction between the *Steady-State* and the *Lumped PAHs* approaches are similar at lower strain rates, whereas the *Steady-State* treatment predicts much higher soot volume fraction at higher strain rates. Such tendency is expected since adiabatic flames tends to equilibrium as the strain rate approaches zero. Non-adiabatic flames tends to extinction with the reduction of the strain rate.

Two different adjustments were investigated for the *Lumped PAHs* approach to have similar soot predictions of the fully coupled case. One assumes the constant value of the particles surface radicals treatment for surface growth of $\xi_{dc} = 0.35$ (half the original value) to reduce the surface growth. The other assumes a precursor dimerization efficiency of $\xi_{nuc} = 0.05$ to limit the nucleation rate. These adjustments were conducted for the strain rate of 50 s^{-1} and evaluated for $a = 10$ s^{-1} and $a = 250$ s^{-1}. The assumption of $\xi_{dc} = 0.35$ resulted in a good agreement of the soot volume fraction (f_v) for all the strain rates analyzed (as shown in Figure 6.3). On the other hand, the assumption of $\xi_{nuc} = 0.05$ tends to overpredict the f_v profile for lower strain rates (10 s^{-1}) and to underpredict it for higher strain rates (250 s^{-1}).

The source term magnitude of the lumped $A4$ is significantly higher compared to the other approaches due to a lower consumption rate by the gas-phase (Figure 6.4.a). It makes clear that the scaling approach introduced in Equation 6.14, $(Y_{A4}/Y_{A4,gas})\dot{\omega}^{-}_{A4,gas}$, cannot reproduce properly the change in the species pool due to the consumption of $A4$ by the soot formation processes as for the cases of the fully or partially coupling between soot and gas. The dependence of larger aromatics on smaller ones and the intrinsic de-

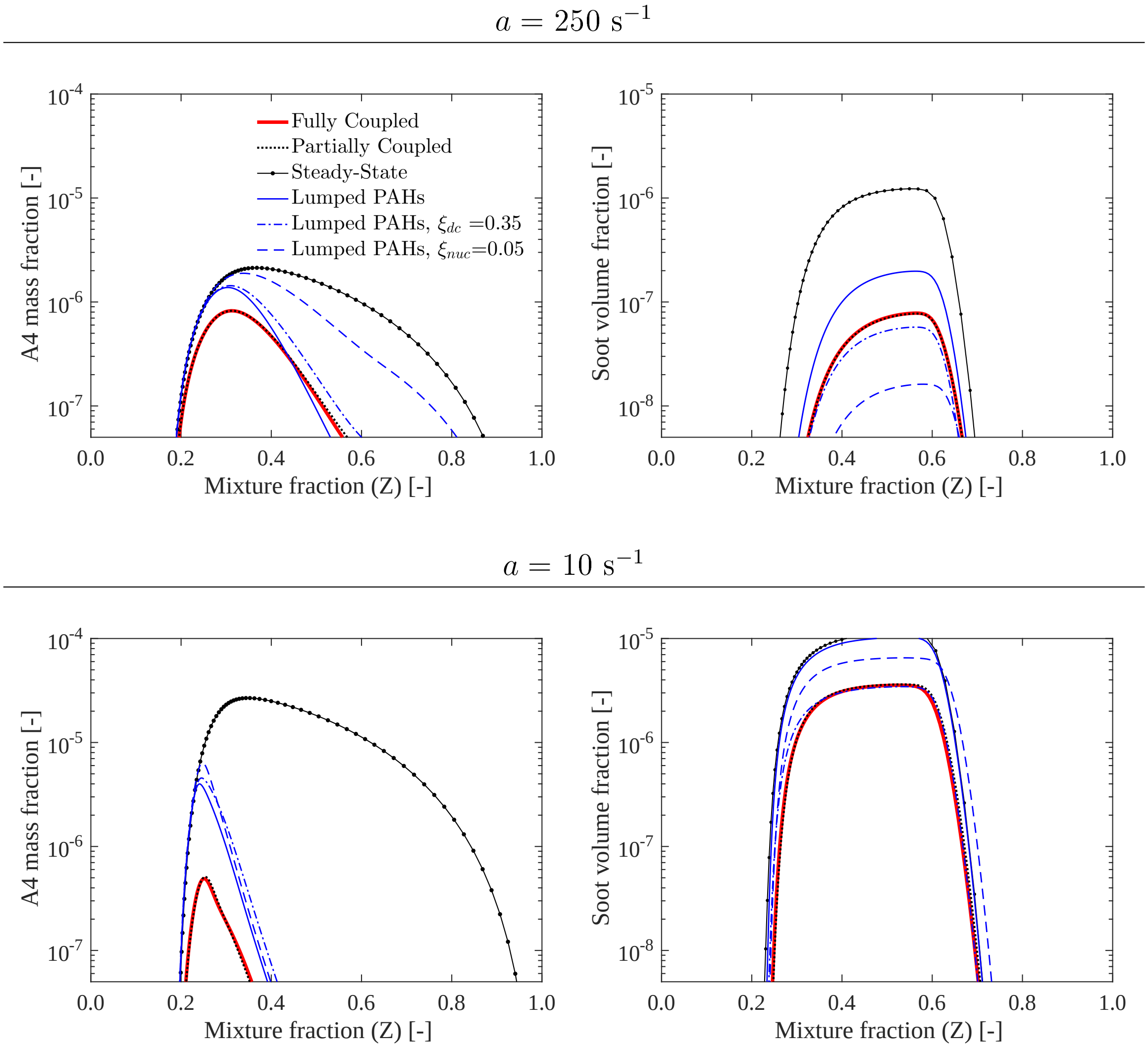

Figure 6.3 – Evaluation of the soot precursor coupling for the strain rates of $a = 250$ s^{-1} (top) and $a = 10$ s^{-1} (bottom). The $A4$ mass fraction of the *Lumped* $A4$ stands for the transported $A4$ mass fraction.

pendence of them on small hydrocarbon species and radicals could explain the differences obtained with the lumped $A4$ assuming the simple linear relaxation approach presented in Equation 6.14, as discussed in [Xuan and Blanquart, 2014]. Figure 6.4.a presents the $A4$ source term accounting for its consumption by nucleation and condensation, which results in a lower peak production and increased consumption near $Z = 0.3$ when compared to the pure gas-phase source term (Figure 6.4.b). The profile for the steady-state approach is equal in Figure 6.4.a and b since there is no consumption of $A4$ by soot formation processes.

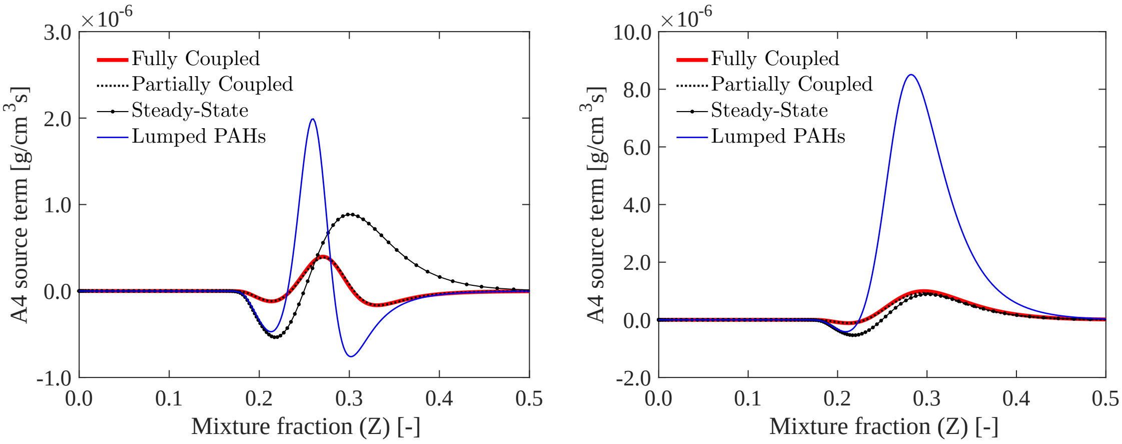

Figure 6.4 – Source term of the transported A4 equation at the strain rate $a = 50\ \mathrm{s}^{-1}$: (a) considering consumption by soot nucleation and condensation and (b) accounting solely gas-phase productions and consumption.

6.3.4 Curvature effects

The curvature effect on flame structure is analyzed for the reference and the oxyfuel flame for the strain rate of 50 s^{-1}. To affect flame structure, as previously mentioned, the curvature radius (k^{-1}) of the flame surface could be disregarded only if it is much larger than the flame thickness (δ_f), which gives that curvature is important if $k \gtrsim 1/\delta_f$. For a non-premixed flame, the flame thickness could be defined base on the diffusion thickness $\delta_{f,D}$ or on the diffusion thickness based on the Z space $\delta_{f,Dz}$ according to [Peters, 2000]:

$$\delta_{f,D} \simeq \sqrt{\frac{D_{st}}{a}}, \qquad\qquad \delta_{f,Dz} \simeq \frac{(\Delta Z)_f}{|\nabla Z|_{st}}, \tag{6.21a}$$

where $D_{st} = \lambda/(\rho c_p)|_{st}$ and $(\Delta Z)_f \simeq 2Z_{st}$, a is the imposed strain rate, the index st refers to the stoichiometric position. Therefore, curvature values for each length thickness are estimated from $k \sim |1/\delta_f|$.

The estimated minimum curvature that would affect the flame structure computed with different flame length thickness is presented in Table. 6.2. It is worth noting that this estimation is carried on a flat flame. Computations were performed for the reference and the oxyfuel flames at the strain rate of 50 s^{-1}. The estimated minimum curvature based on the two diffusion thickness are relatively close since their δ_f scales are of the same order. Furthermore, the estimated minimum curvature values are slightly higher for the oxyfuel flame since this flames is narrower than the reference flame due to the CO_2 addition [Hoerlle and Pereira, 2019].

Table 6.2 – Curvature values proportional to the inverse of the flame thickness ($k \sim 1/\delta_f$) for the strain rate of 50 s^{-1}.

Flames	Z_{st}	$\delta_{f,D}$	k_D	δ_{f,D_Z}	k_{Dz}
$50\%C_2H_4$ + $50\%N_2$ / $28\%O_2$ + $72\%N_2$	0.152	0.375	2.66	0.395	2.53
$50\%C_2H_4$ + $50\%N_2$ / $28\%O_2$ + $72\%CO_2$	0.114	0.274	3.65	0.275	3.64

Since curvatures should be higher than the values presented in Table. 6.2, the effects of constant (positive and negative) curvatures are evaluated for the curvature value of $|k| = 5$ cm^{-1} for both the reference and the oxyfuel flame. In this work, it is defined that the center of curvature lies on the lean side of the mixture for negative (concave) curvatures and on the rich side of the mixture for positive (convex) curvatures.

For a better interpretation of curvature effects on chemical species, it is assumed the uncoupled soot approach with the solution of lumped PAHs presented in Section 6.3.3. Moreover, based on the findings showed in Figure 6.3, the adjustment in the surface growth of $\xi_{dc} = 0.35$ is used to obtain soot volume fractions equivalent to the fully coupled approach.

First, a brief discussion about the CO_2 addition is presented. As detailed discussed in Hoerlle and Pereira, 2019, and in Chapter 5, CO_2 addition influences flame structure principally due to the change in thermodynamic properties and by participating in chemical reactions. The CO_2 also acts as a participating species in the thermal radiation of the flame. In general, the CO_2 addition reduces the flame temperature and suppresses the formation of species directly related to soot formation (as H, OH, CH_2^*, C_2H_2, and PAHs), leading to less soot being formed in the flame. For the current cases, the total replacement of N_2 by CO_2 in the oxidizer mixture reduced the H-radical and the soot precursor mass fraction in approximately 2/3, and the C_2H_2 and the $A1$ mass fraction in approximately 1/2. As consequence, the soot volume fraction became one order of magnitude lower (as will be shown in Figure 6.8).

In the current set of flamelet equations, curvature is introduced as a relative change of the local area trough which transport takes place along progress variable iso-contours. The change of the local area induces both convective and diffusive fluxes of species mass fraction. Positive curvatures enhances the total mass flux towards small mixture fractions while negative curvatures enhances this flux towards high mixture fraction values (as shown in Figure 6.5 for the reference case).

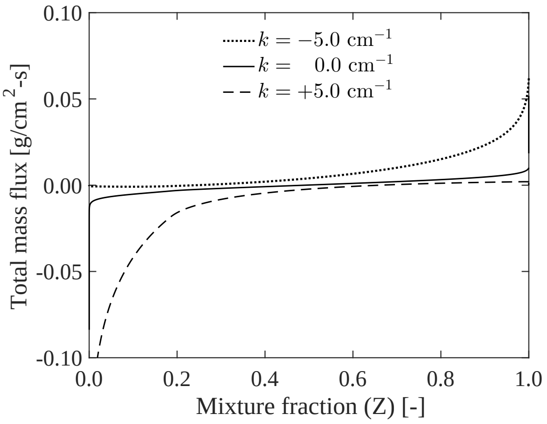

Figure 6.5 – Effects of flame curvature on the total mass flux at the strain rate $a = 50$ s^{-1} for the reference flame.

Figure 6.6 shows the temperature profile for the reference and the oxyfuel flame. Despite the direct effect of CO_2 addition in the oxyfuel flame that tends to reduced flame temperature (higher specific heat of CO_2 being higher than N_2), clearly, those flames responds differently to the curvature effects. Positive curvature reduces the flame temperature in both flames, however, the reference flame is barely affected by negative curvatures while the oxyfuel flame experiences an increase in the maximum temperature. Clearly, this trend is stronger for the oxyfuel flame. This temperature behavior with with flame curvature is in acoordance with the finding of Wang et al., 2007, and is attributed mainly to preferential diffusion effects.

The discussion follows with the curvature effects on chemical species and soot profiles. It is worth mentioning that a direct comparison between the reference and the oxyfuel flames should be carefully conducted since the vertical-axis scale is not the same between the these two flames for a better visualization of the curvature effects.

Preferential diffusion also plays a role on curvature effects as indicated in Figure 6.7 for species with different Lewis number. For positive curvatures, the mass flux of species with $Le > 1$ is induced towards larger mixture fractions while the mass flux of species with $Le < 1$ is induced towards lower mixture fractions. The opposite tendency occurs for negative curvature values. This trend can be observed on the mass fraction profiles of H_2

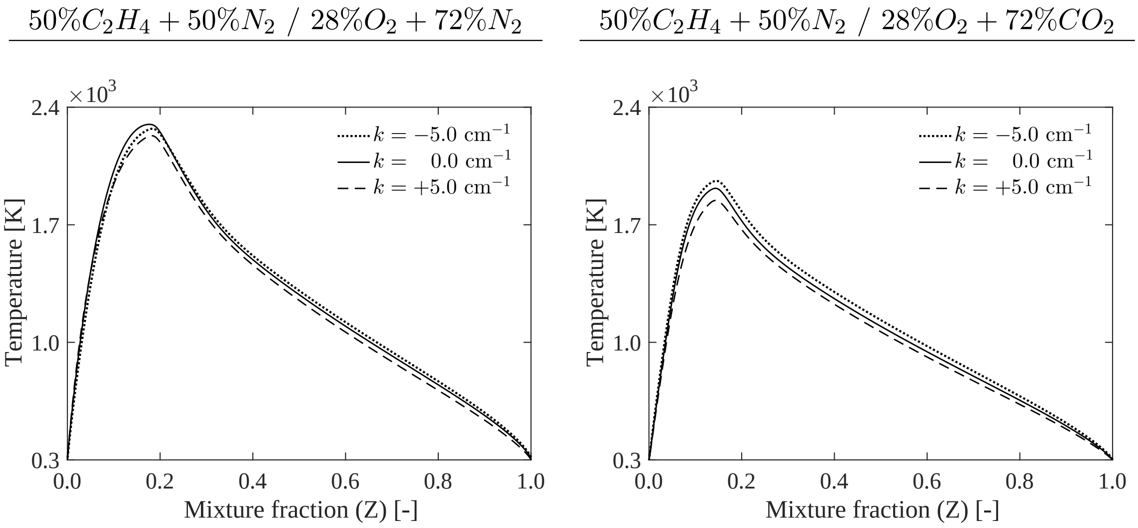

Figure 6.6 – Evaluation of flame curvature on flame temperature for the strain rate $a = 50$ s^{-1} for the reference (left) and for the oxyfuel (right) flames.

($Le \simeq 0.3$) and $A4$ ($Le \simeq 4.0$) presented on Figure 6.7. For these species, the preferential diffusion term becomes higher or, at least, comparable to the convective and normal-diffusive term. In addition to the diffusion of chemical species, Franzelli et al., 2017, observed that negative curvature enhances the heat transport from the flame towards the preheated region, increasing larger PAHS concentration. In the current flames, the convective and normal-diffusive terms are still dominant for species with Lewis number relatively close to unity, as for C_2H_2 ($Le \simeq 1.3$).

Moreover, it is clear from Figure 6.7 that the response of chemical species with the flame curvature changes from the reference to the oxyfuel flame. For the reference flame, curvature (regardless of its sign) tends to reduce the maximum mass fraction of chemical species respective to the flat flame. For the oxyfuel flame, negative curvatures tend to increase the peak of species mass fraction while positive curvatures tend to reduce their maximum mass fraction. This behavior may be related to the increased flame temperature of the oxyfuel flame observed on Figure 6.6 for negative curvatures. One should note, however, that large chemical species concentration (such as PAHs) intrinsically incorporates the curvature effects of small species.

Curvature-induced fluxes influence significantly the soot formation (Figure 6.8). Soot inception occurs at $Z \simeq 0.30$ and $Z \simeq 0.25$ for the reference and the oxyfuel flames, respectively. Then, the particles are transported towards the stagnation plane to higher Z

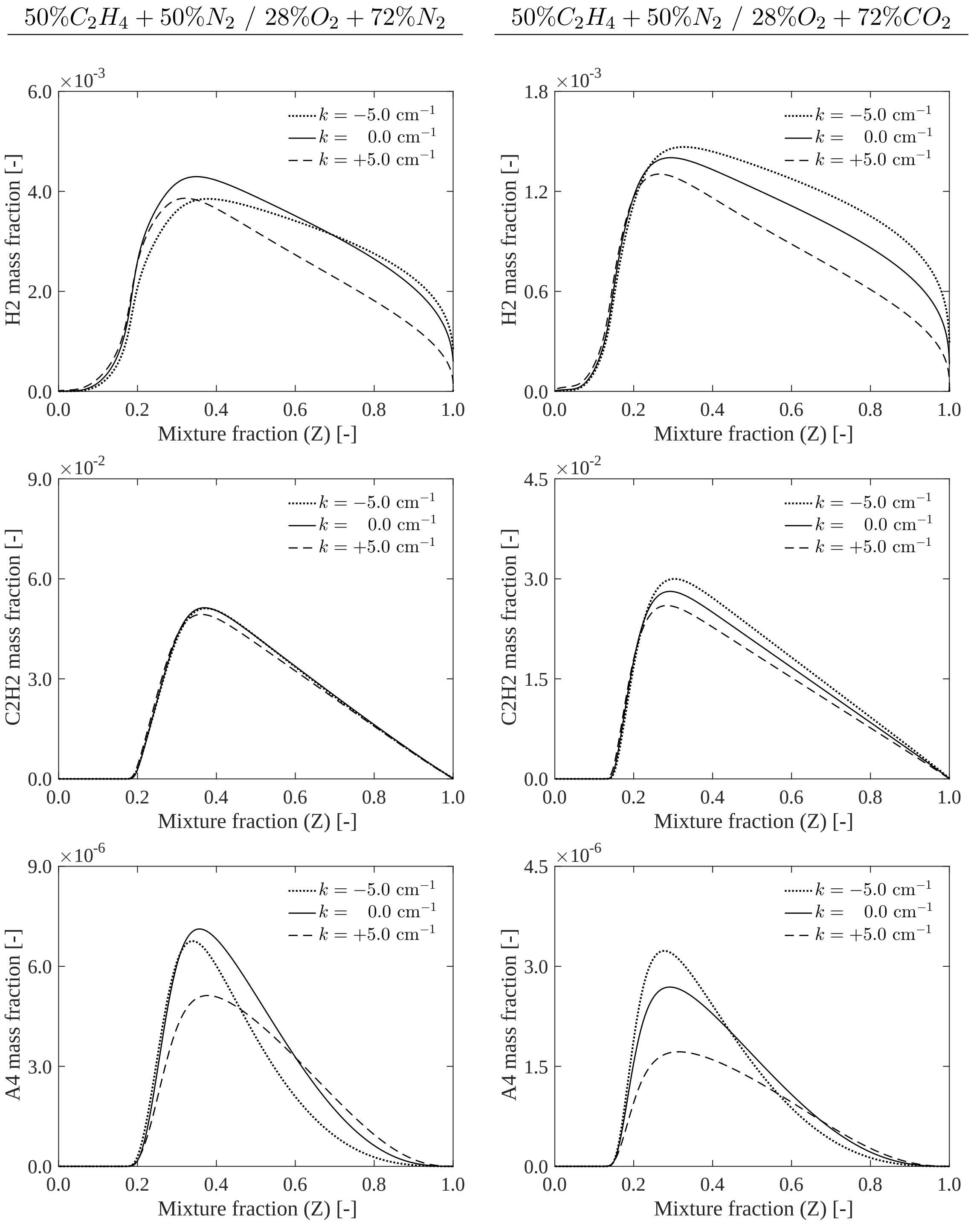

Figure 6.7 – Evaluation of flame curvature on chemical species for the strain rate $a = 50$ s^{-1} for the reference (left) and for the oxyfuel (right) flames. The Lewis' number of those species are $Le_{H_2} \simeq 0.3$, $Le_{C_2H_2} \simeq 1.3$ and $Le_{A4} \simeq 3.7$.

values. The peak value of f_v responds mainly to a direct effect of the gas-phase chemical species shown in Figure 6.7 and secondly to the effects of the flame curvature on the soot fluxes. Positive curvatures enhance the flux of soot towards higher Z values, departing the particles from a more favorable environment for their growth. Together with the reduced $A4$ and C_2H_2 concentration (Figure 6.7) of this case, it leads to lower maximum f_v but with a wider profile. Negative curvatures reduce this soot flux, leaving the particles in a environment very favorable to their growth, resulting in higher maximum f_v values with a narrow profile. For the current cases, the maximum soot volume fraction decreased in one order of magnitude for the positive curvature and increase the same amount for the negative curvature. In general, these effecs of flame curvature on soot particles were already observed by [Lignell et al., 2008; Bisetti et al., 2012; Franzelli et al., 2017].

Besides the strong CO_2 effect, no big differences were observed between the reference and the oxyfuel flames respective to the curvature effects on the soot formation. It is worth nothing that although the maximum concentration of chemical species reduced for negative curvatures for the reference flame, species such as C_2H_2 and $A4$ are barely affected on the soot formation region ($0.2 < Z < 0.3$) except for the H-radical which concentration increased. As consequence, the soot growth is sustained. The soot formation on the oxyfuel flame is much clearly influenced by the chemical species concentration shown in Figure 6.7.

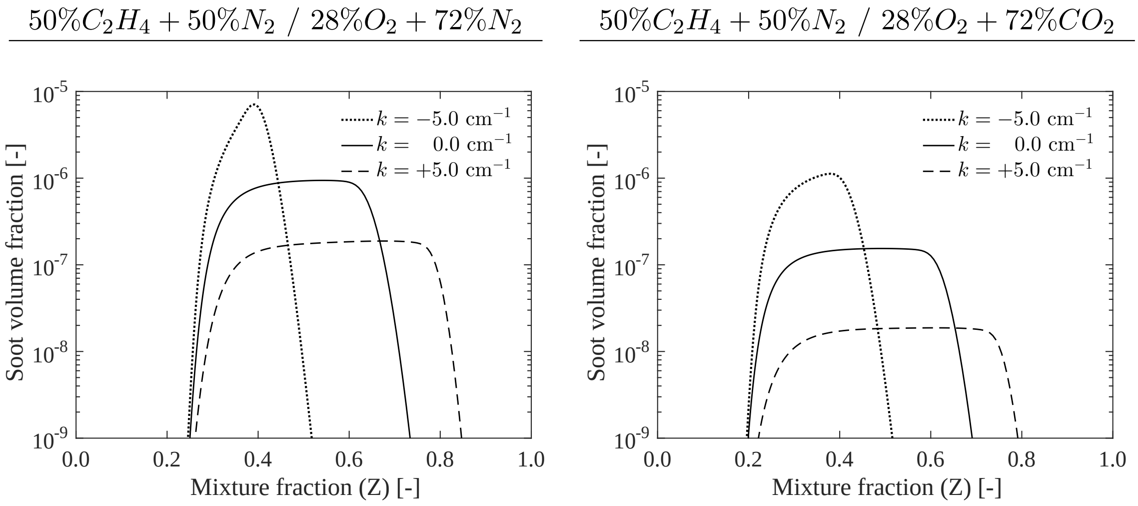
$50\% C_2H_4 + 50\% N_2$ / $28\% O_2 + 72\% N_2$

$50\% C_2H_4 + 50\% N_2$ / $28\% O_2 + 72\% CO_2$

Figure 6.8 – Evaluation of flame curvature on the soot volume fraction for the strain rate of $a = 50$ s^{-1} for the reference (left) and for the oxyfuel (right) flames.

The influence of flame curvature on the soot formation rates are depicted on Figure 6.9. For each analyzed flame, soot formation rates are normalized respective to the maximum value obtained for the planar ($k = 0.0$) case. Only a qualitative comparison can be conducted between those two flame types. In general, the maximum rates become almost one-order of magnitude lower for the oxyfuel flame respective to the reference mainly because the overall reduced temperature (Figure 6.6) and concentration of chemical species (Figure 6.7) due to CO_2 thermodynamic and chemical effects. As can be seen, the maximum rates are enhanced by negative curvatures and diminished by positive curvatures for both flames. The relative reduction of soot formation rates for positive curvatures are almost equivalent between the reference and the oxyfuel flames for positive curvatures. On the other hand, negative curvatures causes a major relative enhancement on those rates (principally for the oxyfuel flame). Part of that may be attributed to the change in temperature profile (Figure 6.6) compared to the flat case.

6.3.4.1 Curvature effects on the particle size distribution

The curvature effect on the particle size distribution function (PSDF) is shown on Figure 6.10 at the maximum f_v position. Interpretation of the PSDFs should be carefully conducted since particles aggregation and fragmentation are not taken into account, and since all collisions are assumed to occurs solely in the free-molecular regime. In this way, the PSDFs only indicate the qualitative tendency of the CO_2 addition and the curvature effects. First, the effects of CO_2 addition is brieffly discussed. As previously observed by Hoerlle and Pereira, 2019, the CO_2 addition shift the PSDF profiles towards lower particles diameters and reduce the deep of the trough. Those tendencies occur because the suppression of $A4$ and C_2H_2 by the CO_2 addition limits both nucleation and surface growth. Moreover, lower number of incipient particles also limits the coagulation rates, which diminish the trough deepness.

The PSDF presents a bimodal shape for almost all cases, except for the positive curvature cases (indicating a transition from the uni-modal to the bi-modal behavior). The curvature effects on the log-normal part of the PSDF presents a well defined behavior. Respective to the planar flames, the negative curvature enhances the soot growth and coagulation, leading to an increase in the particles diameter while the opposite occurs for positive curvatures. The behavior of the trough due to curvature effects, on the other hand, is not so well defined. It is evident that negative curvature shifts the trough to a slightly higher particle diameter (D_p) while turning the trough wider, with the opposite occurring for positive curvatures. However, the number of the smallest particles and the deepness of the trough changes considerably between the different values of curvature

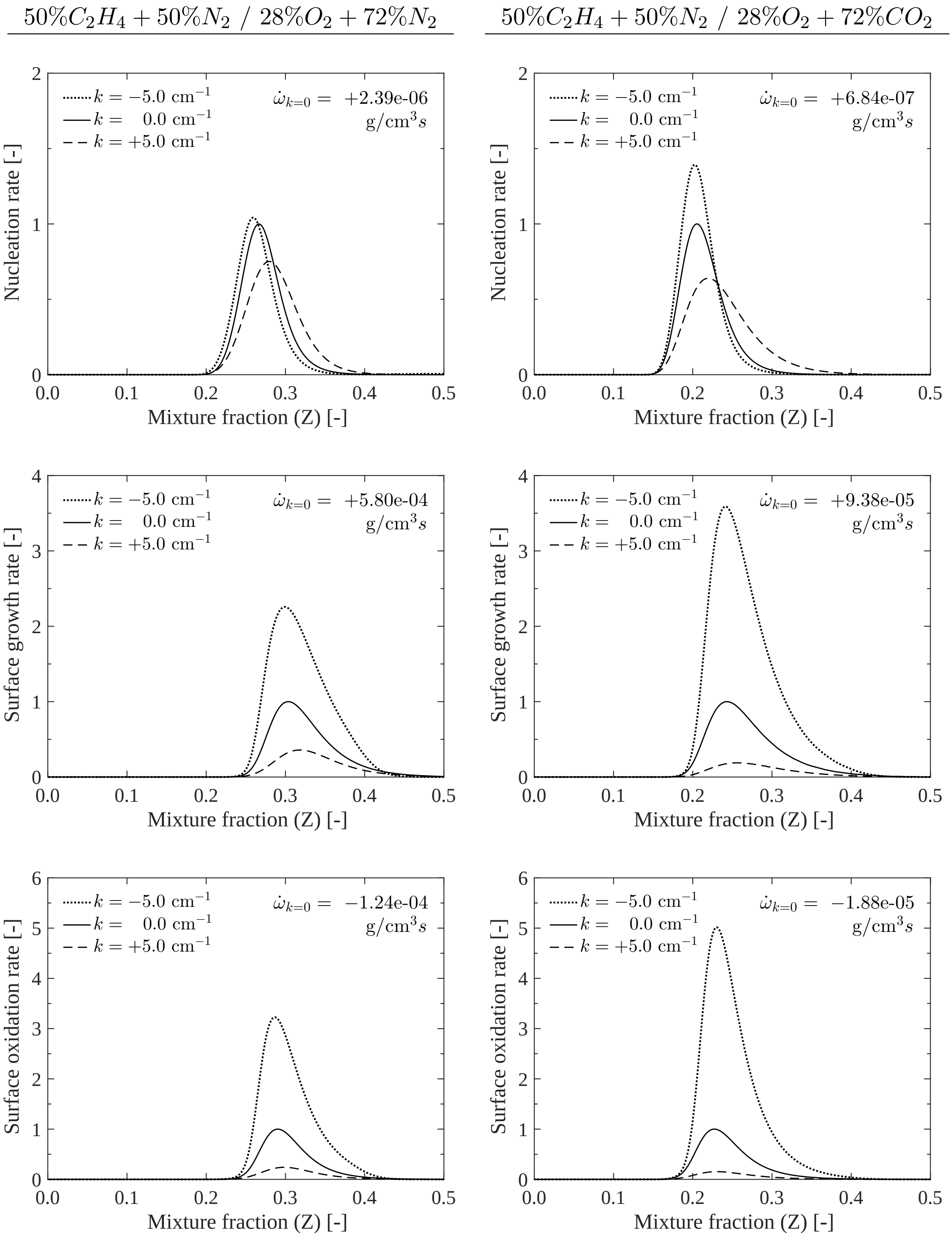

Figure 6.9 – Evaluation of flame curvature on the soot formation rates for the strain rate of $a = 50$ s^{-1} for the reference (left) and for the oxyfuel (right) flames.

and flames. For the reference flame, the positive curvature exhibits a lower number of incipient particles ($D_p \simeq 1$ nm) and trough deepness similar to the the planar flame while negative curvature profile indicates the existence of a bigger number of incipient particles and a shallower trough. For the oxyfuel flame, the negative curvature presents a higher number of incipient particles with a trough deepness similar to the planar case while the positive curvature presents in higher number of incipient particles.

As previously shown in Figure 6.9, the nucleation rate decreases from negative to positive curvatures, and with the CO_2 addition. The higher nucleation rate for the negative curvature leads to an increase number of incipient particles respective to the planar flames, meanwhile, the increase surface growth enhances the collision of those small particles with larger particles what deepens the trough. For the reference flame, the nucleation rate obtained with the negative curvature is only slightly higher than the planar case but the surface growth is more expressive. So that, smaller particles are conditioned to an environment much more favorable to their direct growth due to carbon addition, reducing the probability collisions of smaller-larger particles.

The different behavior of the PSDF between the reference and the oxyfuel flames for the positive curvature is attributed more to the type of the PSDFs. For the oxyfuel flame (lower f_v values among all analyzed cases) the PSDF is essentially uni-modal. In this case, collisions between smaller-larger particles is minimum and the shape of the PSDF is driven basically by surface growth and collisions of larger-larger particles. Justifying the prediction of a higher number density of the first particles even presenting the lower nucleation rate. For the reference flame, the PSDF already presents a bi-modal pattern that allied with the lower nucleation rate results in the lower number of smaller particles compared to the planar case.

6.4 One-dimensional soot modelling of oxyfuel flames with the FGM technique

In this section, the FGM technique is employed to model the oxyfuel flame including preferential diffusion for the one-dimensional counterflow configuration. First the manifold quality is evaluated, then, the capability of the manifold formed by flat flames in capturing, at some extended, curvature effects are verified. The manifold construction and the FGM simulations were then conducted following the procedures described on Section 6.2.2. In this study, soot formation is assumed to be uncoupled from the gas-phase and the lumped PAHs approach is considered as the link between the gas- and solid-phases. The ratio between depleted and conserved radicals for soot surface growth (ξ) is 0.7 for a direct

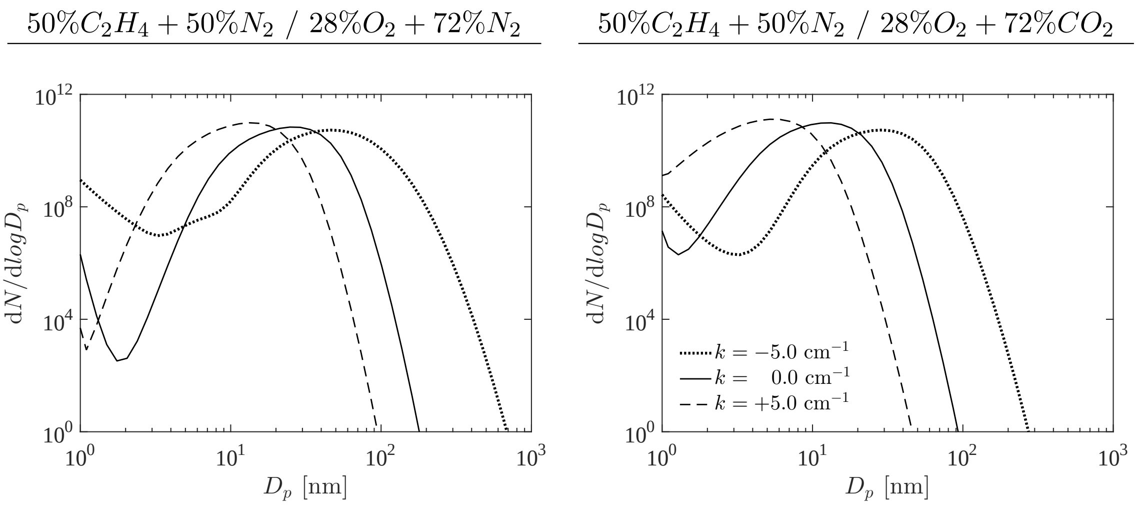

Figure 6.10 – Evaluation of flame curvature on the particle size distribution (at the maximum f_v position) for the strain rate of $a = 50$ s^{-1} for the reference (left) and for the oxyfuel (right) flames.

comparison with the coupled soot model presented in Section 6.3.3.

Soot formation is modeled with the FGM approach solving an explicit transport equations for each section and retrieving required species concentration from the manifold. The coupling between soot and FGM is established by solving transport equations of lumped PAHs (as described on Section 6.3.3) retrieving their source terms from the manifold. Some works [Balthasar et al., 1996; Carbonell et al., 2009] demonstrated that retrieving source terms of the soot transport equations from the manifold for each soot formation processes lead to good soot predictions while being computationally efficient. This approach is straightforward for two-equations soot models, but it would be unfeasible for the current sectional method where approximately 241 entries (condensation, surface growth and oxidation by OH and O_2 for 60 sections plus nucleation for the first section) would be required in the manifold only for the soot model. The large database would make the run-time look-up more time consuming. In addition, particles coagulation still need to be solved because it depends directly on the local particle sizes. Therefore, in the present work all soot formation processes are explicitly solved based on the species concentration and thermodynamic and transport properties stored into the manifold.

6.4.1 Manifold Validation

Several progress variable ($\mathcal{Y}$) definitions were evaluated based on a trial and error approach and the most suited for the present flames was found to be:

$$\mathcal{Y} = \left(\frac{1.0}{MW_{H_2O}} Y_{H_2O} + \frac{1.0}{MW_{CO_2}} Y_{CO_2} + \frac{0.9}{MW_{CO}} Y_{CO} + \frac{0.4}{MW_{H_2}} Y_{H_2} \right. \\ \left. + \frac{1.2}{MW_{C_2H_2}} Y_{C_2H_2} + \frac{20}{MW_{A4}} Y_{A4} \right) * 100.$$

In this equation, all the species weights were multiplied by 100 to reach a maximum progress variable value in order of unity. Despite standard definitions that usually take into account only the major combustion products (H_2O, CO_2, CO and H_2), tow additional species related to soot formation, C_2H_2 and $A4$, were also included. van Oijen et al., 2016, demonstrated that the inclusion of slow chemical species in the $\mathcal{Y}$ definition with increased weighting factors may improve the mapping of its chemical evolution resulting in better predictions by the FGM technique. Therefore, C_2H_2 and $A4$ were included in the $\mathcal{Y}$ definition due to their importance for the soot formation processes. Furthermore, it was shown in [Hoerlle et al., 2017] the importance of including the CO in the progress variable definition to capture the chemical effects of CO_2 addition (principally due to the $CO2 \rightleftharpoons CO$ conversion from reaction $CO2 + H \rightleftharpoons CO + OH$).

Mass fraction of H and C_2H_2 stored in the manifold are shown in Fig. 6.11 as function of the control variables. The transition from steady (above) to unsteady (under) flamelets happens strain rate 1040 s^{-1}. The one-dimensional results for the strain rates of 10 and 250 s^{-1} indicates the region relevant for soot formation as shown in the next section. These two species exemplify the chemical space of species majorly produced and consumed near the stoichiometric position (such as H and OH radicals) and of species that span towards higher mixture fractions (such as CO, C_2H_2, $A1$ and $A4$). It also shows the increase in the C_2H_2 mass fraction with the decrease of the strain rate.

The manifold capability of predicting the thermo-chemical composition space is evaluated in Fig 6.12. This *a priori* analysis is conducted by comparing FGM simulations with detailed ones for one-dimensional flat (zero curvature) counterflow flames for the strain rates of 10, 50 and 250 s^{-1}. A good agreement of the FGM with detailed simulations can be seem in Figure 6.12 for the progress variable and some species important for the soot formation. This agreement also follows for temperature, main chemical species

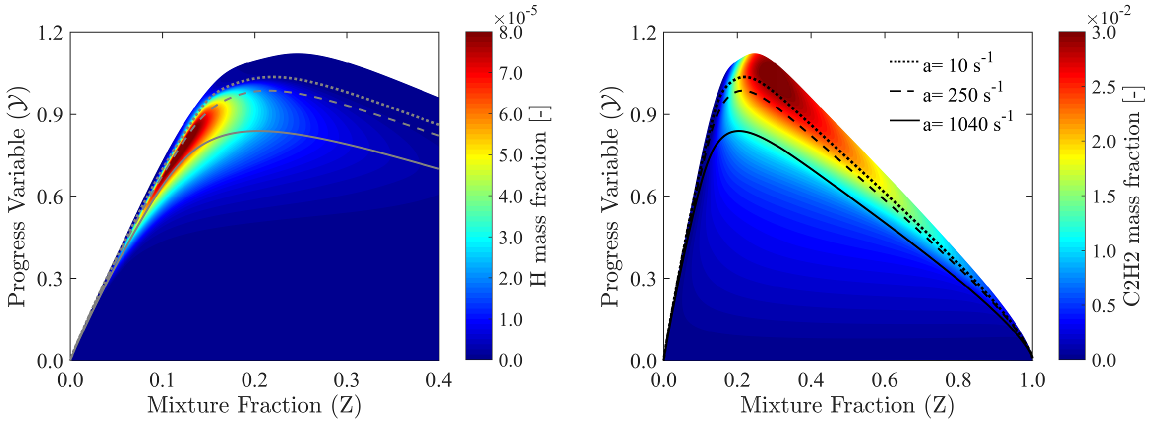

Figure 6.11 – Contours of H and C_2H_2 mass fraction stored in the manifold. Results of Z and $\mathcal{Y}$ reconstructed from detailed flamelets are presented for the strain rate of 10 cm^{-1} ($\cdots$), 250 cm^{-1} (– –) and 1040 cm^{-1} (—).

(H_2O, CO_2, CO and H_2), radicals (O, OH CH_3) and other relevant species for the soot formation processes. Major differences are found at the rich side of the flame, in the range of $0.5 \lesssim Z \leq 1$.

The Lewis number of the control variables can be defined by rewritten the differential diffusion term into Equation 6.22:

$$\frac{1}{Le_{Y_{cv}}} - 1 = \sum_{i=1}^{\mathcal{N}_s} \alpha_i \left(\frac{1}{Le_i} - 1 \right) \left(\frac{\partial Y_i}{\partial Y_{cv,1}} + \sum_{j=2}^{\mathcal{N}_{cv}} \left\{ \frac{\partial Y_i}{\partial Y_{cv,j}} \frac{\partial Y_{cv,j}^{1D}}{\partial Y_{cv,1}} \right\} \right). \tag{6.22}$$

This equation shows that the Lewis number of the control variables are not constant, even though the individual species Lewis number is constant. Figure 6.13 shows the $\mathcal{Y}$ Lewis number increasing from lean to rich mixtures with a major parcel of the manifold assuming values in the range of 0.5 to 1.5. Since the Lewis number depends on the control variable definition, it increases with the mixture fraction due to a higher importance of C_2H_2 and $A4$ at these regions. The Lewis number of Z (not shown) is much more uniform along the entire manifold, ranging between 1.0 and 1.25. The differential diffusion coefficient of control variables ($\mathrm{d}_{Y_{cv}}$) is compared to the the normal diffusion coefficient (λ/c_p) in Figure 6.14. Clearly the normal diffusion is larger than d_Z over the entire mixture fraction space, and larger than $\mathrm{d}_{\mathcal{Y}}$ for $Z \gtrsim 0.2$. The differential diffusion terms peak close to the stoichiomentric mixture fraction for both control variables, assuming peaks values twice as large as the λ/c_p for the progress variable. The peak values slightly changed with

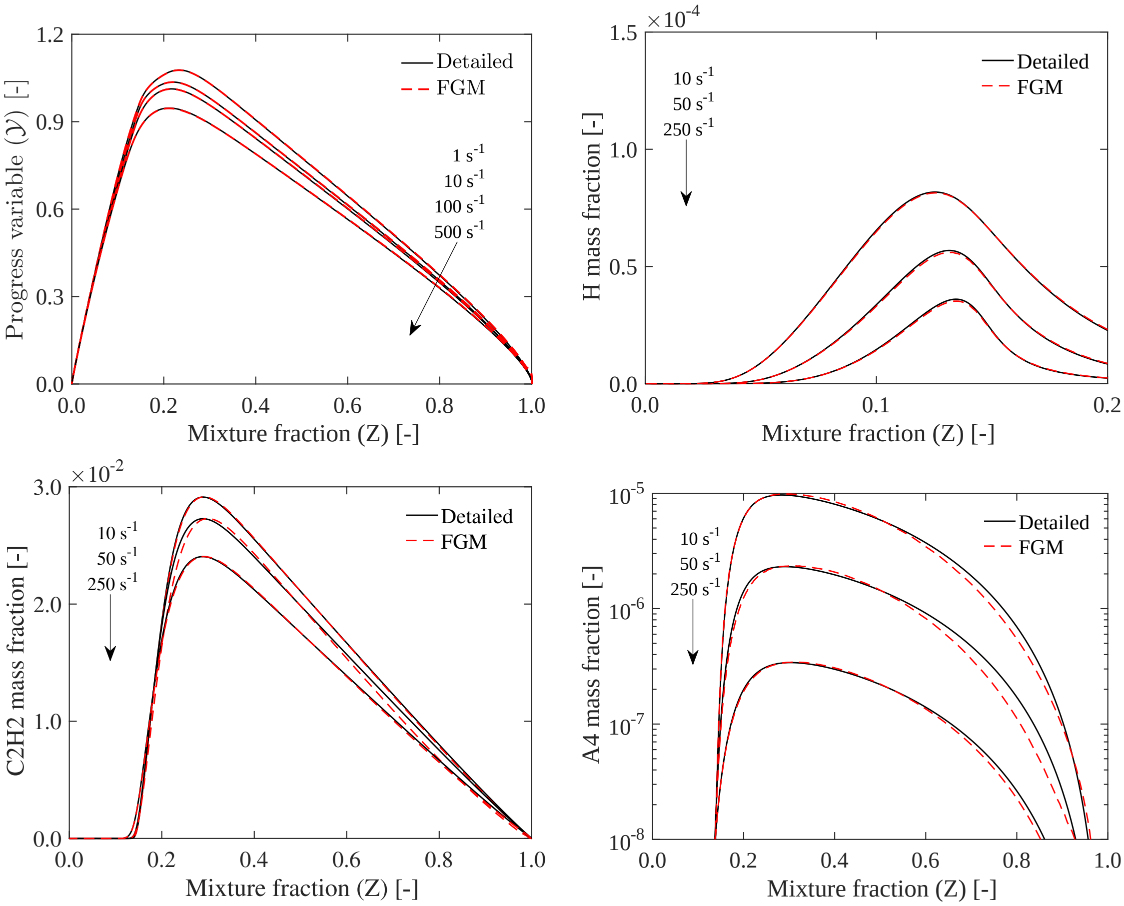

Figure 6.12 – Comparison of soot modelling between FGM and detailed simulations neglecting flame curvature for the progress variable and chemical species.

the strain rates in analyzed range.

6.4.2 Soot modelling with the FGM technique

Figures 6.15 and 6.16 depict the solution of the lumped $A4$ species, the soot volume fraction and number density. Again, a good agreement was obtained between the FGM and the detailed results. Soot is concentrated at $0.2 \lesssim Z \lesssim 0.7$ but formed principally in a region close to $Z \simeq 0.2$ and convected towards larger mixture fraction values (Figure 6.9). Therefore, discrepancies on the chemical species for the FGM solutions at higher mixture fraction values barely affected the soot formation processes. These results show that the FGM technique including preferential diffusion is able to accurately describe soot formation for one-dimensional flames in a wide range of strain rates. One should note, however, that both FGM and detailed simulations assumes that soot and gas-phase are

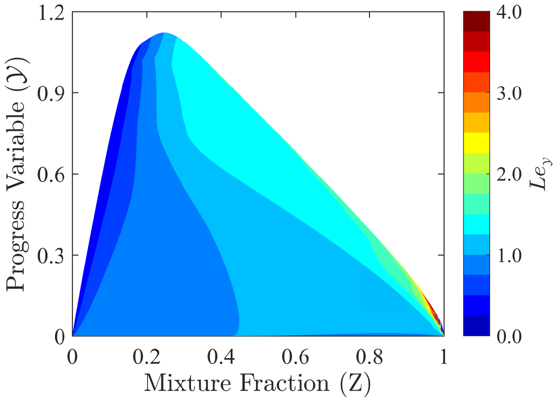

Figure 6.13 – Lewis number of the progress variable stored in the manifold as function of the control variables.

uncoupled trough the lumped PAHs approach. In this way, discrepancies still exist in relation to the fully coupled approach as illustrated in Figure 6.3.

The FGM technique present good accuracy with reduced computational time. Running the current sooting flames in serial in a Intel i-7 3.6 GHz processor, the detailed fully coupled approach (shown in Figure 6.3) took roughly 25 minutes to converge and the detailed uncoupled approach converged in approximately 13 minutes. Meanwhile, the FGM technique required only 4 minutes to reach the converged solution. In other words, the FGM technique was 3 times faster than the equivalent approach of soot model with the detailed simulation (i.e., both approaches assuming the uncoupled soot model with the transport of lumped PAHs). It was observed that most of the computational time is due to the soot model. For the solution of pure gas-phase it was found that the FGM technique was approximately 72 times faster than the detailed simulation. The difference in the computational requirements should be even higher for multidimensional simulations.

6.4.3 Curvature effects with the FGM technique

This section explores the capabilities of the FGM technique in predicting curvature effects from a manifold formed solely by flat flames. Simulations are performed for the one-dimensional counterflow flame at the strain rate of 50 s^{-1}. Figures 6.17 and 6.18 present the results for species mass fraction and the soot volume fraction.

Figure 6.17 depicts the response of lumped $A4$ mass fraction and the soot volume fraction profile to the increase in curvature magnitude (for both negative and pos-

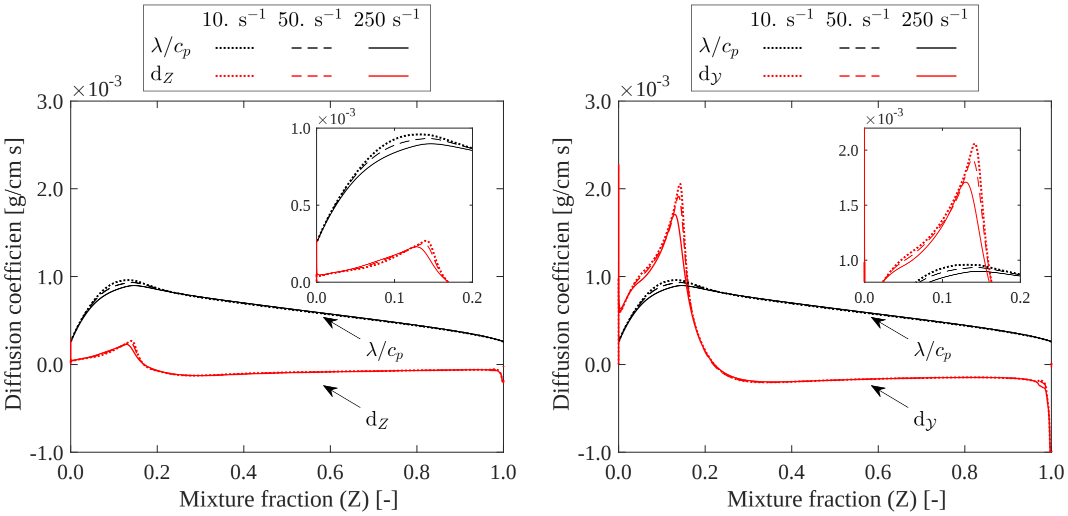

Figure 6.14 – Normal and preferential diffusion terms of the control variables Z (left) and $\mathcal{Y}$ (right) stored in the manifold.

itive values). The findings are in accordance with what was previously observed in Figures 6.7 and 6.8. Positive curvature effects enhance the flux of species with Lewis number greater than unity towards increased mixture fractions, while the opposite occurs for negative curvatures. The detailed simulations show that the lumped $A4$ (which is assumed as soot precursor) is slightly affected with the increase of curvature magnitude, except for very high curvature magnitudes ($|k| = 8$ cm^{-1}) where the peak mass fraction reduces for the negative curvature and increases for positive curvatures. Clearly, the FGM technique is not able to quantitatively predict the effects of a wide range of flame curvatures on the lumped PAHs mass fraction. On the other hand, the qualitative behavior of the curvature effects on the lumped $A4$ mass fraction was captured by the FGM technique. Source terms of the lumped PAHs transport equations were retrieved from the manifold according to [Xuan and Blanquart, 2014]

A qualitative agreement of the soot volume fraction predicted by the FGM technique respective to the detailed simulations is obtained (Figure 6.17). It is primarily attributed to the fact that the most important species to the soot formation processes are slightly affected by curvature in the region where these processes take place for the current flames.

Figure 6.18 presents the results for species mass fraction. For the FGM simulations, all these chemical species are directly retrieved from the manifold. The FGM technique

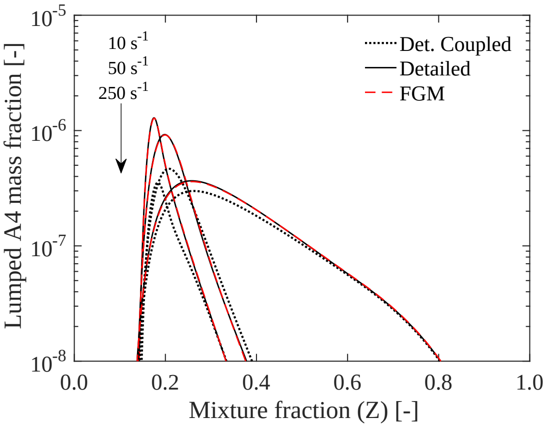

Figure 6.15 – Comparison of soot modelling between FGM and detailed simulations neglecting flame curvature for the lumped $A4$.

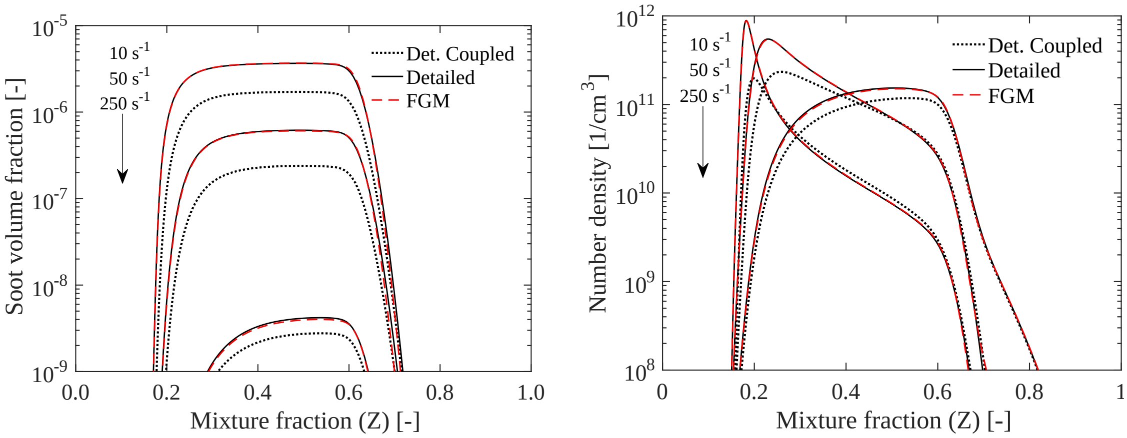

Figure 6.16 – Comparison of soot modelling between FGM and detailed simulations neglecting flame curvature for soot quantities.

predicts the H (principally) and OH mass fraction with a relatively good agreement. One should note, however, that the major concentration of these species is restricted to a very narrow space ($0.1 \lesssim Z \lesssim 0.2$) in the vicinity of the flame sheet and are, therefore, slightly affected by curvature. The comparison for the C_2H_2 mass fraction profile reveals the FGM tends to capture the flat flame profile for all curvature profiles, but with a increased discrepancy at high mixture fraction values with the increase of curvature magnitude. For the PAHs, represented by the $A4$ mass fraction, the FGM technique completely fails in predicting the curvature effects. In fact, the opposite behavior is observed respective to the curvature induced flux and the species lewis number. Taking the negative curvature as example, the FGM technique predicted a $A4$ ($Le = 4.0$) flux towards higher mixture

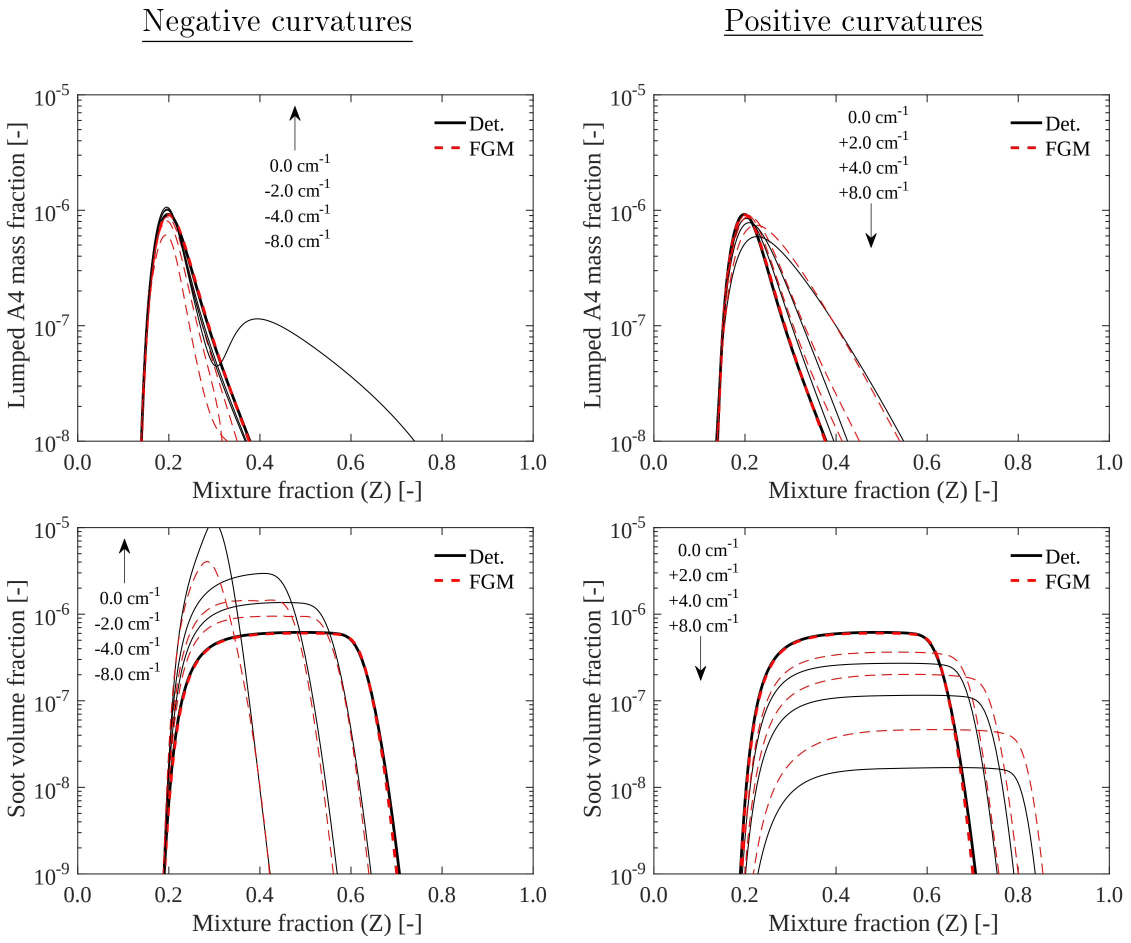

Figure 6.17 – Comparison between FGM and detailed simulations for soot the lumped $A4$ for a wide range of curvatures at the strain rate of 50 s^{-1}.

fraction instead enhancing it towards lower mixture fractions. It should be clear that, the $A4$ mass fraction stands for the direct solution by the gas-phase chemistry (detailed simulation) and direct retrieval from the manifold (FGM) simulations. It is not the solution of the lumped (transported) $A4$ mass fraction.

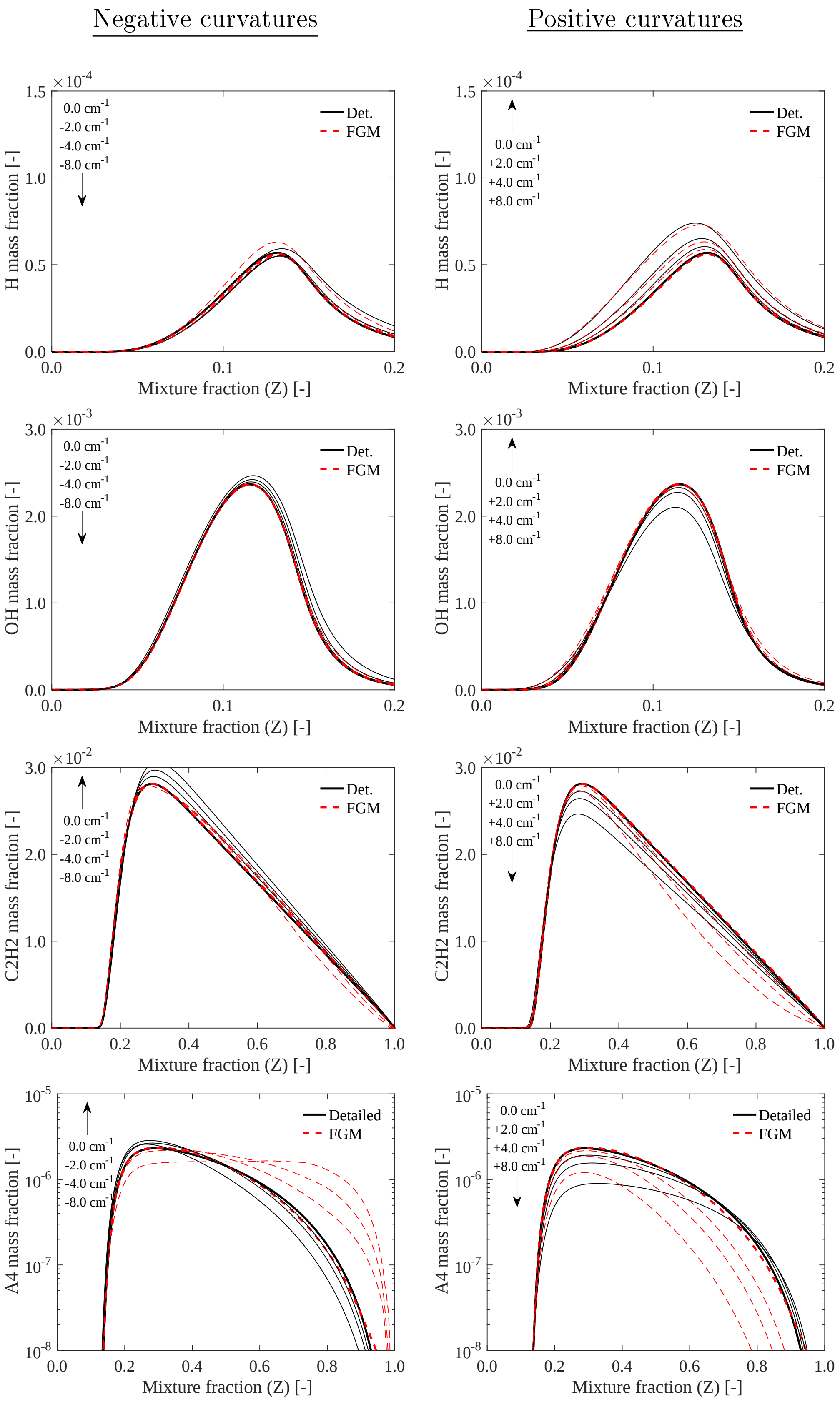

Figure 6.18 – Comparison between FGM and detailed simulations for several chemical species for a wide range of curvatures at the strain rate of 50 s^{-1}.

The location of the flamelets in the manifold is depicted in Figure 6.19. It can be seen that FGM solutions of $\mathcal{Y}$, for imposed curvatures, significantly deviate from the reconstructed detailed results in the range of $0.15 \lesssim Z \lesssim 0.85$. The thermo-chemical composition space do not reproduce the physics of the curved flamelets in that range, although the detailed results for $\mathcal{Y}$ lies inside the manifold, leading to a erroneous solution of the progress variable and further flame reconstruction. As exemplified by the temperature and the $A4$ source term fields, very distinct solution would be obtained from the FGM simulations. The solution of lumped $A4$ are less affected by the manifold formed by flat flames since the peaks of $A4$ production and consumption used in Equation 6.13 and 6.14 are located on $Z \lesssim 0.15$.

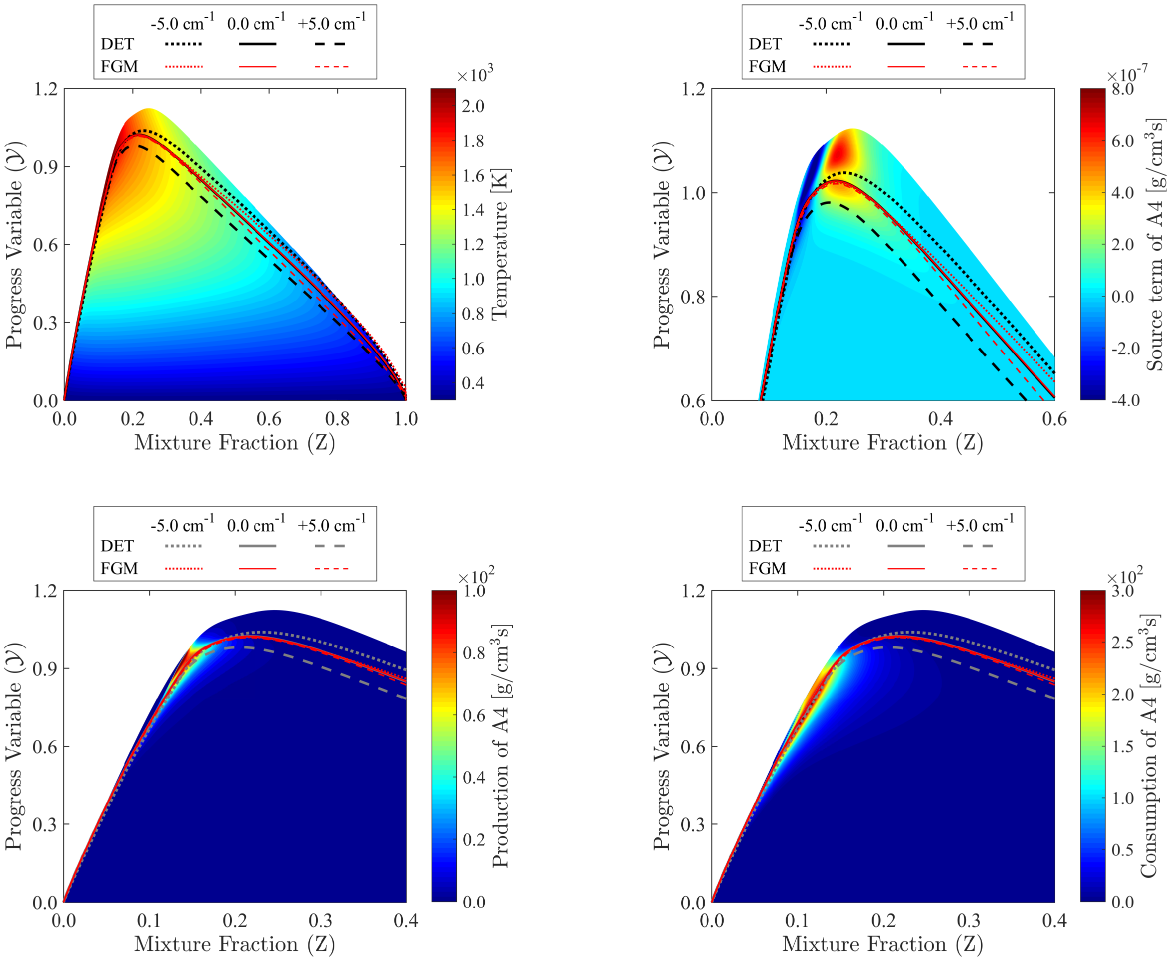

Figure 6.19 – Contours of temperature, $A4$ source term and $A4$ production and consumption rates stored in the manifold, including $\mathcal{Y}$ results from FGM and detailed simulations for curved flamelets.

These results make clear the necessity of extending the current manifold to properly take into account curvature effects. Curvature effects predictions by the FGM technique might be enhanced by simulating detailed flamelets over several amounts of curvatures and tabulating their solutions as function of an additional control variable, leading to an extra dimension to the manifold. That variable could be a scalar with the same diffusion coefficient of H, so that it would map the high diffusive species in the mixture. In a similar way the manifold can also be extended even further by including a model for the tangential diffusion terms in the flamelet calculations.

6.5 Conclusions

A numerical investigation was conducted in order to gain insights about the soot formation modelling with the Flamelet-Generated Manifold (FGM) technique by studying laminar counterflow ethylene non-premixed flames under oxygen enriched and oxyfuel conditions. The influence of the transport properties, the coupling between the soot model and the flamelet technique and the flame curvature effects were explored in one-dimensional simulations with detailed chemistry. Then, the capabilities of the FGM in modelling soot formation were evaluated. Soot formation is accounted for with a detailed Sectional Method accounting for the nucleation, condensation, surface growth and oxidation and coagulation processes.

Detailed one-dimensional simulations ratified the importance of preferential diffusion for predictions of soot formations in laminar flames. Neglecting differential diffusion effects reduces the concentration of larger PAHs (which are recognized as soot precursors) and acetylene (the main surface growth species), therefore, drastically under-predicting the soot volume fractions. The assumption of simplified (polynomial) mixture's conductivity and viscosity instead of mixture averaged properties only slightly affected the soot formation in the current flames.

Two different precursors treatments were examined for modelling the link between the gas- and the solid-phase for uncoupled simulations and compared to a fully coupled case, mimicking the context of FGM simulations. One approach assumed that the soot precursor is in the steady-state. Whereas this assumption is qualitatively valid for lower strain rates, discrepancies became more evident with the increase in the strain-rate. The other approach assumed the solution of lumped PAHs acting as a link between the gas-and the solid-phases. This latter approach, predicted much better the chemical time-scales of the precursor formation and, consequently, the soot volume fraction. Even so, small discrepancies to the fully coupled case were still present since the precursor consumption by the soot formation processes do not interfere in the chemical species pool.

The curvature effect on flame structure is analyzed for the reference and the oxyfuel. Negative curvatures enhances the mass flux of species with $Le > 1$ towards leaner mixture fractions values and the mass flux of species with $Le < 1$ towards richer mixture fractions values. It leads to increased concentration of larger PAHs (such as the $A4$) and C_2H_2 in regions relevant to soot formation. For negative curvatures, soot particles move towards leaner mixtures and higher soot volume fraction is found due to enhanced nucleation and surface growth. The exact opposite occurs for positive curvatures, where lower concentration of species related to the soot formation are found. Besides the strong CO_2 effect, no big differences were observed between the reference and the oxyfuel flames respective to the curvature effects on the soot formation.

Following the *a priori* analysis, one-dimension FGM simulations were performed together with the detailed soot sectional method for the oxyfuel flame. The thermochemical manifold was constructed considering preferential diffusion effects but neglecting curvature effects. The results indicated that the FGM technique with a suitable progress variable is able to correctly predict soot formation (f_v profile, rates of formation and the particle size distribution) over a wide range of strain rates for flat flames. The same manifold was further employed for FGM simulations of curved flames. In this case, it was found that the FGM technique can partially reproduce the behavior of the soot volume fraction with the change in flame curvature. The displacement of soot particles was qualitatively captured by the technique, however, the maximum soot volume fraction was under-predicted for negative curvatures and over-predicted by positive curvatures. Those differences were enhanced with the increase of the curvature magnitude. It is worth pointing out that the computational requirements of the FGM simulations were, in general, up to tree times lower than the detailed chemical kinetics approach for soot modeling and up to seventy times faster when only gas-phase was simulated. The difference in the computational requirements should be even higher for multidimensional simulations.

7 CONCLUDING REMARKS

Soot particles derived from combustion processes has adverse influence on human health and climate change. To reduce the formation of soot particles is of great concern for the academic and industry communities. Furthermore, besides CO_2 being one of the main combustion products, high amounts of CO_2 are present in combustion technologies such as oxyfuel flames due to flue-gas recirculation, which is employed to enhance thermal radiation heat transfer and to reduce NO_X emissions. Both experimental and numerical studies evidenced that CO_2 addition suppresses soot formation by transport, chemical the thermodynamic effects. However, the different factors acting on this suppression are not fully understood yet.

In this thesis, a detailed soot and thermal radiation models were implemented to investigate the mechanisms of soot suppression due to CO_2 addition. Numerical studies were conducted for one-dimensional non-premixed counterflow ethylene flames burning under oxygen-enriched atmospheres. The detail Sectional Soot model considers chemical and physical phenomenological soot formation process to describe the evolution of poly-dispersed soot particles. The thermal radiation models account for the line-by-line (LBL) and the superposition weighted-sum-of-gray-gases (WSGG) for the spectral integration of the radiative properties of a medium formed by CO_2, H_2O and soot. The spatial integration of the radiation intensities is computed by the discrete ordinates method (DOM).

In Chapter 4, the framework for the study of soot formation was validated and the effects of CO_2 addition on soot suppression were investigated. The framework was validated for counterflow flames with soot predictions in a reasonable agreement with measurements and simulations data from literature. In general, the model qualitatively captures the effects of CO_2 addition on soot formation processes. It is known that chemical and thermodynamic factors influence the soot formation processes, but those effects differs when CO_2 is added to the fuel (SF case) or to the oxidizer mixtures (SO case). For a fair comparison, a methodology that assumes the same CO_2 amount at stoichiometric conditions was considered (ESO case). In accordance with the literature, it was found that CO_2 suppresses the formation of large PAHs by reducing principally the formation of H-radical, acetylene (C_2H_2) and benzene ($A1$) which are the main building blocks of large aromatic species. Acetylene and benzene concentration are reduced by depletion of the CH_2^* radicals promoted by the CO_2 addition. The overall chemical effect of CO_2 addition is due to its direct influence on reaction $CO + OH \rightleftharpoons CO_2 + H$. For the same amount of CO_2 in the reaction layer, it was found a more expressive suppression of the aforementioned species concentrations when CO_2 was added to the fuel mixture. Moreover, for the same amount of CO_2 in the reaction layer, it was also found that while chemical effects played a major role on the formation of C_2H_2, C_3H_3 and PAHs for the CO_2 addition on the oxidizer side, both chemical and thermophysical effects were important for CO_2 addition on the fuel side. In both cases, the temperature profile was mainly influenced by thermophysical effects while the soot volume fraction was mainly influenced by chemical effects. As consequence, the main suppression of soot formation is due to reduction on nucleation and surface growth processes. In those simulations, the particle-size distribution reveled to be strongly bimodal and slightly sensitive on the CO_2 addition for the current flames.

In Chapter 5, the WSGG thermal radiation model was verified against the LBL integration method and radiated heat losses by soot and gas-phase were investigated for the same flames explored in Chapter 4. One novelty introduced in this work was that the one-dimension counterflow flame allows the LBL spectral integration to be simultaneously solved with complex chemistry and detailed soot formation models for a wide range of conditions. Results showed that the spectral superposition WSGG model was able to accurately describe general flame structure and soot predictions relative to the LBL integration model. However, small discrepancies were found for the radiative flux, and consequently, for the radiative source term. For the flames with CO_2 addition, the WSGG model tended to overestimate the radiation emission at high temperature regions and to overestimate the radiation absorption at low temperatures towards the reactant with CO_2 addition. The importance of thermal radiation reabsoption was also determined and it was shown the increasing importance of radiation reabsorption with CO_2 addition. Expressive reductions of soot volume fraction were obtained for the SF and the SO cases at maximum CO_2 addition and these reduction was enhanced for thermal radiation models neglecting radiation reabsorption. The evaluation of the dimensionless coefficient of the soot spectral radiation reveled a major influence in the soot volume fraction only for low levels of CO_2 addition. The soot radiation contribution for the SO flame becomes much lower since the CO_2 concentration is much higher in this flame, leading to an increased soot suppression.

Moving toward higher computational efficiency of soot modelling in Chapter 6, the Flamelet-Generated Manifold technique was explored for one-dimensional non-premixed ethylene oxyfuel flames, in the counterflow configuration.

First, the influence of several assumptions frequently adopted on flamelet formalism for soot modelling were evaluated. To achieve that goal, the influence of preferential diffusion, the modelling of slow species as PAHs that acts as soot precursors (forming the link between gas- and the solid-phases) and the impact of flame curvature of soot formation were investigated for detailed one-dimensional flames. PAHs formation and growth are strongly dependent on preferential diffusion effects and, consequently, soot formation processes are also affected. The assumption of unity Lewis number for all species lead to a significant reduction (up to two orders of magnitude) on the maximum soot volume fraction, whereas simplified (polynomial expressions) mixture conductivity and viscosity models played only a secondary role. Several authors showed the importance of flame curvature on multidimensional flames, but only few work explored its effects on soot formation. Moreover, flame curvature is usually neglected on flamelet tabulation methodologies. Therefore, a fundamental study of the flame curvature effects on the soot formation processes was also conducted for the one-dimensional framework. For negative curvatures, soot particles move towards leaner mixtures and higher soot volume fractions were found due to enhanced nucleation and surface growth (principally by surface reaction with C_2H_2). The opposite trend occurred for positive curvatures.

Finally, adiabatic FGM simulations were conducted for modelling soot formation by the Discrete Sectional Method. Tabulations were performed based on the mixture fraction and the progress variable assuming solely flat flames (zero flame curvature). The results demonstrated that differential diffusion effects were captured by the FGM with a good agreement with the full chemistry solution for the overall flame structure for one-dimensional flat flames over a wide range of strain rates. The technique captured the detailed PAHs chemistry up to pyrene by direct retrieval from the manifold, i.e., with no need to solve additional transport equations for those PAH species. Despite that, a sub-mechanism for a lumped A4 was considered to accounts for the mass transfer from the gas- to the solid-phase during the nucleation and condensation processes. For flat flames (zero curvature) the FGM technique was able to quantitatively capture the soot formation compared to detailed chemistry simulations when both approaches assumed the lumped PAH model. However, significant discrepancies exit when they are compared to the fully coupled solid-gas model, indicating that the lumped A4 approach is not able to completely capture all the chemical scales of production and consumption of large PAHs. On the other hand, curvature effects on soot formation and related species were only qualitatively captured considering a manifold created solely by flat flamelets. Improvements could be obtained by expanding the current manifold to take into account those effects. One of the main advantages is that the computational time of FGM simulations was up to tree times lower than detailed chemical kinetics simulations for soot modeling. When only gas-phase was solved, the FGM was up to seventy times faster. The difference in the computational requirements should be even higher for multidimensional simulations.

7.1 Future recommendations

Several improvement could be done for both the soot and thermal radiation models. The formation of particles aggregates need to be included in the soot model. It is well known that particles with diameter $\gtrsim$ 30 nm starts to agglomerate. The formation of fractal aggregates with appropriate collision efficiency would lead to a better prediction of soot properties such as number density and average particle diameter. The inclusion of multiple PAHs dimmerization for the formation of the first particles and the condensation of those multiple PAHs onto soot surface would make the model more in line with physical processes observed experimentally. These improvements could be followed by the assumption of more recent steric factor expressions, what would better capture the number of surface radical sites available to carbon deposition. In terms of thermal radiation, the flames studied in this work could be used to the development of new WSGG coefficients for both the standard (fixed ratio of CO_2/H_2O) and the superposition method. The inclusion of CO as participating species for the superposition WSGG and the LBL would be interesting for flames with high CO_2 concentration owing the conversion reactions between $CO_2 \rightleftharpoons CO$.

The effects of CO_2 addition on the soot formation process were investigated for soot formation counterflow flames. It would be interesting to conduct those studies also for soot formation/oxidation counterflow flames. Those flames presents a high stoichiometric mixture fraction and peak temperature, which enhances the soot formation locally. Since soot particles are formed in the fuel side, they are convected towards the stagnation plane trough a high oxidation region. Therefore, it would allow to investigate the effects of CO_2 addition on a environment more favorable to soot oxidation. Nonetheless, the present soot model should be first validated for formation/oxidation flames. It would be worthwhile to incorporate the updated soot model into a coflow diffusion flame code to test how the model performs under this different environment. Although the soot model is verified against experimental data of several counterflow flames, to conduct experiments for the flames studied in this work would be useful for future soot modellings.

In this thesis, the coupling of the FGM technique with the soot model was investigated at adiabatic conditions. Implementing heat losses into the FGM method is important to model both counterflow flames at lower strain rates or multi-dimensional coflow flames. Moreover, the modelling of soot formation with the FGM technique could be improved by identifying additional important routes for the growth of larger PAHs and by including the related species into the lumped PAH sub-mechanism. Curvature effects could also be evaluated by including this effects into the manifold.

BIBLIOGRAPHY

Combustion Generated Fine Carbonaceous Particles, chapter 1: The role of soot in the health effects of inhaled airborne particles. Karlsruhe University Press, 2009.

Abid, A. D., Camacho, J., Sheen, D. A., and Wang, H. Quantitative measurement of soot particle size distribution in premixed flames – The burner-stabilized stagnation flame approach, **Combustion and Flame**, vol. 156, p. 1862–1870, 2009.

Abid, A. D., Heinz, N., Tolmachoff, E. D., Phares, D. J., Campbell, C. S., and Wang, H. On evolution of particle size distribution functions of incipient soot in premixed ethylene–oxygen–argon flames, **Combustion and Flame**, vol. 154, p. 775–788, 2008.

Adkins, E. M. and Miller, J. H. Extinction measurements for optical band gap determination of soot in a series of nitrogen-diluted ethylene/air non-premixed flames, **Physical Chemistry Chemical Physics**, vol. 17, p. 2686–2695, 2015.

Appel, J., Bockhorn, H., and Frenklach, M. Kinetic modeling of soot formation with detailed chemistry and physics: laminar premixed flames of C2 hydrocarbons, **Combustion and Flame**, vol. 121, p. 122–136, 2000.

Aubagnac-Karkar, D., Bakali, A. E., and Desgroux, P. Soot particles inception and PAH condensation modelling applied in a soot model utilizing a sectional method, **Combustion and Flame**, vol. 189, p. 190–206, 2018.

Aubagnac-Karkar, D., Michel, J.-B., Colin, O., Vervisch-Kljakic, P. E., and Darabiha, N. Sectional soot model coupled to tabulated chemistry for Diesel RANS simulations, **Combustion and Flame**, vol. 162, p. 3081–3099, 2015.

Axelbaum, R. L., Flower, W. L., and Law, C. K. Dilution and Temperature Effects of Inert Addition on Soot Formation in Counterflow Diffusion Flames, **Combustion Science and Technology**, vol. 61, p. 51–73, 1988.

Bai, X., Balthasar, M., Mauss, F., and Fuchs, L. Detailed soot modeling in turbulent jet diffusion flames, **Symposium (International) on Combustion**, vol. 27, p. 1623–1630, 1998.

Balthasar, M., Heyl, A., MauÃŸ, F., Schmitt, F., and Bockhorn, H. Flamelet modeling of soot formation in laminar ethyne/air-diffusion flames, **Symposium (International) on Combustion**, vol. 26, p. 2369–2377, 1996.

Balthasar, M. and Kraft, M. A stochastic approach to calculate the particle size distribution function of soot particles in laminar premixed flames, **Combustion and Flame**, vol. 133, p. 289–298, 2003.

Barlow, R., editor. **International Workshop on Measurement and Computation of Turbulent Nonpremixed Flames (TNF),**. Sandia National Laboratories, 2020.

Barths, H., Peters, N., Brehm, N., Mack, A., Pfitzner, M., and Smiljanovski, V. Simulation of pollutant formation in a gas-turbine combustor using unsteady flamelets, **Symposium (International) on Combustion**, vol. 27, p. 1841–1847, 1998.

Baukal Jr, C. E. **Oxygen-enhanced combustion**. CRC press, 2010.

Bedir, H., T'ien, J., and Lee, H. Comparison of different radiation treatments for a one-dimensional diffusion flame, **Combustion Theory and Modelling**, vol. 1, p. 395–404, 1997.

Bhatt, J. and Lindstedt, R. Analysis of the impact of agglomeration and surface chemistry models on soot formation and oxidation, **Proceedings of the Combustion Institute**, vol. 32, p. 713–720, 2009.

Bilger, R., Starner, S., and Kee, R. On reduced mechanisms for methane—¸air combustion in nonpremixed flames, **Combustion and Flame**, vol. 80(2), p. 135 – 149, 1990.

Bisetti, F., Blanquart, G., Mueller, M. E., and Pitsch, H. On the formation and early evolution of soot in turbulent nonpremixed flames, **Combustion and Flame**, vol. 159, p. 317–335, 2012.

Blacha, T., Domenico, M. D., Gerlinger, P., and Aigner, M. Soot predictions in premixed and non-premixed laminar flames using a sectional approach for PAHs and soot, **Combustion and Flame**, vol. 159, p. 181–193, 2012.

Blanquart, G., Pepiot-Desjardins, P., and Pitsch, H. Chemical mechanism for high temperature combustion of engine relevant fuels with emphasis on soot precursors, **Combustion and Flame**, vol. 156(3), p. 588–607, 2009.

Blanquart, G. and Pitsch, H. Analyzing the effects of temperature on soot formation with a joint volume-surface-hydrogen model, **Combustion and Flame**, vol. 156(8), p. 1614 – 1626, 2009.

Boot-Handford, M. E., Abanades, J. C., Anthony, E. J., Blunt, M. J., Brandani, S., Mac Dowell, N., Fernández, J. R., Ferrari, M.-C., Gross, R., Hallett, J. P., Haszeldine, R. S., Heptonstall, P., Lyngfelt, A., Makuch, Z., Mangano, E., Porter, R. T. J., Pourkashanian, M., Rochelle, G. T., Shah, N., Yao, J. G., and Fennell, P. S. Carbon capture and storage update, **Energy Environmental Science**, vol. 7, p. 130–189, 2014.

Bordbar, M. H., Węcel, G., and Hyppänen, T. A line by line based weighted sum of gray gases model for inhomogeneous CO2–H2O mixture in oxy-fired combustion, **Combustion and Flame**, vol. 161(9), p. 2435–2445, 2014.

Buckius, R. and Tien, C. Infrared flame radiation, **International Journal of Heat and Mass Transfer**, vol. 20, p. 93–106, 1977.

Carbone, F., Cattaneo, F., and Gomez, A. Structure of incipiently sooting partially premixed ethylene counterflow flames, **Combustion and Flame**, vol. 162(11), p. 4138 – 4148, 2015.

Carbonell, D., Perez-Segarra, C., Coelho, P., and Oliva, A. Flamelet mathematical models for non-premixed laminar combustion, **Combustion and Flame**, vol. 156, p. 334–347, 2009.

Cassol, F., Brittes, R., Centeno, F. R., da Silva, C. V., and França, F. H. R. Evaluation of the gray gas model to compute radiative transfer in non-isothermal, non-homogeneous participating medium containing CO2, H2O and soot, **Journal of the Brazilian Society of Mechanical Sciences and Engineering**, vol. 37, p. 163–172, 2015.

Cassol, F., Brittes, R., França, F. H., and Ezekoye, O. A. Application of the weighted-sum-of-gray-gases model for media composed of arbitrary concentrations of H2O, CO2 and soot, **International Journal of Heat and Mass Transfer**, vol. 79, p. 796–806, 2014.

Centeno, F. R., Brittes, R., França, F. H., and da Silva, C. V. Application of the WSGG model for the calculation of gas–soot radiation in a turbulent non-premixed methane–air flame inside a cylindrical combustion chamber, **International Journal of Heat and Mass Transfer**, vol. 93, p. 742–753, 2016.

Centeno, F. R., Brittes, R., França, F. H., and Ezekoye, O. A. Evaluation of gas radiation heat transfer in a 2D axisymmetric geometry using the line-by-line integration and WSGG models, **Journal of Quantitative Spectroscopy and Radiative Transfer**, vol. 156, p. 1–11, 2015.

Centeno, F. R., Brittes, R., Rodrigues, L. G., Coelho, F. R., and França, F. H. Evaluation of the WSGG model against line-by-line calculation of thermal radiation in a non-gray sooting medium representing an axisymmetric laminar jet flame, **International Journal of Heat and Mass Transfer**, vol. 124, p. 475–483, 2018.

Centeno, F. R., da Silva, C. V., and França, F. H. The influence of gas radiation on the thermal behavior of a 2D-axisymmetric turbulent non-premixed methane-air flame, **Energy Conversion and Management**, vol. 79, p. 405–414, 2014.

Charest, M. R., Ömer L. Gülder, and Groth, C. P. Numerical and experimental study of soot formation in laminar diffusion flames burning simulated biogas fuels at elevated pressures, **Combustion and Flame**, vol. 161, p. 2678–2691, 2014.

Chen, J. Y., Liu, Y., and Rogg, B., **CO-H2-N2/Air Diffusion Flames: Thermal Radiation and Transient Effects**, pages 196–223. Springer Berlin Heidelberg, Berlin, Heidelberg, 1993.

Chernov, V., Thomson, M. J., Dworkin, S. B., Slavinskaya, N. A., and Riedel, U. Soot formation with C1 and C2 fuels using an improved chemical mechanism for PAH growth, **Combustion and Flame**, vol. 161, p. 592–601, 2014.

chia Chang, H. and Charalampopoulos, T. T. Determination of the wavelength dependence of refractive indices of flame soot, **Proceedings of the Royal Society of London. Series A: Mathematical and Physical Sciences**, vol. 430, p. 577–591, 1990.

Chippett, S. and Gray, W. The size and optical properties of soot particles, **Combustion and Flame**, vol. 31, p. 149–159, 1978.

Choi, B., Choi, S., Chung, S., Kim, J., and Choi, J. Experimental and numerical investigation of fuel mixing effects on soot structures in counterflow diffusion flames, **International Journal of Automotive Technology**, vol. 12, p. 183, 2011.

Chu, H., Consalvi, J.-L., Gu, M., and Liu, F. Calculations of radiative heat transfer in an axisymmetric jet diffusion flame at elevated pressures using different gas radiation models, **Journal of Quantitative Spectroscopy and Radiative Transfer**, vol. 197, p. 12–25, 2017.

Chung, S.-H. and Violi, A. Peri-condensed aromatics with aliphatic chains as key intermediates for the nucleation of aromatic hydrocarbons, **Proceedings of the Combustion Institute**, vol. 33, p. 693**700, 2011.

Coelho, F. R. and França, F. H. WSGG correlations based on HITEMP2010 for gas mixtures of H2O and CO2 in high total pressure conditions, **International Journal of Heat and Mass Transfer**, vol. 127, p. 105–114, 2018.

D'Alessio, A., Barone, A., Cau, R., D'Anna, A., and Minutolo, P. Surface deposition and coagulation efficiency of combustion generated nanoparticles in the size range from 1 to 10 nm, **Proceedings of the Combustion Institute**, vol. 30(2), p. 2595–2603, 2005.

D'Anna, A. and Kent, J. A model of particulate and species formation applied to laminar, nonpremixed flames for three aliphatic-hydrocarbon fuels, **Combustion and Flame**, vol. 152, p. 573–587, 2008.

de Goey, L., Mallens, R., and Boonkkamp, J. T. T. An evaluation of different contributions to flame stretch for stationary premixed flames, **Combustion and Flame**, vol. 110(1), p. 54–66, 1997.

de Goey, L. and ten Thije Boonkkamp, J. A flamelet description of premixed laminar flames and the relation with flame stretch, **Combustion and Flame**, vol. 119, p. 253–271, 1999a.

de Goey, L. and ten Thije Boonkkamp, J. A flamelet description of premixed laminar flames and the relation with flame stretch, **Combustion and Flame**, vol. 119, p. 253–271, 1999b.

de Goey, L. P. H. and ten Thije Boonkkamp, J. H. M. A Mass-Based Definition of Flame Stretch for Flames with Finite Thickness, **Combustion Science and Technology**, vol. 122, p. 399–405, 1997.

de Swart, J. A. M., Bastiaans, R. J. M., van Oijen, J. A., de Goey, L. P. H., and Cant, R. S. Inclusion of Preferential Diffusion in Simulations of Premixed Combustion of Hydrogen/Methane Mixtures with Flamelet Generated Manifolds, **Flow, Turbulence and Combustion**, vol. 85(3), p. 473–511, 2010.

Demarco, R., Nmira, F., and Consalvi, J. Influence of thermal radiation on soot production in laminar axisymmetric diffusion flames, **Journal of Quantitative Spectroscopy and Radiative Transfer**, vol. 120, p. 52–69, 2013.

Dixon-Lewis, G. Structure of laminar flames, **Symposium (International) on Combustion**, vol. 23, p. 305–324, 1991.

Dobbins, R., Fletcher, R., and Chang, H. The evolution of soot precursor particles in a diffusion flame, **Combustion and Flame**, vol. 115(3), p. 285–298, 1998.

Donini, A., Bastiaans, R., van Oijen, J., and de Goey, L. Differential diffusion effects inclusion with flamelet generated manifold for the modeling of stratified premixed cooled flames, **Proceedings of the Combustion Institute**, vol. 35, p. 831–837, 2015.

Dorigon, L. J., Duciak, G., Brittes, R., Cassol, F., Galarça, M., and França, F. H. WSGG correlations based on HITEMP2010 for computation of thermal radiation in non-isothermal, non-homogeneous H2O/CO2 mixtures, **International Journal of Heat and Mass Transfer**, vol. 64, p. 863–873, 2013.

Du, D., Axelbaum, R., and Law, C. The influence of carbon dioxide and oxygen as additives on soot formation in diffusion flames, **Symposium (International) on Combustion**, vol. 23, p. 1501–1507, 1991.

Dworkin, S., Smooke, M., and Giovangigli, V. The impact of detailed multicomponent transport and thermal diffusion effects on soot formation in ethylene/air flames, **Proceedings of the Combustion Institute**, vol. 32, p. 1165–1172, 2009.

Dworkin, S. B., Zhang, Q., Thomson, M. J., Slavinskaya, N. A., and Riedel, U. Application of an enhanced PAH growth model to soot formation in a laminar coflow ethylene/air diffusion flame, **Combustion and Flame**, vol. 158, p. 1682–1695, 2011.

Eaves, N., Dworkin, S., and Thomson, M. The importance of reversibility in modeling soot nucleation and condensation processes, **Proceedings of the Combustion Institute**, vol. 35, p. 1787–1794, 2015.

Eaves, N. A., Dworkin, S. B., and Thomson, M. J. Assessing relative contributions of PAHs to soot mass by reversible heterogeneous nucleation and condensation, **Proceedings of the Combustion Institute**, vol. 36, p. 935–945, 2017.

Eaves, N. A., Zhang, Q., Liu, F., Guo, H., Dworkin, S. B., and Thomson, M. J. CoFlame: A refined and validated numerical algorithm for modeling sooting laminar coflow diffusion flames, **Computer Physics Communications**, vol. 207, p. 464–477, 2016.

Elvati, P. and Violi, A. Thermodynamics of poly-aromatic hydrocarbon clustering and the effects of substituted aliphatic chains, **Proceedings of the Combustion Institute**, vol. 34, p. 1837–1843, 2013.

EPE. **Brazilian Energy Balance 2016 year 2015**. Empresa de Pesquisa Energética, 2016.

Escudero, F., Fuentes, A., Consalvi, J.-L., Liu, F., and Demarco, R. Unified behavior of soot production and radiative heat transfer in ethylene, propane and butane axisymmetric laminar diffusion flames at different oxygen indices, **Fuel**, vol. 183, p. 668–679, 2016.

Franzelli, B., Cuoci, A., Stagni, A., Ihme, M., Faravelli, T., and Candel, S. Numerical investigation of soot-flame-vortex interaction, **Proceedings of the Combustion Institute**, vol. 36, p. 753–761, 2017.

Frenklach, M. Method of moments with interpolative closure, **Chemical Engineering Science**, vol. 57, p. 2229–2239, 2002a.

Frenklach, M. Reaction mechanism of soot formation in flames, **Physical Chemistry Chemical Physics**, vol. 4, p. 2028–2037, 2002b.

Frenklach, M. New form for reduced modeling of soot oxidation: Accounting for multi-site kinetics and surface reactivity, **Combustion and Flame**, vol. 201, p. 148–159, 2019.

Frenklach, M., Liu, Z., Singh, R. I., Galimova, G. R., Azyazov, V. N., and Mebel, A. M. Detailed, sterically-resolved modeling of soot oxidation: Role of O atoms, interplay with particle nanostructure, and emergence of inner particle burning, **Combustion and Flame**, vol. 188, p. 284–306, 2018.

Frenklach, M. and Wang, H. Twenty-Third Symposium (International) on Combustion Detailed modeling of soot particle nucleation and growth, **Symposium (International) on Combustion**, vol. 23, p. 1559–1566, 1991.

Frenklach, M. and Wang, H. **Detailed mechanism and modeling of soot particle formation**. In *Soot formation in combustion*, pages 165–192. Springer, 1994.

Friedlander, S. K. **Smoke, Dust and Haze: Fundamentals of aerosol dynamics**. Oxford University Press, second edition, 2000.

Gelbard, F., Tambour, Y., and Seinfeld, J. H. Sectional representations for simulating aerosol dynamics, **Journal of Colloid and Interface Science**, vol. 76, p. 541–556, 1980.

Gicquel, O., Darabiha, N., and Thévenin, D. Laminar premixed hydrogen/air counterflow flame simulations using flame prolongation of ILDM with differential diffusion, **Proceedings of the Combustion Institute**, vol. 28, p. 1901–1908, 2000.

Gierth, S., Hunger, F., Popp, S., Wu, H., Ihme, M., and Hasse, C. Assessment of differential diffusion effects in flamelet modeling of oxy-fuel flames, **Combustion and Flame**, vol. 197, p. 134–144, 2018.

Gu, M., Chu, H., and Liu, F. Effects of simultaneous hydrogen enrichment and carbon dioxide dilution of fuel on soot formation in an axisymmetric coflow laminar ethylene/air diffusion flame, **Combustion and Flame**, vol. 166, p. 216–228, 2016.

Guo, H. and Smallwood, G. J. A Numerical Study on the Influence of CO2 Addition on Soot Formation in an Ethylene/Air Diffusion Flame, **Combustion Science and Technology**, vol. 180, p. 1695–1708, 2008.

Guo, H. and Smallwood, G. J. The effect of preferential diffusion on soot formation in a laminar ethylene/air diffusion flame, **Combustion Theory and Modelling**, vol. 15, p. 125–140, 2010.

Han, W., Scholtissek, A., and Hasse, C. The role of tangential diffusion in evaluating the performance of flamelet models, **Proceedings of the Combustion Institute**, vol. 37, p. 1767–1774, 2019.

Harris, S. J. and Kennedy, I. M. The coagulation of soot particles with van der Waals forces, **Combustion Science and Technology**, vol. 59, p. 443–454, 1988.

Hirschfelder, J., Curtiss, C., and Bird, R. **Molecular theory of gases and liquids**. volume 26. Wiley New York, 1954.

Hoerlle, C., Zimmer, L., and Pereira, F. Numerical study of CO2 effects on laminar non-premixed biogas flames employing a global kinetic mechanism and the Flamelet-Generated Manifold technique, **Fuel**, vol. 203, p. 671–685, 2017.

Hoerlle, C. A. and Pereira, F. M. Effects of CO2 addition on soot formation of ethylene non-premixed flames under oxygen enriched atmospheres, **Combustion and Flame**, vol. 203, p. 407–423, 2019.

Hosseini, S. E. and Wahid, M. A. Development of biogas combustion in combined heat and power generation, **Renewable and Sustainable Energy Reviews**, vol. 40, p. 868–875, 2014.

Hottel, H. C. and Sarofim, A. F. **Radiative Transfer (McGraw-Hill Series in Mechanical Engineering)**. McGraw-Hill, 1967.

Hwang, J. and Chung, S. Growth of soot particles in counterflow diffusion flames of ethylene, **Combustion and Flame**, vol. 125, p. 752–762, 2001.

Hwang, J., Lee, W., Kang, H., and Chung, S. Synergistic Effect of Ethylene–Propane Mixture on Soot Formation in Laminar Diffusion Flames, **Combustion and Flame**, vol. 114, p. 370–380, 1998.

IEA. **Key World Energy Statistics**. International Energy Agency, 2016.

Ihme, M. and Pitsch, H. Modeling of radiation and nitric oxide formation in turbulent nonpremixed flames using a flamelet/progress variable formulation, **Physics of Fluids**, vol. 20, p. 055110, 2008.

Ihme, M., Shunn, L., and Zhang, J. Regularization of reaction progress variable for application to flamelet-based combustion models, **Journal of Computational Physics**, vol. 231, p. 7715–7721, 2012.

Johansson, K. O., Dillstrom, T., Elvati, P., Campbell, M. F., Schrader, P. E., Popolan-Vaida, D. M., Richards-Henderson, N. K., Wilson, K. R., Violi, A., and Michelsen, H. A. Radical–radical reactions, pyrene nucleation, and incipient soot formation in combustion, **Proceedings of the Combustion Institute**, vol. 36, p. 799–806, 2017.

Johansson, K. O., Head-Gordon, M. P., Schrader, P. E., Wilson, K. R., and Michelsen, H. A. Resonance-stabilized hydrocarbon-radical chain reactions may explain soot inception and growth, **Science**, vol. 361, p. 997–1000, 2018.

Johansson, R., Leckner, B., Andersson, K., and Johnsson, F. Account for variations in the H2O to CO2 molar ratio when modelling gaseous radiative heat transfer with the weighted-sum-of-grey-gases model, **Combustion and Flame**, vol. 158, p. 893–901, 2011.

Kalvakala, K. C., Katta, V. R., and Aggarwal, S. K. Effects of oxygen-enrichment and fuel unsaturation on soot and NOx emissions in ethylene, propane, and propene flames, **Combustion and Flame**, vol. 187, p. 217–229, 2018.

Kangwanpongpan, T., França, F. H., da Silva, R. C., Schneider, P. S., and Krautz, H. J. New correlations for the weighted-sum-of-gray-gases model in oxy-fuel conditions based on HITEMP 2010 database, **International Journal of Heat and Mass Transfer**, vol. 55(25), p. 7419–7433, 2012.

Katta, V. R., Roquemore, W. M., Menon, A., Lee, S.-Y., Santoro, R. J., and Litzinger, T. A. Impact of soot on flame flicker, **Proceedings of the Combustion Institute**, vol. 32, p. 1343–1350, 2009.

Kazakov, A. and Frenklach, M. Dynamic modeling of soot particle coagulation and aggregation: implementation with the Method of Moments and application to high-pressure Laminar Premixed Flames, **Combustion and Flame**, vol. 114, p. 484–501, 1998.

Kennedy, I. Models of soot formation and oxidation, **Progress in Energy and Combustion Science**, vol. 23(2), p. 95–132, 1997.

Kennedy, I. M., Kollmann, W., and Chen, J.-Y. A model for soot formation in a laminar diffusion flame, **Combustion and Flame**, vol. 81, p. 73–85, 1990.

Kez, V., Liu, F., Consalvi, J., Ströhle, J., and Epple, B. A comprehensive evaluation of different radiation models in a gas turbine combustor under conditions of oxy-fuel combustion with dry recycle, **Journal of Quantitative Spectroscopy and Radiative Transfer**, vol. 172, p. 121–133, 2016.

Kholghy, M. R., Eaves, N. A., Veshkini, A., and Thomson, M. J. The role of reactive PAH dimerization in reducing soot nucleation reversibility, **Proceedings of the Combustion Institute**, vol. 37, p. 1003–1011, 2019.

Kholghy, M. R., Kelesidis, G. A., and Pratsinis, S. E. Reactive polycyclic aromatic hydrocarbon dimerization drives soot nucleation, **Physical Chemistry Chemical Physics.**, vol. 20, p. 10926–10938, 2018.

Kholghy, M. R., Veshkini, A., and Thomson, M. J. The core–shell internal nanostructure of soot – A criterion to model soot maturity, **Carbon**, vol. 100, p. 508–536, 2016.

Khosousi, A. and Dworkin, S. B. Detailed modelling of soot oxidation by O2 and OH in laminar diffusion flames, **Proceedings of the Combustion Institute**, vol. 35, p. 1903–1910, 2015a.

Khosousi, A. and Dworkin, S. B. Soot surface reactivity during surface growth and oxidation in laminar diffusion flames, **Combustion and Flame**, vol. 162, p. 4523–4532, 2015b.

Kim, K.-H., Jahan, S. A., Kabir, E., and Brown, R. J. A review of airborne polycyclic aromatic hydrocarbons (PAHs) and their human health effects, **Environment International**, vol. 60, p. 71–80, 2013.

Kim, T. and Kim, Y. Interactive transient flamelet modeling for soot formation and oxidation processes in laminar non-premixed jet flames, **Combustion and Flame**, vol. 162, p. 1660–1678, 2015.

Kortschik, C., Honnet, S., and Peters, N. Influence of curvature on the onset of autoignition in a corrugated counterflow mixing field, **Combustion and Flame**, vol. 142, p. 140–152, 2005.

Kumar, S. and Ramkrishna, D. On the solution of population balance equations by discretization — I. A fixed pivot technique, **Chemical Engineering Science**, vol. 51, p. 1311–1332, 1996.

Law, C. **Combustion Physics**. Cambridge University Press, 1st edition, 2006.

Lecocq, G., Poitou, D., Hernández, I., Duchaine, F., Riber, E., and Cuenot, B. A Methodology for Soot Prediction Including Thermal Radiation in Complex Industrial Burners, **Flow, Turbulence and Combustion**, vol. 92, p. 947–970, 2014.

Leung, K., Lindstedt, R., and Jones, W. A simplified reaction mechanism for soot formation in nonpremixed flames, **Combustion and Flame**, vol. 87, p. 289–305, 1991.

Li, X., Jia, L., Onishi, T., Grajetzki, P., Nakamura, H., Tezuka, T., Hasegawa, S., and Maruta, K. Study on stretch extinction limits of CH4/CO2 versus high temperature O2/CO2 counterflow non-premixed flames, **Combustion and Flame**, vol. 161, p. 1526–1536, 2014.

Lighty, J. S., Veranth, J. M., and Sarofim, A. F. Combustion Aerosols: Factors Governing Their Size and Composition and Implications to Human Health, **Journal of the Air & Waste Management Association**, vol. 50, p. 1565–1618, 2000.

Lignell, D. O., Chen, J. H., and Smith, P. J. Three-dimensional direct numerical simulation of soot formation and transport in a temporally evolving nonpremixed ethylene jet flame, **Combustion and Flame**, vol. 155, p. 316–333, 2008.

Liu, F., Guo, H., Smallwood, G. J., and Hafi, M. E. Effects of gas and soot radiation on soot formation in counterflow ethylene diffusion flames, **Journal of Quantitative Spectroscopy and Radiative Transfer**, vol. 84, p. 501–511, 2004.

Liu, F., Guo, H., Smallwood, G. J., and Ömer L Gülder. The chemical effects of carbon dioxide as an additive in an ethylene diffusion flame: implications for soot and NOx formation, **Combustion and Flame**, vol. 125, p. 778–787, 2001.

Liu, F., Guo, H., Smallwood, G. J., and Ömer L Gülder. Effects of gas and soot radiation on soot formation in a coflow laminar ethylene diffusion flame, **Journal of Quantitative Spectroscopy and Radiative Transfer**, vol. 73(2–5), p. 409 – 421, 2002.

Liu, F., Karataş, A. E., Ömer L. Gülder, and Gu, M. Numerical and experimental study of the influence of CO2 and N2 dilution on soot formation in laminar coflow C2H4/air diffusion flames at pressures between 5 and 20 atm, **Combustion and Flame**, vol. 162, p. 2231–2247, 2015.

Lou, C., Chen, X., Yan, W., Tian, Y., and Kumfer, B. M. Effect of stoichiometric mixture fraction on soot fraction and emission spectra with application to oxy-combustion, **Proceedings of the Combustion Institute**, vol. 37, p. 4571–4578, 2019.

Lowe, J. S., Lai, J. Y. W., Elvati, P., and Violi, A. Towards a predictive model for polycyclic aromatic hydrocarbon dimerization propensity, **Proceedings of the Combustion Institute**, vol. 35, p. 1827–1832, 2015.

Mansurov, Z. A. Soot Formation in Combustion Processes (Review), **Combustion, Explosion and Shock Waves**, vol. 41(6), p. 727, 2005.

Marchisio, D. L. and Fox, R. O. Solution of population balance equations using the Direct Quadrature Method of Moments, **Journal of Aerosol Science**, vol. 36, p. 43–73, 2005.

Maruta, K., Abe, K., Hasegawa, S., Maruyama, S., and Sato, J. Extinction characteristics of CH4/CO2 versus O2/CO2 counterflow non-premixed flames at elevated pressures up to 0.7 MPa, **Proceedings of the Combustion Institute**, vol. 31, p. 1223–1230, 2007.

Mathur, S., Tondon, P., and Saxena, S. Thermal conductivity of binary, ternary and quaternary mixtures of rare gases, **Molecular Physics**, vol. 12, p. 569–579, 1967.

Mauss, F., Netzell, K., and Lehtiniemi, H. Aspects of modeling soot formation in turbulent diffusion flames, **Combustion Science and Technology**, vol. 178, p. 1871–1885, 2006.

Mauss, F., Netzell, K., Marchal, C., and Moréac, G., **Combustion Generated Fine Carbonaceous Particles**, chapter 28: Modeling the soot particle size distribution functions using a detailed kinetic soot model and a sectional method. Karlsruhe University Press, 2009.

McGraw, R. Description of aerosol dynamics by the Quadrature Method of Moments, **Aerosol Science and Technology**, vol. 27, p. 255–265, 1997.

Mehta, R., Haworth, D., and Modest, M. An assessment of gas-phase reaction mechanisms and soot models for laminar atmospheric-pressure ethylene-air flames, **Proceedings of the Combustion Institute**, vol. 32, p. 1327–1334, 2009.

Menon, A. V., Lee, S.-Y., Linevsky, M. J., Litzinger, T. A., and Santoro, R. J. Addition of NO2 to a laminar premixed ethylene–air flame: Effect on soot formation, **Proceedings of the Combustion Institute**, vol. 31, p. 593–601, 2007.

Mercier, X., Carrivain, O., Irimiea, C., Faccinetto, A., and Therssen, E. Dimers of polycyclic aromatic hydrocarbons: the missing pieces in the soot formation process, **Physical Chemistry Chemical Physics.**, vol. 21, p. 8282–8294, 2019.

Modest, M. F. **Radiative heat transfer**. Academic press, 2th edition, 2003.

Modest, M. F. and Haworth, D. C., **Radiation Effects in Laminar Flames**, pages 85–98. Springer International Publishing, 2016a.

Modest, M. F. and Haworth, D. C., **Turbulence–Radiation Interactions in Atmospheric Pressure Turbulent Flames**, pages 111–136. Springer International Publishing, 2016b.

Morgan, N., Kraft, M., Balthasar, M., Wong, D., Frenklach, M., and Mitchell, P. Numerical simulations of soot aggregation in premixed laminar flames, **Proceedings of the Combustion Institute**, vol. 31, p. 693–700, 2007.

Mueller, M., Blanquart, G., and Pitsch, H. Hybrid Method of Moments for modeling soot formation and growth, **Combustion and Flame**, vol. 156, p. 1143–1155, 2009.

Mueller, M., Blanquart, G., and Pitsch, H. Modeling the oxidation-induced fragmentation of soot aggregates in laminar flames, **Proceedings of the Combustion Institute**, vol. 33, p. 667–674, 2011.

Mueller, M. E. and Pitsch, H. LES model for sooting turbulent nonpremixed flames, **Combustion and Flame**, vol. 159(6), p. 2166 – 2180, 2012.

Najafi-Yazdi, A., Cuenot, B., and Mongeau, L. Systematic definition of progress variables and Intrinsically Low-Dimensional, Flamelet Generated Manifolds for chemistry tabulation, **Combustion and Flame**, vol. 159, p. 1197–1204, 2012.

Naseri, A., Veshkini, A., and Thomson, M. J. Detailed modeling of CO2 addition effects on the evolution of soot particle size distribution functions in premixed laminar ethylene flames, **Combustion and Flame**, vol. 183, p. 75–87, 2017.

Nemitallah, M. A., Habib, M. A., Badr, H. M., Said, S. A., Jamal, A., Ben-Mansour, R., Mokheimer, E. M. A., and Mezghani, K. Oxy-fuel combustion technology: current status, applications, and trends, **International Journal of Energy Research**, vol. 41, p. 1670–1708, 2017.

Neoh, K., Howard, J., and Sarofim, A. **Soot oxidation in flames**. In *Particulate carbon: formation during combustion*, pages 261–282. Springer Science & Business Media, 1981.

Netzell, K., Lehtiniemi, H., and Mauss, F. Calculating the soot particle size distribution function in turbulent diffusion flames using a sectional method, **Proceedings of the Combustion Institute**, vol. 31, p. 667–674, 2007.

Niu, Y.-S., Vervisch, L., and Tao, P. D. An optimization-based approach to detailed chemistry tabulation: Automated progress variable definition, **Combustion and Flame**, vol. 160, p. 776–785, 2013.

Oh, K. C. and Shin, H. D. The effect of oxygen and carbon dioxide concentration on soot formation in non-premixed flames, **Fuel**, vol. 85, p. 615–624, 2006.

Olson, D., Pickens, J., and Gill, R. The effects of molecular structure on soot formation: II. Diffusion flames, **Combustion and Flame**, vol. 62, p. 43–60, 1985.

Ono, H., Dobashi, R., and Sakuraya, T. Thermophoretic velocity measurements of soot particles under a microgravity condition, **Proceedings of the Combustion Institute**, vol. 29, p. 2375–2382, 2002.

Orbegoso, E. M., da Silva, L. F. F., and Serfaty, R. Comparative study of thermal radiation properties models in turbulent non-premixed sooting combustion, **Numerical Heat Transfer, Part A: Applications**, vol. 69, p. 166–179, 2016.

Park, S. and Rogak, S. A novel fixed-sectional model for the formation and growth of aerosol agglomerates, **Journal of Aerosol Science**, vol. 35, p. 1385 – 1404, 2004.

Patterson, R. I. A. Convergence of Stochastic Particle Systems Undergoing Advection and Coagulation, **Stochastic Analysis and Applications**, vol. 31, p. 800–829, 2013.

Peters, N. Laminar diffusion flamelet models in non-premixed turbulent combustion, **Progress in Energy and Combustion Science**, vol. 10, p. 319–339, 1984.

Peters, N., editor. **Turbulent Combustiom**. Cambridge University Press UK, 2000.

Pierce, C. D. and Moin, P. Progress-Variable approach for large-eddy simulation of non-premixed turbulent combustion, **Journal of Fluid Mechanics**, vol. 504, p. 73–97, 2004.

Pitsch, H., Chen, M., and Peters, N. Unsteady flamelet modeling of turbulent hydrogen-air diffusion flames, **Symposium (International) on Combustion**, vol. 27, p. 1057–1064, 1998.

Pope, C. J. and Howard, J. B. Simultaneous Particle and Molecule Modeling (SPAMM): An Approach for Combining Sectional Aerosol Equations and Elementary Gas-Phase Reactions, **Aerosol Science and Technology**, vol. 27, p. 73–94, 1997.

Qi, C., Zheng, S., and Zhou, H. Calculations of thermal radiation transfer of C2H2 and C2H4 together with H2O, CO2, and CO in a one-dimensional enclosure using LBL and SNB models, **Journal of Quantitative Spectroscopy and Radiative Transfer**, vol. 197, p. 45–50, 2017.

Raj, A., Sander, M., Janardhanan, V., and Kraft, M. A study on the coagulation of polycyclic aromatic hydrocarbon clusters to determine their collision efficiency, **Combustion and Flame**, vol. 157, p. 523–534, 2010.

Rapacioli, M., Calvo, F., Joblin, C., Parneix, P., and Spiegelman, F. Vibrations and Thermodynamics of Clusters of Polycyclic Aromatic Hydrocarbon Molecules: The Role of Internal Modes, **The Journal of Physical Chemistry A**, vol. 111, p. 2999–3009, 2007.

Richter, H., Granata, S., Green, W. H., and Howard, J. B. Detailed modeling of PAH and soot formation in a laminar premixed benzene/oxygen/argon low-pressure flame, **Proceedings of the Combustion Institute**, vol. 30, p. 1397–1405, 2005.

Richter, H. and Howard, J. Formation of polycyclic aromatic hydrocarbons and their growth to soot - a review of chemical reaction pathways, **Progress in Energy and Combustion Science**, vol. 26, p. 565 – 608, 2000.

Rodrigues, L. G. P., Machado, I. M., Ziemniczak, A., Pereira, F. M., Pagot, P. R., and França, F. H. R. Comparisons between Numerical Simulations and Experimental Measurements of Radiative Heat Flux for a Series of CH4/N2 Diluted Laminar Non-Premixed Flames, **Combustion Science and Technology**, vol. 0, p. 1–22, 2019.

Rothman, L., Gordon, I., Barber, R., Dothe, H., Gamache, R., Goldman, A., Perevalov, V., Tashkun, S., and Tennyson, J. HITEMP, the high-temperature molecular spectroscopic database, **Journal of Quantitative Spectroscopy and Radiative Transfer**, vol. 111, p. 2139–2150, 2010.

Roy, S. P. **Aerosol-dynamics-based soot modeling of flames**. PhD thesis, The Pennsylvania State University, 2014.

Roy, S. P. and Haworth, D. C. A Systematic Comparison of Detailed Soot Models and Gas-Phase Chemical Mechanisms in Laminar Premixed Flames, **Combustion Science and Technology**, vol. 188, p. 1021–1053, 2016.

Sabbah, H., Biennier, L., Klippenstein, S. J., Sims, I. R., and Rowe, B. R. Exploring the Role of PAHs in the Formation of Soot: Pyrene Dimerization, **The Journal of Physical Chemistry Letters**, vol. 1, p. 2962–2967, 2010.

Saffaripour, M., Veshkini, A., Kholghy, M., and Thomson, M. J. Experimental investigation and detailed modeling of soot aggregate formation and size distribution in laminar coflow diffusion flames of Jet A-1, a synthetic kerosene, and n-decane, **Combustion and Flame**, vol. 161, p. 848–863, 2014.

Saggese, C., Ferrario, S., Camacho, J., Cuoci, A., Frassoldati, A., Ranzi, E., Wang, H., and Faravelli, T. Kinetic modeling of particle size distribution of soot in a premixed burner-stabilized stagnation ethylene flame, **Combustion and Flame**, vol. 162, p. 3356–3369, 2015.

Salenbauch, S., Cuoci, A., Frassoldati, A., Saggese, C., Faravelli, T., and Hasse, C. Modeling soot formation in premixed flames using an Extended Conditional Quadrature Method of Moments, **Combustion and Flame**, vol. 162(6), p. 2529 – 2543, 2015.

Santoro, R., Semerjian, H., and Dobbins, R. Soot particle measurements in diffusion flames, **Combustion and Flame**, vol. 51, p. 203–218, 1983.

Schlup, J. and Blanquart, G. Reproducing curvature effects due to differential diffusion in tabulated chemistry for premixed flames, **Proceedings of the Combustion Institute**, vol. 37, p. 2511–2518, 2019.

Scholtissek, A., Chan, W. L., Xu, H., Hunger, F., Kolla, H., Chen, J. H., Ihme, M., and Hasse, C. A multi-scale asymptotic scaling and regime analysis of flamelet equations including tangential diffusion effects for laminar and turbulent flames, **Combustion and Flame**, vol. 162, p. 1507–1529, 2015.

Seaton, A. and Donaldson, K. Nanoscience, nanotoxicology, and the need to think small, **The Lancet**, vol. 365, p. 923–924, 2005.

Shrestha, G., Traina, S. J., and Swanston, C. W. Black Carbon's Properties and Role in the Environment: A Comprehensive Review, **Sustainability**, vol. 2, p. 294–320, 2010.

Singh, J. **Detailed soot modelling in laminar premixed flames**. PhD thesis, University of Cambridge, 2006.

Singh, J., Patterson, R. I., Kraft, M., and Wang, H. Numerical simulation and sensitivity analysis of detailed soot particle size distribution in laminar premixed ethylene flames, **Combustion and Flame**, vol. 145, p. 117–127, 2006.

Sirignano, M., Ghiassi, H., D'Anna, A., and Lighty, J. S. Temperature and oxygen effects on oxidation-induced fragmentation of soot particles, **Combustion and Flame**, vol. 171, p. 15–26, 2016.

Sirignano, M., Kent, J., and D'Anna, A. Modeling Formation and Oxidation of Soot in Nonpremixed Flames, **Energy Fuels**, vol. 27, p. 2303–2315, 2013.

Slavinskaya, N. and Frank, P. A modelling study of aromatic soot precursors formation in laminar methane and ethene flames, **Combustion and Flame**, vol. 156, p. 1705–1722, 2009.

Slavinskaya, N. A., Riedel, U., Dworkin, S. B., and Thomson, M. J. Detailed numerical modeling of PAH formation and growth in non-premixed ethylene and ethane flames, **Combustion and Flame**, vol. 159(3), p. 979 – 995, 2012.

Smooke, M., Long, M., Connelly, B., Colket, M., and Hall, R. Soot formation in laminar diffusion flames, **Combustion and Flame**, vol. 143, p. 613–628, 2005.

Smooke, M., McEnally, C., Pfefferle, L., Hall, R., and Colket, M. Computational and experimental study of soot formation in a coflow, laminar diffusion flame, **Combustion and Flame**, vol. 117, p. 117–139, 1999.

Smooke, M. D. and Giovangigli, V. Formulation of the premixed and nonpremixed test problem, **Lecture Notes in Physics**, vol. 384, p. 1–28, 1991.

Smyth, K. C. and Shaddix, C. R. The elusive history of $m \simeq 1.57\breve{}0.56i$ for the refractive index of soot, **Combustion and Flame**, vol. 107, p. 314–320, 1996.

Snelling, D. R., Liu, F., Smallwood, G. J., and Ömer L. Gülder. Determination of the soot absorption function and thermal accommodation coefficient using low-fluence LII in a laminar coflow ethylene diffusion flame, **Combustion and Flame**, vol. 136, p. 180–190, 2004.

Solovjov, V. P. and Webb, B. W. An efficient method for modeling radiative transfer in multicomponent gas mixtures with soot, **Journal of Heat Transfer**, vol. 123, p. 450–457, 2001.

Somers, L. M. T. **The simulation of flat flames with detailed and reduced chemical models**. PhD thesis, Eindhoven University of Technology, 1994.

Sorensen, C. M. Light Scattering by Fractal Aggregates: A Review, **Aerosol Science and Technology**, vol. 35, p. 648–687, 2001.

Taine, J. A line-by-line calculation of low-resolution radiative properties of CO2-CO-transparent nonisothermal gases mixtures up to 3000 K, **Journal of Quantitative Spectroscopy and Radiative Transfer**, vol. 30, p. 371–379, 1983.

Takahashi, F. and Glassman, I. Sooting Correlations for Premixed Flames, **Combustion Science and Technology**, vol. 37, p. 1–19, 1984.

Tang, Q., Mei, J., and You, X. Effects of CO2 addition on the evolution of particle size distribution functions in premixed ethylene flame, **Combustion and Flame**, vol. 165, p. 424–432, 2016.

Teini, P. D., Karwat, D. M., and Atreya, A. Observations of nascent soot: Molecular deposition and particle morphology, **Combustion and Flame**, vol. 158, p. 2045–2055, 2011.

Thomson, M. and Mitra, T. A radical approach to soot formation, **Science**, vol. 361, p. 978–979, 2018.

Thynell, S. T. Discrete-ordinates method in radiative heat transfer, **International Journal of Engineering Science**, vol. 36, p. 1651–1675, 1998.

Totton, T. S., Misquitta, A. J., and Kraft, M. A quantitative study of the clustering of polycyclic aromatic hydrocarbons at high temperatures, **Physical Chemistry Chemical Physics**, vol. 14, p. 4081–4094, 2012.

Turns, S. R. **An Introduction to Combustion: Concepts and Applications**. McGraw-Hill, USA, 2th edition, 2000.

Underschultz, J., Dodds, K., Michael, K., Sharma, S., Wall, T., and Whittaker, S. **Carbon Capture and Storage**. In Devasahayam, S., Dowling, K., and Mahapatra, M. K., editors, *Sustainability in the Mineral and Energy Sectors*, pages 437–451. CRC Press, Boca Raton, 2016.

van Oijen, J., Donini, A., Bastiaans, R., ten Thije Boonkkamp, J., and de Goey, L. State-of-the-art in premixed combustion modeling using flamelet generated manifolds, **Progress in Energy and Combustion Science**, vol. 57, p. 30–74, 2016.

van Oijen, J. A. **Flamelet-Generated Manifolds: development and application to premixed laminar flames**. PhD thesis, Eindhoven University of Technology, 2002.

van Oijen, J. A. and de Goey, L. P. H. Modelling of Premixed Laminar Flames using Flamelet-Generated Manifolds, **Combustion Science and Technology**, vol. 161, p. 113–137, 2000.

Vandsburger, U., Kennedy, I., and Glassman, I. Sooting counterflow diffusion flames with varying oxygen index, **Combustion Science and Technology**, vol. 39, p. 263–285, 1984.

Verhoeven, L., de Andrade Oliveira, M., Lantz, A., Li, B., Li, Z., Luijten, C., van Oijen, J., AldÃ©n, M., and de Goey, L. A numerical and experimental study of Polycyclic-Aromatic Hydrocarbons in a laminar diffusion flame, **Proceedings of the Combustion Institute**, vol. 34, p. 1819–1826, 2013.

Verhoeven, L., Ramaekers, W., van Oijen, J., and de Goey, L. Modeling non-premixed laminar coflow flames using flamelet-generated manifolds, **Combustion and Flame**, vol. 159, p. 230–241, 2012.

Vervisch, P. **Soot and NOx modeling dedicated to Diesel engine**. PhD thesis, Ecole Centrale Paris, 2012.

Veshkini, A., Dworkin, S. B., and Thomson, M. J. A soot particle surface reactivity model applied to a wide range of laminar ethylene/air flames, **Combustion and Flame**, vol. 161, p. 3191–3200, 2014.

Veshkini, A., Dworkin, S. B., and Thomson, M. J. Understanding soot particle size evolution in laminar ethylene/air diffusion flames using novel soot coalescence models, **Combustion Theory and Modelling**, vol. 20, p. 707–734, 2016a.

Veshkini, A., Eaves, N. A., Dworkin, S. B., and Thomson, M. J. Application of PAH-condensation reversibility in modeling soot growth in laminar premixed and non-premixed flames, **Combustion and Flame**, vol. 167, p. 335–352, 2016b.

Wang, H. Formation of nascent soot and other condensed-phase materials in flames, **Proceedings of the Combustion Institute**, vol. 33, p. 41–67, 2011.

Wang, H., Du, D., Sung, C., and Law, C. Experiments and numerical simulation on soot formation in opposed-jet ethylene diffusion flames, **Symposium (International) on Combustion**, vol. 26, p. 2359–2368, 1996.

Wang, H., Yao, M., Yue, Z., Jia, M., and Reitz, R. D. A reduced toluene reference fuel chemical kinetic mechanism for combustion and polycyclic-aromatic hydrocarbon predictions, **Combustion and Flame**, vol. 162, p. 2390–2404, 2015a.

Wang, P., Hu, S., and Pitz, R. W. Numerical investigation of the curvature effects on diffusion flames, **Proceedings of the Combustion Institute**, vol. 31, p. 989–996, 2007.

Wang, Y. and Chung, S. H. Effect of strain rate on sooting limits in counterflow diffusion flames of gaseous hydrocarbon fuels: Sooting temperature index and sooting sensitivity index, **Combustion and Flame**, vol. 161, p. 1224–1234, 2014.

Wang, Y. and Chung, S. H. Formation of doot in counterflow diffusion flames with carbon dioxide Dilution, **Combustion Science and Technology**, vol. 188, p. 805–817, 2016a.

Wang, Y. and Chung, S. H. Strain rate effect on sooting characteristics in laminar counterflow diffusion flames, **Combustion and Flame**, vol. 165, p. 433–444, 2016b.

Wang, Y., Raj, A., and Chung, S. H. A PAH growth mechanism and synergistic effect on PAH formation in counterflow diffusion flames, **Combustion and Flame**, vol. 160, p. 1667–1676, 2013.

Wang, Y., Raj, A., and Chung, S. H. Soot modeling of counterflow diffusion flames of ethylene-based binary mixture fuels, **Combustion and Flame**, vol. 162, p. 586–596, 2015b.

Wen, J. Z., Thomson, M. J., Lightstone, M. F., and Rogak, S. N. Detailed kinetic modeling of carbonaceous nanoparticle inception and surface growth during the pyrolysis of C6H6 behind shock waves, **Energy & Fuels**, vol. 20, p. 547–559, 2006.

Wen, Z., Yun, S., Thomson, M., and Lightstone, M. Modeling soot formation in turbulent kerosene/air jet diffusion flames, **Combustion and Flame**, vol. 135, p. 323–340, 2003.

Wilke, C. R. A Viscosity Equation for Gas Mixtures, **The Journal of Chemical Physics**, vol. 18(4), p. 517–519, 1950.

Williams, T., Shaddix, C., Jensen, K., and Suo-Anttila, J. Measurement of the dimensionless extinction coefficient of soot within laminar diffusion flames, **International Journal of Heat and Mass Transfer**, vol. 50, p. 1616–1630, 2007.

Wright, D. L., McGraw, R., and Rosner, D. E. Bivariate Extension of the Quadrature Method of Moments for modeling simultaneous coagulation and sintering of particle populations, **Journal of Colloid and Interface Science**, vol. 236, p. 242–251, 2001.

Xu, F., Sunderland, P., and Faeth, G. Soot formation in laminar premixed ethylene/air flames at atmospheric pressure, **Combustion and Flame**, vol. 108, p. 471–493, 1997.

Xu, H., Hunger, F., Vascellari, M., and Hasse, C. A consistent flamelet formulation for a reacting char particle considering curvature effects, **Combustion and Flame**, vol. 160, p. 2540–2558, 2013.

Xuan, Y. and Blanquart, G. Numerical modeling of sooting tendencies in a laminar co-flow diffusion flame, **Combustion and Flame**, vol. 160, p. 1657–1666, 2013.

Xuan, Y. and Blanquart, G. A flamelet-based a priori analysis on the chemistry tabulation of polycyclic aromatic hydrocarbons in non-premixed flames, **Combustion and Flame**, vol. 161, p. 1516 – 1525, 2014.

Xuan, Y. and Blanquart, G. Effects of aromatic chemistry-turbulence interactions on soot formation in a turbulent non-premixed flame, **Proceedings of the Combustion Institute**, vol. 35, p. 1911–1919, 2015.

Yapp, E. K., Chen, D., Akroyd, J., Mosbach, S., Kraft, M., Camacho, J., and Wang, H. Numerical simulation and parametric sensitivity study of particle size distributions in a burner-stabilised stagnation flame, **Combustion and Flame**, vol. 162, p. 2569–2581, 2015.

Yen, M. and Abraham, J. Soot and nitric oxide modeling in reacting diesel jets with an unsteady flamelet progress variable model, **Proceedings of the Institution of Mechanical Engineers, Part D: Journal of Automobile Engineering**, vol. 230, p. 503–513, 2016.

Yuan, C. and Fox, R. Conditional Quadrature Method of Moments for kinetic equations, **Journal of Computational Physics**, vol. 230, p. 8216–8246, 2011.

Yuan, C., Laurent, F., and Fox, R. An Extended Quadrature Method of Moments for population balance equations, **Journal of Aerosol Science**, vol. 51, p. 1 – 23, 2012.

Zhang, Q. **Detailed modeling of soot formation/oxidation in laminar coflow diffusion flames**. PhD thesis, University of Toronto, 2009.

Zhang, Q., Guo, H., Liu, F., Smallwood, G., and Thomson, M. Modeling of soot aggregate formation and size distribution in a laminar ethylene/air coflow diffusion flame with detailed PAH chemistry and an advanced sectional aerosol dynamics model, **Proceedings of the Combustion Institute**, vol. 32, p. 761–768, 2009a.

Zhang, Q., Thomson, M., Guo, H., Liu, F., and Smallwood, G. A numerical study of soot aggregate formation in a laminar coflow diffusion flame, **Combustion and Flame**, vol. 156, p. 697–705, 2009b.

Zhang, Y., Liu, F., and Lou, C. Experimental and Numerical Investigations of Soot Formation in Laminar Coflow Ethylene Flames Burning in O2/N2 and O2/CO2 Atmospheres at Different O2 Mole Fractions, **Energy & Fuels**, vol. 32, p. 6252–6263, 2018.

Zhao, B., Yang, Z., Li, Z., Johnston, M. V., and Wang, H. Particle size distribution function of incipient soot in laminar premixed ethylene flames: effect of flame temperature, **Proceedings of the Combustion Institute**, vol. 30, p. 1441–1448, 2005.

Ziemniczak, A., Coelho, F. R., Pereira, F. M., Pagot, P. R., and França, F. H. R. Evaluation of the discretization in the spectral resolution for the solution of the line-by-line method in problems with participating gases, **Journal of the Brazilian Society of Mechanical Sciences and Engineering**, vol. 41, p. 354, 2019.

Zimmer, L. **Numerical study of soot formation in laminar ethylene diffusion flames**. PhD thesis, Federal University of Rio Grande do Sul, 2016.

Zimmer, L., Pereira, F. M., van Oijen, J. A., and de Goey, L. P. H. Investigation of mass and energy coupling between soot particles and gas species in modelling ethylene counterflow diffusion flames, **Combustion Theory and Modelling**, vol. 21, p. 358–379, 2017.

APPENDIX A – Kinetic Mechanisms influence in soot precursors prediction

A comparison of kinetic mechanisms and their influence in soot precursors prediction is done in this section. Simulations were done for the incipiently sooting ethylene counterflow flame experimentally studied by Carbone et al., 2015, at atmospheric conditions. The fuel stream is a mixture of 33% C_2H_4 + 67% N_2 and the oxidizer stream if composed by 22.9% O_2 + 77.1% N_2, both in molar basis.

One-dimensional steady-state flames were solved with the CHEM1D [Somers, 1994] code. The conservation equations describes the conservation of mass, stretch rate, chemical species and enthalpy. A computational domain of 2 cm length was discretized with 400 equidistant points. The strain rate was defined such that the simulated temperature profile meets the experimental data, which resulted in the value of $a = 90$ s^{-1}. Since it is a incipiently sooting flame at a relatively high strain rate, soot formation and thermal radiation were neglected in the modelling.

Four kinetic mechanisms (Table A.1) able to describe polyciclic-aromatic hydrocarbons up to 4-rings were evaluated, including the reduced toluene reference fuel of Wang et al., 2015a. This later mechanism predicts PAHs up to pyrene and was well validated with shock tube ignition delays, laminar flame speeds and species profiles in premixed flames, with homogeneous charge compression ignition and direct injection compression ignition engine combustion data. The mechanism presented by Chernov et al., 2014 (which is an update from the DLR mechanism [Slavinskaya et al., 2012]) did not converge for this flame in the current code.

Table A.1 – Brief description of the kinetic mechanism evaluated for the prediction of soot precursors.

Mech. Name	Size (Sp./Reac.)	Reference	Comments
KM2	203/1346	Wang et al., 2013	for C1-C4 with PAH up to A7
BPP	148/928	Blanquart et al., 2009	for C2-C4 with PAH up to A4
ABF	101/544	Appel et al., 2000	for C2 with PAH up to A4
Wred	109/543	Wang et al., 2015a	for C2-C7 with PAH up to A4

Predicted temperature and major species profiles are indicated in Figure A.1 together with the reference data . Reference measurements for temperature were performed using either thermocouples (TC) or thin filament pyrometry (TFP). Maximum temperature predicted by the $KM2$ and the BPP mechanisms are approximately 2000 K, whereas the ABF mechanism predicted around 1980 K. The good agreement between numerical and experimental data for the maximum temperature and the width of the thermally affected region of the flame ratify the assumptions of neglecting soot and radiation in the modelling. In comparison with the reference data, the CO mole fraction was similarly predicted by all the kinetic mechanism whereas the prediction of H_2 become worst as the size of the mechanism increase. The acetylene (C_2H_2) formation was well captured by the $KM2$ mechanism. Its prediction is important since C_2H_2 is the main responsible for soot growth due to carbon deposition. The maximum C_2H_2 prediction is obtained for the ABF mechanism.

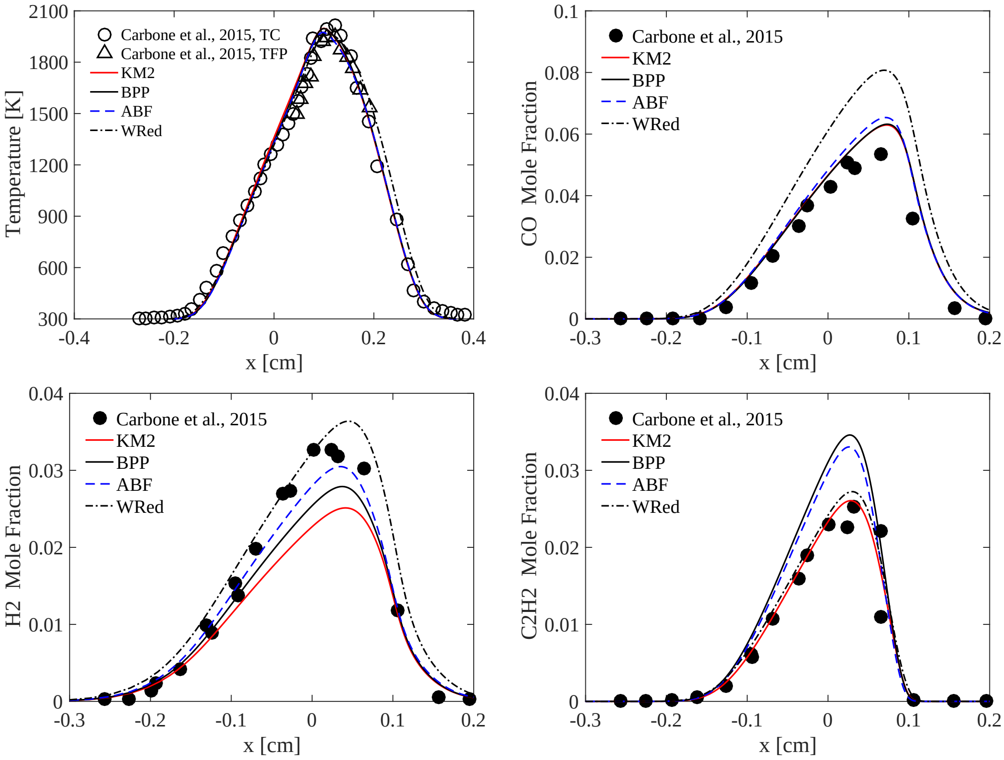

Figure A.1 – Temperature profile and major chemical species mole fraction.

Numerical results are compared with experimental data from the reference for C1-C5 species in Figure A.2. The C1-C5 species include methane and representatives of stable intermediates in the process leading to the first aromatic ring and to the aromatic growth. It is worth mention that C_3H_4 include its isomers allene ($A-C_3H_4$) and propyne ($P-C_3H_4$). Results for the different kinetics mechanisms shows that KM2 and the BPP mechanisms perform similarly for the prediction of intermediate species. On the other hand, ABF predictions are much less accurate.

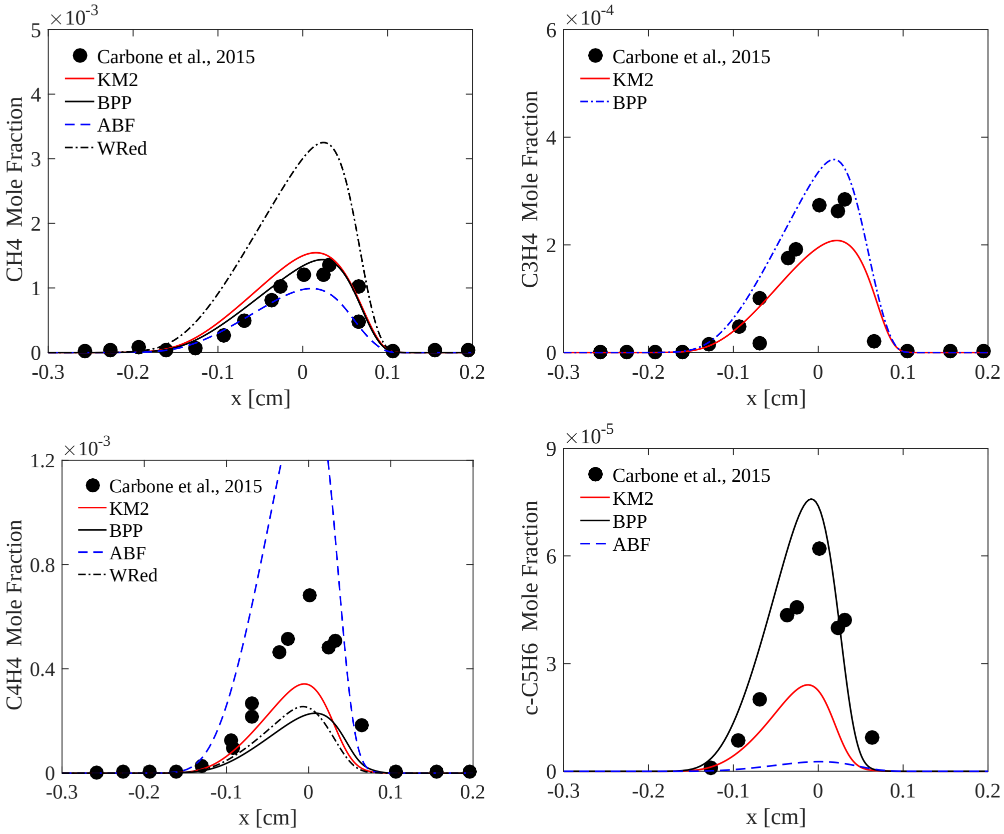

Figure A.2 – C1-C5 intermediate species mole fraction.

Aromatics mole fraction profiles are compared in Figure A.3. All the mechanisms performed very distinctly in predicting the formation of small aromatics. Benzene ($A1$) is well predicted by the BPP and the ABF mechanism whereas the KM2 mechanism underpredicts its concentration in ∼ 40%. Naphthalane ($A2$) mole fraction was underpredicted by the ABF and the KM2 mechanisms and overprediceted by the BPP mechanism. Experimental data is not provided for three and 4-ring aromatics, however, some works [Wang et al., 2013, 2015b] demonstrated the better capability of the KM2 mechanism in predicting $A3$ and $A4$ concentrations. Thus, one may assume the KM2 results for these larger aromatic species as reference. It is observed that the $A3$ and $A4$ maximum mole fraction predicted by the ABF and the BPP mechanisms is, respectively, three and six times lower. Excpet for the $A3$ mole fraction, the Wred mechanism expressively overpredict the formation of aromatics up to four rings. Since pyrene ($A4$) is usually assumed as soot precursor and for condensation on the soot surface, soot models are very sensible to the gas-phase predictions by the kinetic mechanisms and, therefore, a reduced number of soot particles should be expected when using the ABF or the BPP mechanisms.

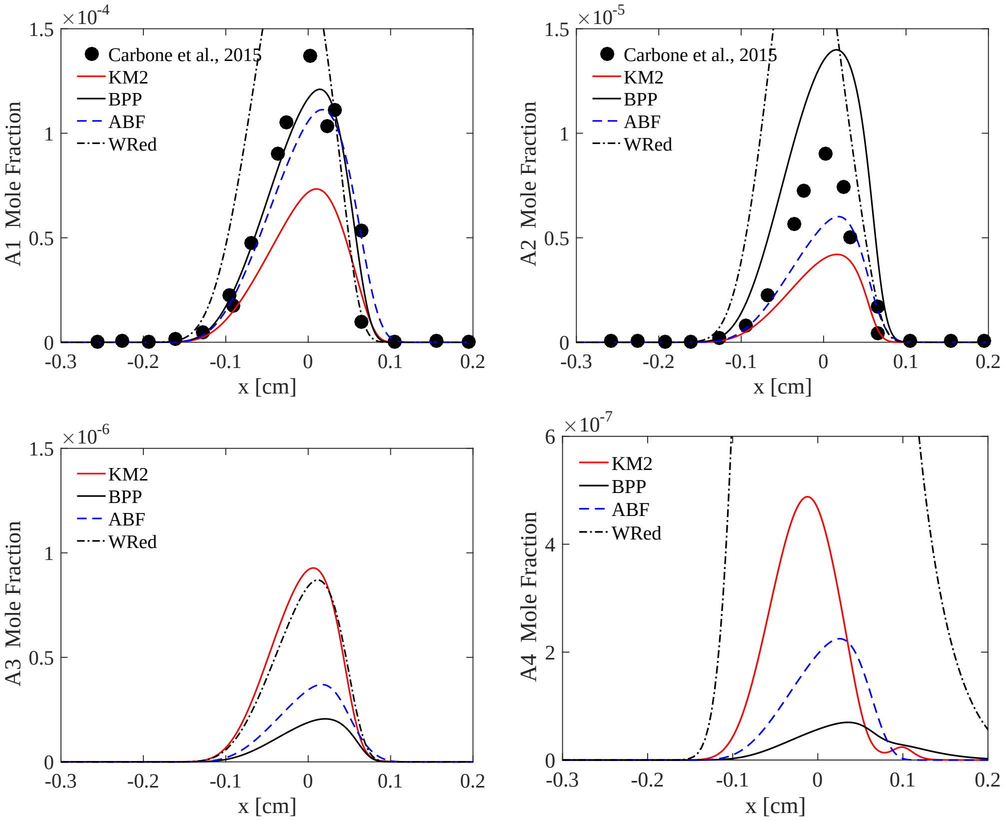

Figure A.3 – Polyciclic-Aromatics Hydrocarbon mole fractions.

APPENDIX B – Soot Sectional algorithm verification

Verification of the soot sectional method implementation is performed for a premixed flame explored by Roy, 2014, with a similar soot sectional method. This flame was experimentally investigated by Xu et al., 1997, and Menon et al., 2007. It consists of a rich ethylene/air premixed flame at atmospheric conditions and 298 K. The equivalence ratio is $\phi = 2.64$ (C/O=0.88). The mixture composition is 15.60% C_2H_4 - 17.73% O_2 - 66.67%N_2.

Simulations were conducted with the Chem1D code considering the same DSM parameters of the reference [Roy, 2014]. In general, this consist in solving the soot model presented in Section 3.4 assuming 25 sections, describing the soot surface reaction by the HACA-based mechanism with reactions SR1 to SR6, solving the chemistry with kinetic mechanism of Appel and co-workers [Appel et al., 2000] and fully coupling the solid and the gaseous phases. In addition, the experimental temperature profile is implemented in the code in detriment of solving energy conservation equation. The code was verified for two parameters variants of the DSM as described in the next sections. A comparison of chemical species, as C_2H_2 and OH presented a good agreement with the reference as shown in Figure B.1.

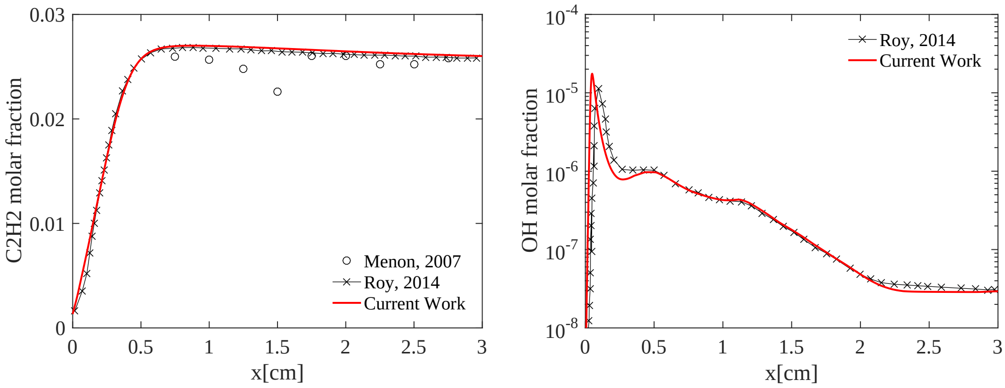

Figure B.1 – Mole Fraction of C_2H_2 and OH.

B.1 First approach

The first approach assumes unity steric factor ($\alpha = 1$) and depletion of surface radicals (reaction SR4a in the HACA-based mechanism, Equation 3.33). The soot volume fraction (f_v) and total number density (N) are shown in Figure B.2. The particle size distribution function ($\mathrm{d}N/\mathrm{d}log(D_p)$) is shown in Figure B.3. In general, a good agreement with the reference model of Roy, 2014, is achieved. Although, a great discrepancy exist between the the numerical models and the experimental data.

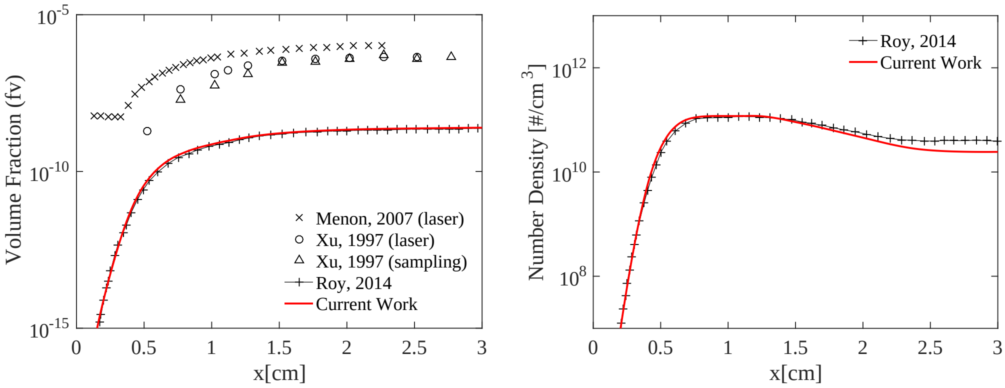

Figure B.2 – Results for soot volume fraction (f_v) and total number density (N) for the Approach 1.

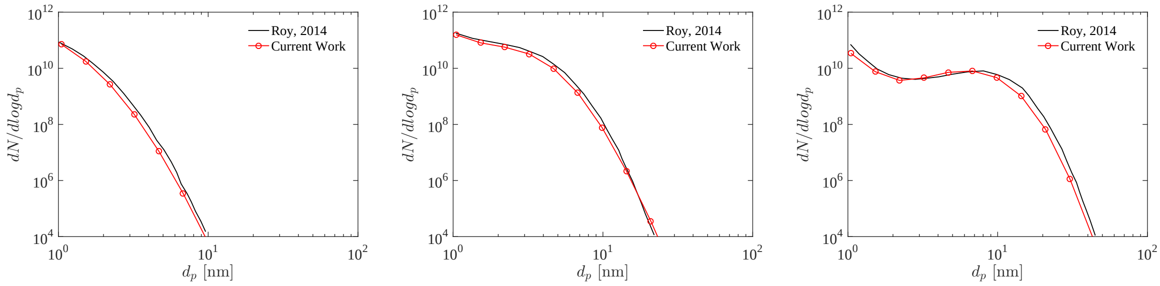

Figure B.3 – Particle size distribution function for the Approach 1 of the soot model at the positions of 0.5 cm (left), 1.0 cm (middle) and 2.5 cm (right).

B.2 Second approach

The second approach assumes the steric factor (Equation 3.34) as function of particles diameter and flame temperature ($\alpha = f(d_p, T)$) following Appel et al., 2000 and the conservation of surface radicals (reaction SR4b of Table 3.1 and Equation 3.33) in the HACA-based mechanism. The soot volume fraction (f_v) and the total number density (N) are shown in Figure B.4. The particle size distribution is shown in Figure B.5.

Figures B.4 and B.5 show that the agreement with the literature (when considering $\alpha = f(d_p, T)$ and conservation of particle surface sites) is comparable to the previous results. Only small difference were found for soot volume fraction and total number density.The shape of the particle size distribution is also well captured.

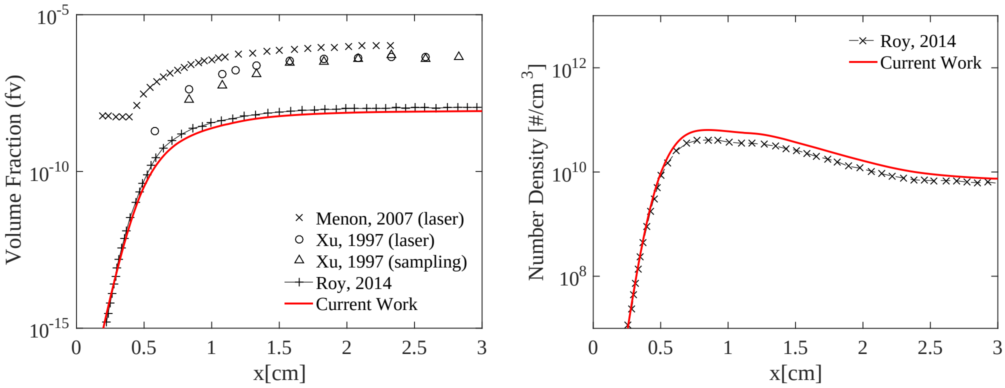

Figure B.4 – Results for soot volume fraction (f_v) and total number density (N_{total}) for the Approach 2.

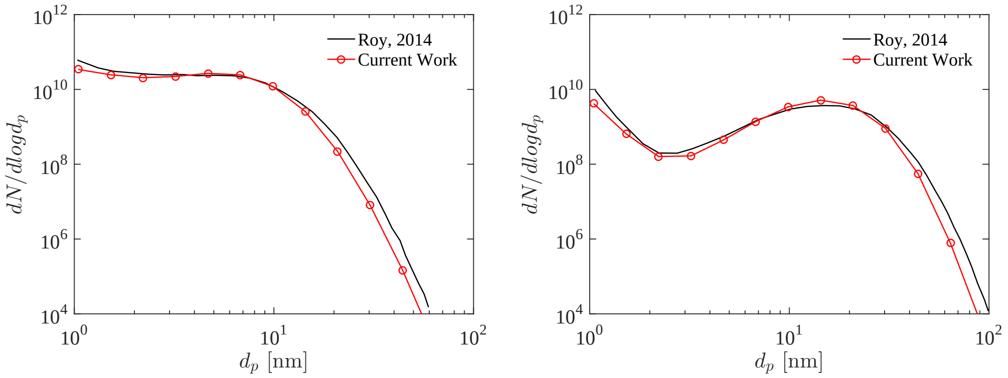

Figure B.5 – Particle size distribution function for the Approach 2 of the soot model at the positions of 1.0 cm (left) and 2.5 cm (right).

APPENDIX C – Assessment of the DSM in laminar non-premixed counterflow flames

Combustion problems are modeled with a set of partial differential equations that describes conservation of total mass, mass of species, momentum, energy and stretch in an one-dimensional approximation [de Goey and ten Thije Boonkkamp, 1999a]. The equation system is solved with the code CHEM1D, 2016, for steady state conditions. The mechanism KM2 [Wang et al., 2013] is assumed to describe the chemistry based on the assessment of the kinetic mechanism presented in Appendix A. The diffusion coefficients are mixtureaveraged with the diffusion velocity of each individual gas species being computed assuming a Fick-like diffusion. The conservation of the total mass is assured througth the correction of the diffusion flux for the main species N_2. Wilke's semi-empirical formula [Wilke, 1950] is assumed for the viscosity computation and Mathur's combination-averaging approach [Mathur et al., 1967] is used to compute the thermal conductivity. The DSM implemented in this work is fully detailed in Section 3.4 and verified in Appendix B with the reference data. The present approach considers that soot particles are solid and modeled as a distinct dispersed phase, interacting with the gaseous phase. The gas-phase and the particulate-phase are fully coupled following Zimmer et al., 2017. The semi-empirical two-equation soot formation model of Liu et al., 2001, (refereed as Two-Eq.S.M.) is also considered for comparison .

C.1 Influence of the coagulation model and the number of sections

A sensitivity study was performed to identify the influence of the number of sections and different coagulation models in soot predictions. The counterflow flame studied by Wang et al., 2015b, was chosen as the target flame. The strain rate was defined such that the simulated temperature profile meets the numerical data of the reference, which resulted in the value of $a = 120$ s^{-1}. The soot model is the same described in Section 3.4, but assuming the steric factor as function of particles diameter and flame temperature ($\alpha = f(d_p, T)$) following Appel et al., 2000, and conservation of surface radicals (reaction SR4b of Table 3.1 and Equation 3.33 in the HACA-based mechanism.

The coagulation model is the main responsible for describing particles size distribution. Two coagulation methods are compared in Figure C.1: the model of Gelbard et al., 1980, (refereed as GS1980) and the model of Kumar and Ramkrishna, 1996, (refereed as KR1996). To avoid numerical integrations and its great impact in the computational time, it was assumed a constant mean particle size for each section. However, the impact of assuming only one or additional mean particles size (sub-sections) in soot predictions considering the coagulation model of Gelbard and Seifield is not clear. Hence a sensitivity study of the number of sub-sections in the Gelbard and Seifield was also included in Figure C.1. Those comparisons were conducted assuming 30 sections.

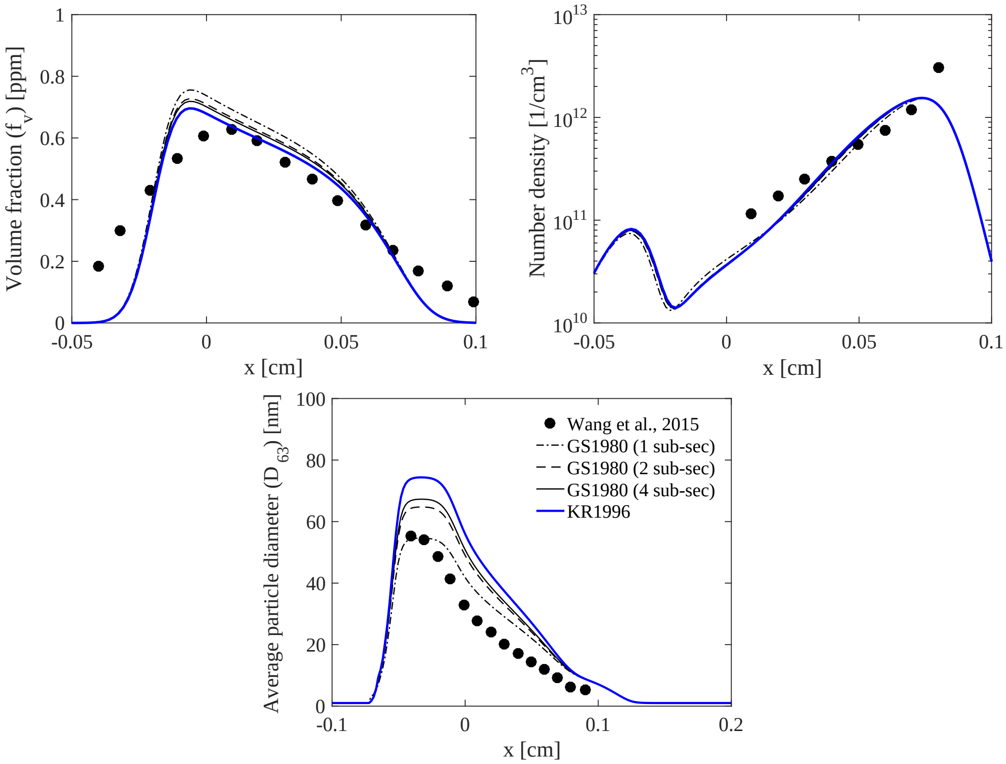

Figure C.1 – Comparison of coagulation models for soot volume fraction (f_v), total number density (N_{total}) and average diameter (D_{63}).

It is observed that the influence of the coagulation model in the soot volume fraction and number density are minimal. On the other hand, differences between the models are higher for the average particle size. Particles diameter depends on both the soot volume fraction and number density, such that, for a constant f_v a reduction or increase in N_{total} would lead, respectively, to an increase or reduction in the average particles diameter. The slightly lower prediction of volume fraction, near $x = 0.0$ cm, achieved by the KR1996 model explains its higher particle diameter. Exactly the opposite occurs for the GS1980 model when only one sub-section is assumed. Predictions by the GS1980 model tends to an asymptotic when more than one sub-section is assumed.

Discrete Sectional methods for aerosols predictions are sensible to the total number of sections. Sensitive analysis of the number of section in the soot volume fraction, number density and average particle diameter are shown in Figure C.2. Results for the GS1980 coagulation model are obtained assuming two sub-sections per each size class. It is observed that the results became less sensitive to the number of sections approximately at 60 sections. Additionally, the computational cost increase significantly with the number of sections since additional transport equations are solved in the equation system.

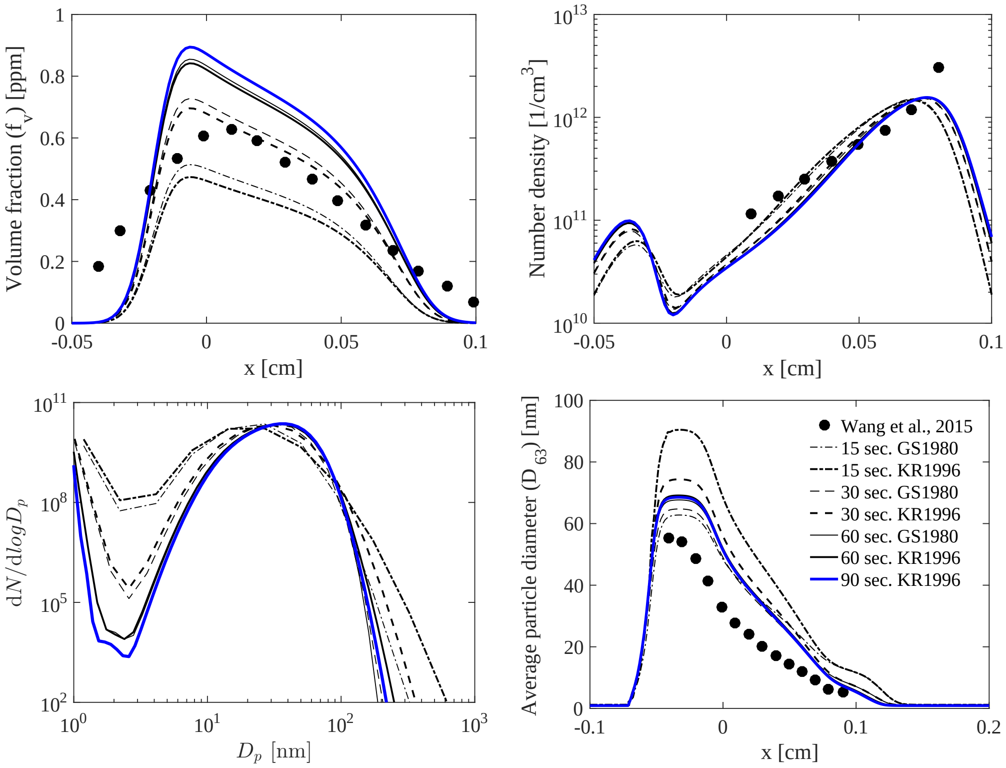

Figure C.2 – Influence of the number of sections in predicting soot volume fraction (f_v), total number density (N_{total}), normalized particle size distribution ($\mathrm{d}N/\mathrm{d}(logD_p)$) average diameter ($D_{63}$).

The computational time of the simulations discussed before is indicated in the Figure C.3. Results indicates that the maximum soot volume fraction approximates an asymptotic solution with 60 sections. However, the computational time increases significantly with the number of sections, principally for the GS1980 model when two or more sub-sections are considered per sections. Based on these findings, one may conclude that adequate solutions require at least 60 sections. The computational time in the order of 10^3 seconds may become prohibitive for large systematic studies, even for one-dimensional simulations. Hence, simulations with the KR1996 or the GS1980 (assuming two sub-sections) models for 30 sections could be used without much impact on final results of soot volume fraction. However, major deviations would be found for the particles size distribution for this case. Results for 30 sections provide a good relation between accuracy and computational time for the discrete sectional method. One should note that discrepancies between the coagulation models, the number of sections and the computational time may be larger in flames with increased soot productions.

The computation cost is much more influenced by the coagulation model. For the case of 30 sections, assuming the GS1980 with one sub-section as reference, it was observed an increase in the computational time in 2.8× and 10.3× for 2 and 4 sub-sections, respectively. The computation cost of the KR1996 is compatible to the reference (only 1.3× higher). Clearly from Figure C.3, the computational cost increases exponential with the number of sections.

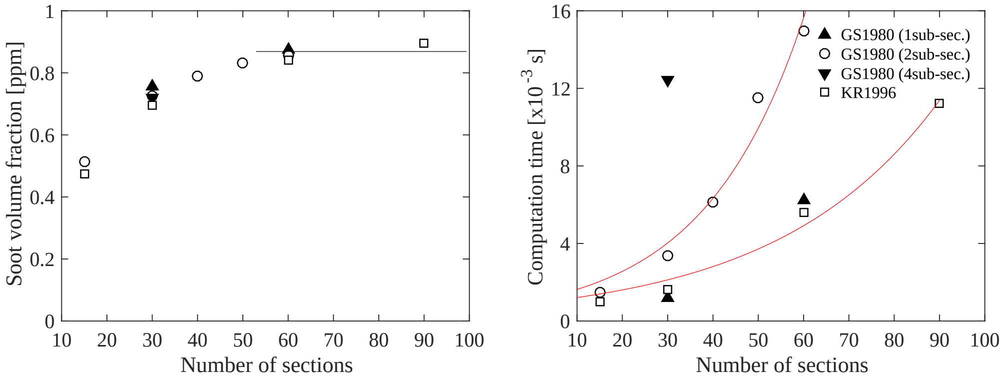

Figure C.3 – Maximum soot volume fraction (left) and computational time (right) of the simulations presented in Figures C.1 and C.2.

C.2 Effect of several soot model parameters

The intend of this section is gain insights about the influence of DSM variants on the predictions of soot formation in counterflow non-premixed flames. Table C.1 summarize all variants considered for comparison. The model variants consist in to evaluate: the influence of assuming that all radical sites are available ($\alpha = 1$) versus a temperature- and particle-size-dependent steric factor correlation ($\alpha = f(d_p, T)$); when the standard HACA-based mechanism (SR1 to SR6) or the extended HACA-based mechanism (SR1 to SR9) are able to predict the surface process; whether active soot surface radical sites are depleted (SR4a) or conserved (SR4b) in surface reactions; the consistency of different coagulation models.

To assume that surface radicals are fully depleted (no longer available) or conserved (remain available) during C_2H_2 addition represents the extremes of the process. In reality, the concentration of dehydrogenated sites (C^*_{soot}) involved during the process of surface growth may lay in between these extremes. Thus an adjusted constant ξ_{dc}, varying between 0 (for fully depleted) and 1 (for fully conserved), is introduced. Variants of the surface radicals treatment provide another indication of the relative importance of surface reactions.

Table C.1 – Brief description of the DSM parameters variants evaluated for the prediction of soot content in non-premixed flames.

Variant	Steric Factor	HACA	Surface Radicals	Coagulation	Sections number
1	SR1 to SR6	$\alpha = 1$	Depleted (SR4a)	KR1996	60
2		$\alpha = f(d_p, T)$	Conserved (SR4b)		
3				GS1980	60 (1 sub-sec.)
4					60 (2 sub-sec.)
5			ξ_{dc}(Cons.-Dep.)+Dep.	KR1996	60
6	SR1 to SR9	$\alpha = 1$	Depleted (SR4a)	KR1996	60
7		$\alpha = f(d_p, T)$	ξ_{dc}(Cons.-Dep.)+Dep.		

C.2.1 Adiabatic low sooting counterflow flame

The reference is a counterflow non-premixed flame explored by Wang et al., 2015b. It consist of a pure ethylene flame at atmospheric conditions with the oxidizer being formed by 25% of O_2 and 75% of N_2, in molar basis. Reactants temperature are equal to 300 K. The strain rate in the current work was defined such that the simulated flame structure meets the numerical data of the reference. Soot formation and heat losses by thermal radiation are neglected in this part of the work. Figure C.4 demonstrate the agreement with the reference data for a strain rate equal to a = 120 s^{-1}, condition in which effects of thermal radiation are minimum [Zimmer et al., 2017].

Variants of the DSM are compared for soot volume fraction (f_v), number density, particle size distribution at maximum f_v position and the average particles diameter (D_{63}). Following Santoro et al., 1983, a general definition of average diameters of particles can

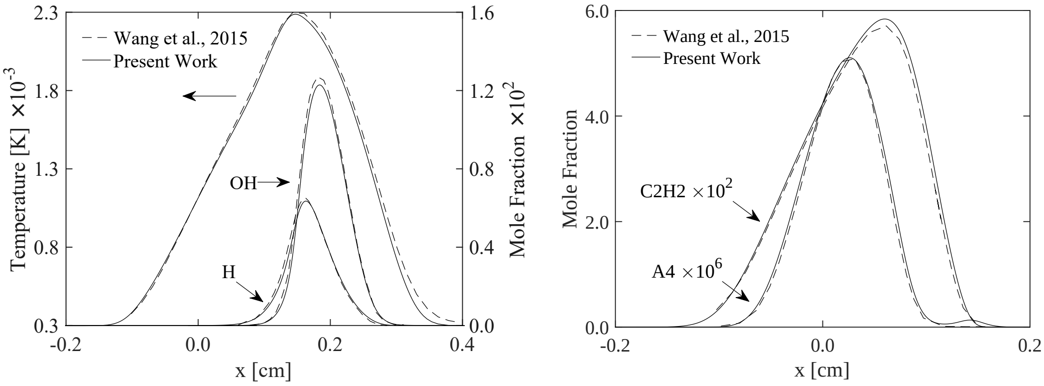

Figure C.4 – Comparison between numerical predictions of the flame structure at $a = 120\ \mathrm{s}^{-1}$, neglecting soot formation and thermal radiation.

be written as

$$D_{pq} = \left(\frac{\sum_{i=0}^{\infty} N_i D_i^p}{\sum_{i=0}^{\infty} N_i D_i^q} \right)^{\frac{1}{p-q}} , \tag{C.1}$$

where D_i is the diameter of the particle with size class i. This definition corresponds to the moment ratio of p^{th} and q^{th} order. Thus, D_{63} is the mean diameter corresponding to the ratio of the sixth and third moments. Santoro et al., 1983, determined the D_{63} experimental parameter from laser scattering, where the scattering cross section is proportional to the sixth moment of particle diameter.

Results of a two-equation soot model [Zimmer et al., 2017] are included for comparison. It underpredicts the volume fraction in 38% while the number density is approximately three orders of magnitude higher. The average particles diameter remain closer to 20 nm.

The first set of comparisons (Figure C.5) consist in evaluate the coagulation model. A sensitivity study of the influence of number of sections and the coagulation model have been conducted in Section C.1, where it was shown that solutions tends to an asymptotic for the number of sections near 60, but requiring an elevated computational time. The sensitivity study shows that, ideally, at least two sub-sections during the computation of GS1980 [Gelbard et al., 1980] coagulation model should be assumed. In general, solutions for simulations with 60 sections for the KR1996 (*Variant 2*) and the GS1980 with two sub-sections (*Variant 4*) are equivalent. The assumption of only one sub-section in the GS1980 model (*Variant 3*) is included for comparison since the effect of sub-sections were previously explored assuming 30 sections in Figure C.1. This approach clearly do not impact significantly the predictions of soot volume fraction (f_v) although major discrepancies are found for the average particle diameter and the particle size distribution. The results tendency with the variant is similar to the one observed in the *a priori* study on Figure C.1. Since the computational requirement of *Variant 3* is equivalent to the KR1996 model, the usage of the later model is recommended.

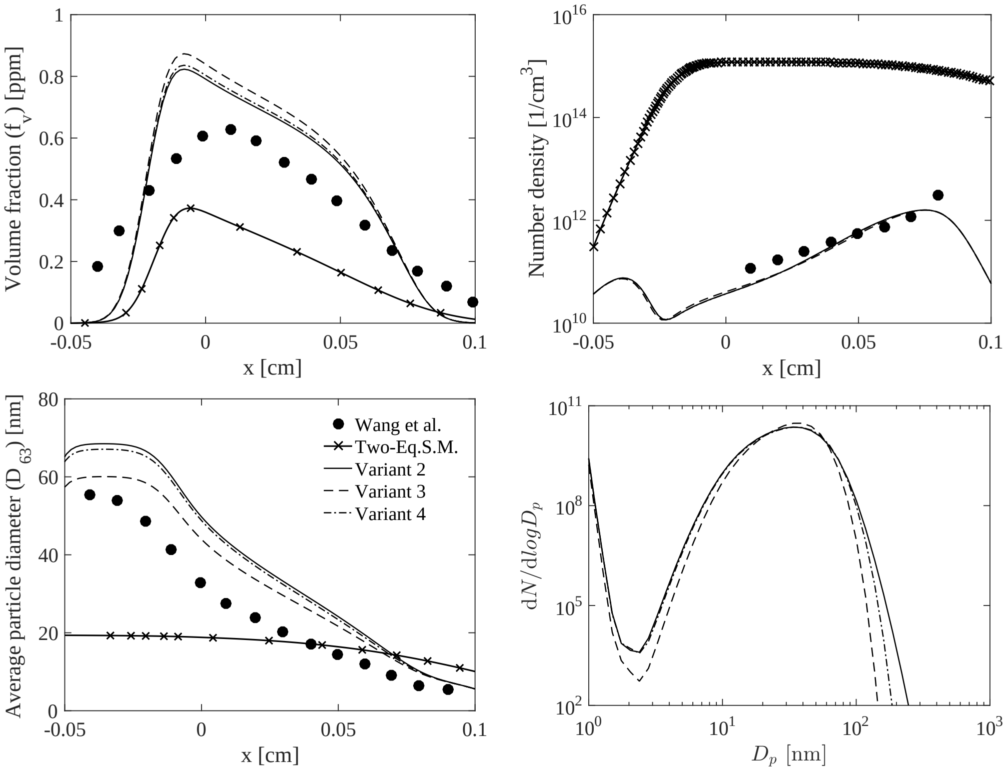

Figure C.5 – Comparison between coagulation model variants of the DSM for the soot formation flame studied by Wang et al., 2015a.

The second set of comparisons consist in evaluate the depletion of conservation of surface radicals, the extension of the HACA-based mechanism [Wang et al., 2015b] and a proposed adjustment of the surface radicals treatment. It is observed that the *Variants* 1 and 6 (which assume that all radical sites are available for surface growth in the standard HACA-based mechanism plus the assumption of fully depletion of surface radicals) hardly fails in predicting the soot content of the flame (Figure C.6). When depleted surface sites are assumed, the effects of additional reactions in the surface growth mechanism (*Variant 6*) are unnoticeable. On the other hand, the assumption of fully conserved surface radicals (reaction SR4b in the HACA-based mechanism) of *Variants* 2 to 4 in

Figure C.5 demonstrated to be essential for non-premixed flames soot modelling. Based on *Variants* 2 and 4, assuming variable steric factor and fully conserved surface radicals, the maximum soot volume fraction and the average particle diameter tends to be, respectively, 42% and 22% higher than the experimental data as shown in Figure C.5. Reactions SR7 to SR9 play a more significant role when conserved surface sites are assumed (not shown), reaching maximum soot volume fraction of 1.1 ppm (almost twice the experimental data). Clearly, a model assuming $\alpha = f(d_p, T)$ and SR4a produce even less soot whereas assuming $\alpha = 1$ and SR4b significantly enhance the soot growth.

It was observed that the assumption of completely depleted or conserved surface sites tends to under or over-predicts the soot content in the current flame. Variants considering that the concentration of dehydrogenated sites lays in between the extremes are presented in Figure C.6. For the current flame it was observed that the adjusted constant should be approximately $\xi_{dc} = 0.8$ to reproduce experimental data. Same value was maintained for the standard and the extended HACA-based mechanism. In this case, both *Variants* 5 and 7 were able to reproduce soot quantities closer to the reference data. Those results suggest that soot characteristics are much more sensible to the ξ_{dc} values than the inclusion of reactions SR7-SR9

C.2.2 Non-adiabatic moderate soot formation counterflow flame

The reference is a counterflow non-premixed flame explored by Hwang and Chung, 2001, and Vandsburger et al., 1984. It consist of a pure ethylene flame at atmospheric conditions with the oxidizer being formed by 28% of O_2 and 72% of N_2, in molar basis. Reactants temperature are equal to 300 K. The strain rate in the current work was defined such that the simulated flame structure meets the numerical data of the reference. The agreement was successful for a strain rate of approximately $a = 40\ \mathrm{s}^{-1}$, condition in which effects of thermal radiation should not be disregarded. Heat losses by thermal radiation are modeled assuming the grey-gas approximation in the optically thin limit.

The assessment of the current model is demonstrated in Figure C.7 for the best variant models encountered in App. C.2.1. The experimental soot volume fraction and the predicted total mass growth are adequately predicted by the DSM. On the other hand, the difference in the number density and mean particle diameter is more prominent. The

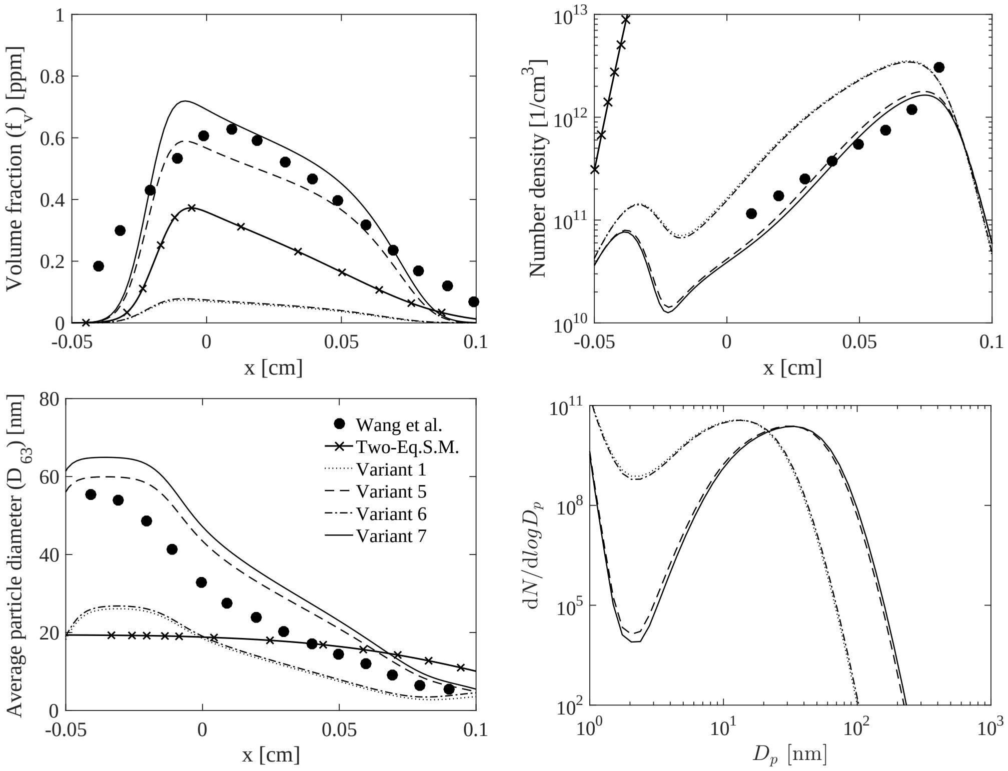

Figure C.6 – Comparison between variants of the DSM for the soot formation flame studied by Wang et al., 2015a.

computed mean particle diameter, which is equivalent to the D_{10} is given by

$$\overline{Dp} = \frac{\sum_{i=1}^{Ns} N_i \bar{d}_{p,i}}{N_{total}}, \tag{C.2}$$

where $\bar{d}_{p,i}$ is the mean particle diameter of size class i. The number density and the mean particle diameter are directly related. At $x \simeq -0.025$, region of the maximum f_v, it is observed a drastic reduction of the number of particles due to an increase of particles coalescence. Consequently, bigger particles are found in this region. Assuming $\xi_{dc} = 0.9$ for the treatment of surface radicals for *Variant 5* and *Variant 7* improve significantly the soot volume fraction predictions by the model. The difference of 0.4 ppm between these two variants is due to the inclusion of additional reactions on the HACA-based mechanism. Differences between *Variant 2* and *Variant 3* are due to coagulation models. A simulation similar to *Variant 7* but assuming fully conserved surface radicals (reaction SR4b), not shown, predicted a $f_{v,max} = 3.4$ ppm whereas *Variant 7* predicted $f_{v,max} = 2.6$ ppm. Clearly the prediction of the two-equation semi-implicit soot model, for the current kinetic mechanism, is far from the reference data.

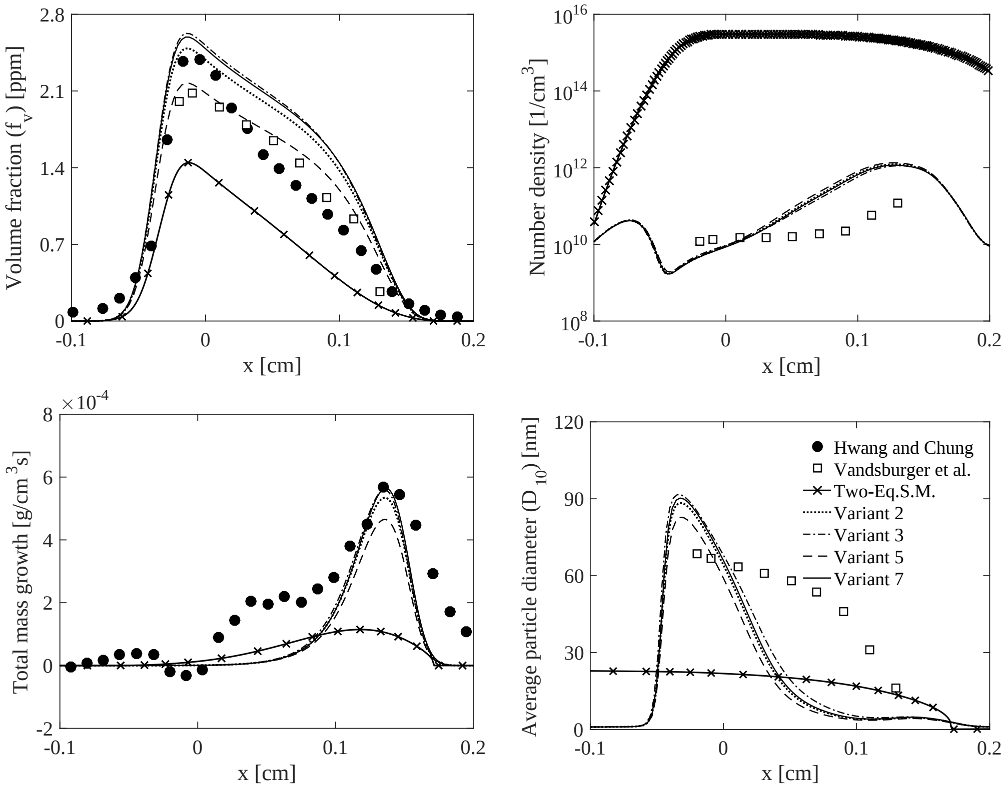

Figure C.7 – Comparison between variants of the DSM for the soot formation flame studied by Hwang and Chung, 2001.

C.2.3 Non-adiabatic soot formation/oxidation counterflow flame

The reference is a counterflow non-premixed flame explored by Hwang and Chung, 2001. It consist of burning a mixture of ethylene (25%) and nitrogen (75%) with the oxidizer formed by 90% of O_2 and 10% of N_2 at atmospheric conditions. Compositions in molar basis. Reactants temperature are equal to 300 K. Figure C.8 presents the flame structure and the agreement with the numerical data of the reference.

Variants of the DSM are compared in Figure C.9 for soot volume fraction and total soot mass growth. It is observed that *Variant 1* and *Variant 2* tends of overpredict significantly the soot mass growth, indicating that this flame is very sensitive to both the assumption of $\alpha = 1$ or the fully conserved surface radicals. Althouth its oxidation is also expressive, the soot volume fraction for these two variants reaches values of approximately 1.5 ppm while the reference value is about 0.2 ppm. An additional simulation assuming depleted surface radicals but with variable steric factor ($\alpha = f(d_p, T)$) predicted a soot volume fraction close to 0.1 ppm. Adjusting the treatment of the surface radicals to

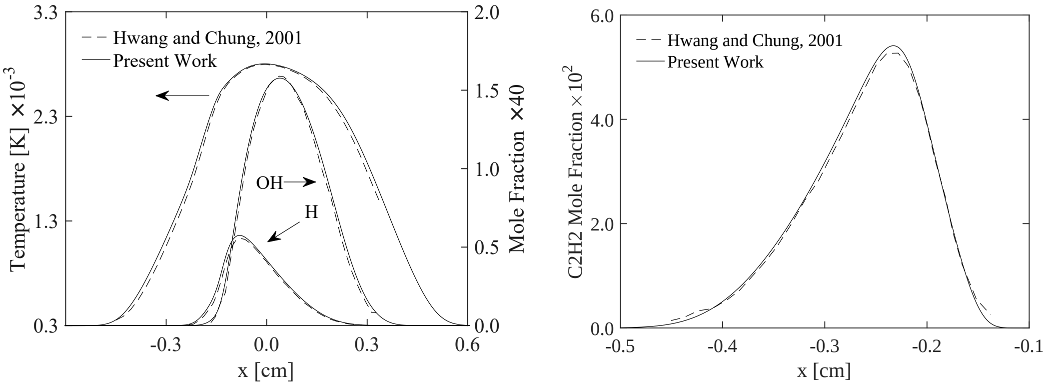

Figure C.8 – Comparison between numerical predictions of the flame structure at $a = 40$ s^{-1} for the soot formation/oxidation ethylene flame.

$\xi_{dc} = 0.2$ makes *Variant 5* and *Variant 7* to meet the experimental data. The semi-empirical Two-Equation soot model did not converge for the current flame.

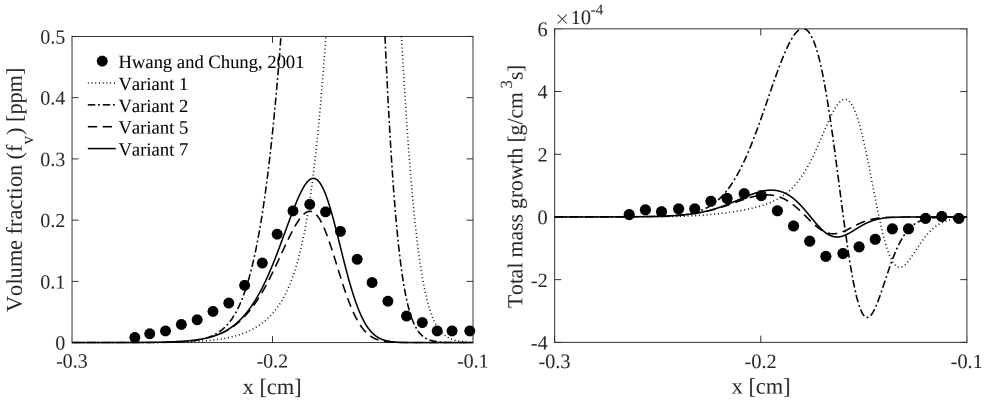

Figure C.9 – Comparison between variants of the DSM for the soot formation/oxidation flame studied by Hwang and Chung, 2001.

C.3 Conclusion

Several key soot model parameters has been explored. The assessment has been performed for three different laminar non-premixed ethylene flames with distinct sooting characteristics. It includes adiabatic soot formation, non-adiabatic soot formation and non-adiabatic soot formation/oxidation flames. It was observed that soot characteristics are very sensitive to to variations in surface growth processes. For the soot formation flames, the assumption of conserved surface radicals with variable steric factor presented results closer to the experimental data. For soot formation/oxidation flamesOn the other hand, it is more adequate to assume depleted surface radicals with variable steric factor to approach the reference data. Adjusting the number of surface sites available for surface growth was sufficient to achieve a good agreement with the experimental data from the references. It was also observed that the role of additional surface reactions (SR7 - SR9) in the HACA-extended mechanism was important only when the conservation of surface radicals was assumed. Sooting characterístics are much more sensible to the surface radicals treatment than the inclusion of reacions SR7-SR9 in the HACA-based mechanism.